THE UNIVERSITY OF MICHIGAN

INDUSTRY PROGRAM OF THE COLLEGE OF ENGINEERING

THE COALESCENCE OF MICRON-SIZE DROPS IN LIQUID-LIQUID DISPERSIONS IN FLOW PAST FINE-MESH SCREEN

Carl G. Vinson, Jr.

A dissertation submitted in partial fulfillment
of the requirements for the degree of
Doctor of Philosophy in the
University of Michigan
1964

January, 1965

IP-691

ACKNOWLEDGEMENT

The author is indebted to many individuals for their advice and encouragement during the course of this work. Gratitude is particularly due the following:

Professor S. W. Churchill, chairman of the doctoral committee, for his leadership, many suggestions and critical analysis.

Professors R. L. Curl, G. Parravano, H. J. Smith, M. R. Tek, J. O. Wilkes, C.-S. Yih and J. L. York for their discussions and criticism.

Professor W. C. Bigelow for the suggestion of fine-mesh screen for the coalescing medium.

Mr. F. B. Drogosz for his enthusiastic advice and assistance in the construction and operation of the experimental equipment.

Many colleagues, particularly Mr. D. R. Johnson, for suggestions and help throughout the work.

The shop personnel of the Department of Chemical and Metallurgical Engineering for their skill and interest.

The Industry Program of the College of Engineering for support and assistance in the preparation of this dissertation in its final form.

The Proctor and Gamble Company and the Diamond Alkali Company for their respective fellowships.

TABLE OF CONTENTS

TABLE OF CONTENTS (CONT'D)

LIST OF TABLES

LIST OF TABLES (CONT'D)

LIST OF FIGURES

LIST OF FIGURES (CONT'D)

LIST OF FIGURES (CONT'D)

LIST OF FIGURES (CONT'D)

ABSTRACT

The coalescence of dispersions of organic solvent drops, whose diameters were between two and four microns, from solvent-in-aqueous-solution dispersions in flow past fine-mesh screens was studied quantitatively. Drop concentrations were calculated from forward angle scattering measurements. A surface treatment caused the screens to have a strong affinity for the drops and removed screen wettability as a variable. Measurements were performed at Reynolds numbers between 0.008 and 5.1 based on the properties of the aqueous solution, the interstitial velocity and the size of the interstice of the screen. Over this range, interstitial velocity, screen filament width and continuum viscosity had the strongest effect on coalescence. Coalescence declined as any one of these variables was increased. With an increase in drop viscosity over the range of 0.8 to 24 centipoise, coalescence increased slightly. Interfacial tension above 30 dynes per centimeter had no effect. Although intermediate levels were not studied, an interfacial tension below 11 dynes per centimeter was accompanied by a decline in coalescence. The high initial coalescence at 11 dynes per centimeter suggested that desorption of the screen treating agent occurred in systems of low interfacial tension.

A correlation was prepared which predicts the coalescence of the drops in the dispersions used. The correlation and experimental observations showed that over the range of variables studied the salient factors were the relation between drop and screen interstice size,

viscous shear and the adhesion of the coalesced material to the filaments. These factors were expected to be important in other fiber packed coalescers and for water-in-solvent dispersions. Some of the data employed appeared to manifest drop inertia in addition to the above three factors. The coalescence on various numbers of layers of screen could be related by computing the compound fractional decrease in drop concentration from the fractional decrease on one layer of screen.

The drop size distributions of the coalesced material which was broken off of the filaments were not measured. Visco-elastic and electric double layer effects were not studied.

INTRODUCTION

Coalescence is the process by which two or more packets of liquid combine into one. The process is usually initiated by a collision between the packets which is of sufficient force to rupture any intervening film of molecules. Once the packets are in physical contact, the process is completed by surface forces. Fibrous filters are an attractive means of implementing the coalescence of microscopic drops in liquid-liquid dispersions. Their effectiveness arises from their ability to hold up a substantial quantity of the drop phase in the flow, and to provide a tortuous flow path through the material retained. The probability that a dispersion drop, which moves through the interstices, will coalesce with the retained material is enormous in comparison with the probability that the drop will be caused to coalesce with other drops by random molecular motion.

The problem of removing drops from liquid-liquid dispersions frequently arises when it is necessary to separate two liquid phases which have been in such intimate contact that the drops of the discontinuous phase do not settle readily because they are too small or the density difference is too slight. In such circumstances, the fiber-packed coalescer is the simplest and most economical separating device.(50)

The quantitative experiments in the related field of aerosol filtration have greatly facilitated the design of fibrous gas filters.(49,54,62,63) However, measurements of the coalescence of liquid-liquid dispersions on fibrous beds have not been equally definitive. Burtis and Kirkbride measured the extent of desalting of crude oil on beds of

Fiberglas.(7,8) Since the crude oils they used contained many trace components in addition to salt, an accurate description of the physical properties of the water-in-crude systems was not possible. Although simple mixtures of organic compounds and water were used, subsequent investigations have relied upon qualitative appraisals of the extent of coalescence. Measurements of neither the drop concentration distribution nor microscopic bed geometry were made.

The goal of this investigation was to determine the effect of flow rate, microscopic bed dimensions and physical properties on the coalescence of dispersions on a single type of fiber-like medium. The medium was fine-mesh nickel screen which was treated to have reproducible surface characteristics. The screen permitted exact definition of its geometric characteristics. Light scattering measurements by the moving lens-pinhole method(13,14) were used to measure drop concentrations and size distributions. Pressure drop was not simultaneously measured since it did not appear to be relevant to coalescence. Pressure drop correlations for the flow through fibrous media are available.(9,24,28,52,61) Visco-elastic and electrical double layer effects were not examined. When present, such effects would be likely to predominate and reduce the effectiveness of a simple fiber-packed coalescer.

Literature Survey

Burtis and Kirkbride appear to have been the first to make a comprehensive study of coalescence on fibrous medium.(7,8) In a study of desalting of brine-in-crude oil emulsions by Fiberglas, they found that desalting improved with decreased velocity, decreased viscosity and increased bed density. The effect of increased bed density was attributed to a reduction in the size of the interstices.

Rose(50) reported on the findings of Voyutskii _et al._,(58) who found, for the clarification of water-in-oil emulsions, a flow velocity above which coalescence on the fibrous bed was negligible. Highly hydrophilic media were prone to clog with water. Some compromise on the degree of wettability of the filaments was indicated. They ascribed the effectiveness of the bed to its total surface area rather than to the sizes of the interstices or filaments.

In an investigation of the removal of suspended water from aircraft fuel, Arthur D. Little, Inc. concluded that clarification improved with decreased pore size but at the expense of pressure drop.(1) Hydrophilic fibers had a greater affinity and retaining capacity for water and gave a more complete water removal. However, at the outlet of a bed of these fibers, a honeycomb structure of water films tended to form and to disintegrate into a secondary water-in-oil dispersion. It was suggested that the foam could be eliminated by a coarse hydrophobic mat at the bed outlet.

Rose compared several media for a variety of oil-in-water and water-in-oil dispersions.(50) Fiber wettability was paramount in most cases. However, the ability of Teflon fiber to coalesce water from kerosene was attributed to electrostatic effects. Cotton and glass, two inherently polar substances, removed some of the water from isobutanol; the interfacial tension of the isobutanol-water system was 2.1 dynes per centimeter. No inherently hydrophobic filament was capable of removing isobutanol drops from water. Low interfacial tension was generally accompanied by a low level of coalescence. The failure of all of the media studied to remove nitrobenzene from water was thought to be caused by the polarizing action of nitrobenzene. Wherever it occurred, foaming at the outlet of the bed could be eliminated by making the bed more compact. It was noted that coalesced material tended to accumulate at particular sites in the bed.

Uhl and Furini recently reviewed a number of the mechanisms of coalescence.(56)

Aerosol filtration is similar to coalescence on fibrous media with respect to geometry and some physical property variables. Two reviews of aerosol theory and experiment are available.(12,25) Witzmann was one of the first to study aerosol filtration.(62) He condensed dye vapor to form fogs whose average particle diameter was 0.24 micron. A colorimetric measurement gave the particle concentration. Using filter papers and porous glass filters, he found that the percentage of dye absorbed by the filter was considerably increased as the pore size was reduced. The larger drops were more readily removed when the fog was passed through a given filter. He stated that the particle must wet the surface of the filter in order to achieve satisfactory efficiency.

The increase in the extent of filtration with an enlargement of the ratio of particle size to interstitial distance has been confirmed.(26,49,54) Thomas and Lapple(54) found that at a velocity of 1.2 feet per minute flow direction had no effect on aerosol collection on a filter whose total thickness was 0.54 inch. However, the lack of an effect of gravity was conditioned by the sub-micron aerosol particles employed.

Interesting conclusions on the filtration of sulfuric acid mists were presented by Fairs.(21) He found that highly hydrophilic filters clogged readily with entrapped acid and filter performance was impaired.

Organization

This thesis has three main sections. The theoretical section considers four steps in the process of coalescence on fibrous filters. References to previous work are made in the discussion of each step. A comprehensive theory was not constructed because of a current lack of understanding of the microscopic characteristics of a liquid-liquid and of a liquid-solid interface which influence each step. The experimental section treats the construction of the equipment and experimental procedures. A portion is devoted to a summary of the theory of the calculation of particle size distributions from forward-angle-scattering measurements. The final section deals with the analysis of experimental data. The postulated mechanisms are tested with the data and a correlation predicting the coalescing ability of fibrous media is presented.

PART I

THEORY

THE CONCEPT

The coalescence of drops in liquid-liquid dispersions is considered to involve four steps. First, the flow brings a drop into juxtaposition with a filament of the filter except for an interposed microscopic layer or film of continuous phase. Second, the film thins and ruptures. Third, the drop spreads on the filament and coalesces with other spread-out drops. Fourth, the coalesced material accumulates until it either drains off the matrix of filaments or is shorn away by the flow.

It is possible that the drops are merely trapped at certain places in the matrix without making physical contact with the filaments. The trapped drops would be enlarged by direct impingement by other drops in the flow and finally would be carried away. The assumption of mere entrapment does not offer a satisfactory explanation of the wide difference in coalescence performance which has been observed for different types of filter media.(50) The more plausible explanation is that the drops do make physical contact with the filaments. A variation in the affinity between the drops and the filaments would alter the drops' ability to wet and cling to the filaments.

It is unlikely that the removal of drops from dispersions occurs by filling the pores of the filter. The drops are usually small in comparison with the interstices.

The juxtaposition between the drop and the filament may be termed "mathematical capture,""virtual capture" or "interception."

Interception is considered to occur under the influence of gross hydrodynamic effects. The drops in the moving dispersion are treated as infinitesimal particles which neither interact nor disturb the flow. Each drop whose trajectory passes within the drop radius of the filament is assumed to be intercepted by the filament. When the drop concentration is low and the drops are small compared with the interstices, this is a useful approximation. However, when the surface of the drop is only a fraction of the radius away from the filament, the flow of the intervening fluid is affected by the distance of separation, by the motion of the drop and by short range forces between the drop and the filament. The behavior of the film between the filament and the intercepted drop is logically set apart from the gross hydrodynamic effects which are considered to lead to drop interception. If the film ruptures to allow the drop to make physical contact with the filament, surface forces on the filament are predominant. They determine the ease of spreading and coalescence on the filament and the ability of the dispersed phase to adhere. The coalesced material is considered to be detached from the filaments by the gross hydrodynamic effects of the flow.

DROP INTERCEPTION IN A LAMINAR FLOW

The motion of the continuous phase of a dispersion through a stationary matrix of fibers is given by the complete Navier-Stokes equations for an incompressible fluid. If the particles are small and dilute, the effect of the particles on the flow can be ignored. The equations in cartesian co-ordinates are:

$$\frac{D\vec{U}}{D\tau} = -\frac{1}{\rho_C}\,\text{grad}\,(P + \rho_C\Omega) + \nu_C\nabla^2\vec{U} \tag{1}$$

$$\frac{\partial u_x}{\partial x} + \frac{\partial u_y}{\partial y} + \frac{\partial u_z}{\partial z} = 0 \tag{2}$$

The terms in Equations (1) and (2) have the following meanings:

τ is time;
x, y and z refer to position in cartesian co-ordinates;
$\vec{U}$ is the velocity vector;
u_x, u_y and u_z are the components of the velocity vector in the positive x, y and z directions, respectively;
ρ_C is the density of the continuum;
P is the pressure;
Ω is the body force potential per unit mass of fluid, which can compromise, for example, the portentials of gravity, electrostatic force, and magnetic force;
and,
ν_C is the kinematic viscosity of the continuum and equals μ_C/ρ_C, where μ_C is the continuum viscosity.

If the motion is steady and very slow, the substantial derivative can be neglected in Equation (1).

The criterion for the solid sphere behavior of a drop falling in a gravity field is $|\rho_D - \rho_C| g d_P^2/\gamma_{CD} \leq 0.1$.(33) In this group, ρ_D is the drop density, d_P is the drop diameter, g is the acceleration of gravity, and γ_{CD} is the interfacial tension between the dispersed and continuous phases. If, instead of gravity, the acceleration is due to hydrodynamic forces, the criterion assumes the following form: $|\rho_D - \rho_C| U^2 d_P/\gamma_{CD} \leq 0.1$, where U is a characteristic velocity and U^2/d_P is a liberal estimate of particle acceleration. If U is less than ten centimeters per second this condition is easily satisfied by a drop whose diameter, d_P, is 10^{-3} centimeters, even for very low values of interfacial tension.

Coalescence is usually accomplished at velocities of one foot per minute or less. A Reynolds number for a ten-micron drop which moves in water at a velocity of one foot per minute would be 0.05. The Stokes drag relation is applicable.

If a liquid-liquid dispersion is dilute, the drops experience little interaction. Each drop can be considered to act as an isolated particle. On the basis of an equation given by Fuks,$^{(25)}$ the following expression can be written for the motion of a spherical particle at low Reynolds numbers in a fluid which moves in a slow and steady manner.

$$\frac{\pi}{6}\rho_D d_P^3 \frac{d\vec{W}}{d\tau} = 3\pi\, d_P \mu_C (\vec{U} - \vec{W}) + \sum_i F_i$$

$$- \frac{1}{2}\frac{\pi}{6}\rho_C d_P^3 \frac{d\vec{W}}{d\tau} - \frac{3}{2} d_P^2 \sqrt{\pi\rho_C\mu_C}\int_0^\tau \frac{d\vec{W}}{d\xi}\frac{d\xi}{\sqrt{\tau-\xi}} \qquad (3)$$

where $\vec{W}$ is the velocity vector of the particle, the summation, $\sum_i F_i$, is the composite of forces other than drag which act on the particle and ξ is a dummy variable. The first term on the right gives the effect of Stokes drag and the third and fourth terms give the effect of the medium on the acceleration of the particle. The fourth term on the right may be integrated if it is assumed that the particle acceleration is constant over the period of time in which it occurs. Rearrangement after integration gives:

$$\left\{\frac{\pi}{6} d_P^3 \left(1 + \frac{1}{2}\frac{\rho_C}{\rho_D}\right) + 3 d_P^2 \sqrt{\pi\rho_C\mu_C\tau}\right\}\left(\frac{dW}{d\tau}\right) =$$

$$= 3\pi d_P \mu_C (\vec{U} - \vec{W}) + \sum_i F_i \qquad (4)$$

Equation (4) may be made dimensionless by the following substitutions: $\tilde{\tau} = 2\tau U_\infty / d_F$, $\tilde{\vec{U}} = \vec{U}/U_\infty$, and $\tilde{\vec{W}} = \vec{W}/U_\infty$. In this conversion, d_F is the diameter of the filaments in the fibrous bed and

U_∞ is the upstream or superficial velocity of the continuum which is taken parallel to the x axis. When these substitutions are made in Equation (4) and the resulting expression is divided by $3\pi d_P \mu_C U_\infty$, the following is obtained:

$$\left[\beta\left(2 + \frac{\rho_C}{\rho_D}\right) + 6\left(\frac{\rho_C \beta}{\pi \rho_D}\right)^{1/2}\right] \left(\frac{d\vec{W}}{d\tau}\right) = \vec{\tilde{U}} - \vec{\tilde{W}} + \frac{1}{3\pi U_\infty \mu_C d_P} \sum_i F_i \qquad (5)$$

where

$$\beta = \frac{1}{18} \frac{\rho_D U_\infty d_P^2}{\mu_C d_F} \qquad (6)$$

The parameter β is known as the inertial parameter in aerosol technology. It is the ratio of the kinetic energy of the particle relative to the work done by viscous forces when the particle is stopped in the distance of one filament radius. The parameter measures the tendency of the suspended particle to exhibit its inertia and collide with an obstacle in the flow. It has been shown that a β of 1/16 is the minimum value at which a particle in air can by its own inertia collide with a cylinder.(5,25) Suppose an aqueous continuum were flowing at a velocity of one foot per minute past a filament having a diameter of ten microns. The inertial parameter for a particle or drop whose density is two grams per cubic centimeter and whose diameter is ten microns would be 0.0028. In this case, the coefficient of reduced acceleration in Equation (5) would be 0.134. Were the continuum air, only the 2β would be important in the coefficient. Since the limiting value of 2β for inertial impaction is 0.125, the example suggests that inertia comes into play under the conditions chosen.

In the coalescence example cited, the preponderant term in the coefficient of reduced acceleration is:

$$\frac{6}{\sqrt{\pi}}\left(\frac{\rho_C\beta}{\rho_D}\right)^{1/2} = \left(\frac{2\rho_C U_\infty d_P^2}{\pi\,\mu_C d_F}\right)^{1/2} \tag{7}$$

Since Equation (7) involves no physical property of the particle, it can be concluded that the inertia of the particle depends primarily upon the inertia of an equal volume of continuum, which appears to be dragged along by the particle. The choice of the acceleration scale is arbitrary. Another choice which was found to be more meaningful for coalescence is based upon the degree of convective acceleration experienced by the particle volume of continuum over the half width of an interstice: $u_y(\partial u_x/\partial y) \sim (2U_o^2/d_I)$, where d_I is the width of the interstice and U_o is the interstitial velocity. This choice leads to the following modified inertial parameter for coalescence, when U_o also replaces U_∞ in the Stokes drag:

$$\beta' = \left(\frac{2\rho_C d_P^2 U_o}{\pi\, d_I \mu_C}\right)^{1/2} \tag{8}$$

The d_I in Equation (8) replaces the d_F in Equation (7). If d_F and d_I are of comparable size, the limiting value of 2β in aerosol studies should also be applicable to β' .

If, in the above example of drop inertia, the drop diameter were reduced slightly, the coefficient of the reduced acceleration would fall below 0.125 and the insignificance of inertia would be inferred. If drag were the only other force acting, Equation (5) would reduce to:

$$\vec{\tilde{W}} = \vec{\tilde{U}} \tag{9}$$

The motion of the drop is indistinguishable from the continuum.

The postulate of Equation (9) forms the basis for the calculation of particle interception.(41) The calculation of the extent of particle interception reduces to a calculation of the maximum percentage of the flow of a homogeneous fluid which passes within a drop radius of the filaments. In viscous flow, the velocity profile is symmetrical about each obstacle in an ordered array of obstacles. Figure 1, for an array of parallel cylinders, shows that the closest approach of the streamlines to the cylinders is in the constriction, $x = 0$.

Interception by Equally-spaced Parallel Cylinders

Miyagi obtained a periodic solution for the two-dimensional viscous flow perpendicular to an array of parallel, equally-spaced, cylinders.(44) His idealization is a fair representation of laminar flow through a fibrous bed.

Miyagi used the viscous flow equations of two-dimensional flow.

$$\frac{\partial P'}{\partial x} = \mu_C \nabla^2 u_x \tag{10}$$

$$\frac{\partial P'}{\partial y} = \mu_C \nabla^2 u_y \tag{11}$$

$$\frac{\partial u_x}{\partial x} + \frac{\partial u_y}{\partial y} = 0 \tag{12}$$

The P' is the sum of the static pressure and the body force potential per unit volume, $P + \rho_C \Omega$. The co-ordinates were as shown in Figure 1 with the origin at the center of one of the cylinders and the x axis parallel to the upstream velocity and perpendicular to the plane of the cylinders. The boundary conditions for the flow of the cylinders through the fluid, which is at rest at infinity, were:

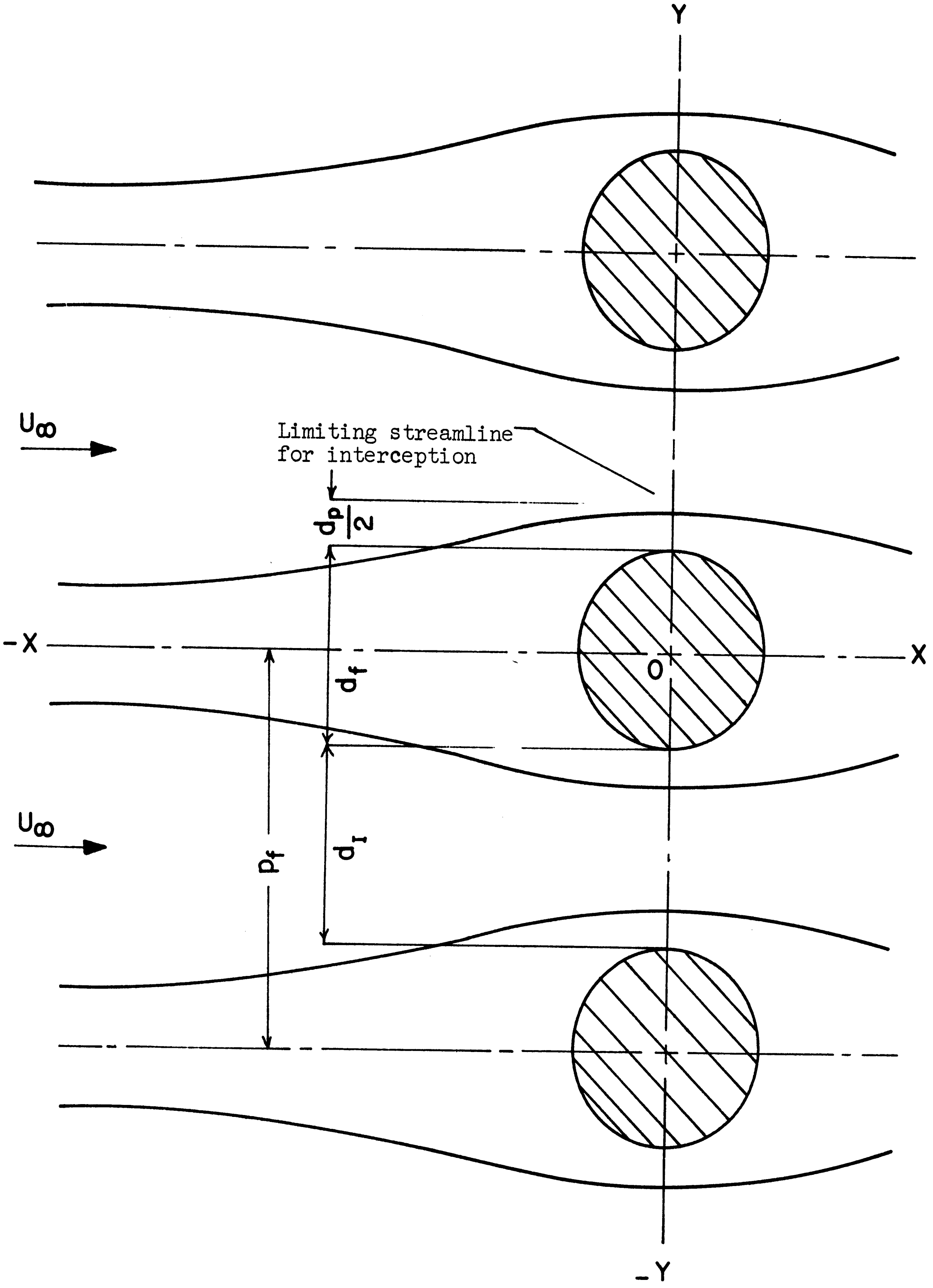

Figure 1. Laminar Flow Past Parallel Cylinders.

$$\left.\begin{aligned} u_x &= -U_\infty \\ u_y &= 0 \end{aligned}\right\} \text{ at the surface of the cylinders} \qquad (13)$$

$$u_x = u_y = 0 \quad \text{at} \quad x = \pm\infty \qquad (14)$$

The Laplacian of the vorticity was obtained by differentiating Equation (10) with respect to y and Equation (11) with respect to x and subtracting.

$$\frac{\partial}{\partial x}\nabla^2 u_y - \frac{\partial}{\partial y}\nabla^2 u_x = \nabla^2\omega = 0 \qquad (15)$$

$$\omega = \frac{\partial u_y}{\partial x} - \frac{\partial u_x}{\partial y} \qquad (16)$$

Complex variables were introduced: $z = x + iy$; $\bar{z} = x - iy$. Under the transformation, $w = u_x - iu_y$, Equations (15) and (16) become:

$$\nabla^2\omega = \frac{\partial^2\omega}{\partial z\partial\bar{z}} = 0 \qquad (17)$$

$$\omega = 2i\,\frac{\partial w}{\partial\bar{z}} \qquad (18)$$

The solution for ω was given as:

$$\omega = \Omega(z) + \bar{\Omega}(\bar{z}) \qquad (19)$$

An expression for $\Omega(z)$ which satisfied Equation (17) and was periodic throughout the flow field had the form:

$$\Omega(z) = \frac{2\pi U_\infty}{i\ p_F} \sum_{n=0}^{\infty} a_{2n} \frac{d^{2n}}{d\zeta^{2n}} \coth \zeta \tag{20}$$

where $\zeta = \pi z/p_F$ and where p_F is the pitch of the cylinders. Equation (13) was substituted into Equation (15) and the integration with respect to $\bar{z}$ performed. The boundary condition at infinity, $w = 0$, generated:

$$\begin{aligned} \frac{w}{U_\infty} &= a_o \left[\ln(2 \sinh \bar{\zeta}) + \ln(2 \sinh \zeta) - (\zeta + \bar{\zeta}) \coth \zeta \right] \\ &+ \sum_{n=1}^{\infty} a_{2n} \left[\frac{d^{(2n-1)}}{d\zeta^{(2n-1)}} \coth \bar{\zeta} - (\zeta + \bar{\zeta}) \frac{d^{2n}}{d\zeta^{2n}} \coth \zeta \right] \\ &+ \sum_{n=1}^{\infty} b_{2n} \frac{d^{2n-1}}{d\zeta^{2n-1}} \coth \zeta \end{aligned} \tag{21}$$

The series coefficients, a_o, a_{2n} and b_{2n}, were determined by the boundary condition at the surface of the cylinders, $w/U_\infty = -1$. The coefficients were delivered in terms of infinite series in the group, $\pi d_F/2p_F$. If $d_F/p_F \geq 2/\pi$, the convergence of the series coefficients was questionable.

In order to compute the maximum amount of fluid approaching within particle capture distance of the filament, only the velocity in the constriction, $x = 0$, is required.

$$\begin{aligned}\left(\frac{u_x}{U_\infty}\right)_{x=0} = 1 + a_0 \ln 2(1-Y) &+ \frac{2(a_2+b_2)+8(a_4+b_4)+32(a_6+b_6)+128(a_8+b_8)+ \dots}{1 - Y} \\ &- \frac{24(a_4+b_4)+480(a_6+b_6)+(84\cdot 96)(a_8+b_8)+ \dots}{(1 - Y)^2} \\ &+ \frac{960(a_6+b_6)+(128\cdot 120)(a_8+b_8)+ \dots}{(1 - Y)^3} \\ &- \frac{16\cdot 7!(a_8+b_8)+ \dots + \dots}{(1 - Y)^4}\end{aligned} \tag{22}$$

In Equation (22), $Y = \cos\left(\frac{2\pi y}{P_F}\right)$. In principle Equation (22) can be integrated from $y = d_F/2$ to $y = (d_F+d_P)/2$. However, with the limited number of coefficients available, the equation does not quite satisfy the boundary condition at the surface of the cylinder. The convergence of the numerators of Equation (22) could not be ascertained. The Miyagi solution does indicate the importance of the relation between drop diameter, filament diameter and filament pitch. The relation between the filament thickness and filament pitch determines the flow profile. The relation between the drop size and interstitial distance determines the fraction of the flow which is intercepted at a drop radius from the filament.

Single Interstice Model of Interception

Since the greatest volume of fluid comes into the proximity of the filament surfaces in the interstice, a simple approach to the calculation of drop interception is to obtain a flow profile which is specific for the interstice. Only the axial velocity component is present. Fuks suggested that particle interception in aerosol filtration be calculated with the assumption that the fibers are aligned in a hexagonal array which is perpendicular to the flow.(25) It was suggested that the velocity profile for fully developed laminar flow between parallel plates be used for the interstitial flow profile. The distance between the plates was the width of the interstice. Although a useful approach, the flow profile in an interstice can hardly be fully developed. It is likely that the actual profile would be much flatter, as suggested by Wang and Longwell in a study of laminar flow at the entry section of two parallel plates.(59)

Since the filaments in a fibrous mat are laid down in a random fashion, it is possible to view the interstice as a circular pore. This is a fair approximation for a fine-mesh screen. Following Fuks, the flow profile for fully developed laminar flow in a pipe can be assumed.

$$u_x = 2U_o \left(1 - (2r/d_I)^2\right) \qquad (23)$$

In Equation (23), d_I is the diameter of the interstices, r is the radial distance from the center and U_o is the average interstitial velocity.

A more suitable profile might be that for the flow through an isolated elliptical aperture in a thin wall. Hasimoto(32) obtained this profile as an extension of the theory given by Lamb.(39) The describing equations were the ones used by Miyagi, Equations (10), (11) and (12), with the origin at the center of the aperture. The boundary conditions were:

$$\vec{U} = 0 \quad \text{on the wall of the aperture,} \quad x = 0 \tag{24}$$

$$P' = P = \mp P_\infty/2 \quad \text{as} \quad x \text{ goes to } \pm\infty \tag{25}$$

where body forces were neglected, and where P_∞ is the pressure at infinity. Because of symmetry, only the positive half space was considered. The solution which was given is:

$$\vec{U} = i\,\Phi - x \operatorname{grad} \Phi \tag{26}$$

$$P = -2\,\mu_C(\partial\Phi/\partial x) \tag{27}$$

where i is the unit vector in the x direction. The function Φ was shown to be the potential function for the ideal flow past an ellipsoid having an infinitesimal thickness along the x axis. Lamb gave the following expression for the flow potential:

$$\Phi = Cx \int_{\lambda}^{\infty} \frac{d\lambda}{\lambda^{3/2}(A^2+\lambda)^{1/2}(B^2+\lambda)^{1/2}} \tag{28}$$

where C is a constant and λ is the positive root which satisfies

$$\frac{x^2}{\lambda} + \frac{y^2}{A^2+\lambda} + \frac{z^2}{B^2+\lambda} = 1 \tag{29}$$

The A and B are the major and minor radii of the ellipse. Using the method of Lamb, it can be shown that

$$\Phi = \frac{2C}{AB}\left(1 - \frac{y^2}{A^2} - \frac{z^2}{B^2}\right)^{1/2} \tag{30}$$

where C is a constant. Substitution of Equation (30) into Equation (26) gives for a circular aperture

$$u_x = 3/2\ U_o \sqrt{1 - (2r/d_I)^2} \tag{31}$$

In their analysis of laminar flow between two parallel plates, Wang and Longwell found that the entrance velocity profile was nearly flat.(59) A flat velocity profile in the interstice would give an upper limit to the fraction of the drops intercepted. For the circular interstice

$$u_x = U_o \tag{32}$$

Equations (23), (31), and (32) may be integrated between the limits $(d_I-d_P)/2$ and $d_I/2$. Division by the total flow through the interstice gives the fraction of the particles or drops which are intercepted in the flow through the interstice.

$$f_{\substack{\text{laminar}\\ \text{pipe}}} = \frac{4\pi U_o \int_{(d_I-d_P)/2}^{d_I/2} r(1-(2r/d_I)^2)dr}{(\pi/4)\ U_o\ d_I^2}$$

$$= \left[2(d_P/d_I) - (d_P/d_I)^2\right]^2 \tag{33}$$

$$f_{\substack{\text{isolated}\\\text{hole}}} = \left[2(d_P/d_I) - (d_P/d_I)^2\right]^{3/2} \qquad (34)$$

$$f_{\substack{\text{flat}\\\text{profile}}} = 2(d_P/d_I) - (d_P/d_I)^2 \qquad (35)$$

Equations (33), (34), and (35) are plotted in Figure 2. The curves for the isolated hole and the flat profile are considered more representative. In all cases, d_P/d_I has a strong effect on mathematical capture. Interception in a single hole gives no indication of the effect of filament size.

INTERCEPTION BY BODY FORCES

Equation (5) shows that a dispersion drop can, under the influence of body forces, exhibit motion which is independent of the continuum. Two body forces frequently encountered are gravity and electrostatic repulsion. In analogy with the limiting coefficient of reduced particle acceleration of aerosol theory, a body force is not expected to be significant unless its ratio to Stokes drag is in the vicinity of 0.125, say at least 0.1 .

Gravitational Force

Gravity can create a relative particle velocity parallel or transverse to the main flow or both. A settling velocity component parallel to the flow affects any phenomena in coalescence which depend on the period of contact between the drop and the filament. A perpendicular settling velocity component causes drops which, for example,

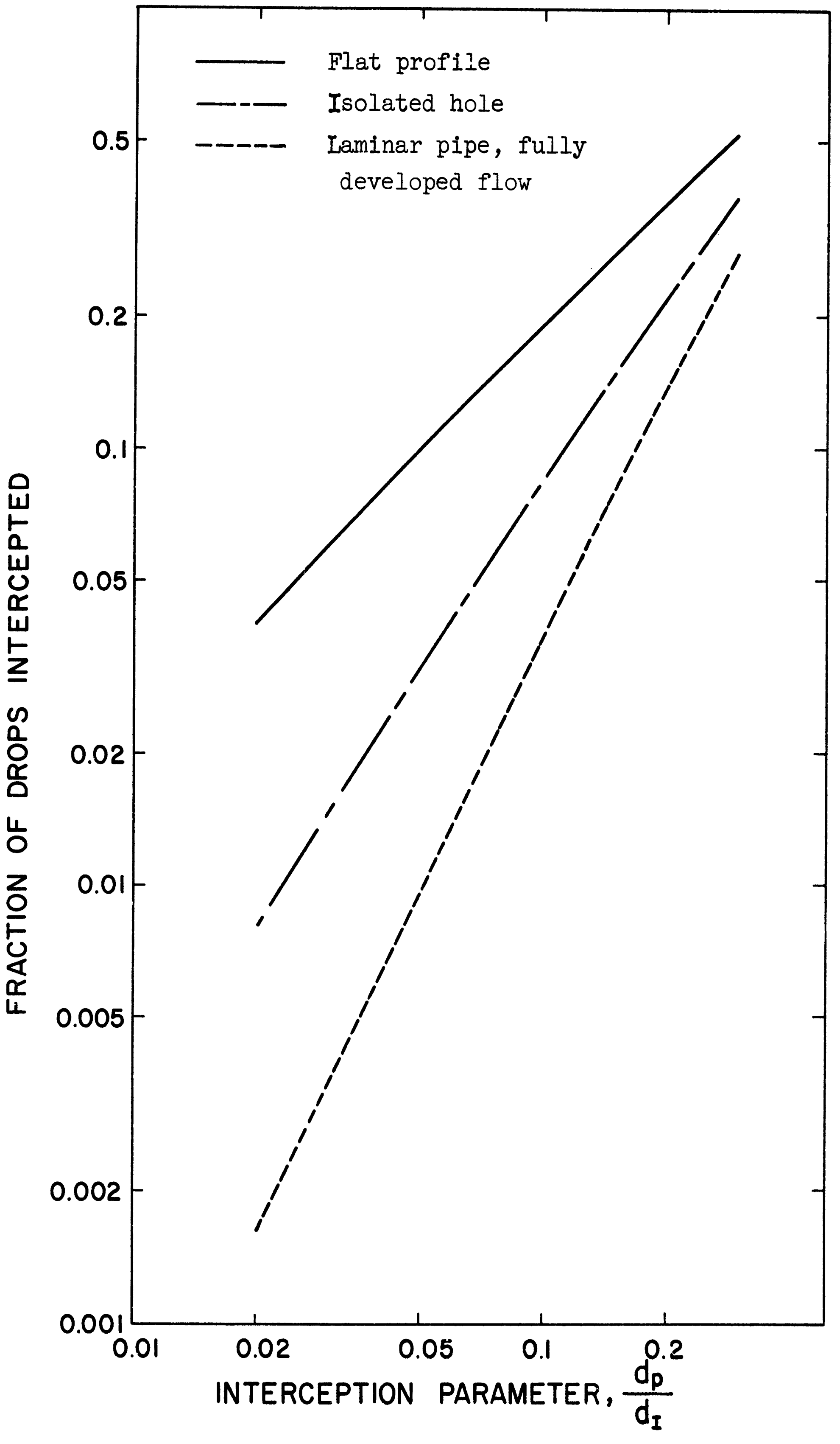

Figure 2. Predicted Drop Interception in a Circular Interstice.

are lighter than the continuum to settle toward the upper-half surface and away from the lower-half surface of filaments which are inclined to the vertical. These tendencies completely offset each other; a gravity component transverse to the flow has no effect. The ratio of the gravitational force to Stokes drag is:

$$\frac{\vec{F}_g}{3\pi\mu_C d_P U_\infty} = \frac{(\pi/6)(\rho_D-\rho_C)d_P^3\,\vec{g}}{3\pi\mu_C d_P U_\infty} = \frac{1}{18}\,\frac{(\rho_D-\rho_C)d_P^2\,\vec{g}}{U_\infty\mu_C} \qquad (36)$$

In order to estimate a maximum size of this parameter, let it be assumed that ten-micron drops having a density of 2.0 grams per cubic centimeter are suspended in water which is moving through a fibrous medium at a superficial velocity of 0.1 foot per minute. The dimensionless gravitational force would have a value of 0.11. In this case of extreme density difference, a gravitational force acting parallel to the upstream velocity could have a noticable effect. The effect is sensitive to drop diameter and becomes negligible as the diameter decreases.

Electrostatic Repulsion

Drops which acquire an ionic charge on their surface are subject to electrostatic forces. These drops can be made to move and coalesce upon the application of an electric field. The forces of interest here are those which arise from the interaction of ionic double layers around the drops and filaments.

Various treatments of double layer potentials and double layer forces are available.(2,18,42,57) The appearance of an electrical double layer is attributed to the preferential adsorption of ions of one kind at a liquid-solid or a liquid-liquid interface. The interfacial charge is shielded in the liquid by a somewhat diffuse layer of ions of the opposite charge known as the double layer. In polar solvents such as water, the ion concentration is usually sufficient to suppress the double layer to a thickness of 0.1 micron or less. In organic solvents, the double layer can be as thick as one micron. If a double layer appears, the potential is usually in the range of 10 to 100 millivolts. Because of the thin double layer, the electrostatic forces are highly localized. The repulsion between a micron-size drop and a filament in a fibrous mat can be considered, to a good approximation, to be free of interactions caused by the presence of other filaments and drops.

Current double layer theory is based upon the Poisson relation between charge density and potential.

$$\nabla^2\psi = -\frac{\overline{q}}{\epsilon\,\epsilon_o} \tag{37}$$

In Equation (37), ψ is the potential; $\overline{q}$, the volumetric charge density; ϵ , the dielectric constant of the solvent; and, ϵ_o , the permittivity of free space. The volumetric charge density is given by the Boltzmann distribution of electrostatic energy caused by the presence of ions.

$$\overline{q} = E \sum_k \nu_k n_{o_k} e^{-E\nu_k\psi/RT} \tag{38}$$

In Equation (38), n_{o_k} is the concentration of the k-th ionic specie in the bulk solution, ν_k is its valence, E is a Faraday, R is the gas constant and T is the absolute temperature. Derjaguin solved Equations (37) and (38) for the force of repulsion between two equal spheres under the assumption that the pair of surfaces remained at constant and equal potentials of less than 20 millivolts.(18) Although hydrodynamic forces were not taken into account, his equation would be applicable where the motion of the surfaces is slow. For a pair of univalent electrolytes, the solution for the force of repulsion between spheres of diameter d_P was:

$$F_e = \frac{\pi \epsilon \epsilon_o d_P \psi_o^2}{\delta} \left[1 - \tanh\,(h/2\delta)\right] \tag{39}$$

In Equation (39), ψ_o is the potential at the surface, h is the minimum distance between surfaces, and δ is the double layer thickness, which in the general case is computed as:

$$\delta = \left[\frac{\epsilon \epsilon_o RT}{E^2 \sum_k n_{o_k} \nu_k^2}\right]^{1/2} \tag{40}$$

In practice, ψ_o can be estimated from the zeta potential of electrophoresis measurements.

Equation (39) is not an exact description of the electrostatic repulsion between a charged drop and filament. Constant and equal surface charges and equal charge distributions in the continuum adjoining the surfaces are required. If the filament remains coated with a film of the dispersed phase, the double layer would be located at the interface between the film and the continuum. The surface potentials on the drop and the filament might, in such a case, be equal but the charge distributions would not be. In some cases the surface potentials diminish upon the approach of the surfaces.

In spite of these restrictions, Equation (39) is useful in estimating the magnitude of the electrostatic force when the surface potentials are low. The ratio with the Stokes drag is:

$$\frac{F_e}{3\pi U_\infty \mu_C d_P} = \frac{\epsilon \epsilon_o \psi_o^2}{3\delta \mu_C U_\infty} \left[1 - \tanh \frac{h}{2\delta}\right] \tag{41}$$

In order to obtain a liberal estimate of this ratio, let it be assumed that a dispersion of drops in water is moving at an upstream velocity of 0.1 foot per minute through a fibrous bed. Assume surface potentials of 20 millivolts on the filaments and drops and double layer thicknesses of 0.01 micron. The force ratio of Equation (41) for values of h of 0.01, 0.03 and 0.1 micron would be 10.15, 1.82 and 0.001, respectively. In this case, the electrostatic force would be decidedly localized and would be effective with respect to film thinning rather than drop interception. Suppose instead, that the drop were dispersed in a hydrocarbon whose dielectric constant is two and whose viscosity is 0.5 centipoise. The force ratio for a surface potential of 20 millivolts, double layer thicknesses of one micron and an h of 0.01 micron would be 0.0094 and would not increase appreciably on closer approach. In this case the effect of the double layer interaction between a drop and the filament would penetrate deeper into the flow but the effect would be everywhere negligible. Because of the low tolerance for ions, surface potentials above 20 millivolts are scarcely possible in hydrocarbons.

Brownian Diffusion

The random character of Brownian motion prevents its inclusion in the force balance for the drop. Brownian diffusion enhances mathematical capture by moving drops which would otherwise bypass the filaments into a position of interception. Brownian motion is a consequence of the random molecular impacts on the particle. Einstein gave an expression for the Brownian diffusion coefficient.(12)

$$D_{Br} = \frac{kT}{3\pi\mu_C d_P} \tag{42}$$

The k is Boltzmann's constant. Invoking random walk theory, Langmuir computed the average absolute value of particle displacement in a certain direction within the time, τ , where ζ is the displacement.(41)

$$\zeta = \left(\frac{4}{\pi} D_{Br}\tau\right)^{1/2} \tag{43}$$

Langmuir treated the combined effects of interception and Brownian diffusion on aerosol capture by an isolated cylinder. He assumed that all particles making mathematical contact with the filament remain in contact. In the vicinity of the cylinder, there was no counter diffusion. In the case of liquid-liquid dispersions, this is equivalent to assuming that all drops which are intercepted remain adjacent to the filament. He computed an effective contact time for each of the bypassing streamlines and a corresponding uni-directional displacement of the particles on the streamlines. If ζ was greater than or equal to the distance of motion necessary for contact with the filament, the particle was assumed to be intercepted.

With the assumption of no counter diffusion, Langmuir's approach can be adopted in the calculation of the maximum extent of Brownian diffusion. For this purpose, the simple interstitial velocity profile of an isolated hole, Equation (34), is used. Let it be assumed that the average contact time along the flow streamlines in the interstice is given by the filament radius over the flow velocity along the streamline. Then the extent of interception would be:

$$\Sigma f = f_{\text{interception}} + f_{D_{Br}} = \left[2\left(\frac{2\zeta+d_P}{d_I}\right) - \left(\frac{2\zeta+d_P}{d_I}\right)^2\right]^{3/2} \tag{44}$$

$$\zeta = \left(\frac{2}{\pi}\,\frac{D_{Br}d_F}{u_x}\right)^{1/2} \tag{45}$$

The maximum diffusion distance is found from a simultaneous solution of Equations (31) and (45).

$$\zeta_{max}\left[2\left(\frac{d_P+2\zeta_{max}}{d_I}\right) - \left(\frac{d_P+2\zeta_{max}}{d_I}\right)^2\right]^{1/4} = \left(\frac{4}{3\pi}\,\frac{D_{Br}d_F}{U_o}\right)^{1/2} \tag{46}$$

A characteristic parameter in this solution is the ratio of the diffusion distance at the average interstitial velocity to the radius of the circular interstice.

$$\frac{2\zeta}{d_I} \simeq \left(\frac{4}{\pi}\,\frac{D_{Br}d_F}{U_o d_I^2}\right)^{1/2} = \left(\frac{4kTd_F}{3\pi^2 U_o d_P d_I^2 \mu_c}\right)^{1/2} \tag{47}$$

As an example of the extent of diffusion, let it be assumed that a dispersion of one-micron drops in water at 20°C is flowing at a velocity of 0.1 foot per minute past a fibrous mat whose interstices and filaments have the dimensions of ten microns. The maximum diffusion distance would be 0.15 micron. The fraction of the drops intercepted in the presence of Brownian diffusion according to Equations (42) and (46) would be 0.12 as compared with 0.083 without Brownian diffusion. The example shows that Brownian diffusion could substantially increment the interception of small drops in a continuous phase which moves at a low velocity and has a low viscosity. Judgment on the actual extent of Brownian diffusion must be deferred until the ability of a drop of micron size to adhere to a filament in the presence of an intervening film has been clarified.

FILM THINNING

In the treatment of drop interception or mathematical capture, it was assumed that the drop has no effect on the flow pattern of the continuum. However, once interception has occurred and the drop almost touches the filament, the behavior of the film of continuous phase between the drop and the filament is strongly affected by the presence of the drop. The success of drop capture by the filament depends upon the thinning of the film of continuous phase to the point of rupture.

The exact nature of the motion of an intercepted drop along the surface of a filament is not known. If the flow is tangent to the surface, the intercepted drop can be considered to move tangent to the surface but separated from it by a microscopic layer of continuum. If the curvature of the filament is large in comparison with the drop, the filament can be considered flat. The efflux of liquid from the separating layer would be similar to the thinning of a continuum film between a flat surface and a stationary drop. Because of the large surface pressure, a micron-size drop would remain spherical when approaching the surface.

Charles and Mason have calculated the rate of approach of a sphere to a flat surface with the assumption that the liquid leaving the separating layer is in laminar flow.(11) In order to obtain an analytic solution, the sphere was considered equivalent to a paraboloid of revolution having the same radius of curvature as the sphere at the point of closest approach to the plate, Figure 3. Cylindrical co-ordinates were used with the origin on the flat surface at the point of closest approach. The equation of the paraboloid was:

$$\xi = h + \frac{r^2}{d_P} \tag{48}$$

where ξ is the distance parallel to the z axis between the paraboloid and the flat surface, r is the radial position and h is the distance of minimum separation. The equation given for the rate of radial efflux, u_r, of fluid as the sphere approaches the plane at a velocity $-dh/d\tau$ was:

$$u_r(r,z) = -\frac{3z(\xi - z)r \frac{dh}{d\tau}}{\xi^3} \tag{49}$$

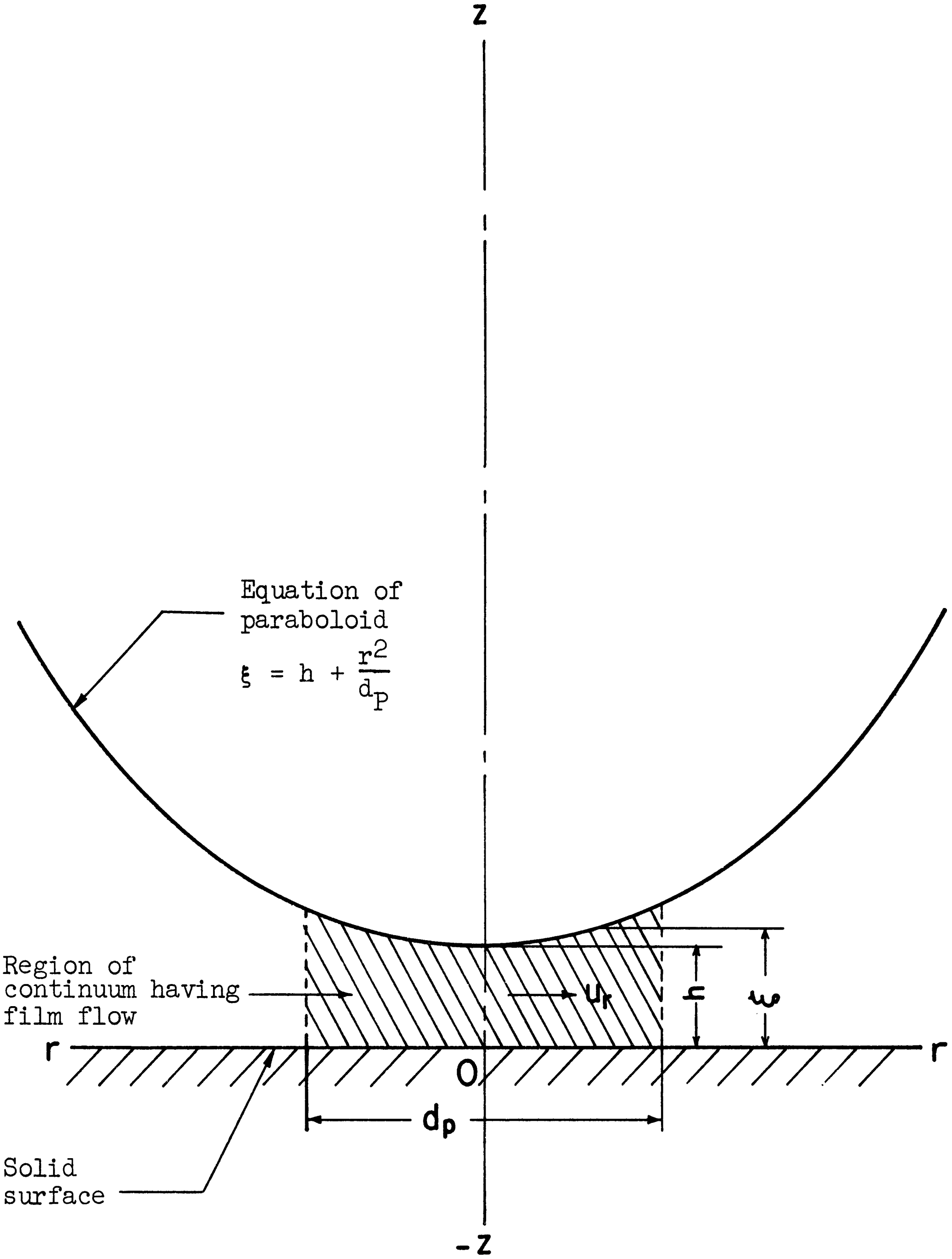

Figure 3. Idealized Efflux of Continuum from Region Between Sphere and Flat Surface.

Energy dissipation by the film was equated to the product of the normal force, F_n , applied at the surface of the paraboloid and the rate of motion of the sphere normal to the surface, $\frac{dh}{d\tau}$. The square of the vorticity was integrated over the volume between $0 \leq z \leq \xi$ and $0 \leq r \leq d_P/2$ under the restriction, $h \ll d_P$. The resulting solution for $-dh/d\tau$ was:

$$\frac{-dh}{d\tau} = \frac{2(-F_n)h}{3\pi\mu_c d_P^2} \tag{50}$$

The normal force is positive in repulsion. Equation (50) was integrated to give:

$$\ln (h_1/h_2) = -\frac{2}{3\pi}\frac{F_n\tau}{\mu_c d_P^2} \tag{51}$$

where h_1 is the initial film thickness at the onset of virtual contact and h_2 is the thickness of the film after a time, τ . Equation (49) was verified by MacKay and Mason for h/d_P less than 0.1.(43) They photographed the approach of nylon spheres, whose diameters ranged between 0.3 and 0.6 centimeters, to a horizontal glass plate immersed in oil. They were able to measure the distance of separation down to ten microns.

Derjaguin and Titijevskaya studied the drainage of films between bubbles which were three millimeters in diameter.(19) They found that the films formed at a thickness of about one micron. At about 0.1 micron, the films acquired a uniform thickness between the deformed bubbles. Drainage then proceeded at a reduced rate to a thickness of 0.03 to 0.04 micron. At this point, thin spots began to appear and rupture eventually occurred through a thin spot. The life of the film was proportional to the diameter of the deformed surfaces bounding the film.

Brownian motion has been suggested as the cause of film rupture.(46) Rupture was considered probable when the film was no thicker than the average distance of random molecular motion. If Brownian motion were the cause, the extent to which the film must thin would depend upon molecular properties of the liquid. These would be reflected by the molecular weight and viscosity of the two liquids. Interfacial tension would influence the extent of interfacial perturbations.

Let H be the ratio of h_1/h_2 between the onset of film behavior and the point of rupture at a specified probability. The term, H , would be a function of d_P and the molecular properties of the liquids. Using Equation (51), an inequality can be stated, which predicts rupture at or above the specified probability.

$$\ln H \leq -\frac{2}{3\pi}\frac{F_n \tau}{\mu_C d_P^2} = -\frac{C}{3\pi}\frac{F_n d_F}{\mu_C U_o d_P^2} \qquad (52)$$

In Equation (52), C is a constant and $d_F/2U_o$ is a characteristic contact time.

The hydrodynamic forces are the most prominent in causing a normal stress on the film between the filament and intercepted drop. If inertia is negligible, the normal stress is proportional to Stokes drag. Substitution into Equation (52) yields

$$\ln H \leq \frac{C'}{3\pi} \cdot \frac{3\pi U_o \mu_C d_P d_F}{U_o d_P^2 \mu_C} = C' \frac{d_F}{d_P} \tag{53}$$

where C' is a new constant. Only dimension variables remain. In Stokes flow, the film-thinning normal stress exists only upstream of the interstitial constriction. Drop inertia can contribute substantially to the normal stress. Substitution of the product of Stokes drag and the modified inertial parameter into Equation (52) gives

$$H \leq \frac{C''(\rho_C \mu_C U_o / d_I)^{1/2} \; U_o d_P^2 d_F}{U_o d_P^2 \mu_C} = C'' \left(\frac{\rho_C U_o d_F^2}{\mu_C d_I} \right)^{1/2} \tag{54}$$

where C" is a second new constant. In the case of inertia, film thinning is enhanced by velocity.

As shown by the example on electrical effects, small double layer potentials could seriously impede the motion of a drop toward a filament. Substitution of Equation (39) into (52) results in an expression whose right hand side is identical with Equation (41) except for a constant. Although the double layer force of the example does not assert itself until h is about 0.03 micron, this separation would probably exceed the separation at which rupture is imminent.(19) As the distance of separation decreased, the example showed that the double layer forces would rise rapidly and probably would prevent further film thinning. Some other means would be necessary to affect coalescence.

Natural attractive forces between bodies could be an important cause of film rupture for films of microscopic thickness. The expression given by Hamaker(31) for the attraction between a sphere and a flat plate, when $h << d_p$, is:

$$F_a = - \frac{A}{12} \frac{d_P}{h^2} \tag{55}$$

The presently accepted value of the constant A is about 5×10^{-14} ergs.(17) When F_a is substituted in the right side of Equation (52), the following is obtained:

$$\ln H \leq \frac{A \, d_F}{36 \pi h^2 d_P \mu_C U_o} \tag{56}$$

For a one-micron drop in water, a film thickness of 0.1 micron, a filament diameter of ten microns and a stream velocity of 0.1 foot per minute, the right side of Equation (56) has the value of 0.1. The attractive force would increase rapidly with a further decrease in film thickness.

Surface elasticity, which is the consequence of surface-active agents, probably has no effect on virtual capture. However, it could have a profound effect on film rupture. Surface elasticity could prevent interfacial perturbations and make film rupture extremely difficult.(36) Were molecular orientation near the interface a concomitant, the drainage of the film also would be impeded. Surface-active agents are likely to become adsorbed on the filament and to change the properties of the surface.

Of the stresses which contribute to film thinning, the stresses of Stokes flow and short range attraction are inversely proportional to drop diameter. Inertial stresses increase with velocity. A low continuum viscosity makes the film mobile and offers less resistance to Brownian motion in the film and at the interface. A low interfacial tension would offer less resistance to interfacial perturbations.

SPREADING AND COALESCENCE ON THE FILAMENT

When the drop makes physical contact with the filament, the amount of spreading depends upon the affinities between the continuum, the drop and the filament. The spreading coefficient of the dispersed phase, S_D , expresses the change in interfacial tension along the surface of the filament when a thin layer of dispersed phase displaces the continuum from the filament. A new liquid-liquid interface is formed in the process. Its tension on the three-phase boundary between the two liquids and the filament acts in the same direction as the tension between the dispersed phase and the filament.

$$S_D = \gamma_{SC} - \gamma_{SD} - \gamma_{CD} \qquad (57)$$

The interfacial tensions, γ , in Equation (57) are for the solid-continuum, the solid-drop and the drop-continuum interfaces, respectively. A positive value of S_D signifies a net reduction in interfacial tension in this process. The dispersed phase displaces the continuum spontaneously and can form a film of molecular thickness on the surface. On the other hand, if $S < -2\gamma_{CD}$, the continuum spontaneously displaces the dispersed phase. If $0 \geq S \geq -2\gamma_{CD}$, a state of static equilibrium is reached in which the liquid-liquid interface meets the surface in the contact angle, θ , measured through the dispersed phase.

$$\gamma_{SC} = \gamma_{SD} + \gamma_{CD} \cos \theta \tag{58}$$

The smaller the contact angle between the filament and a drop in physical contact, the larger the area of contact and the greater the probability that the drop will encounter and coalesce with another drop on the surface of the filament. The drops flow together under the influence of surface forces. If the drop spreads spontaneously on the filament, the chances for coalescence are excellent.

Rate of Spreading

Gillespie found that the rate of spreading of various liquids on porous papers was proportional to $\gamma \cos \theta/\mu$, where γ is the surface tension of the spreading liquid and μ , its viscosity.(27) Davies and Rideal cited data which show that the rate of spreading of various materials on an oil-water interface is roughly proportional to the spreading coefficient of the material in question divided by the sum of the viscosities of the water and the oil.(17) Their compilation shows that the initial rate for the spreading of various solvents on a hydrocarbon-water interface is above 20 centimeters per second, while the steady state rate is above three centimeters per second. If the steady state value is typical of the rate of spreading of micron-size drops, then spreading would generally be rapid in comparison with the flow velocity near the filament surface. In coalescence, the average interstitial velocity is normally less than one centimeter per second.

If spreading is spontaneous and the filament remains coated, incident drops would coalesce directly with the film. The rate of spreading of a liquid upon itself would be more rapid than on a solid because of the mobility of the liquid surface. Again, the rate of spreading would not appear to be a limiting factor.

Adhesion

In order to allow ample time and opportunity for coalescence, the dispersed phase must adhere to the filaments and be held up for union with other drops in the incident flow. An attempt is generally made to correlate the force of adhesion between the solid and the liquid with the reversible work of adhesion or the heat of immersion of the solid.(20,64) However, these quantities disclose nothing about the ability of the liquid to withstand shear stress.(53) In the presence of shear stress, the static equilibrium condition expressed by Equation (58) would no longer hold. For example, when a drop slides down an inclined solid, the receding contact angle at the trailing edge is less than the equilibrium angle and the advancing contact angle at the leading edge is greater.

In coalescence, the adhesive force tangent to the surface would tend to retard the stripping of a drop which had just made physical contact. The larger packets of dispersed phase which resulted from the coalescence of many single drops would protrude further into the flow and would have a greater tendency to be stripped from the surface. The coalesced material would be expected to collect at and be removed from the downstream portion of the filament. Figure 4 pictures a globule of coalesced material appended at the rear of a filament by the hydrodynamic forces which operate on the liquid-liquid interface. A microscopic view of a point in the three-phase junction is shown. The liquid-liquid interface near the surface of the filament is considered to be a flat sheet which is hinged at the three-phase junction. An interaction between the hydrodynamic stress normal to the sheet and the molecular forces near the junction causes the sheet to be deflected from its equilibrium inclination, θ , to a smaller inclination, θ' . The deflection produces a net force on the junction which is directed into the dispersed phase. However, motion of the junction is impeded by an energy barrier which comprises adsorption, possible chemical bonding and surface roughness.(34,38) These factors can be considered to constitute a frictional tension, γ_F . For an ideal solid, $\gamma_F = 0$. The sum of the interfacial tensions acting on the three-phase junction tangent to the surface of the filament is given by:

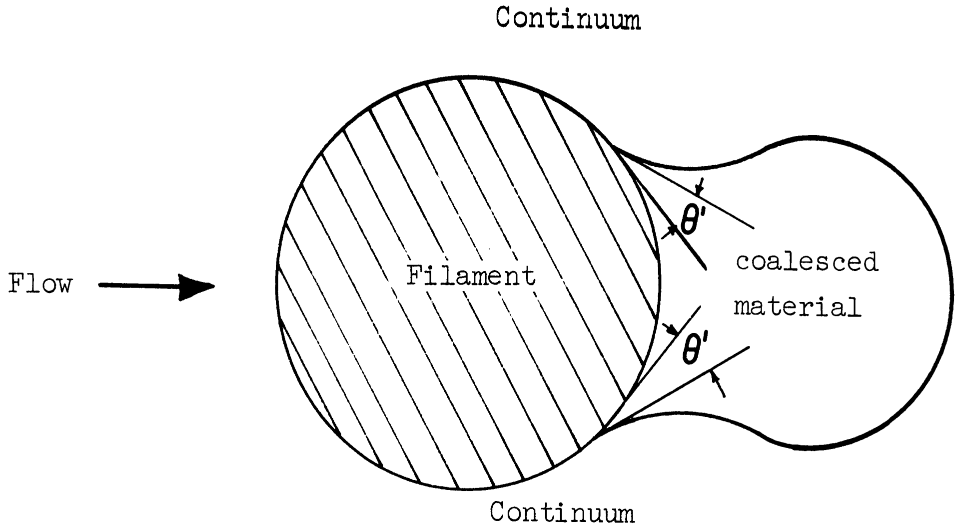

Coalesced Material Appended Downstream of
Filament by Flow

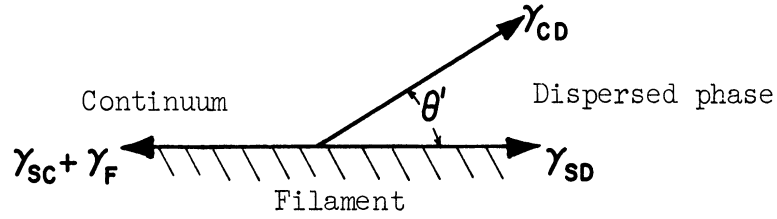

Three Phase Junction in Detail

Figure 4. Forces Acting on Boundary Line Between Dispersed Phase, Continuum and Filament.

$$\Gamma = \gamma_{SC} - \gamma_{SD} - \gamma_{CD} \cos \theta' + \gamma_F \qquad (59)$$

where the sum, Γ , is positive if the net force is directed into the interface between the continuum and the filament. If Γ is negative, the junction tends to move and decrease the area of contact between the filament and the coalesced material. At some point, the curvature of the liquid-liquid interface would become appreciable at the junction and would tend to deflect the interface away from the filament. Further motion of the junction would cease unless the normal stress on the liquid-liquid interface increases or the interface stretches in such a way that its curvature is reduced. The resistance offered by interfacial tension to an increase in curvature would partially offset the negative contribution of interfacial tension in Equation (59).

If the forces of lateral adhesion exceed the cohesive forces of the dispersed phase, rupture is likely to occur in the accumulated dispersed phase rather than at the liquid-solid interface. Failure in the dispersed phase would be expected when it spreads.(53) The reversible work of adhesion in the presence of the continuum exceeds the work of cohesion.

Since the resistance to break-off is related to either the lateral adhesive force or the cohesiveness of the dispersed phase, a suitable dimension for the break-off resistance would be force per unit length of the three-phase boundary. Let γ^* be the break-off resistance. A dimensionless group can be formed from the ratio of γ^*

and the work done by viscous shear in deforming the surface of the coalesced material. The latter is proportional to the viscous shear stress and some dimension characteristic of the coalesced material. The most natural choice for this dimension is the filament width, since the coalesced material would accommodate to the dimension of the filament. The ratio of γ^* to the work done by viscous forces is therefore proportional to $\gamma^* d_I / U_o \mu_C d_F$.

If γ^* is limited by forces of adhesion, the properties of the solid surface are probably most influential in determining γ^* . An increase in γ_{CD} would probably cause a change in the affinity of the surface for one of the liquids relative to the other. Any change in γ_{CD} , above a limiting value, probably evokes a parallel change in $\gamma_{SC} - \gamma_{SD}$ in such a way that the dynamic equilibrium of Equation (59) is not greatly altered. When adhesion is strong enough to cause cohesion to be the limiting factor, the γ^* would shift its dependency to γ_{CD} . At sufficiently low levels of γ_{CD} , the similarity of the liquids probability eliminates the preferential affinity of the surface. Filaments whose affinity for the drop phase is created by an adsorbed layer would be particularly vulnerable in this respect. Although a low γ_{CD} would probably be inimical to coalescence, the low γ_{CD} would not encourage the redispersion of the coalesced material because of the large accompanying increase in interfacial pressure.

Collapse of Drop onto Filament

When a drop can spread either spontaneously or to a low contact angle, the interfacial pressure of the drop, $4\gamma_{CD}/d_P$, is available for driving the drop into the existing or spreading film. Charles and Mason have observed this interesting process in the coalescence of drops between 0.1 and one millimeter in diameter on a flat surface of the parent liquid.(10,11) Their observations are summarized in Figure 5. Under the action of the surface stress, the rupture area in the film grows quickly to approximately the drop diameter and the collapsing drop is compressed into a column of liquid from which a daughter drop is necked-off. The formation of successive daughter drops was observed through as many as seven cycles. The diamter of each successive drop was about half that of its predecessor. They suggested that the formation of successive daughter drops could continue into sub-micron diameters. The formation of secondary drops could be prevented by the addition of a surface-active agent or by keeping the viscosity ratio, μ_D/μ_C, below 0.02 or above 11. Wiegand studied the coalescence of pairs of drops having diameters of about 1.5 centimeters in a liquid continuum.(60) He found that coalescence occurs without secondary drop formation. However, immediately after the two drops combine into a prolate ellipsoid, two small lobes appear at

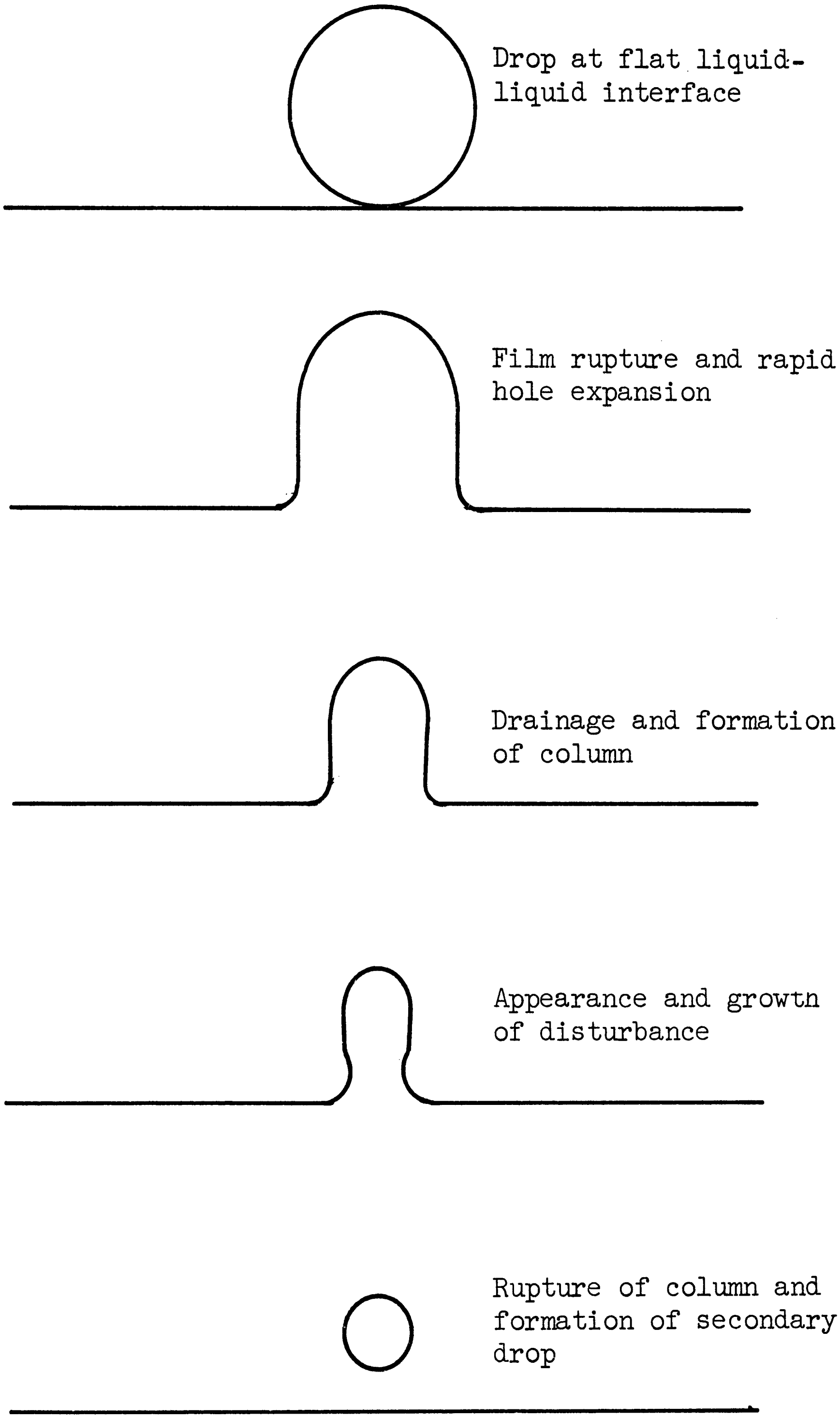

Figure 5. Stage-by-Stage Coalescence at a Liquid-Liquid Interface.

opposite ends of the ellipsoid along the axis of the centers of the two original drops.

DROP BREAKAWAY

Ideally, the coalesced material would flow off the fibrous mat as a continuous stream or intermittently as large drops. However, under certain conditions, the dispersed phase formed a foam at the bed outlet.(1,50) The foam tended to disintegrate into fine drops. It was thought that the foam could be eliminated by packing the outlet of the bed with coarse fibers which had an affinity for the continuum.(1) Rose found that the phenomenon could be countered by increasing the packing density of the bed.(50)

Tomotika conducted a classical analysis of the varicose oscillations of a thread of fluid immersed in a second fluid.(55) His calculations showed that the temporal oscillation of the thread, $A(\tau)$, had the form:

$$A(\tau) = A_o e^{i\Omega(\tau)} \tag{60}$$

where A_o is the initial amplitude and $\Omega(\tau)$ is the temporal growth function.

$$i\Omega(\tau) = \frac{\gamma_{CD}\left(1 - \frac{4\pi^2 a^2}{\lambda^2}\right)}{2\mu_C a} \; G\left(\frac{2\pi a}{\lambda}, \frac{\mu_D}{\mu_C}\right) \tag{61}$$

In Equation (61), a is the radius of the undisturbed thread, λ is the wave length of the disturbance, G is a function and μ_D is the viscosity of the liquid in the thread. Corresponding to each viscosity ratio, there was a wave length, λ , for which $i\Omega(\tau)$ was a maximum. The wave length corresponded to the most rapidly growing disturbance. The λ had a minimum value of about 12a at viscosity ratios between 0.1 and 1.0. A drop which forms from a section of the original cylinder of this length has a radius about twice that of the original thread. According to Equation (61), an elevated interfacial tension speeds the growth of all disturbances without discrimination. The measurements of Mason and co-workers generally confirm Tomotika's calculation.(10,51)

In the laminar flows of coalescence, it is possible that sheets of threads of material which extend downstream of the coalescing medium would undergo varicose oscillations similar to those predicted by Tomotika. Under the action of surface forces, these fragments of dispersed phase would probably assume a thickness comparable to the diameter of the filament from which they were shorn. If the filaments at the outlet of the bed are large in comparison with the drops in the feed, then the drops broken away should also be large by comparison.

In summary, the coalescence of drops on fibrous media is an interesting but involved process. Some of the forces are associated with the properties of liquids and the liquid-solid interface. There is no hope for a complete elucidation of coalescence phenomena until more information about these properties is available. It is evident that a study of coalescence on the macroscopic scale can at best yield an empirical correlation of the measurable variables and indicate the predominant forces and relationships.

PART II

EXPERIMENTAL

INTRODUCTION

This study of coalescence was performed by using light scattering to measure the extent of drop removal from dispersions as they flowed through the coalescing medium. Layers of fine-mesh screen were used as an idealization of the typical fiber-packed coalescer. The screens were attractive on two counts. They were compact and produced a regular flow pattern. The screens permitted a study of the geometric characteristics of a fibrous medium. The flow system in which the dispersion moved was quite simple. It comprised the screen coalescer, a flow measuring device and optical cells on either side of the coalescer in which the dispersion drop concentrations were analyzed. The optical instrument for the analysis was considerably more involved. Optical rather than chemical means were preferred for measuring drop concentrations. An optical measurement could be performed quickly on the flowing dispersion itself with no disturbance of the flow.

Light transmission measurements are not useful for gauging the concentration of micron-size drops. For micron-size drops, the scattering coefficient, K, in the Beer-Lambert law is strongly influenced by the drop size.

$$\ln \frac{I_o}{I_t} = \frac{\pi}{4} c \, d_p^2 \, K t \qquad (62)$$

In the Beer-Lambert equation, I_o/I_t is the ratio of the flux in an incident collimated beam relative to the flux remaining in the collimated beam after passage through a cell of thickness t containing a dispersion whose particles have a diameter d_p and a concentration c . The scattering coefficient, K , is the amount of incident flux of unit intensity scattered in all directions divided by the projected cross section of the sphere causing the scattering.

Chin(13,14) demonstrated that forward angle light scattering measurements can be used to measure particle size distributions in suspensions of particles between ten and forty microns in diameter. Drops in troublesome hazes and dispersions are usually between one and ten microns in diameter. It appeared that the moving lens-pinhole method used by Chin could be extended to lower diameters.

The method could have several disadvantages. Although the measurements are rapid, the calculation of the particle concentration requires automatic computation and will be delayed unless a specialized analog circuit is available. Narrow fractions of microscopic spheres are required for calibration. These may or may not be commercially available in the desired size. The method is limited to dilute dispersions, because multiple scattering voids the theory. Dispersions encountered in practice are usually dilute.

SUMMARY OF THEORY OF FORWARD ANGLE SCATTERING MEASUREMENTS

The theory of the calculation of particle size distribution from forward angle flux measurements was given by Chin. The salient features of the method are repeated because they are useful in an evaluation of the method.

The Beer-Lambert law was modified in two respects. The I_t in Equation (62) refers strictly to the transmitted flux exclusive of all scattered flux. A light detector behind the dispersion cell includes some of the scattered light in its view. The Beer-Lambert law was modified by Gumprecht and Sliepcevich to relate the incident flux to the total flux leaving the dispersion within the cone of half angle θ.(29,30)

$$\ln\left[(I(\theta) + I_t)/I_o\right] = -(\pi/4)d_p^2cK(\theta)t \qquad (63)$$

The $K(\theta)$ is the scattering coefficient which relates the amount of incident flux of unit intensity scattered outside the forward polar angle θ to the projected cross section of the sphere causing the scattering. The $I(\theta)$ is the amount of flux scattered within the forward cone of half angle θ. An approximate relation between $K(\theta)$ and K is provided by Rayleigh's theory of diffraction.

$$\frac{K(\theta)}{K} = R(\theta) = \frac{1 + J_0^2(\alpha\theta) + J_1^2(\alpha\theta)}{2} \qquad (64)$$

In Equation (64), $R(\theta)$ is the ratio of scattering coefficients; J refers to the Bessel function of the first kind, whose order is given by the subscript; and, α is the reduced particle circumference, $\pi d_p/\lambda$, where λ is the wave length of the incident light.

The second modification was the generalization of the Beer-Lambert law to a mixture of spheres having a continuous concentration distribution, $dc/d\alpha$, with respect to α.

$$\frac{4\pi}{t\lambda^2} \ln \frac{I_t + I(\theta)}{I_o} = - \int_0^\infty R(\theta) K\alpha^2 \left|\frac{dc}{d\alpha}\right| d\alpha \qquad (65)$$

After Equation (64) is substituted for $R(\theta)$, the derivative of Equation (65) with respect to θ is:

$$\frac{4\pi}{t\lambda^2 \, [I(\theta)+I_t]} \frac{dI(\theta)}{d\theta} = \int_0^\infty \frac{K\alpha^2 J_1^2(\alpha\theta)}{\theta} \left|\frac{dc}{d\alpha}\right| d\alpha \qquad (66)$$

The Mellin transformation was shown to be suitable for the calculation of the function, $K\alpha^2 \, dc/d\alpha$.

$$K\alpha_i^2 \left|\frac{dc}{d\alpha}\right|_i = -2\pi \int_0^\infty B(\theta) J_1(\alpha_i\theta) Y_1(\alpha_i\theta) \alpha_i \theta d\theta \qquad (67)$$

$$B(\theta) = \int_0^\infty \frac{d}{d\theta} \theta J_1^2 (\alpha\theta) K\alpha^2 \left|\frac{dc}{d\alpha}\right| d\alpha$$

$$= \frac{4\pi}{t\lambda^2} \frac{d}{d\theta} \left[\frac{\theta^2}{I(\theta) + I_t} \frac{dI(\theta)}{d\theta} \right] \qquad (68)$$

In Equations (67) and (68), $\left|\frac{dc}{d\alpha}\right|_i$ is the concentration distribution at α_i , $\alpha_i = \pi d p_i/\lambda$, and Y refers to the Bessel function of the second kind.

Application to a Lens-pinhole Detector

In a lens-pinhole detector, the transmitted and scattered light is brought to a focus. A light-sensitive detector with a pinhole aperture traverses the focal plane. At each distance, s , from the optical axis, the sensor detects a portion of the light scattered at the angle θ, where for small angles,

$$s/b = \tan\theta \cong \theta \tag{69}$$

The distance, b, is the focal length of the lens. Assuming an ideal lens, Equation (69) was shown to be independent of the source of scattering in front of the lens as long as the scattered ray does not pass outside of the periphery of the lens.$^{(29)}$

Figure 6 shows that a sensor which has a small aperture of diameter a sees a portion of the light falling between the angles $\theta - \frac{1}{2}\Delta\theta$ and $\theta + \frac{1}{2}\Delta\theta$ when the center of the aperture is the distance s from the optical axis, where s and θ are related by Equation (69). If the sensor receives the flux, $F(\theta)$, at position s, the following relations hold:

$$F(\theta) = \frac{a}{8s}\frac{\Delta I(\theta)}{\Delta\theta}\Delta\theta \tag{70}$$

$$\Delta\theta = \frac{a}{b}\frac{1}{(1+\tan^2\theta)} \tag{71}$$

To a good approximation if $\theta \leq 0.15$ radian,

$$\frac{dI(\theta)}{d\theta} \cong \frac{\Delta I(\theta)}{\Delta\theta} = \frac{8b^2\tan\theta(1+\tan^2\theta)}{a^2} \cong \frac{8b^2\theta}{a^2}F(\theta) \tag{72}$$

For dilute dispersions, the total scattered flux is small compared with the transmitted flux; $I(\theta) + I_t \cong I_t$. The I_t may

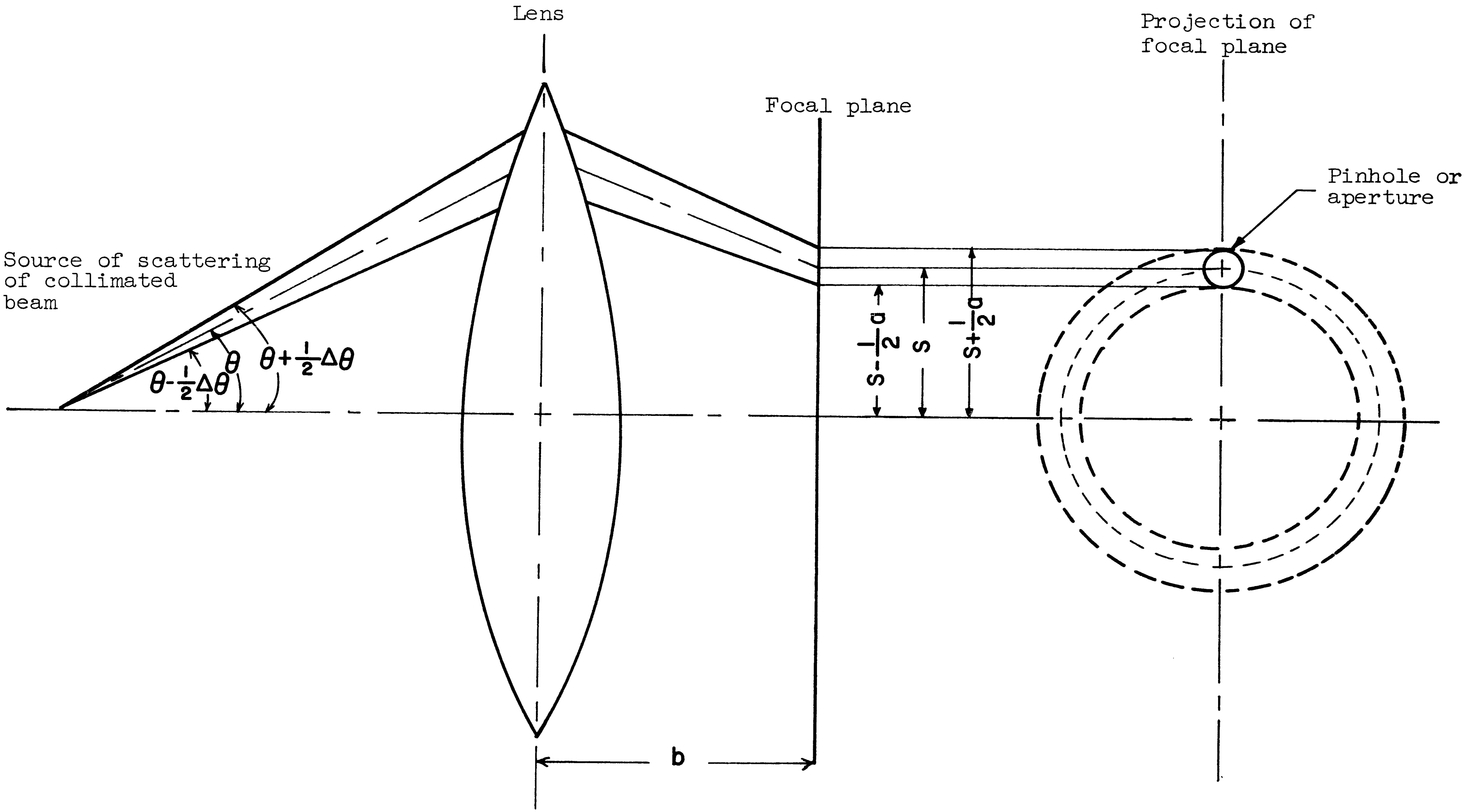

Figure 6. Relation Between Angle of Scattering and Position of Pinhole.

be placed outside of the integrals in Equations (67) and (68) and equated to $F(0)$, the flux received by the sensor at the optical axis.

This is the extent of the theory given by Chin. In all succeeding discussion, the Mellin transformation was modified to suit the present application.

Numerical Approximation of Mellin Transformation

The concentration distribution may be expressed in terms of volume fraction, ϕ , per unit particle size.

$$\left(\frac{d\phi}{d(d_P)}\right)_i = \frac{d}{d(d_P)} \int_0^{\infty} \frac{\pi}{6} d_P^3 \left(\frac{dc}{d\alpha}\right)_i d\alpha = \frac{\pi^2}{6\lambda} d_P^3 \left(\frac{dc}{d\alpha}\right)_i \tag{73}$$

Chin found that $B(\theta)$ attenuates rapidly for Pyrex spheres between 10 and 40 microns in diameter. Although the attenuation was not quite as rapid in this study, the infinite integral in Equation (67) could be truncated at some angle, θ_m , where $B(\theta)$ became sufficiently small. The resulting definite integral was integrated by parts to eliminate the derivative in the integrand. In the limit, as θ goes to zero, $J_1(\alpha\theta)$ goes to $\alpha\theta$. By Equation (66), $\left(\frac{dI(\theta)}{d\theta}\right)_{\theta=0} = 0$. Integration of Equation (67) by parts between the limits of zero and θ_m gives:

$$K\alpha_i \left(\frac{dc}{d\alpha}\right)_i = \frac{8\pi^2}{t\lambda^2} \left\{ - JY(\alpha_i\theta_m) \frac{\theta_m^3}{I_t + I(\theta)} \left(\frac{dI(\theta)}{d\theta}\right)_{\theta_m} + \int_0^{\theta_m} M(\alpha_i\theta) \frac{\theta^2}{[I_t+I(\theta)]} \left(\frac{dI(\theta)}{d\theta}\right) d\theta \right\} \tag{74}$$

where,

$$JY(\alpha_i \theta_m) = J_1(\alpha_i \theta_m)\ Y_1(\alpha_i \theta_m) \tag{75}$$

and,

$$M(\alpha_i \theta) = \alpha_i \theta \left[J_0(\alpha_i \theta)\ Y_1(\alpha_i \theta) + J_1(\alpha_i \theta)\ Y_0(\alpha_i \theta)\right] - J_1(\alpha_i \theta)\ Y_1(\alpha_i \theta) \tag{76}$$

After the substitution of $F(0)$ for $I_t + I(\theta)$ and substitution of Equations (72) and (73), Equation (74) may be solved for $[d\phi/d(d_P)]_i$.

$$\left(\frac{d\phi}{d(d_P)}\right)_i = \frac{64\pi^3 b^2 d_{P_i}{}^2}{6t\lambda^2 a^2 K F(0)} \left\{ - JY(\alpha_i \theta_m)\ \theta_m^4\ F(\theta_m) + \int_0^{\theta_m} \theta^3 M(\alpha_i \theta)\ F(\theta) d\theta \right\} \tag{77}$$

The integral of Equation (77) can be approximated by numerical integration using the trapezoidal rule. The trapezoidal rule is preferred because of the oscillatory character of $M(\alpha\theta)$. The scattered flux vanishes at $\theta = 0$.

$$\left(\frac{d\phi}{d(d_P)}\right)_i = \frac{64\pi^3 b^2 d_{P_i}}{6t\lambda^2 a^2 K F(0)} \left[- JY(\alpha_i \theta_m)\ \theta_m^4 F(\theta_m) + \Delta\theta \sum_{j=1}^{m-1} \theta_j^3 M(\alpha_i \theta_j) F(\theta_j) + \frac{1}{2}(\Delta\theta)\theta_m^3 M(\alpha_i \theta_m) F(\theta_m) \right] \tag{78}$$

The subscript, m , simultaneously denotes the angle of truncation and the number of intervals of size $\Delta\theta$ into which the integral is divided. The θ_j refers to the angular position at the end of each interval. Since the quotients $F(\theta_j)/F(0)$ are formed, relative units may be used for the flux.

When particle diameter is measured in microns, Equation (78) has dimensions of 1/micron. If the particle size distribution is calculated at one-micron intervals, each point value of the distribution is an estimate of the particle concentration in the bracketing one-micron interval. The diameter at which the point value of the distribution is calculated can be regarded as the average diameter of the one-micron interval. Since these practices were adopted, the terms "concentration of particles of size dp_i" and "concentration distribution at size dp_i" are used interchangeably.

DESIGN OF THE LENS-PINHOLE DETECTORS

Two lens-pinhole detectors were constructed in order to measure the flux distributions on either side of the coalescer. The detectors were in many respects similar to the units designed by Gumprecht,(29) Chin,(13,14) and Clark.(15) In a lens-pinhole detector, a monochromatic collimated beam of circular cross section is allowed to fall upon a thin slab of the dispersion being examined. The scattered and transmitted light passing from the cell in the forward direction is brought to a focus by a condensing lens. The flux distribution is detected by a sensor or multiplier phototube, which traverses the focal plane. The sensor is fronted by a circular aperture or "pinhole," which limits its view to a small circular disc. The photomultiplier generates a current which is proportional to the flux received. The current is run to ground across a resistor and a voltage proportional to the incident flux is displayed on a continuous recorder.

In intermittent operation, two lens-pinhole detectors can share either the light source or the sensor. Neither arrangement has inherently more electrical stability. The use of only one sensor avoids duplication of appurtenant electronic circuitry and traversing mechanisms. This arrangement was selected because of its reduced complexity and cost of construction. If only one is used, the sensor must be located off of the main optical axis of each detector. Mirrors would be used to deflect the light beam to the sensor. Shutters would determine which detector was in operation.

Essential Design Features

The components of the detectors were mounted inside light-proof and dust-proof closures. The closures were supported on an existing angle structure bolted to the laboratory floor and wall. Two channel-steel optical benches served as the mounting tracks for the components of the detectors.

The light beams received by the sensor were made monochromatic by the selection of the light sources and two filters. Mercury lamps were convenient sources of discontinuous radiation. The line at 5461°A was chosen. The radiation was furnished by type C-H3, 85-watt mercury lamps. The ultraviolet end of the mercury spectrum was removed by Wratten 77-A filters. The second filter was the S-11 photocathode surface of the Dumont 6291 photomultiplier. This surface does not respond to infrared and has approximately 50 percent of maximum sensitivity at 5461°A. These provisions yielded a monochromatic beam with an estimated 96 percent spectral purity.

Figure 7 is a schematic drawing of the lens-pinhole detectors and the flow system. In each detector, light from the mercury lamp was collimated by the condensing lens, L_1 , and passed through the Wratten filter. At this point the beam had the cross section of the lamp filament. The cross section was reduced to a circular disc by focusing the beam on a 1/16-inch diameter pinhole with lens L_2 . The emergent circular beam was collimated by lens L_3 for passage through the dispersion cell. Lens L_4 focused the transmitted light on the horizontal plane traversed by the aperture of the sensor; the beam direction was turned approximately 90° by the front surface mirror. A 1/8-inch aperture limited the view of the sensor. The traverse of the sensor extended about 0.11 radian on either side of the optical axes of the two detectors. The approximation of Equation (72) was satisfactory over this range. Since the sensor and the recorder chart moved at constant speed, distance on the chart was proportional to polar angle traversed.

Electrical Circuits

It was necessary to regulate lamp and sensor voltages in order to minimize variations in the flux incident upon the dispersion cells. Lamp voltages were regulated by a Sola constant-voltage transformer rated for 500 V.A. and 118-volts output $\pm$ one percent on an input voltage between 95 and 130 volts. The output was supplied to the two ballast transformers for the mercury lamps. The ballast raised the voltage to the 400-volt level required for lamp operation. The ballast had power factors of 50 percent. In order to maintain the regulation of the transformer, a capacitance of 24 micron-farads was

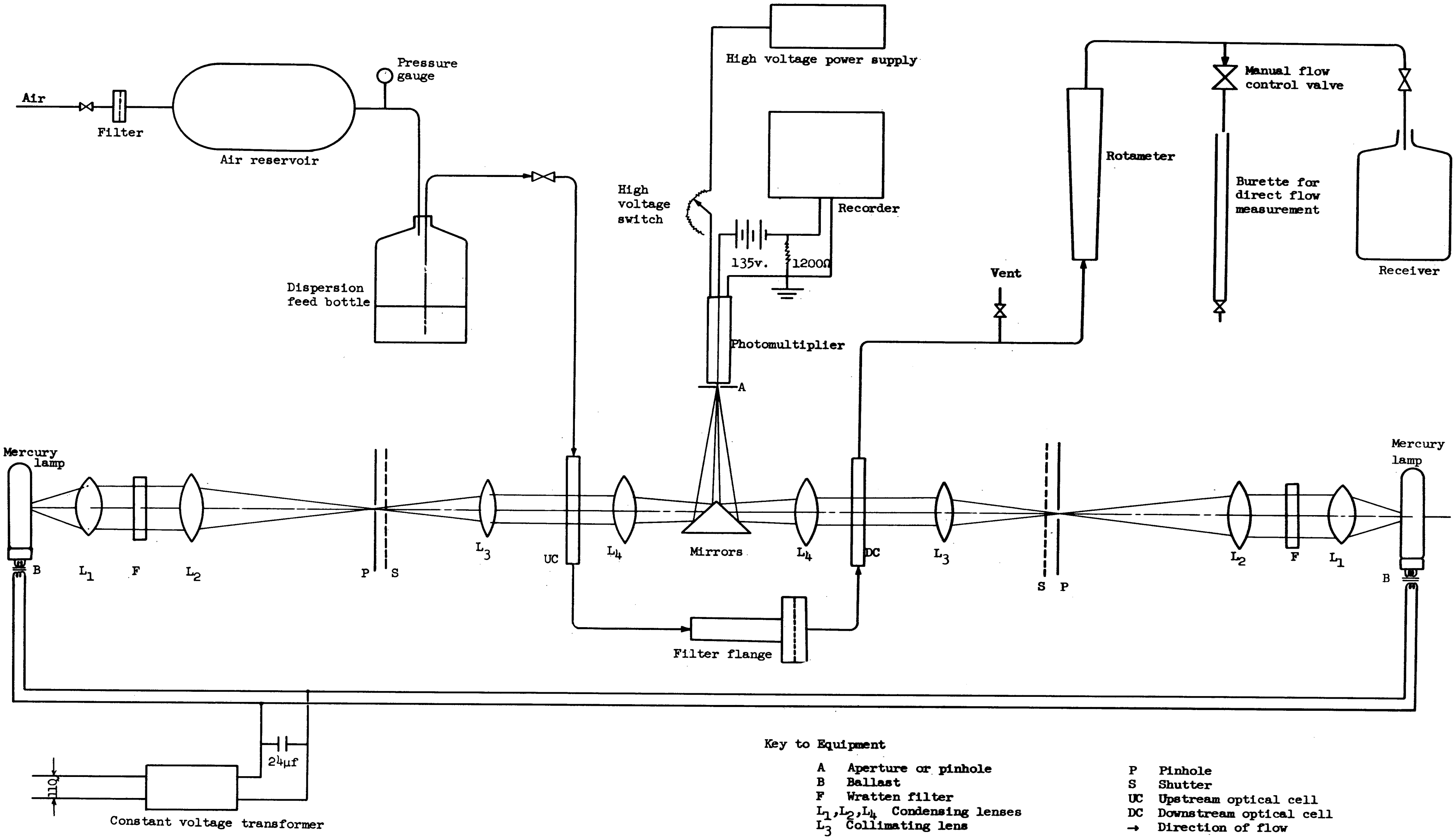

Figure 7. Schematic Diagram of Equipment.

connected in parallel with the ballasts. Wire rated for 600 volts was used between the ballasts and the lamps.

The photomultiplier was energized by a large negative d.c. potential. The potential was furnished by a Furst Electronics model 710-PR d.c. power supply. This unit could be set to a desired output between -300 and -1500 volts with about one percent regulation. In order to assist the regulation, the input was supplied from the constant voltage transformer.

A Brown Electronik recorder, model number 153-184-x-66, was employed. The recorder had a full scale deflection on a ten-millivolt signal. The response was linear with respect to voltage. The chart speed was ten inches per minute. Since the focal length of the L_4 lens was 13.5 inches, the sensor's rate of traverse of 1.5 inches per minute was equivalent to 0.01 radian in 0.09 minute according to Equation (69). Thus, 0.9 inch of chart was equivalent to 0.01 radian.

The sensor used in this investigation was a Dumont 6291 photomultiplier having 10 stages. It had a diameter of 1-1/2 inches and a length of 4-1/2 inches exclusive of the pins. The photocathode was located at the flat end of the tube. Chin and Clark had favored this tube because of the low noise level and favorable photocurrent amplification. At 145 volts per stage, the tube is rated for an amplification of 2×10^6. The dark current at this level was about 0.4 microamp. Most of the measurements were made at 130 volts per stage or less. At this level, the tube had good stability, and the dark current was scarcely detectable.

Figure 8 is a schematic of the photomultiplier circuit, which is essentially that used by Clark. In practice, the power supply was held at a constant voltage in the neighborhood of -1460 volts d.c. Tube amplification was decreased in fixed decrements by adding fixed resistances in series with the tube. Switching was accomplished with a Centralab type 9000 heavy-duty single-pole switch. A shorting-type switch was used to prevent arcing. Precision resistors having resistances within one percent of the stated value were used throughout the photomultiplier circuit. The current developed by the photomultiplier was run to ground across a 1200-ohm resistor. At a full scale deflection of the recorder, the photomultiplier was delivering an anode current of 8.3 microamps. This was well within the limit deemed satisfactory for long tube life and low fatigue. The photomultiplier had a linear response, as Figure 65 in Appendix A shows.

The power supply, switch and 1200-ohm resistor were supported in a cabinet for electronic components. The recorder was fastened to the laboratory wall at eye level and the cabinet was secured overhead with the switch in easy reach. Grounded-shielded cable was used between the components of the photomultiplier circuit in order to eliminate electromagnetic pickup.

Details of Black Boxes and Supporting Structure

Figure 9 shows in partial detail the arrangement of the components of the lens-pinhole detectors and gives the dimensions of the black boxes. The central closure contained the photomultiplier while the horizontal closure housed the equipment of the two detectors. The

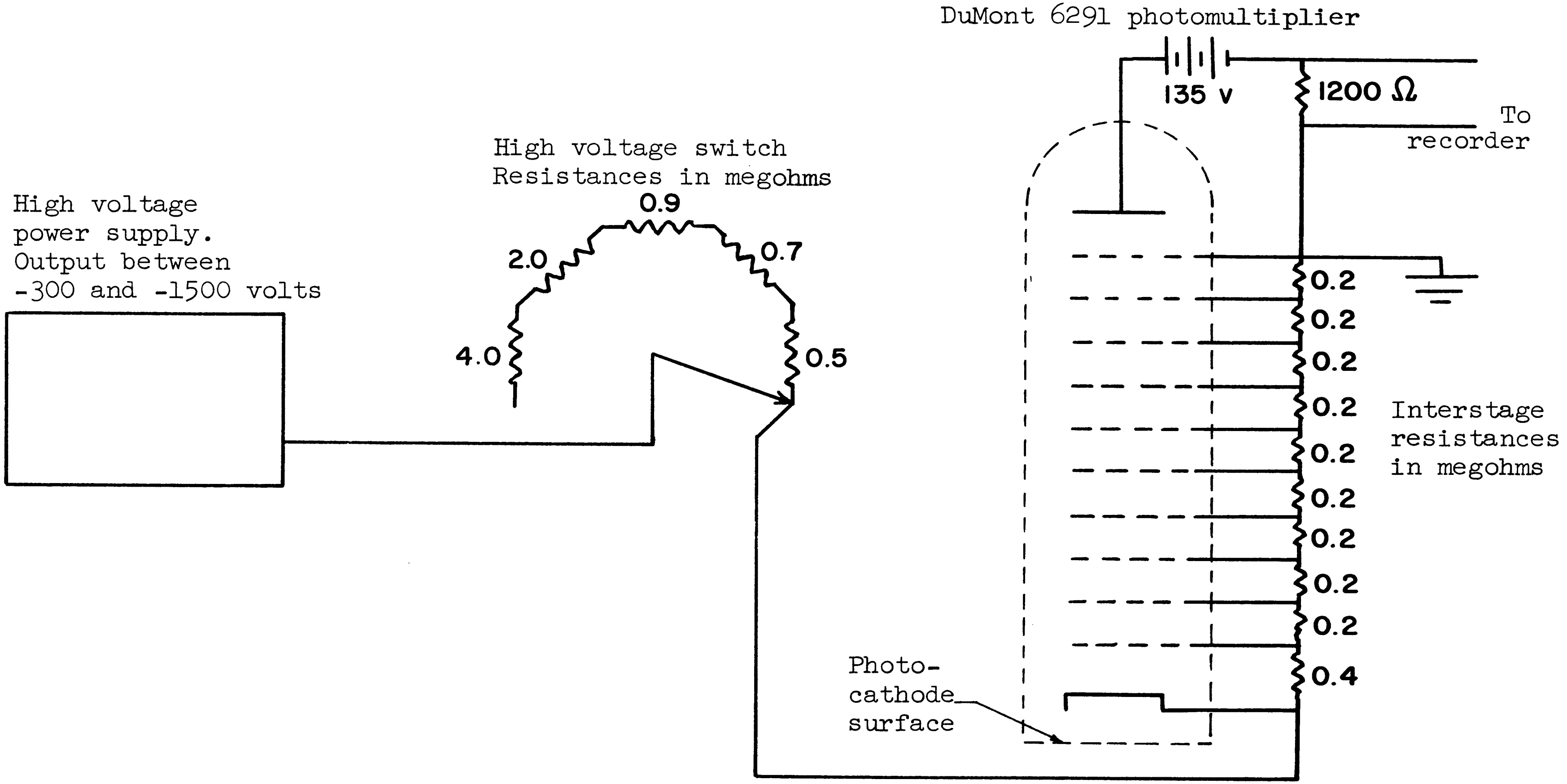

Figure 8. Photomultiplier Circuit.

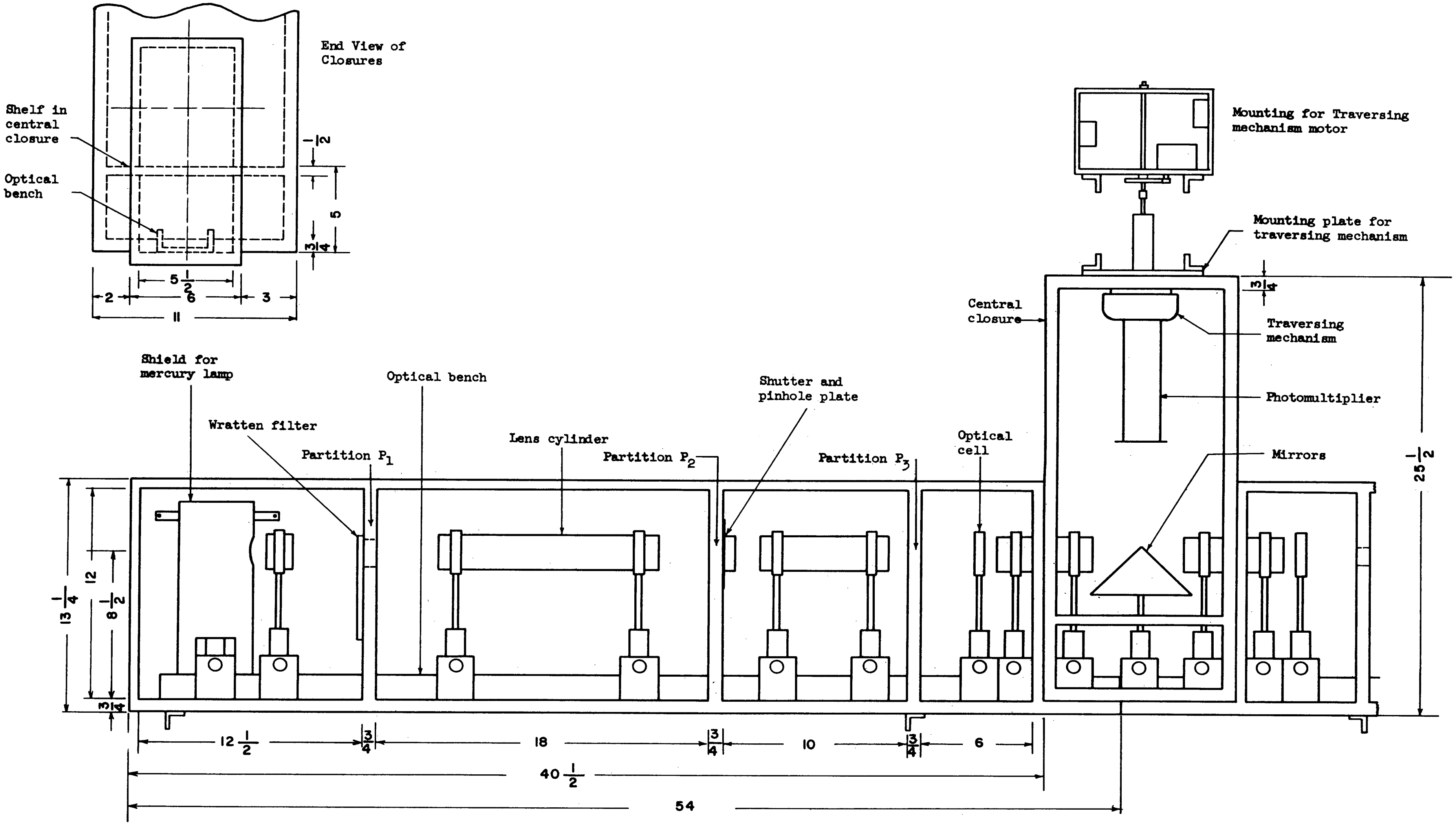

Figure 9. Detail of Light-Proof Closures.

optical benches, which supported the equipment of the detectors, were bolted through the bases of the horizontal closures to the angle steel structure. The frame of the traversing mechanism was bolted through the top of the central closure to the levelled support plate. The closures were constructed from 3/4- and 1/2-inch plywood. Step joints were used throughout to minimize the leakage of light.

The front view in Figure 9 shows the closures with their covers removed. The partitions in the horizontal closures reduced stray reflections and served as beam diaphragms. The shelf in the central box shielded the photomultiplier from any light entering along the slot which was cut in the bottom for the optical benches. The location of the partitions was determined by the focal lengths of the lenses and the need of sufficient clearance for manual adjustments. The optical axis of each detector was 8-1/2 inches above the base of each horizontal closure. Holes were centered 8-1/2 inches above the bottom of each partition in order to pass the light beam. Holes were drilled through the center ends of the horizontal closure into the central closure to allow the beams to fall upon the mirrors. A slot was cut at the bottom of each partition to accomodate the optical bench.

The front cover of the horizontal black boxes was divided into sections along the center of each partition. Each compartment could be opened individually and the influx of dust was thereby minimized. All surfaces of the closures were painted flat black.

Miscellaneous Equipment and Equipment Supports

The lenses, lamps, mirrors and dispersion cells were secured to the optical bench foundation by means of optical bench clamps. Each component was supported on a section of 3/8-inch drill rod, which could be inserted in the optical bench clamp. If the component and support were centered with respect to the drill rod, the component would be approximately centered with respect to the optical bench.

The support for each lamp was a two-inch square steel plate welded to the top of the drill rod. The ceramic base for the lamp was fastened to the plate.

Figure 10 shows the supports for the lenses and the optical cells. The lenses were mounted in cylinders which are to be described. With the exception of lens L_1, two ring supports were used to cradle each cylinder. The rings were cut from 2-inch steel pipe or 1-3/4-inch brass pipe and machined round on the inside. The rod was cemented into the radial hole with epoxy resin.

The supports for the optical cells were fabricated from steel as shown and joined with silver solder. The end slots held the optical cell perpendicular to the light beam. The supports for the two-inch square Wratten filters were similar in design to the supports for the optical cells. Since the Wratten filters did not require accurate centering, the filter holders were screwed to partition P_1 such that the filter covered a 1-1/2-inch hole, which was drilled at the optical axis for the light beam.

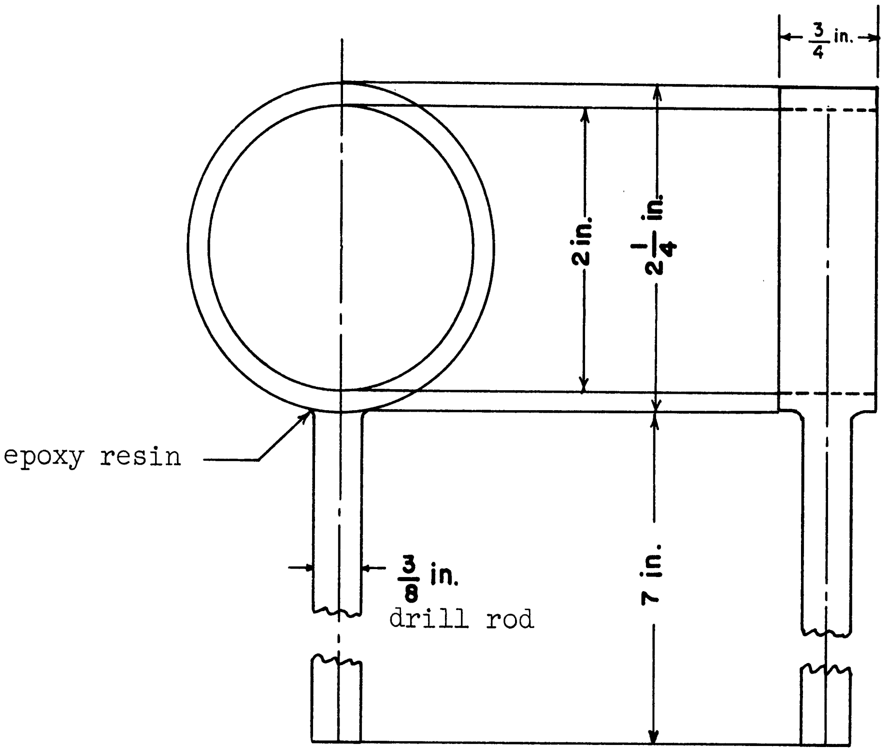

Ring Support for Lens Cylinders

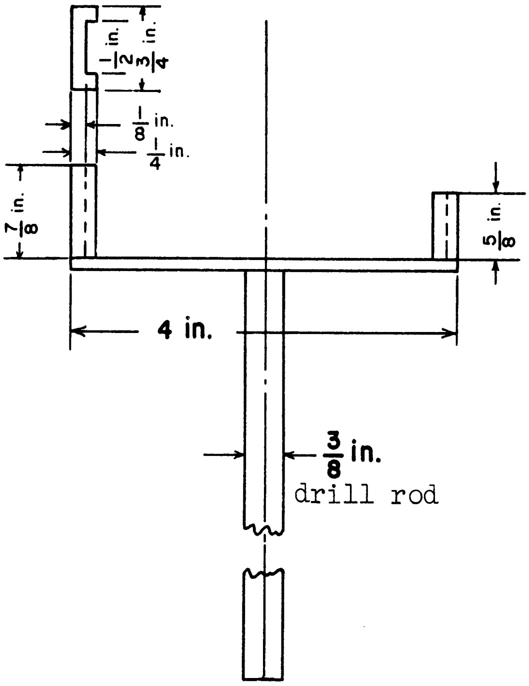

Optical Cell Support

Figure 10. Supports for Components of Detector.

The mirrors were supported on two brass isosceles right triangles as shown by Figure 11. The mounting had hinges to permit the adjustment of the inclination of the mirrors. Two adjusting screws threaded into a brass strip along the steel base plate. The front-surface mirrors used had the dimensions of 1/8 x 2-1/2 x 3 inches.

In order to minimize the distortion of the beams reflected from the horizontal optical axes, the detectors were designed such that the mirrors would be inclined as nearly as possible at 45° to the axes of the horizontal beams. Strips of black electrical tape were attached to the edges of the mirrors in order to eliminate extraneous reflections.

In each detector, a pinhole, which had a diameter of 1/16 inch, was used to reduce the image of the lamp filament to a circular disc. The pinhole was drilled in five-mil brass shim stock and silver soldered over the 1/4-inch hole in the center of the 4 x 4-inch brass support plate. The support plate was fastened behind partition P_2 over a two-inch hole which was drilled at the optical axis of the partition.

Since the beam behind the pinhole was of small diameter, the shutter for the detector was also secured to the back of the pinhole support plate. The fitting for mounting the shutter was screwed to the support plate. The shutter could be attached or detached without disturbing the other components of the detector. The cable release entered the compartment through a grommet in a steel plate which was fastened to the edge of partition P_2 and which was flush with the inside of the compartment cover. The plate blocked the entrance of light through the hole in the cover.

Exposed surfaces of all of the parts were painted flat black.

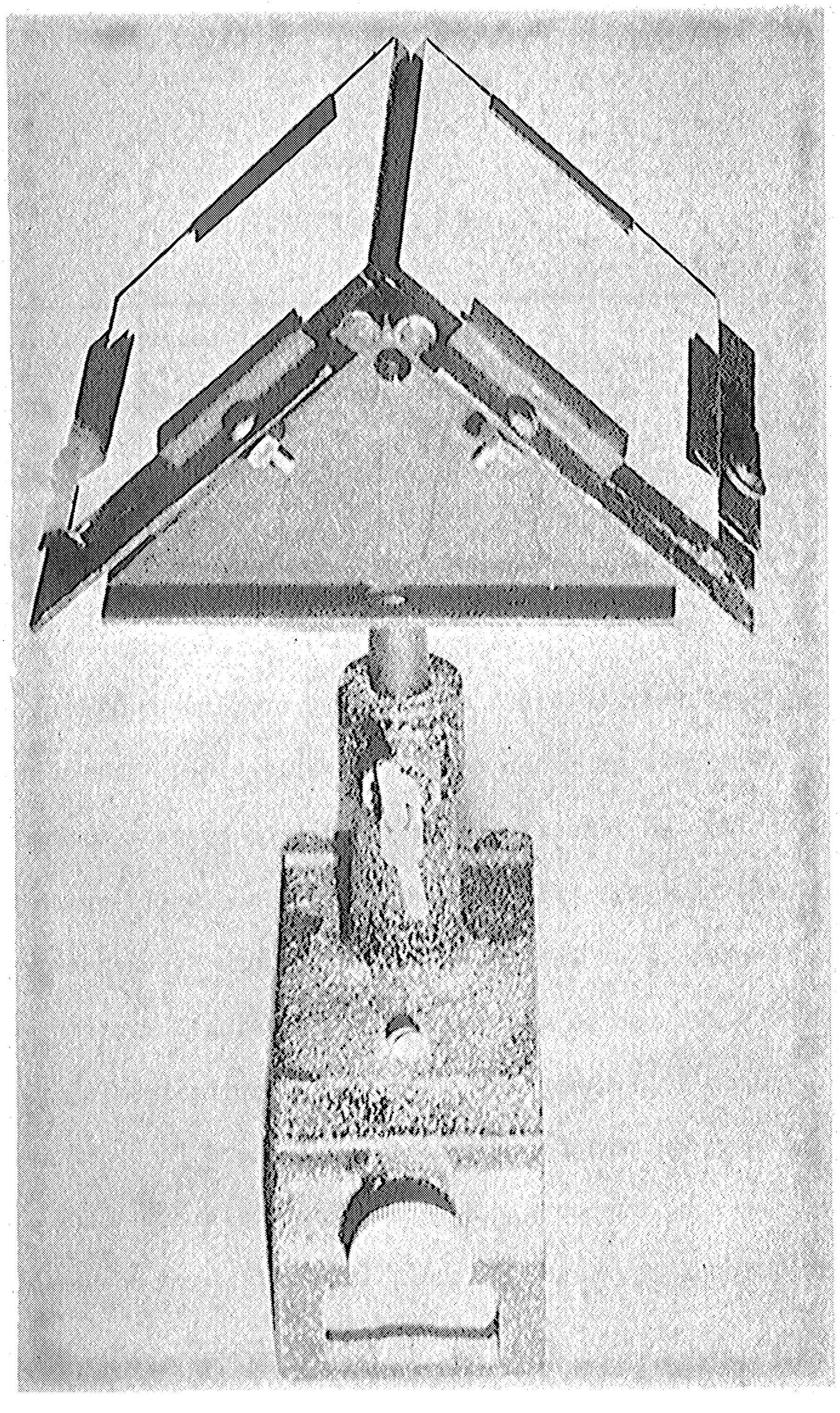

Figure 11. Mirror Assembly.

Lenses

Table I gives the dimensions of the lenses employed in the detectors.

TABLE I

LENS CHARACTERISTICS

Lens Designation	Diameter mm.	Focal Length mm.	Original Mounting
L_1	46	79	none
L_2	48	343	none
L_3	35	176	threaded
L_4	48	343	none

These lenses were obtained as military surplus equipment. Coated lenses were used in order to reduce reflection. The cylinders used for mounting the lenses were machined from brass tubing. For lenses L_2, L_3 and L_4, the cylinders were two-piece units which were similar to telescopes. The section holding the lens screwed onto a second stationary section to allow accurate focusing. Two ring supports were used to hold these cylinders in the optical axis. A layer of plastic tape was wrapped around the cylinders in order to give a snug fit in the ring supports. Because of space limitations and the less critical focus required of them, lenses L_1 were housed in short cylinders which required only one ring support.

Since the pinholes had a diameter of 1/16 inch and the L_3 lenses had a focal length of 175 millimeters, the divergence of the beams was 0.00453 radian or 15.6 minutes. A high degree of collimation is required since the Rayleigh theory is based on perfect parallelism of the incident beam. One-inch holes were drilled in partitions P_3 to admit the collimated beams from the L_3 lens to the optical cell compartment.

It was desirable to have lens L_4 as close to the optical cell as possible in order to include a maximum amount of the scattered flux within the periphery of the lens. On the other hand, if each lens L_4 were close to its mirror, the vertical travel of the beam to the aperture of the sensor would be extended. This would allow the mirrors to be inclined more nearly at 45° and the distortion of the beam due to oblique reflection would be minimized. These requirements were compromised by positioning each L_4 lens approximately in the planes of the center ends of the horizontal closures. Each L_4 cylinder was made just long enough to bridge between a ring support in the optical cell compartment and another in the central black box, Figure 9. The central closure was designed to be narrow such that the supports for the L_4 cylinder almost touched the mirrors. With this positioning, the L_4 lenses were between six and seven inches from the mirrors. The reflected beams had an approximately equal distance of travel to the focal plane. The elevation of the mirror mounting was adjusted such that the centers of the partially converged beams were about 1/4 inch below the upper edges of the mirrors. With this arrangement, the aperture of the photomultiplier moved nearly directly above the areas of reflection. An inclination of about 43.5° from the horizontal was required of the mirrors. The vertical axis of the incident beam was elongated by 0.2 percent by the reflection. The required elevation of the aperture above the mirrors determined the height of the central black box.

Lamp Shields

Each 85-watt mercury lamp generated about 300 B.T.U. per hour. Since the lamp was enclosed, some provision for heat removal was required. Water cooling was preferred to air circulation because of the prevalence of dust with the latter. The lamps also required shields to intercept the ultraviolet radiation except along the beam axis. Water cooling coils could conveniently be mounted on each shield.

Each shield was fabricated from an aluminum sheet which was rolled into the form of a cylinder four inches in diameter and about ten inches in length. A hole to pass light down the optical axis was cut before rolling. Slots were cut out of the bottom of the shields in order to allow them to fit over the optical bench clamps supporting the lamps. The shield rested on the optical bench and enclosed the lamp and support without touching either. Struts were added at the top to support the shield against the back of the black box. About six loops of 1/4-inch O.D. copper tubing were wrapped around each shield and were held in position with brass clips. The ends of the coil protruded from the bottom-front corner of the lamp compartment through grommets in a steel rectangle. The rectangle was screwed to the edges of the base and end of the lamp compartment such that it was flush with the inside of the cover and closed the hole in the cover for the tubing. The shield and the tubing were painted flat black. A lamp could be changed without interrupting the flow of water by unscrewing the plate, shield struts and lamp bench clamp and bending the copper tubing while moving the shield and lamp out of the compartment.

Traversing Mechanism and Driver

It was essential that the sensor be moved across the focal plane of the two L_4 lenses with virtually no lash. Low friction was also desirable. These requirements were met by the component of a gun- or bomb-sighting device pictured in Figure 12. The aluminum frame measured approximately 5 x 9 inches and supported the two ball bearing splines. The carriage ran on the splines over a 3-1/2-inch traversing distance with no perceptible lash. The worm had 20 threads per inch. A drive shaft with a mating bevelled gear could be brought in through the hole in the frame. On the underside of the frame, a machined surface around the hole was available for mounting.

As indicated by Figure 9, the traversing mechanism was mounted with its frame against the top of the central closure. The carriage ran perpendicular to the optical benches with about equal traversing distances on either side of the center of the benches. In addition to four screw holes for securing the frame, a hole 1-3/8 inch in diameter was drilled through the 1/4-inch mounting plate and the top of the central closure to accomodate the drive shaft and bevelled gear. A synchronous chart drive motor, which operated through a speed reducer, turned the drive shaft at 30 r.p.m. The drive shaft was coupled to the speed-reducer

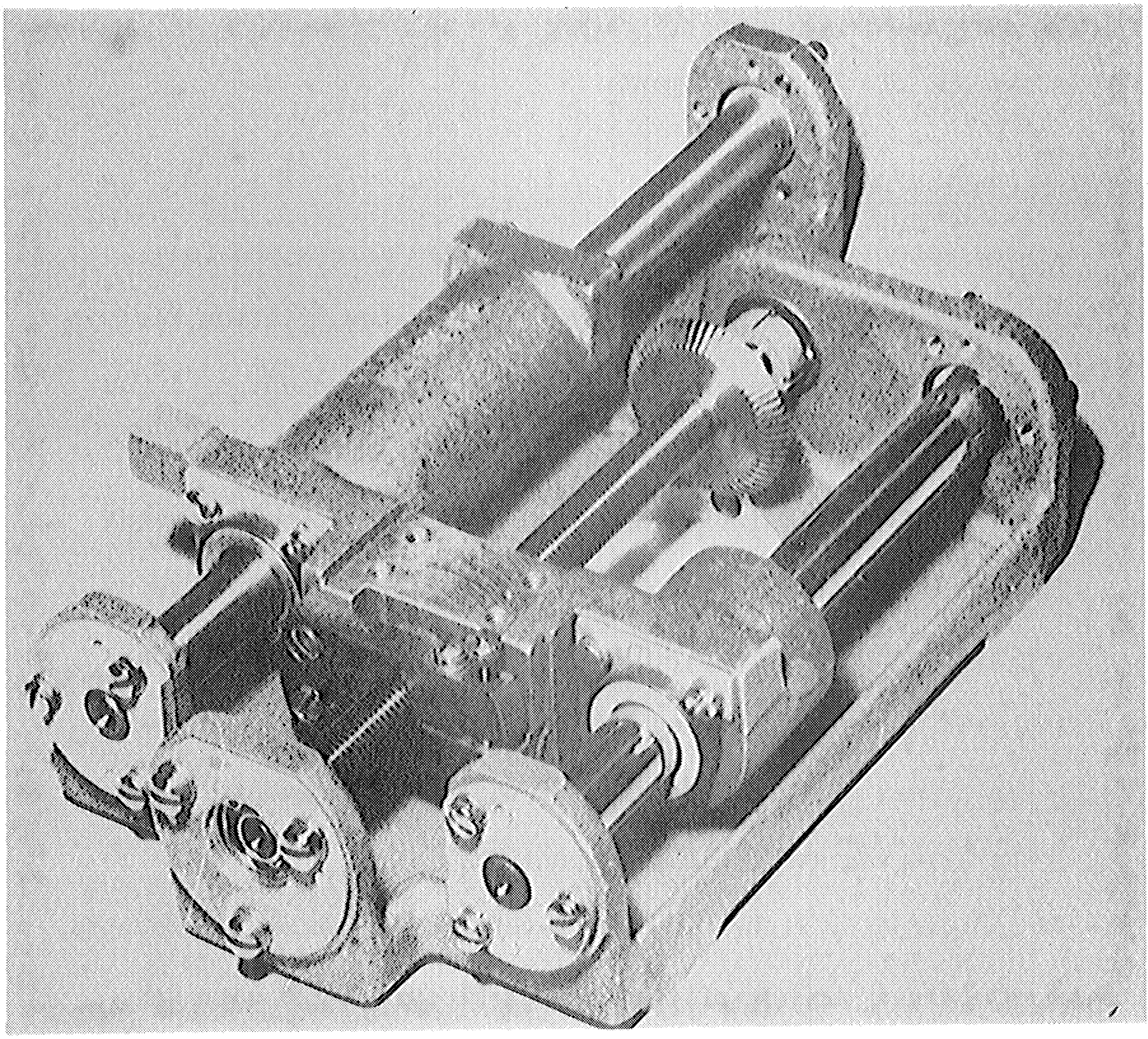

Figure 12. Traversing Mechanism.

shaft through a section of rubber tubing which absorbed the gear vibrations of the speed reducer. Figure 13 shows the mounting of the drive shaft. The drive-shaft housing was designed to seat in the hole in the frame of the traversing mechanism. The bevelled gear at the lower end of the shaft was a duplicate of the gear on the worm shaft. When the traversing mechanism was fastened to the mounting plate through the flange and the closure, light leakage was prevented by the contact between the flange and the top of the central closure.

The motor and speed reducer were mounted in a convenient brass box about eight inches above the mounting plate. The speed reducer shaft ran in two sets of ball bearings on either side of the brass box. The brass box was positioned such that the drive shaft and speed reducer shaft were in line and almost in contact.

The direction of rotation of the motor was changed by reversing the polarity of the field. The circuit for accomplishing this is shown in Figure 14. The key element in this circuit was a triple-pole double-throw coil. The two microswitches were actuated by the stud on the traversing carriage at either end of the traverse. They were positioned on a bar attached to the side of the frame. Leads from the microswitches were plugged into a socket at the top of the central closure. The leads from the socket ran out of the central closure through a light-proof cap. A second plug and socket allowed the leads from the traversing mechanism to be connected or disconnected readily.

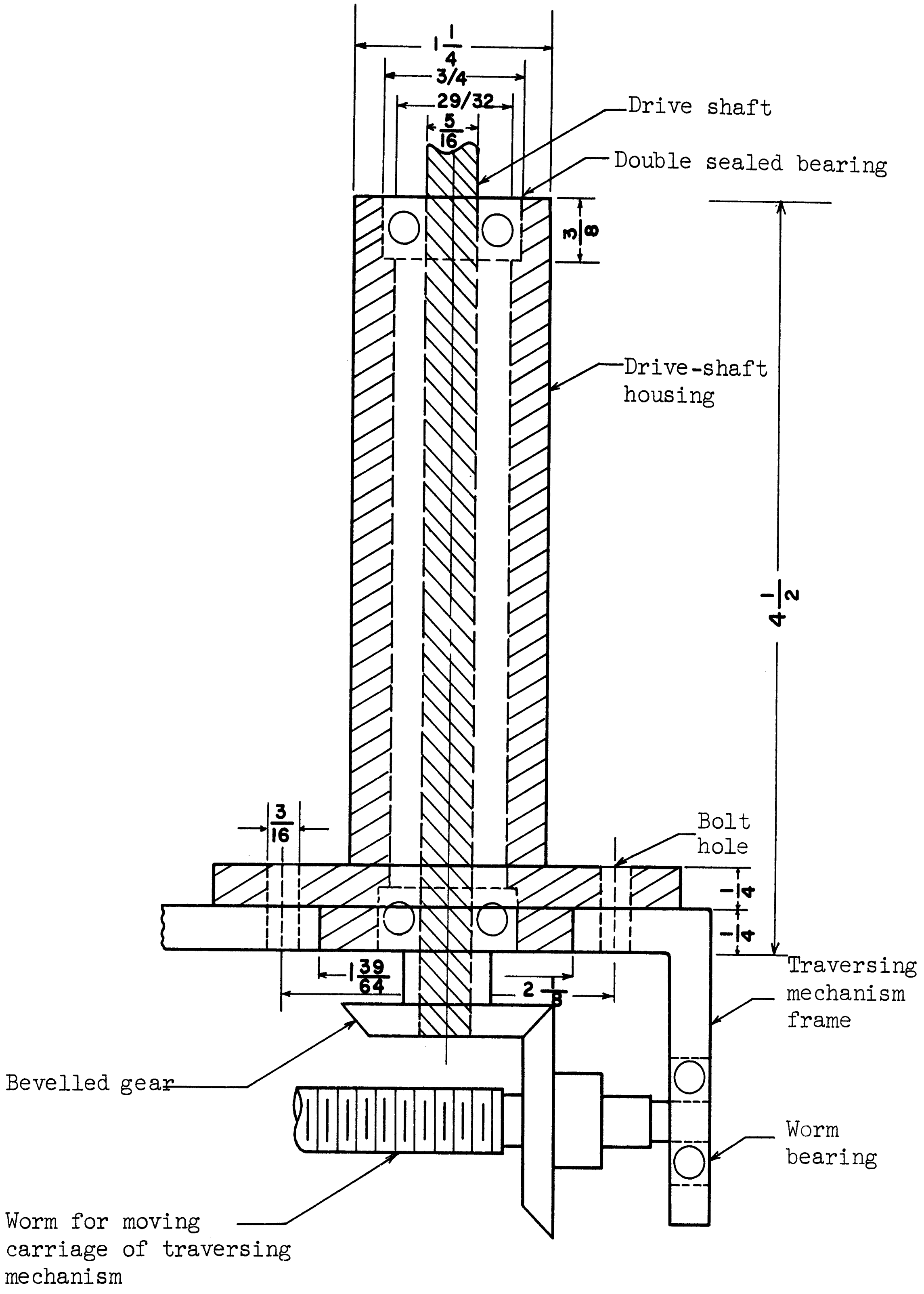

Figure 13. Drive-Shaft Housing and Linkage with Traversing Mechanism.

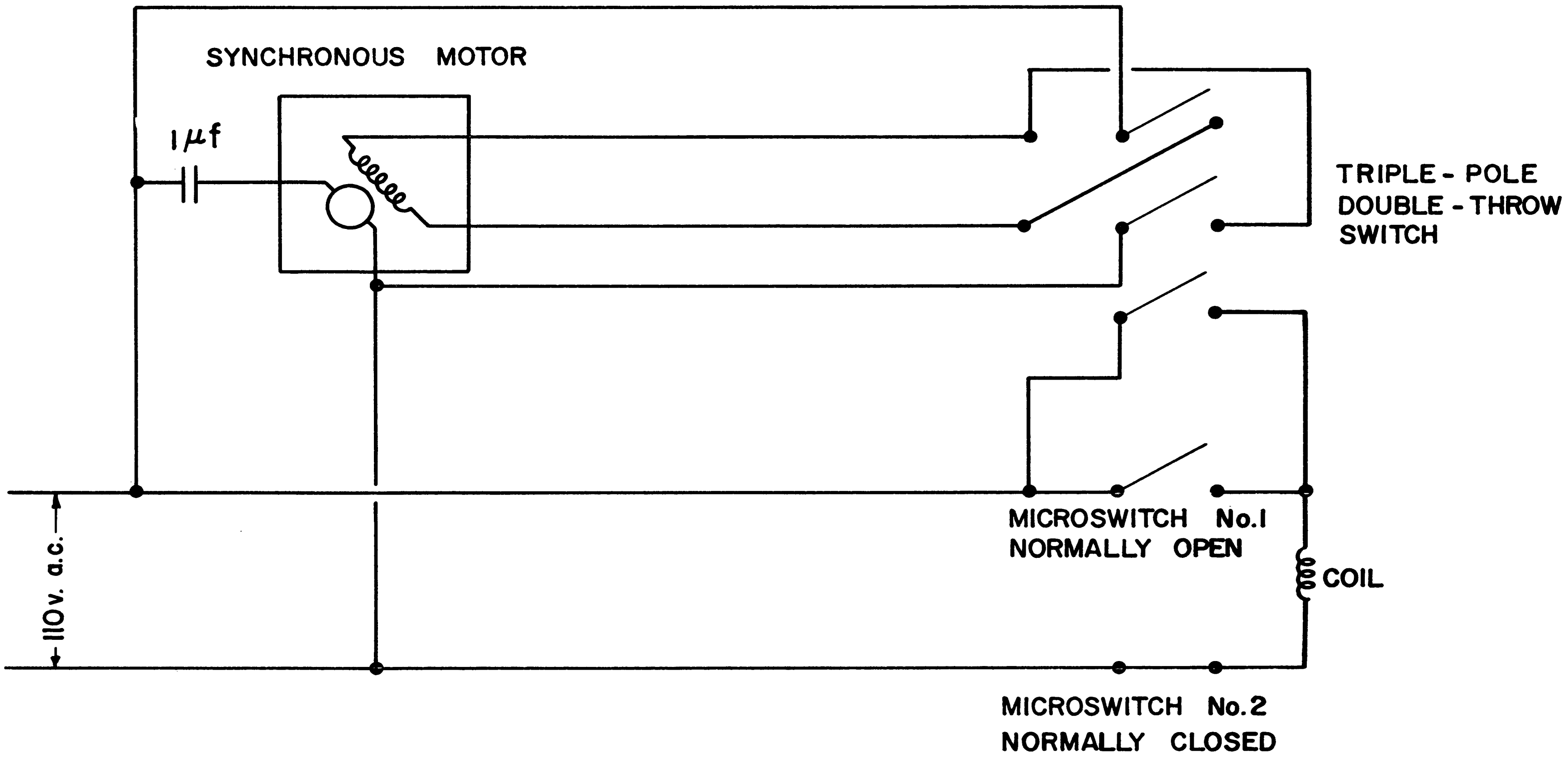

Figure 14. Circuit for Reversing Motor.

Photomultiplier Housing

The housing for the photomultiplier had several functions. It was a light shield. It held the tube face downward to the carriage such that the tube was neither under stress nor able to move within the carriage. It held the aperture against the photocathode surface. The photomultiplier cylinder was designed to be detachable from the carriage in order to allow removal of the photomultiplier without disturbing other items of equipment.

Figure 15 shows the various pieces of the photomultiplier housing assembly. When the tube and the pin base were plugged together and inserted in the brass tube, the pin base rested on the shoulder inside the cylinder. The slots at the top of the cylinder accomodated the high voltage and anode current leads. A grommet on each lead held the lead securely in the slot. The mounting cup for the cylinder was fastened to the carriage of the traversing mechanism. The cylinder slipped into the cup and was supported by four Allen screws. A brass spacer and a thin steel plate, 4 x 6 inches, were fastened between the carriage and the mounting cup. The plate obscured most of the splines and the worm from stray reflections.

The aperture of the photomultiplier consisted of a 1/8-inch hole drilled in 0.010-inch brass shim stock. The aperture was silver soldered to a disc-shaped plate which was fastened to the flange at the bottom of the photomultiplier cylinder. The enlarged holes in the aperture plate allowed the aperture to be shifted to the most sensitive spot on the photocathode. The aperture was just large enough to contain

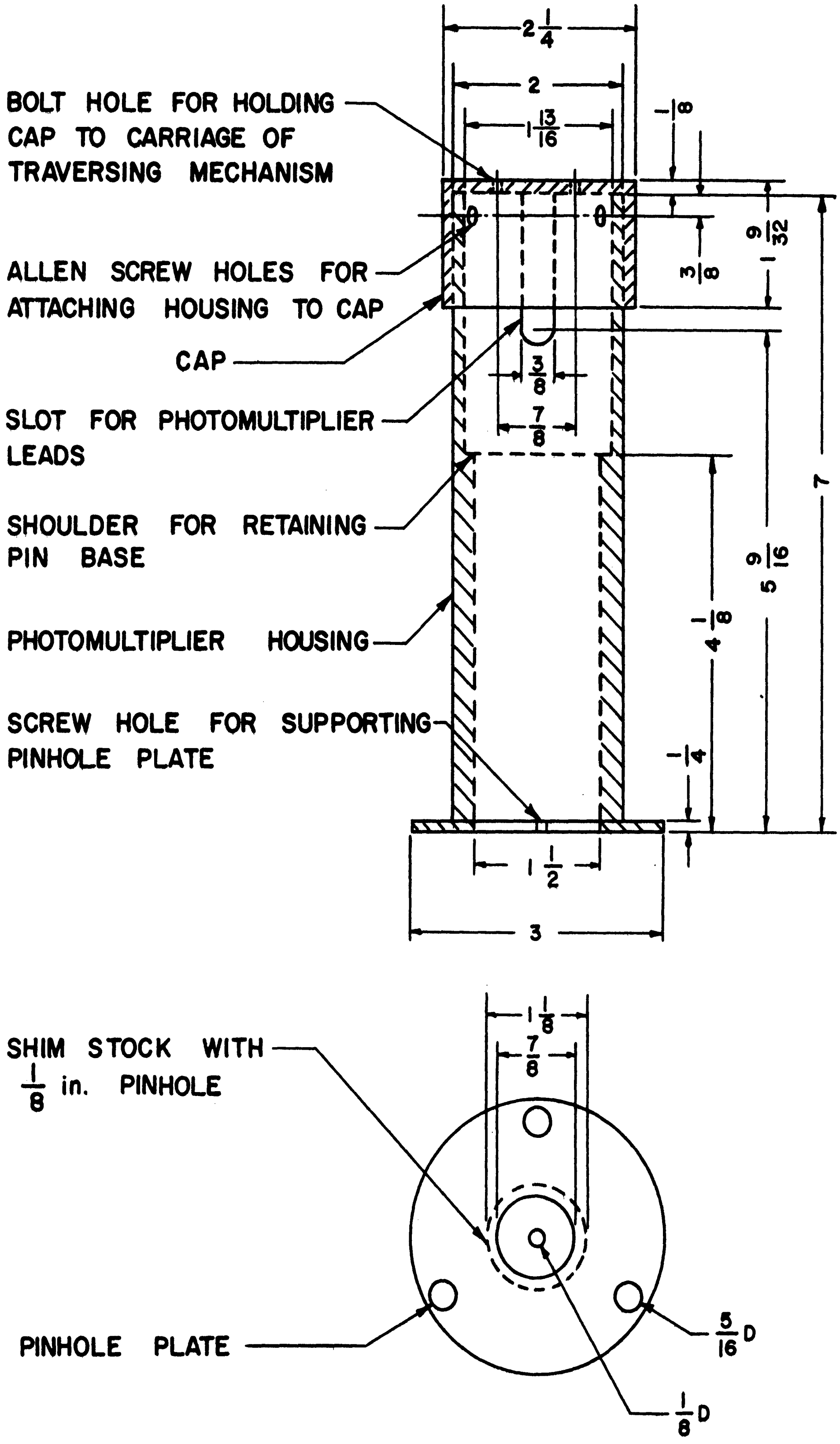

Figure 15. Photomultiplier Housing.

the focused beams from the detector. In order to prevent undue localized fatigue of the photocathode, a disc of diffuse glass was cemented to the inside of the aperture. A drop of immersion oil afforded optical coupling between the diffuse glass and the photocathode. With the photocathode resting flush against the diffuse glass, two opposed holes were drilled through the cylinder into the phenolic pin base. Screws, which were threaded into these holes, held the pin base and photomultiplier stationary. Flat black paint was applied to all components of the photomultiplier cylinder.

The leads from the pin base were joined to high-voltage sockets which were mounted on the outside of the central closure. The flanges on the sockets were broad enough to prevent light leakage through the holes for the leads. The sockets could be dismantled and the connecting pins pulled into the closure. In this way, the leads could be freed from the side of the closure without any solder connections being broken.

Alignment and Focusing of Optical Equipment

The optical benches were levelled in the same horizontal plane. The lenses were raised to the desired 8-1/2-inch elevation above the bases of the horizontal closure by means of machined steel spacing blocks which fit between the optical bench and the lens cylinders. The L_1 lens in each detector was situated approximately one focal length away from the filament fo the lamp. The other lenses were focused according to the procedure given by Clark.(15) The lens,

L_2 , was adjusted to focus the image of the filament on the pinhole plate. The image of the pinhole from lens L_3 was reflected back to the pinhole. Lens L_3 and the pinhole plate were adjusted to focus the reflected image of the pinhole on the pinhole. The mirror mounting was raised until the centers of the converging beams from the L_4 lenses were 1/4 inch below the top edge of either mirror. The apex of the mirrors was squared with the sides of the central closure. The traversing mechanism was aligned with a perpendicular member which was fastened to one of the optical benches. The L_4 lenses were focused to converge the beams on the aperture plate. Finally, the mirrors were inclined to bring the beams into the path of the aperture.

FLOW SYSTEM

Figure 7 shows the simplicity of the flow system. It consisted of a feed bottle, optical cells, coalescer, a flow measuring device, two valves, and 1/4-inch O.D. copper tubing to carry the dispersion from one unit to the next. The flow was controlled at the needle valve downstream.

It was imperative that a clean and contaminant-free dispersion be fed to the coalescer. Corrosion products could plug the screens. Surface-active agents, if present, would vitiate the measurements. Glass construction would tend to ensure cleanliness. However, copper and brass were preferred because of their ability to withstand mechanical stress, their ease of fabrication, the availability of fittings and their resistance to attack by water and a wide range of organic solvents. These metals do not tend to accumulate electrostatic charge.

In commercial practice, coalescence is normally performed at flow velocities in the range of one foot per minute. Pressurized air was the obvious choice for driving liquid through a small coalescer. Other factors favoring pressurized air were the batch nature of the experiment, freedom from contamination by pump seals and economy.

The main components in the flow system were the optical cells and the coalescer. Construction of a coalescing medium whose filaments were microscopic and evenly spaced would have proven a formidable, if not an altogether impossible, undertaking. The suggestion of fine-mesh nickel screens was one of the keys to this study. Construction of a flange to hold the commercially available screens presented no notable problems. However, the problems associated with the optical cells limited the scope of the experiment.

Nickel Screens

In order to ascertain the effects of filament spacing and diameter on the removal of microscopic drops from dispersions, various grids of parallel filaments were desired. Since the fibers in a fibrous bed have a random orientation, the bed can be considered to comprise microscopic pores. Fine-mesh screen would represent a cross section of the pores. The screen is also a representation of two perpendicular arrays of parallel, equally-spaced fibers. Although similar, the flow near the screen would not be equivalent to the flow past parallel cylinders. Fine-mesh screen seems to be the only feasible type of grid. The cross-bracing of the screen imparts a structural rigidity in the presence of flow. This would be lacking in a single series of parallel filaments.

Screen was available in mesh as fine as 1500 lines per inch. The filament pitch in this screen was about 17 microns. This was less than one order of magnitude larger than the drops present in the homogenized dispersion. In order to obtain appreciable coalescence, it was desirable to have the interstice approach the drops in size. The screens chosen had a relatively low percent free area. Most of the screens had interstitial openings equivalent to the filament thickness; the open area was 25 percent. Other screens having various percentages of free area were procured in order to allow independent variation of either the filament thickness or the interstitial distance. Table II gives the dimensionsof the fine-mesh screens used in this study. All screens were planar. The 400-mesh and the 40-mesh screens were obtained from the C.O. Jelliff Manufacturing Company of Southport, Connecticut. These screens were formed by electroplating. The screens of finer mesh were fabricated by Buckbee Mears Company of Saint Paul, Minnesota, by means of a photo-etch process. Figure 16 gives microphotographs of the screens. The fine screens attest to the advantage of the photoforming in comparison with electrodepositation. The 400-mesh, 26 percent open-area screen was sold as a 36 percent open-area product. However, the microphotograph gives evidence of over-plating.

The low values of screen thickness to filament size implies that the filaments are not circular cylinders. An examination under the microscope with reflected light showed that they were elliptical. Figure 17 is an example of the surface irregularities on the center of the filaments of the 500-mesh screen. Since the screens were quite

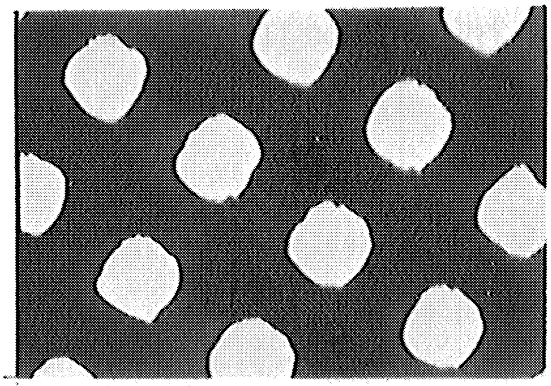

400-Mesh, 26% Open-Area, x300

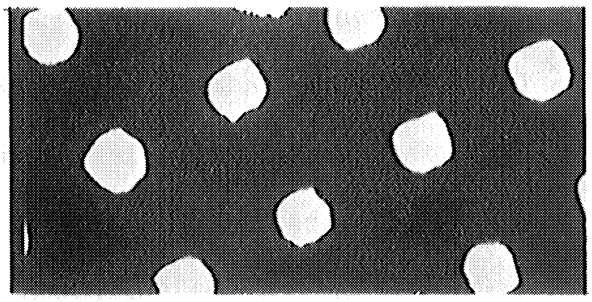

400-Mesh, 16% Open-Area, x300

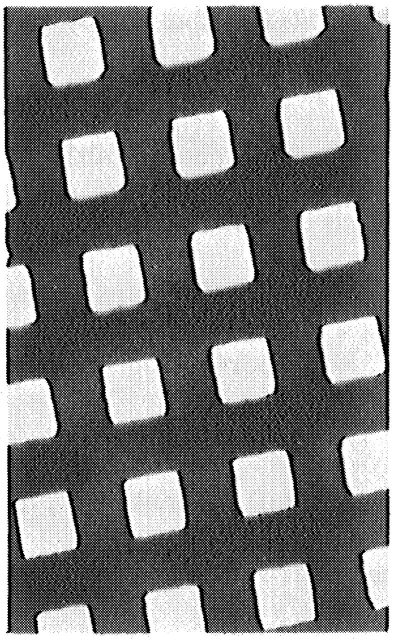

500-Mesh, 25% Open Area, x300

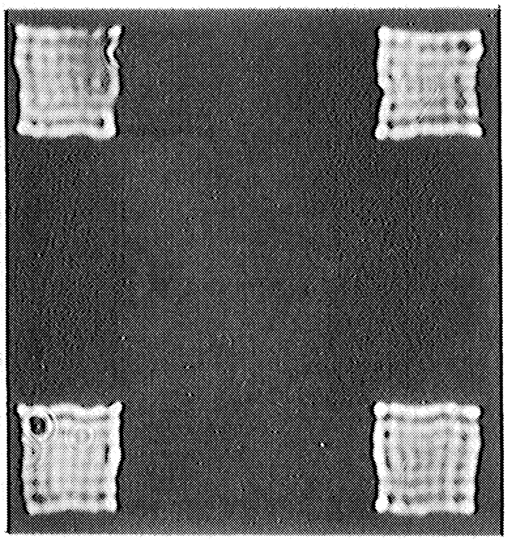

750-Mesh, 9% Open-Area, x1375

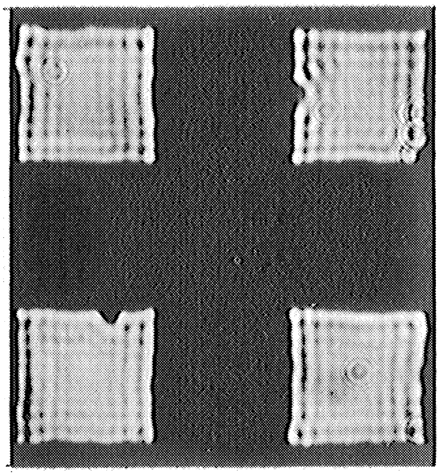

100-Mesh, 25% Open-Area, x1375

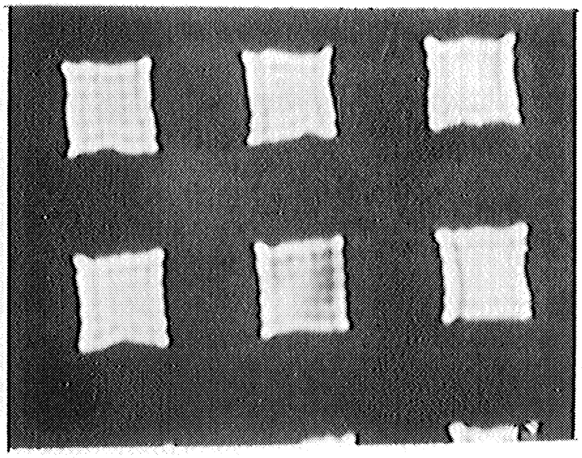

1500-Mesh, 25% Open-Area, x1375

Figure 16. Photomicrographs of Screen Grids.

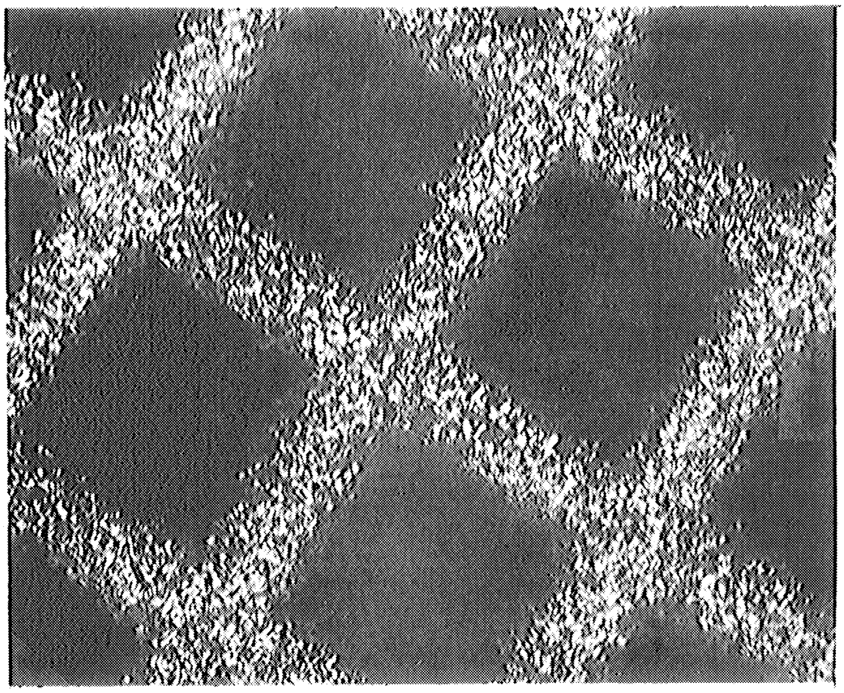

500-Mesh, 25 Percent Open-Area Screen, x1375

Figure 17. Typical Micro-Structure of Screen Surface.

TABLE II

DESCRIPTION OF NICKEL SCREENS

Screen Mesh lines per inch	% Cross Sectional Open Area	Thick-ness $z \times 10^3$ cm.	Filament Width $d_F \times 10^3$ cm.	Interstice Width $d_J \times 10^3$ cm.	Thickness to Filament Width Ratio z/d_F
400	26	1.3	3.14	2.21	.414
400	16	2.0	3.89	2.46	.525
500	25	1.9	2.54	2.54	.75
750	9	1.8	2.41	0.98	.76
1000	25	0.64	1.27	1.27	.50
1500	25	0.25	0.85	0.85	.33
40*	50	6.1	11.2	45.5	.555

* support screens

thin, it was extremely likely that they would rupture if a large area were perpendicular to the flow. A relatively heavy 40-mesh screen was used as a support for the fine screens. The screens were available in nickel, copper and precious metals. Nickel was selected because of its resistance to corrosion by water and by many organic solvents and because screens of it were the least expensive.

A large bed diameter was desirable because low linear flow rates could be attained at volumetric flow rates which were sufficiently great that drop settling in the flow channels would not be excessive. However, a large bed diameter would entail a long diverging section from the 1/4-inch copper tubing. The associated large holdup volume would partially nullify the advantage of a more rapid rate of flow. Moreover, the cost of the screen precluded a large diameter. As a compromise, the diameter of the bed was set at 1/2-inch. A die for cutting discs from the sheets of screen was machined from a three-inch section of 1/2-inch drill-rod and hardened.

Screen Treating

It was shown that the characteristics of the filaments are very important in determining the extent of coalescence.(50) Since metals typically do not have an inherent affinity for polar or non-polar materials, the affinity of the metallic surface depends upon the means of cleaning. The affinity of the metallic surface is prone to change over a period of time or in abusive circumstances.(6,35) Since there was no means of following the change of surface energy of the screen, it was imperative to treat the screens such that they would have a strong affinity for the dispersed phase. Screen wettability would then not be a limiting factor in the experiment.

Since the limitations of the optical cells prohibited a study of the behavior of water-in-oil dispersions, it was sufficient to render the screens organophilic. Octadecylamine, which was used to treat glass elsewhere,(22) was used with success on the nickel screens. This amine is insoluable in water and has a limited solubility in aliphatic hydrocarbons and alcohols. Although octadecylamine conferred an organophilic property to the screens, it evidently did not create spreading conditions. A metal surface, which was coated with the amine and immersed in water, allowed incident cyclohexane drops to flatten out to a contact angle of about 20°. For screen treating, a nearly saturated solution of the amine was prepared in the proportion of 0.1 gram of octadecylamine in 100 milliliters of normal heptane. The discs of fine screen were cleaned in isopropanol vapor, rinsed in normal heptane and stored in corked flasks containing the treating solution. During the final series of runs it was found that the amine had a large temperature coefficient of solubility. As the temperature rose a few degrees, the solution appeared to become unsaturated and to desorb some of the amine from the screens. In order to control the surface condition, the flask containing the screens to be used in a forthcoming run was cooled until a light suspension of the amine was visible. This insured complete coverage of the nickel surface. The support screens were stored in normal heptane without octadecylamine.

Filter Flange

With the available screens, the largest expected value of d_P/d_I was expected to be about 0.25. According to Figure 2, most of the drops would not be intercepted and the interception would decline as d_P/d_I declined. It was desirable that the coalescer be able to hold several layers of screen in order that the effects of a change of conditions would be more clearly revealed. It was not the purpose of this experiment to study the interactions between screens spaced at microscopic distances. A wide spacing relative to the filament width was used.

Figure 18 gives the design of the filter flange. The recess in the downstream section allowed the insertion of up to five layers of support and coalescing screen. A Teflon washer was positioned on top of each layer. The washer served as a gasket and a spacer between layers. The washers were cut from 1/16-inch Teflon sheet. They had an O.D. of 1/2 inch and an I.D. of 0.40 inch. This I.D. constituted the working cross section of the flange and corresponded to the diameter of the flow channel in the downstream section below the shoulder of the

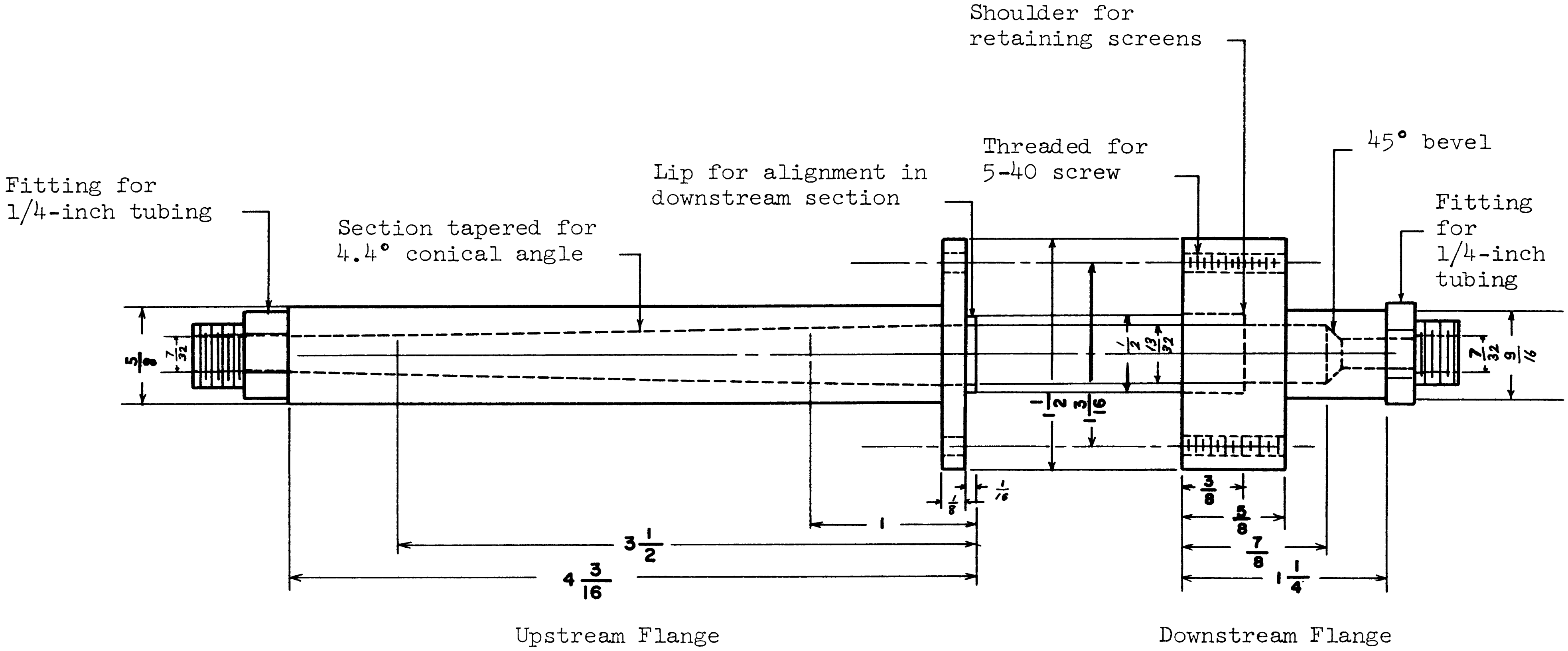

Figure 18. Flanges for Coalescing Filter.

recess for the screens. At the outlet of the flange, the diameter of the flow channel necked down to that of a brass fitting for 1/4-inch tubing. The fitting was silver soldered to the outlet of the downstream section.

The function of the upstream section was to expand the flow from the 1/4-inch tubing to the working diameter of the flange without inducing eddies. In designing the section, the interests of perfectly laminar flow were compromised with the desire to keep the holdup volume between the two optical cells at a minimum. The diverging section had a conical angle of about 5°. The straight section upstream of the screens was limited to a length which would not permit the full development of a flow profile. Since the presence of the screens would exert a straightening effect on the flow, it seemed that the absence of fully developed flow would have little or no effect on the extent of coalescence. The lip, which protruded beyond the flange, fitted into the downstream recess, pressed upon the washer farthest upstream, and sealed the flow channel against leakage. Four Allen screws held the upstream and downstream sections together. A bolt along a major diameter of the downstream section secured the filter flange to the angle steel structure.

Optical Cells

The optical cells permitted an assay of the dispersions upstream and downstream from the coalescer. The optical cells designed for the calibration measurements with glass spheres differed from the optical cells or flow cells for the coalescence measurements. The flow cell required an upstream section which expanded the flow from the 1/4-inch tubing to the working width of the cells without inducing eddies. The calibration cell did not have the upstream section because it would have increased the volume of suspension needed to fill the cells.

The prime concern in the design of the optical cells was their thickness. The thinner the cells, the greater the concentration of dispersion at the onset of multiple scattering. However, if it were too thin, the cell's resistance to flow would be high and it would be difficult to clean. It was also necessary that the area of view be sufficient to accept the entire collimated beam. The design adopted for the calibration cell is shown in Figure 19. The cell was constructed of three plies of brass sheet 0.050 inch thick. The inner ply shaped the area of view and determined the cell thickness. The two outer plies formed the side walls of the cells. Optically flat microscope slides were used for the windows. These were cut to fit in the 1-1/2 x 2-inch hole in each outer ply such that the flow channel had a uniform thickness over the length of the cell. The brass retaining blocks at either end held the three plies together. The assembly was joined with silver solder. The access holes in the retaining blocks were threaded to accomodate the fittings for the 1/4-inch tubing. After silver soldering, the faces of the central ply in the window recesses were flattened and made parallel by an end milling operation. The finished thickness of the spacer was taken as the thickness of the cell.

The bare brass structure of the optical cells constituted light reflecting surfaces. Cover plates were fabricated and painted to shield the crucial area between the two retaining blocks. Holes were drilled through the three plies for the attachment of the cover plates.

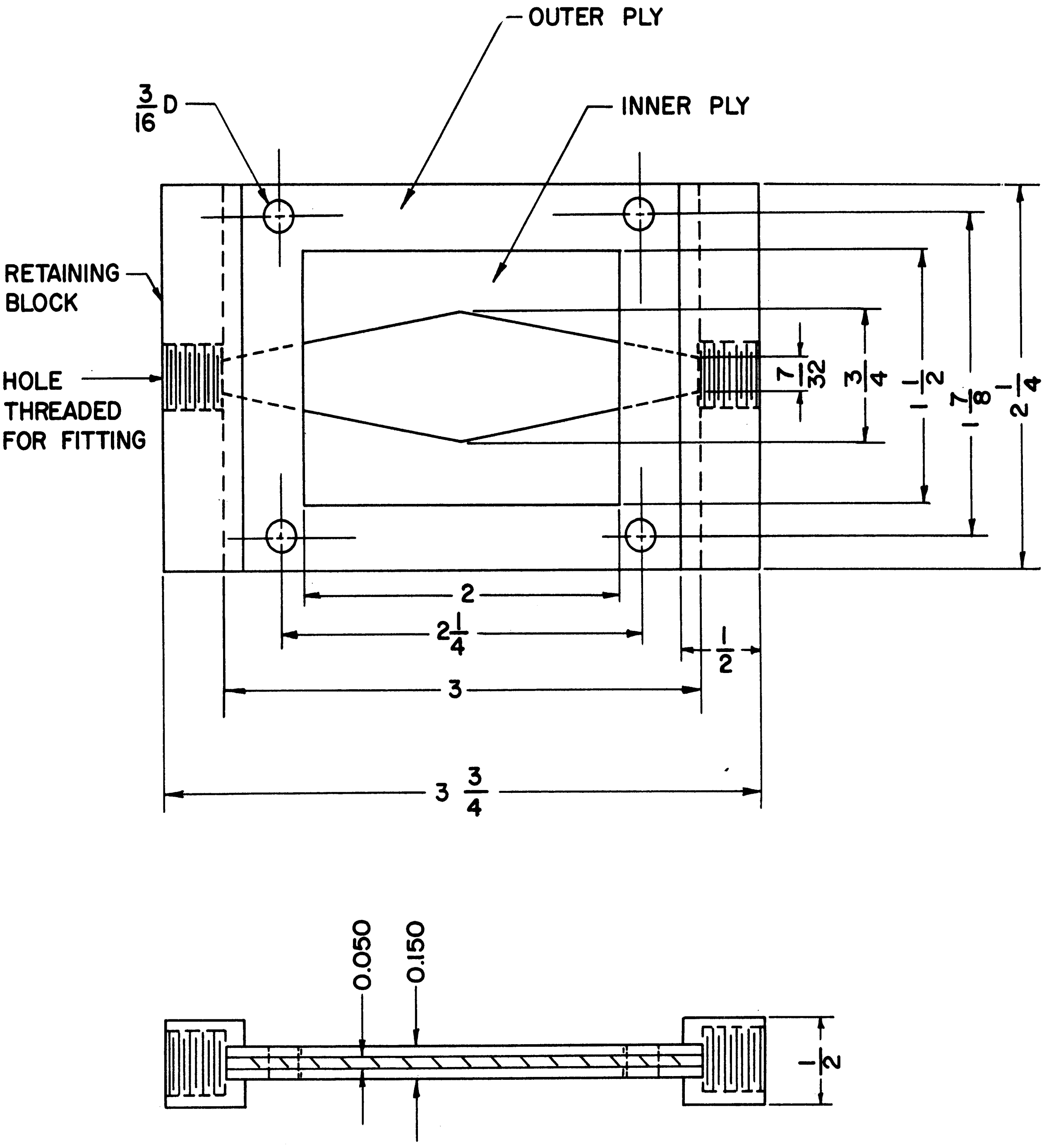

Figure 19. Optical Cell for Calibration Measurements.

Figure 20 is a photograph of a fully assembled flow cell. The window section was almost the same as for the calibration cell except for the upstream part of the central ply. It was shaped for a 6° divergence from the inside diameter of the 1/4-inch tubing to the maximum cell width of 3/4 inch. The two brass shoulders at the upstream end of the optical section were screwed together through the three plies. The shoulders provided sufficient width to fill the upstream slot in the cell support. Threaded holes in the ends of the fitting blocks allowed the optical cells to be screwed to the bottom plate of the optical cell support.

The greatest difficulty in cell construction was the seal between the inset windows and the outer brass plies. The initial intent was to use external Teflon gaskets and to bolt the assembly between steel flanges. However, in view of the cell design, the glass windows could not withstand the stress. A flexible gasket would have lacked chemical inertness. Sauereisen Number One ceramic cement proved an acceptable sealant for the calibration cells. However, the ceramic cement could not withstand the erosive conditions encountered in the flow cells. Since no chemically inert sealant was available, epoxy resin was used for the flow cells. In order to prevent the gradual dissolution of the epoxy resin and contamination therefrom, it was necessary to restrict the experimental liquids to aliphatic alcohols and hydrocarbons.

A second difficulty was encountered in the operation of the flow cells. By virtue of their hydrophilic nature, the glass windows

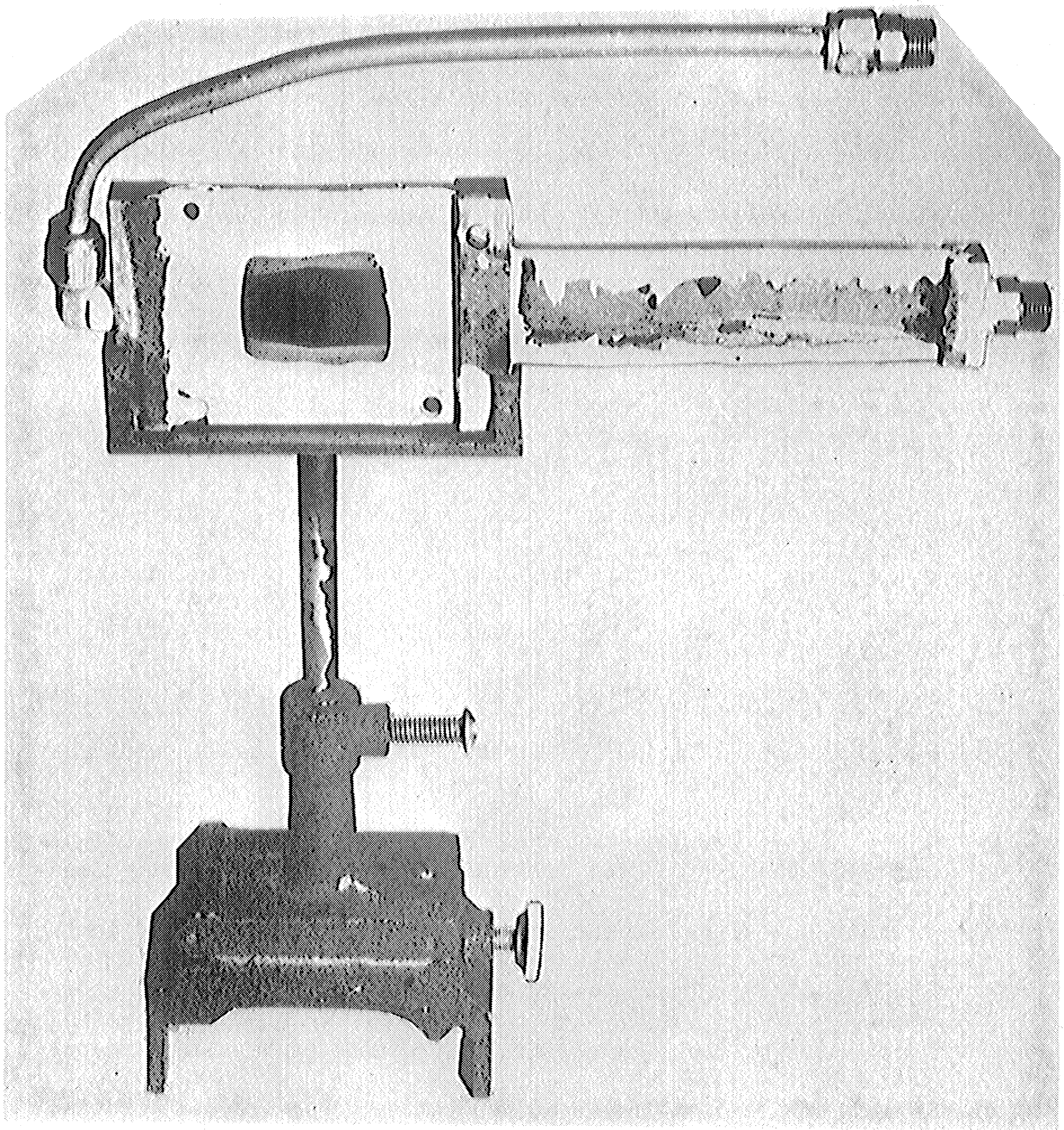

Figure 20. Assembled Flow Cell.

fogged rapidly in the presence of a flowing dispersion of water-in-solvent. An attempt to eliminate this tendency by pretreating the windows with octodecylamine was unsuccessful. When used in the presence of aliphatic alcohols and hydrocarbons, Plexiglas windows became wormed with surface cracks, which produced intense scattering. Plexiglas had the added disadvantage of being soft and easily scratched. Lacking any other plastic material, the experiment was limited to the measurement of the coalescence of dispersions of mild organic solvents in water and in water solutions. The limitation favored economy and safety.

Since there was no flow through the calibration cell, one of the access holes was sealed with a brass plug. The cell was loaded through a short riser, which was screwed to the other hole. An elbow and a loop of tubing were screwed into the downstream retaining block of each flow cell. The tubing delivered the cell effluent to the front exterior of the optical cell compartment. Cell compartment covers with holes were required by the flow cells.

Flow Control and Measurement

The dispersion flow was controlled manually by means of a needle valve at the point of discharge from the flow channel into the receiver. A rotameter was located immediately upstream from the valve. During the preliminary runs, the flow rate measurements were based upon clear fluid calibration of the rotameter. Upon suggestion, calibration was attempted with a sample of dispersion. This attempt made it clear that the microscopic drops, however dilute, were accumulating on the bore and the float of the rotameter and altering the characteristics of the rotameter. Thereafter, the flow was measured directly by timing the flow of the effluent from the valve into a burette. The rotameter was retained as a flow indicator. The correction of the rotameter-measured flow rates is discussed in the Data Analysis section.

Flow Drive and Flow Channels

A 2100-cubic-inch oxygen cylinder was used as the pressure reservoir for driving the flow. Air from the laboratory main was admitted through a letdown valve and a Fiberglas filter. The reservoir was equipped with a mercury manometer and a vent valve. A five-gallon glass bottle was used as the feed container. The rubber stopper holding the dip tube for the feed and the line from the reservoir was clamped to the neck of the bottle. In order to guard against possible mishap, the bottle was enclosed in a 30-gallon can. A stainless steel needle valve with Teflon packing was situated between the feed bottle and the upstream flow cell in order to facilitate the assembly of the flow system prior to a run. The tubing between the downstream cell and the rotameter had a tee with a valve for venting air as a run was started. The flow tubing could be conveniently dismembered for cleaning and for the removal of all major components of the flow system.

CALIBRATION MEASUREMENTS

Calibration of the light scattering detectors was necessary to show that the lens-pinhole method in conjunction with the calculation procedure and the Mellin transformation was capable of replicating a known particle size distribution with a reasonable degree of accuracy. It was also necessary to show that the intensity of scattering was related to particle concentration. Calibration was performed by examining the scattering distribution obtained from suspensions of microscopic glass spheres. The measurements parallelled the experimental work of Chin.

Preparation of Glass Spheres

At the outset it was thought that an equivalence of the relative index of refraction in the calibration and coalescence measurements was necessary to insure a similar variation of the light scattering coefficient with particle diameter. This militated in favor of a solid having a relatively low index of refraction, since it was anticipated that dispersions having relative indices of refraction less than unity would be used. Pyrex glass was chosen. Morey gives 2.23 and 1.48, respectively, for the density and index of refraction of Pyrex.(45) The index of refraction measured in this work was 1.475. Micron-diameter Pyrex glass spheres, not available commercially, were made according to the procedure of Bloomquist and Clark.(3) From the work of Penndorf,(47) it later became evident that the variation of the light scattering coefficient could be adequately characterized if the absolute value of the difference between one and the relative index of refraction were about the same in the calibration and coalescence measurements. It appears that the use of commercially available polystyrene spheres of micron diameter might have been possible. These would have given a relative index of refraction greater than one in any permissible suspending solvent.

The essential details of the preparation of glass spheres have been adequately described elsewhere.(3,29) The spheres were separated into size fractions by allowing the spheres to settle in water. Although this was a time consuming procedure, settling and decantation was preferred to elutriation because of the more uniform velocities across the settling beaker. Narrow-cut fractions were collected in the range of size between 1.5 and ten microns. The various size fractions were stored under water until use.

Figure 21 shows photomicrographs at 1800x of a two- to three-micron fraction and an eight- to ten-micron fraction of spheres. The two- to three-micron fraction corresponds closely to the drop size distributions in the homogenized dispersions. The particle size distributions for these two fractions were estimated from a series of photomicrographs. The projected sphere diameter could be measured within 0.25 millimeter. Since a one-micron interval projected as 1.8 millimeters, it is estimated that the particle counts for each size interval of one micron were within 30 percent of the correct value for the eight- to ten-micron fraction. For the two- to three-micron fraction, the average projected diameter was about 4.0 millimeters.

Preparation of Suspensions of Glass Spheres

A suspension for the calibration measurements was prepared by suspending a known weight of spheres from the desired size fraction in a known volume of solvent having the desired index of refraction and the same density as Pyrex. Brominated organic solvents were attractive co-constituents of the suspending solvent because of their

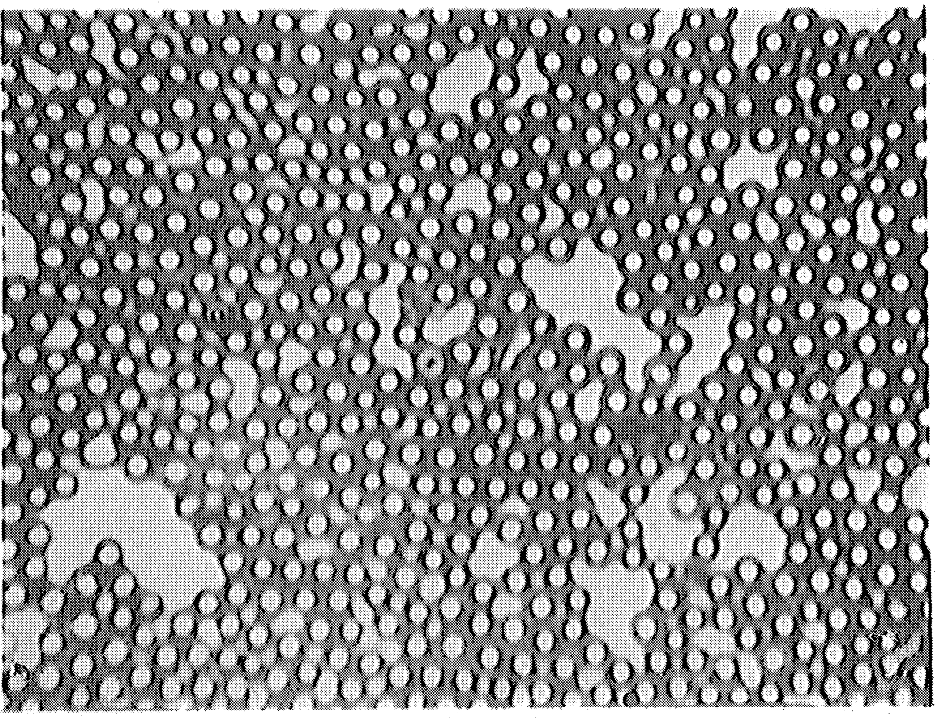

2-3-Micron Fraction, x1800

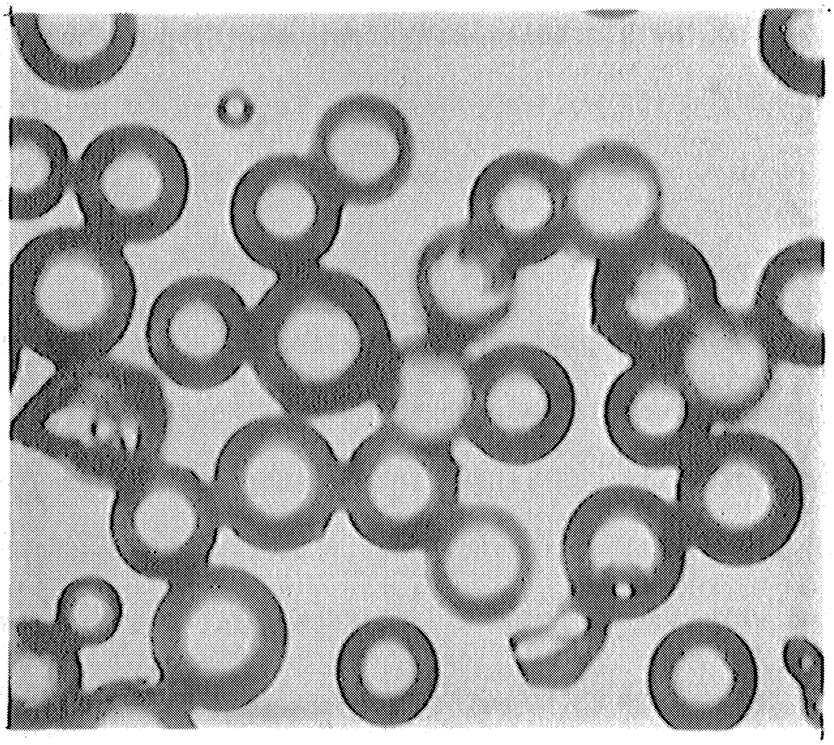

8-10-Micron Fraction, x1800

Figure 21. Photomicrographs of Fractions of Glass Spheres.

high density and index of refraction. The solvent mixture was prepared in the proportion of 60 volumes of 1,1,2,2-tetrabromoethane, 40 volumes of chlorobenzene and three volumes of isopropanol. The third ingedient was necessary to stabilize the suspension of spheres against flocculation. The index of refraction of the solvent was about 1.58, the exact figure varying slightly from batch to batch. The relative index of refraction of the Pyrex spheres was between 0.93 and 0.935.

The Pyrex spheres agglomerated as they were dried. The problem was solved with an octadecylamine surface coating(22) and ultrasonic agitation. About 100 milligrams of dried spheres of the desired size were weighed into a solution of about 20 milliliters of isopropanol containing 50 milligrams of octadecylamine, and the mixture was subjected to ultrasonic agitation. Residual agglomerates were removed by repeated settling. The particulate spheres were allowed to settle, and the alcohol solution was decanted. About 20 milliliters of suspending solvent was added in order to prepare a particulate suspension of about 0.1 volume percent spheres.

Measurement Procedure

During the course of the calibration measurements the suspension of spheres was diluted successively in order to find whether the scattering intensity was linear in concentration as predicted by Equation (78). The calibration cell was rinsed with the suspending solvent and filled with the suspension. The scattering patterns were obtained in both detectors by the methods described in the next sub-section. The cell was then rinsed with chlorobenzene to remove all glass particles.

Part of the virgin suspension was diluted with suspending solvent. The measurement procedure was repeated until scattering patterns had been obtained on three or four levels of concentration. Most of the remaining initial suspension was pipetted into a tared aluminum evaporating dish and dried for a gravimetric determination of the volume fraction of spheres present. The calibration measurements were performed primarily with the two- to three-micron fraction of spheres, since the drops in the homogenized dispersions were found to be of this size.

Procedure for Light Scattering Measurements

The procedure whereby the angular flux distribution curves were obtained was the same for the calibration measurements and the coalescence runs. The flux distributions were obtained by allowing the photomultiplier to scan the scattered flux from the upstream and downstream detectors. Since it was necessary for the photomultiplier to execute one cycle of motion forward and back, this measurement was termed a "traverse." The mercury lamps and high voltage supply were normally allowed to run continuously to eliminate the fatigue and transients of starting. The optical cells were positioned as closely as possible to the L_4 lenses in order that the scattered rays from as wide a forward cone as possible could enter lens L_4 . Multiple reflections between the diffusor in front of the sensor and the windows of the optical cells were avoided by tilting the optical cells slightly toward their respective L_4 lenses with small wedges under the optical bench clamps. The inclinations of the mirrors were adjusted to center the focused transmitted beams on the aperture of the photomultiplier. The compartments were closed. With one of the transmitted beams still centered in the aperture, the photomultiplier was energized by the lowest voltage available through the high voltage switch. The power supply output was adjusted such that the response registered by the recorder was between four and five millivolts. The photomultiplier was now fully excited and ready for the measurements.

In the case of the calibration measurements, the calibration cell was placed in one of the detectors and the shutter for that detector was opened. With the chart drive on, a half traverse was started at the rear of the central black box and terminated at the front. The position of the high voltage switch was changed as needed to keep the photomultiplier output between 1.5 and ten millivolts. At the end of the half traverse, the photomultiplier was de-energized and returned to the rear of the central closure while the calibration cell was moved to the opposite detector. The shutters were reversed and a second half traverse was performed. These two half traverses completed the calibration measurements at a given concentration level.

In the case of the coalescence measurements, a complete traverse forward and back was executed. The upstream measurements were performed on the forward half cycle and the downstream measurements on the backward. When the synchronous motor reversed its direction, the shutters were reversed. At the end of the traverse, the chart displayed the two scattering distributions back-to-back.

At some point during a series of traverses, cathode current amplification for the various scales of the high voltage input was measured relative to one of the scales. In chart editing, the outputs recorded for the various scales were converted to the units of one of the scales.

For a series of traverses with a certain continuous phase fluid or for the calibration measurement, blank traverses were performed in which the optical cells were loaded with the continuous phase fluid. These traverses gave the inherent scatter of the optical equipment. The flux distribution of the blank was subtracted from all traverses with that solvent in order to obtain the net flux distribution of the dispersion.

Figure 22 shows a typical scattering pattern. The central node of transmitted light established the position of the optical axis from which the forward angles were measured. The distribution of scattered flux was approximately symmetrical about the node. The rather abrupt decline of scattered flux at the ends of the traverse were caused by the intersection of the scattered flux with the edge of L_4 lens. The flux was measured at fixed intervals of angle, normally 0.01 radian, from the directly transmitted beam. These values were substituted into Equation (78) for the numerical approximation of the Mellin integral.

Calculation of Particle Concentrations from Distributions of Scattered Flux

In addition to the verification of the lens-pinhole method, a second expected fruit of the calibration measurements was the disclosure

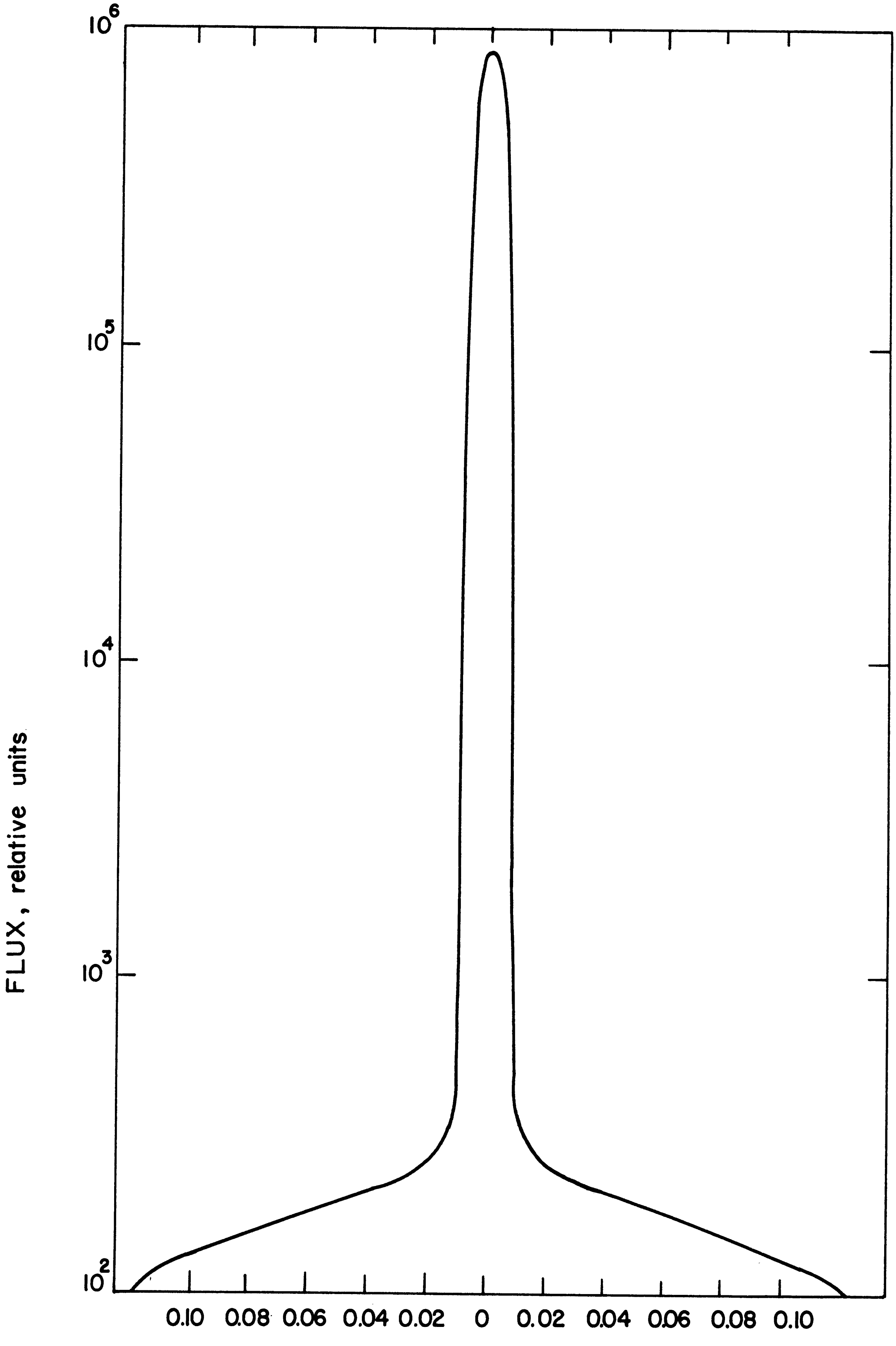

Figure 22. Flux Detected by Sensor.

of the proper method of truncating the numerical approximation to the Mellin transformation, Equation (78), and the appropriate size of the angular interval.

It is likely that any numerical approximation is unique over a narrower range of sizes than the parent integral. In the calibration and coalescence measurements, the limiting diameters were separated by a factor of two or less. For such a range, the flux patterns produced unique concentration distributions. However, for particles in the two- to four-micron range, each point on the computed distribution did not literally represent the concentration of particles within the range d_P to $d_P + d(d_P)$. The transformation made the concentration distribution more diffuse. Each point of the computed distribution appeared to be related to the concentration of particles over a one- to two-micron range which contained the point diameter, d_P . This character of the transformation is demonstrated in Appendix B .

In Equation (78), the angular frequency of oscillation of the Bessel function kernel, $M(\alpha\theta)$, is proportional to α or to d_P. For larger particles, $M(\alpha\theta)$ executes more cycles over a fixed span of θ and more information is conveyed. A shorter angular interval, $\Delta\theta$, would be required in the numerical integration to discern this information. For particles between two and four microns, it was found that an interval of 0.01 radian was satisfactory for the numerical integration.

Trial calculations using the scattering patterns obtained from the calibrations showed that the optimum point of truncation of the Mellin integral was at the angle at which the flux function of the integrand of Equation (68) vanished:

$$d/d\theta\,[\theta^2 I(\theta)] = d/d\theta\,[\theta^3 F(\theta)] = 0 \qquad (79)$$

In order to perform the calculation indicated by Equation (79), it was assumed that the scattered flux received by the sensor varied linearly with an increase in θ from the largest angle at which measurements were possible. The slope was equal to $1/\Delta\theta$ times the difference between the $F(\theta_j)$ for the two outermost θ_j of the chart record. The linear relation for $F(\theta)$ was inserted in Equation (79). The θ_m was taken as the integer multiple of the angular increment nearest to the angle computed by Equation (79). If θ_m exceeded the maximum θ_j of the measurements, the values of $F(\theta_m)$ and the additional $F(\theta_j)$ were supplied from linear relation assumed for $F(\theta)$. Since $F(\theta)$ was often nearly linear at the limiting angle, the linear extrapolation appeared to be a good assumption.

The extra-bracket coefficient in Equation (78) can be simplified somewhat by the introduction of the pertinent dimensions of the lens-pinhole detectors. Using a focal length, b , of 13.5 inches, an aperture diameter, a , of 1/8 inch and a wave length, λ , of 0.5461 micron, Equation (78) becomes

$$\frac{d\phi}{d(d_P)_i} = \frac{510\, d_{P_i}^{\;2}}{tKF(0)} \left[-\theta_m^{\,4} F(\theta)_m\, JY(\alpha_i\theta_m) \right.$$

$$\left. + \Delta\theta \sum_{j=1}^{m-1} \theta_j^{\,3} F(\theta_j) M(\alpha_i\theta_j) + \frac{1}{2}(\Delta\theta)\theta_m^{\,3} F(\theta_m) M(\alpha_i\theta_m) \right. \qquad (80)$$

In this equation, the particle diameter is in microns and the cell thickness, t , in inches. The particle concentration distribution function is delivered in units of volume per volume per micron.

In view of the narrow particle distributions, it was unnecessary to perform the concentration calculations over an extended range of size. The distribution was subtended at those sizes for which the calculated particle concentrations were negative. The Bessel function kernel of the terms of the summation in Equation (80) started from a negative value and remained negative up to an argument of about 1.25. Very small particles did not have positive terms in the summation up to the point of truncation. For these particles, an inadequate representation of the kernel was obtained. Were they present in appreciable quantity, the slope of $F(\theta)$ would have been small and the point of truncation by the criterion adopted would have been forced up to an angle at which positive terms would have appeared in the summation. Whenever the summation contained no positive terms, the size distribution was arbitrarily set to zero. Were they actually present, any tails in the size distribution would be lost by the truncation.

The values of the scattering coefficient, K , in Equation (80) were estimated from the tables and data compilation of Penndorf.(47) The scattering coefficient weighted the values of the integral according to the ability of the particles of each size to scatter light.

The value of F(0) was measured from the height of the node in units of chart divisions. The value of F(0) decreased slightly with increased concentration, which indicated some beam attenuation due to scattering.

Summary of Calibration Work

Figures 23 and 24 compare calculated concentration distributions with the distributions from the microscope assay of the two- to three- and the eight- to ten-micron fractions, respectively. The concentrations of spheres of each size are expressed on a relative basis. The correspondence of the concentration from the two detectors is fair for the eight- to ten-micron fraction but excellent for the two- to three-micron fraction.

Table III shows how the computed suspension concentrations changed as a suspension of the two- to three-micron spheres was diluted by a factor of 2.25. At these levels of concentration, (0.0025 to 0.0056 volume percent) the computed concentrations from both detectors closely followed the concentration changes while preserving the particle size distributions. For suspensions of greater concentration, the calculated data showed ten to 20 percent less change in solids concentration than had actually occurred. Multiple scattering was indicated. As a rule of thumb, the optical density of a dispersion whose total concentration is c of particles of average diameter d_p should not exceed 0.5 if multiple scattering is to be avoided.

$$\ln I_0/I = \pi/4\ K\ d_p^2\ ct = 3/2\ K\ \phi t/d_p \leq 0.5 \qquad (81)$$

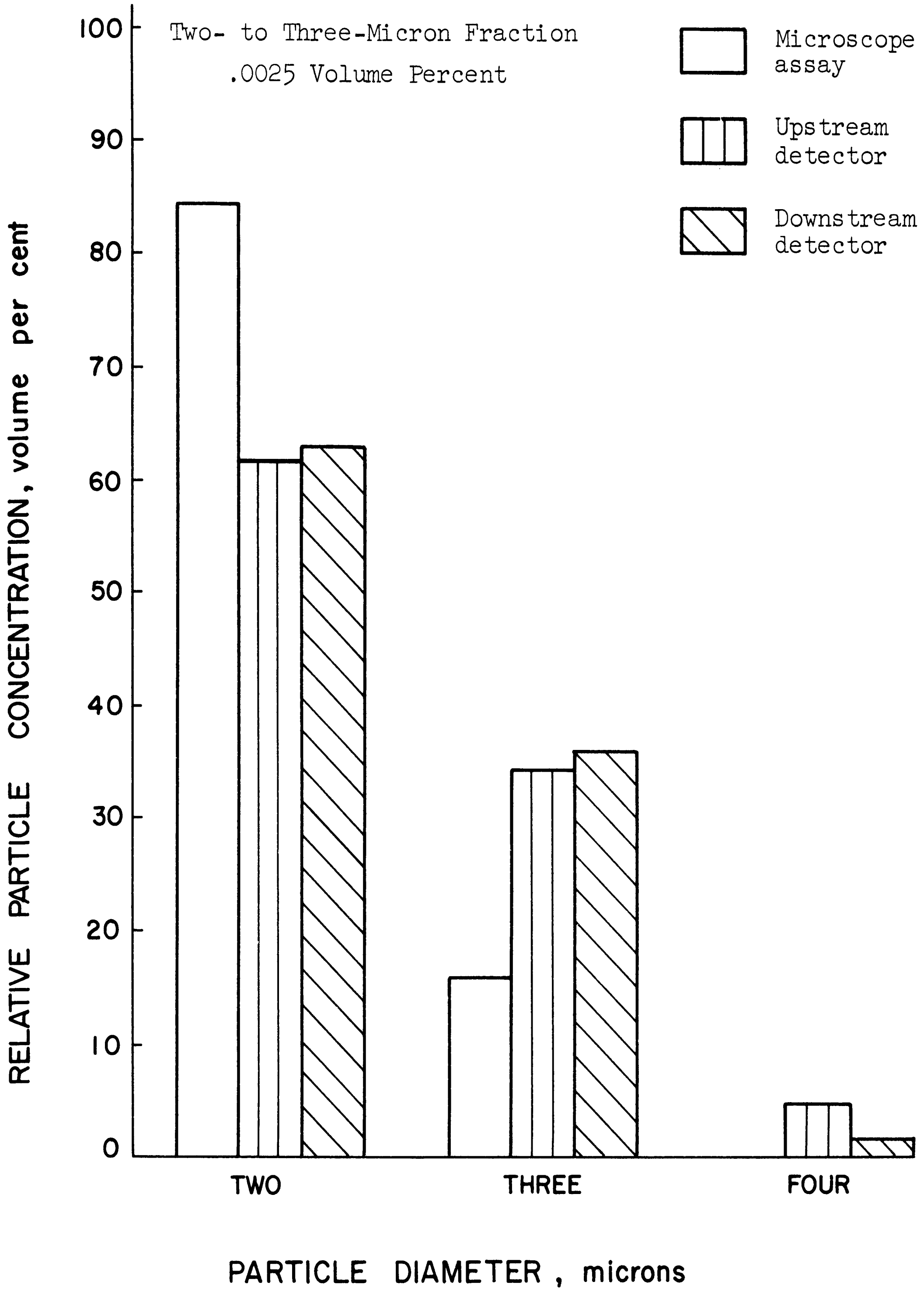

Figure 23. Comparison of Particle Concentration Distributions Obtained by Microscope and by Light Scattering.

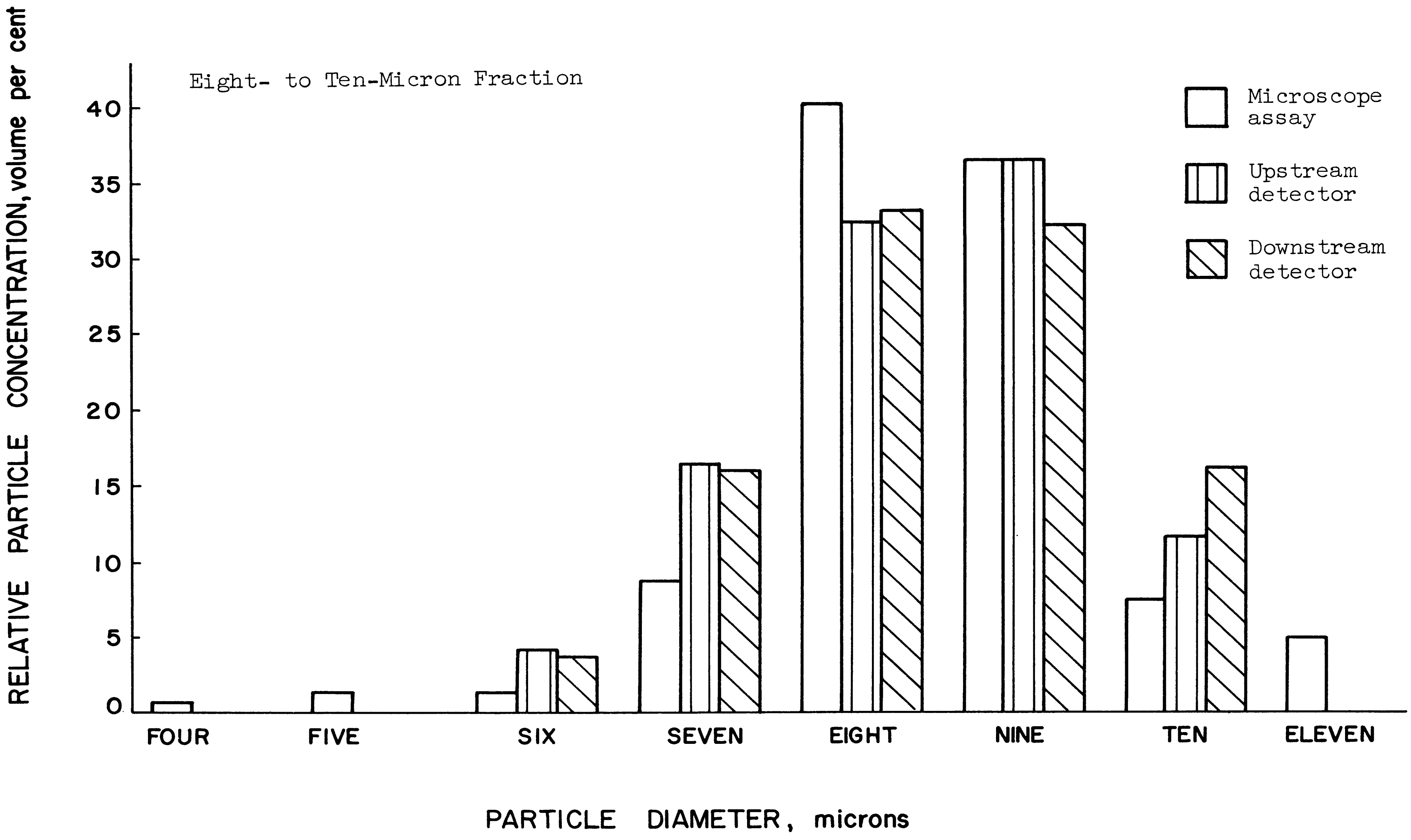

Figure 24. Comparison of Particle Concentration Distributions Obtained by Microscope and by Light Scattering.

TABLE III

EFFECT OF DILUTION ON CALCULATED CONCENTRATION OF TWO- TO THREE-MICRON FRACTION OF PYREX SPHERES

Sphere Size	Computed Concentration at 0.00563 V%				Computed Concentration at 0.0025 V%				Microscope Assay
	$\phi_i \times 10^5$		Volume Fraction		$\phi_i \times 10^5$		Volume Fraction		
micron	up-stream	down-stream	up-stream	down-stream	up-stream	down-stream	up-stream	down-stream	Volume Fraction
2	25.23	30.85	.632	.657	10.71	13.18	.614	.628	.842
3	13.92	16.10	.349	.343	5.97	7.53	.342	.358	.158
4	0.74	0.01	.019	.000	0.77	0.29	.044	.014	.000
Total	39.89	46.96			17.45	21.00			

Ratio of Total Concentrations

Upstream = 39.89/17.45 = 2.29

Downstream = 46.96/21.00 = 2.24

Dilution Ratio = 2.25

Detector Coefficients

0.00563 V%	0.0025 V%
C_U = 5.63/39.89 = .141	C_U = 2.5/17.45 = .143
C_E = 5.63/46.96 = .120	C_E = 2.5/21.00 = .119

The ϕ is the total volume fraction concentration. For the two-micron Pyrex spheres, K was approximately one and the cell had a thickness of 0.050 inch. By this criterion, the volume fraction of two-micron particles should be no greater than 5×10^{-4} cm.^{3}/cm.^{3} In the coalescence measurements, the drop concentrations were limited such that the scattered flux did not exceed the flux associated with the greater sphere concentration of Table III.

Table III shows that the computed total particle concentration in the upstream detector was about seven times larger than the particle concentration measured by gravimetric means. In the downstream detector it was about nine times larger. In order to obtain the particle concentration which was measured by gravimetric means, the computed total particle concentrations had to be multiplied by factors. These factors are termed "detector factors," C_U and C_E, for the upstream and downstream detectors, respectively. These factors are included under Table III. They would be independent of concentration were the detectors accurately following changes in concentration. For the eight- to ten-micron fraction, the detector factors were about 0.44 and 0.37 for the upstream and downstream detectors, respectively.

The lack of consistency of the factors for the two fractions of spheres and the extent of the departure of the factors from unity show that the measurements were in error with regard to absolute particle concentration. In the calculation of fractional coalescence, the drop concentrations in the downstream and upstream cells were ratioed. There was no need for true concentrations. It was merely necessary that the two detectors give the same relative particle distributions for the same dispersion and that the total calculated concentrations accurately follow changes in concentration. The data of Table III show that the detectors satisfied these requirements for the two- to three-micron fraction of spheres.

For a monodisperse suspension, the relative index of refraction affects the intensity level of the scattered flux without altering the angular distribution. For a fixed mixture of sizes, a change in relative index of refraction would cause a change in the flux distribution. But were the changes in the scattering coefficients correctly recognized, then the calculation algorithm would be likely to yield the same concentration distribution. The calibration at a relative index of refraction of 0.93 was taken as evidence that the detection and calculation procedures were reliable in measuring fractional coalescence at all of the relative indices of refraction encountered.

Appendix B gives the flux distributions for the data of Table III and of Figures 23 and 24. A sample calculation of particle concentration is presented.

Errors in Calibration Measurements

The difference between the calculated total particle concentration and the gravimetrically measured concentration was considered to be caused largely by low measured values of the transmitted flux, F(0) , the limited available flux distributions and the approximation of diffraction theory. Were the incident collimated beams less divergent, the node shown in Figure 22 would probably have been sharper and higher. It is estimated that the measurements of transmitted flux could have been too low by a factor of two or three.

The fact that the empirical factors for the two- to three-micron fraction were lower than those for the eight- to ten-micron fraction was caused in part by the limited flux distribution available for the former. The Bessel function product in Equation (67) oscillates. For the two-micron particles, the negative of the integrand remained positive up to the angle of truncation. Since the integration represented only the positive half cycle for these particles, the calculated concentrations were too high. More cycles were represented by the integrations in the eight- to ten-micron fractions. The calculated concentrations more nearly approximated the gravimetric concentration.

A larger angle of truncation was required for the two- to three-micron fraction. Diffraction theory becomes less accurate as θ grows. The error in the diffraction theory value of $R(\theta)$ is compounded by the fact that the Mellin transformation utilizes the derivative, $dR(\theta)/d\theta$. An accurate estimate of the error of the diffraction theory value of $dR(\theta)/d\theta$ requires calculations of $R(\theta)$ according to Mie theory. Some values are available in the table prepared by Gumprecht and Sliepcevich.(29,30) The α values of the two-, three- and four-micron particles were 11.5, 17.25 and 23.0, respectively. Gumprecht and Sliepcevich tabulated $R(\theta)$ for the two theories at intervals of 1° for α values of 20 and 30 and for a relative index of refraction of 1.33. For the two theories, the finite difference quotients, $\Delta R(\theta)/\Delta\theta$, are about the same at small angles. Between 6° and 7°., or approximately

0.10 and 0.12 radians, the Mie finite difference is about half that of diffration theory. Since θ_m was 0.15 radian for the two- to three-micron fraction, 50 percent was taken as a crude estimate of the average error in the diffraction theory value of $dR(\theta)/d\theta$. The average error would be somewhat less for the eight- to ten-micron fraction since the θ_m was 0.13 radian.

Other errors of minor importance arose from the measurements and the method of calculation. Anomalies in the detectors could have caused errors in the scattering patterns. These errors are discussed by Boll and Sliepcevich.(4)

Most of the errors in the scattering patterns which could have been caused by slight instability in the mercury lamps and the photomultiplier were recognized and corrected by smoothing the scattering patterns. It is estimated that the average error in transcribing the scattering patterns was one chart division or 0.04 millivolt. Since the average chart reading was four millivolts, the average relative error in recording the flux distributions was one percent. Instabilities which affected the node of transmitted flux were difficult to detect. The average error in the transcribed value of the transmitted flux was considered to be two percent. Since the quotient of the scattered over the transmitted flux was formed, the average error caused by chart transcription and undetected disturbances was three percent.

Some of the K values had to be estimated from curves furnished by Penndorf.(47) These estimates could have been in error by five percent.

A small error arose in each term of the summation of Equation (77) from the approximation of the function $\tan\theta(1 + \tan^2\theta)$ by θ, Equation (72). This error was considered to be offset by the assumption that the total flux, $I(\theta) + I_t$, was equal to I_t.

Since the numerical integration was truncated near an angle at which the flux function of Equation (68) vanished, a change of the point of truncation by 0.01 radian would have a relatively small effect on the calculated concentrations. A calculation described in Appendix B shows that for the two- to three-micron fraction, a change in the θ_m by 0.01 radian from the optimum location would cause a 1.5, three and 30 percent change in the concentrations of the two-, three- and four-micron particles, respectively. The four-micron concentration was particularly sensitive since it was at the tail of the distribution. An error in the extrapolation could have a greater effect, particularly for a lengthy extrapolation. In order to obtain a liberal estimate of the error of extrapolation, the slope of the extrapolation was changed by ten percent for one of the flux distributions of the two- to three-micron fraction, Appendix C. A change in the point of truncation was required. The calculated concentrations of the two-, three- and four-micron fraction changed by eight, five and 68 percent, respectively.

The error associated with the size of the angular interval, $\Delta\theta$, was assessed by halving the interval to 0.005 radian for the two- to three-micron fraction and to 0.0025 radian for the eight- to ten-micron fraction and by recalculating the concentrations. The concentrations of the two-, three- and four-micron particles changed by

0.2, 1.0 and ten percent, respectively. The concentration of the eight-micron particles in the eight- to ten-micron fraction changed by three percent. The comparison shows that the angular intervals used were satisfactory for particles which were important in the particle size distributions.

The extent of the change in the detector coefficients between the two- to three-micron fraction and the eight- to ten-micron fraction indicates that relative distributions computed for a broad range of particle sizes including two- and three-micron particles would be in error. The relative concentration of the small particles would be too great. When two- and three-micron particles were present, it appeared that the limiting diameters of the distribution should be separated by not more than a factor of two.

EXPERIMENTAL PROCEDURE

The exploration of the effects of process conditions, physical properties and screen geometry and coalescence consisted of five parts. Each part consisted of a number of runs. The variable of interest was changed from run to run. In each run, traverses were performed over a range of flow rates. In this way the effect of the variable on the relation between coalescence and flow rate could be discerned. The five parts were:

1. examination of effect of number of layers of screen and flow direction using cyclohexane dispersed in water;
2. examination of the effect of screen geometry using cyclohexane dispersed in water;

3. variation of dispersed phase viscosity using mixtures of cyclohexane and "fin oil," a light mineral oil, in water;

4. elucidation of the effect of low interfacial tension using mixtures of cyclohexanol or isobutanol and cyclohexane in water;

5. variation of continuous viscosity dispersing cyclohexane or n-octane in water-and-glycerol solutions.

Because of the limitations on the materials of construction of the flow cells, all of the successful coalescence studies were performed with water or a water solution as the continuous phase. On the basis of theory, it is reasonable to assume that a reversal of the phases in the dispersion would have no effect on the coalescence relationships. The effect of screen wettability was not studied because the surface characteristics of the screens could not be quantified. As discussed, the surface of the screens was subjected to a uniform treatment which encouraged good wettability by the organic phase. The effect of drop size also was not explored because the size of the drops could not be conveniently varied.

Physical Properties of Liquid-Liquid Systems

The physical properties of the liquid-liquid systems employed are shown in Table IV. High purity was not demanded of the regents used. Practical grade materials could be employed as long as no surface-active agents were present. Distilled water from the Department of Chemical and Metallurgical Engineering reservoir was used without further purification. Aliphatic solvents were chosen in order to minimize the attack on the epoxy resin cement of the optical cells. High boiling points were desired in order to minimize drop evaporation caused by

TABLE IV

PHYSICAL PROPERTIES OF LIQUID-LIQUID SYSTEMS

System	Density at 20°C gm./cm.^{3}			Viscosity at 20°C centipoise			Interfacial Tension 20°C dyne/cm.	Index of Refraction, 22°C		
	ρ_D	ρ_C	$\rho_D - \rho_C$	μ_D	μ_C	μ_D/μ_C		disp. phase	cont. phase	disp./cont.
Cyclohexane in Water	0.779	1.00	-0.221	0.885	1.0	0.885	53.0	1.424	1.333	1.067
75 V% Cyclohexane, 25 V% Fin Oil, in Water	0.793	1.00	-0.207	1.46	1.0	1.46	53.0	1.4354	1.333	1.076
50 V% Cyclohexane, 50 V% Fin Oil, in Water	0.807	1.00	-0.193	3.00	1.0	3.00	53.0	1.4476	1.333	1.084
33 V% Cyclohexane, 67 V% Fin Oil, in Water	0.817	1.00	-0.183	5.13	1.0	5.13	53.0	1.4512	1.333	1.089
20 V% Cyclohexane, 80 V% Fin Oil, in Water	0.825	1.00	-0.175	10.14	1.0	10.14	53.0	1.458	1.333	1.092
Fin Oil in Water	0.836	1.00	-0.164	24.0	1.0	24.0	53.0	1.466	1.333	1.10
Cyclohexane in 35 V% Glycerol, 65 V% Water	0.779	1.091	-0.312	0.885	2.8/25°	0.278	—	1.424	1.385	1.028
Cyclohexane in 50 V% Glycerol, 50 V% Water	0.779	1.143	-0.364	0.885	6.2/22° 5.17/27°	0.126 0.151	—	1.424	1.404	1.014
Normal Octane in 56.7 V% Glycerol, 43.3 V% Water	0.704	1.150	-0.446	0.55	7.5/27°	0.073	—	1.390	1.413	0.984
Normal Octane in 60 V% Glycerol, 40 V% Water	0.704	1.156	-0.452	0.55	10.8/28° 9.4/27°	0.051 0.059	33.0	1.390	1.418	0.981
10 V% Cyclohexanol, 90 V% Cyclohexane, in Water Saturated with Cyclohexanol	0.798	0.998	-0.200	0.966	1.026	0.941	11.1	1.4267	1.336	1.070
11 V% Cyclohexanol, 89 V% Normal Heptane, in Water Saturated with Cyclohexanol	0.714	0.998	-0.284	0.55	1.026	0.536	7.6	1.394	1.336	1.044
50 V% Cyclohexanol, 50 V% Normal Heptane, in Water Saturated with Cyclohexanol	0.822	0.998	-0.176	1.95	1.026	1.90	4.7	1.4254	1.336	1.068
50 V% Isobutanol, 50 V% Normal Heptane, in Water Saturated with Isobutanol	0.740	0.980	-0.240	0.58	1.01	0.557	2.7	1.390	1.340	1.037

frictional heating in homogenization. Surface-active agents were avoided. Avoidance of all trace impurities of other types was considered superfluous because of the possibility of trace contamination during homogenization and in flow through the copper tubing.

The coalescence runs were performed at laboratory temperature and substantially at the ambient pressure. Because of the relative insensitivity of liquid physical properties to temperature changes of the order of several degrees, no elaborate measures were taken to insure isothermal conditions. Some control of temperature was necessary to prevent a change in the solubility of the dispersed phase in the continuum. During the course of a run, the laboratory temperature was held within 2°C. Prior to the run, the freshly prepared feed dispersion was brought to the laboratory temperature. The extremes of temperature variation throughout the work were 16°C and 27°C.

The liquid densities in Table IV were calculated from pure liquid densities(40) according to the volume fraction composition of each phase. The interfacial tensions were measured with a du Nouy tensionmeter and the indices of refraction were obtained with a Bausch and Lomb refractometer. Liquid viscosities were measured with an Oswald viscosimeter. Since viscosity is moderately influenced by temperature, the viscosity measurements were conducted at the temperature of the respective runs.

Preparation of Dispersion

The dispersion was prepared on a Manton-Gaulin laboratory homogenizer. In this machine, liquid is forced through two valves at pressure in excess of 1000 pounds per square inch and is disintegrated into small uniform packets. The homogenizer was constructed of stainless steel and had Teflon gaskets. It was dismantled and the parts were rinsed with hot water after each period of use. Normally, the charge consisted of three liters of distilled water and ten milliliters of the material to be dispersed. The latter was increased whenever the relative index of refraction was less than 1.05 in order to compensate for the decrease in the scattering coefficient, K . Dispersions were prepared with an excessive drop concentration in order to minimize the volume of liquid processes in the homogenizer. The smallest drops obtainable in cyclohexane-in-water dispersions were in the two- to three-micron range. It was not possible to increase the drop size on the homogenizer without increasing the heterogeneity of the dispersion. As the viscosity of either phase was increased, the drops became smaller. For these dispersions, the homogenizer had to be carefully adjusted in order to obtain two- and three-micron drops without an excessive compliment of other drop sizes. The disperion was transferred to the feed bottle and diluted to a level at which multiple scattering would not occur.

Preparation for a Run

In order to ratio the drop concentrations upstream and downstream from the coalescer, the ratio of the detector factors was required. Because of the gradual change in the mercury lamps, the ratio was measured prior to each run. One of the flow cells was flushed and filled with a portion of the dispersion which had been diluted to the level of single scattering. Three half traverses were performed, the first and third in one detector and the second in the other. The check run in the one detector assessed the extent of any drop settling. The calculation of the ratio of detector coefficients, C_E/C_U, is described in the section on coalescence calculations.

Before a run, it was necessary to bring the windows of the flow cells into a strongly hydrophilic condition such that the adhesion of the organic phase drops either would not occur or would be delayed several hours. The cells were rinsed with water, with isopropanol to insure the removal of all organics, and again with water. The hydrophilic treatment was affected by loading the cells with a concentrated solution of sodium hydroxide and allowing them to stand for ten minutes or longer. The cells were then rinsed repeatedly with distilled water. When properly cleaned, water would film evenly across the windows.

While the hydrophilic treatment was in progress the filter flange was assembled. Both sections of the filter flange were rinsed with isopropyl alcohol. The first support was positioned in the downstream section of the flange. One coalescing screen was withdrawn from its octodecylamine treating solution, rinsed in n-heptane and positioned on top of the support. The Teflon spacer-gasket was pushed into position against the coalescing screen. The assembly continued in this fashion until the required number of coalescing screens with supports and spacers had been inserted. All five spacers were required to prevent leakage from the joint between the two sections of the flange. The upstream section was positioned and the two sections were bolted together.

The rinsing of the flow cells was begun after the assembly of the filter flange and continued during the assembly of the flow system tubing. When thoroughly rinsed, the flow cells were filled with distilled water and clamped in their respective compartments. The optical cell compartment covers were positioned.

The flow system was deaerated by allowing the feed to flow into the tubing as the system was assembled. By first deaerating the upstream flow system, a negligible quantity of air was blown through the screens at the start of a run. After assembly, residual air in the screens, downstream cell and downstream flow section was forced out through the bleed valve at the apex of the downstream run of tubing. A flow was established at about 30 milliliters per minute in order to fully saturate the screens with the dispersed phase. After the inclination of the mirrors was adjusted, the traverses could proceed.

Run Procedure

The first traverse of a run was usually performed at a high rate of flow, 100 milliliters per minute. At this level, little or no coalescence occurred for most screens, and a base level of coalescence was established. The subsequent traverses were performed at a series of flow rates at which coalescence was expected. Most of these ranged between 2.0 and 30 milliliters per minute or average upstream linear velocities between 0.08 and 1.25 feet per minute. Between traverses, the flow rate was boosted to the vicinity of 100 cubic centimeters per minute for about a minute in order to wash the flow cells free from nascent fog and in order to wash any large globules of dispersed phase from between the layers of screen.

The time at which equilibrium was reached by the system at a given rate of flow could not be accurately gauged because of fluctuations in the feed concentration. The measurement procedure allowed ample time for the attainment of equilibrium. The flow rate was established and the upstream half traverse was taken. The downstream half traverse was delayed until the volume of holdup between the flow cells was renewed by the flow. Assuming plug flow, the dispersion viewed in the upstream traverse would be passing through the downstream cell during the downstream traverse. During the time in which the holdup between the flow cells was renewed once, the holdup between the coalescer and the downstream cell was replaced five times. The volume of the flow system between cells was about 25 cubic centimeters. The downstream half traverse was immediately preceded by a second upstream half traverse. Although coalescence calculations were normally based on the first upstream half traverse, the second half traverse indicated the extent of change in the feed dispersion during the time allowed for the attainment of equilibrium. The downstream traverse was delayed in this manner for rates of flow less than nine cubic centimeters per minute. At greater rates, one full traverse was sufficient. For flow rates between six and nine cubic centimeters per minute, the downstream traverse came after the cell-to-cell holdup had been renewed. For these rates, the coalescence was calculated from the average of concentrations computed from the two upstream traverses.

During a run, the feed dispersion gradually coarsed because of the ensuing drop-drop coalescence. The gradually increasing rate of settling during a run dictated that the traverses at low rates of flow, which entailed relatively long delays between the initial upstream half-traverse and the downstream half-traverse, be performed while the feed was fresh. The flow rates for the sequence of traverses was progressively increased. Occasional check traverses were performed. Drop settling in the fresh feed made traverses at flow rates less than 1.5 cubic centimeters per minute of questionable validity. Moreover, at very low rates of flow, the cell windows were prone to fog. At 30 cubic centimeters per minute, coalescence ceased for the coarser screens.

In many cases, the runs were duplicated to check the consistency of the results. For every liquid-liquid system studied, it was necessary to ascertain the inherent settling and coalescence in the flow channels at various flow rates. Inherent coalescence was measured by runs with only the supports present.

COALESCENCE CALCULATIONS

Coalescence calculations were performed by simply computing the net fraction of drops removed between the upstream and downstream flow cells. The scattering patterns were converted into drop concentrations via the Mellin integral approximation. Gross fractional coalescence was obtained from the ratio of drop concentrations in the downstream und upstream cells. Introduction of the ratio of detector coefficients brought the concentrations to the same relative level. The net fractional coalescence was obtained by correcting the gross coalescence for the amount of inherent coalescence on the support screens and in the flow channel at the velocity in question. Fractional coalescence was calculated for the two-, three- and four-micron drops of the dispersions. Calculated concentrations of larger drops were relatively small and showed a wide range of variation. Satisfactory inherent coalescence correlations could not be obtained for larger drops.

Calculation of Ratio of Detector Coefficients

The ratio of detector coefficients was calculated from the calibration measurements taken prior to each run. The flux distributions were used instead of the calculated concentrations. Integration of Equation (80) over all particle sizes gives the total volume fraction of particles, ϕ.

$$\phi = \int_0^\infty \frac{d\phi}{d(d_P)} d(d_P) = \frac{510}{tF(0)} \sum_{j=1}^{m} \theta_j^3 F(\theta_j) \cdot H(\theta_j) \qquad (82)$$

The expressions for the $H(\theta_j)$ are:

$$H(\theta_j) = \Delta\theta \int_0^\infty \frac{d_P^2}{K} M(\alpha\theta_j) \, d(d_P) \qquad 1 \leq j \leq m-1 \qquad (83)$$

$$H(\theta_m) = \int_0^\infty \frac{d_P^2}{K} \left[\frac{1}{2} \Delta\theta M(\alpha\theta_m) - \theta_m J_1(\alpha\theta_m) \, Y_1(\alpha\theta_m) \right] d(d_P) \qquad (84)$$

If the flux distribution were obtained in one of the detectors, multiplication of Equation (82) by the detector coefficient would give the absolute total particle concentration. The ratio of detector coefficients may be obtained from Equation (82) by use of the upstream and downstream flux distributions for the same dispersion. The product of the total calculated concentration and the detector coefficient would be equal for the two detectors. The ratio C_E/C_U would equal ϕ_U/ϕ_E, where the subscripts U and E refer to the upstream and downstream detectors and ϕ is the total calculated drop concentration.

$$\frac{C_E}{C_U} = \frac{\phi_U}{\phi_E} = \frac{F_E(0)}{F_U(0)} \cdot \frac{\sum_{j=1}^{m} F_U(\theta_j) \cdot H(\theta_j)}{\sum_{j=1}^{m} F_E(\theta_j) \cdot H(\theta_j)} \tag{85}$$

Cell thickness vanishes if the same cell is used for both measurements. The coefficient functions, $H(\theta_j)$, are identical for both detectors. The identical dispersion in each detector implies flux distributions which are related by a common factor at every point. Thus the ratio of sums can be expressed simply by the ratio of two flux measurements at identical angular positions.

$$\frac{C_E}{C_U} = \frac{F_E(0)}{F_U(0)} \cdot \frac{F_U(\theta_j)}{F_E(\theta_j)} \tag{86}$$

In practice there were slight differences between the flux distributions obtained in the upstream and downstream cells. An average ratio of the flux measurements was obtained from quotients at angular positions of 0.09, 0.10 and 0.11 radians. The fluxes at these positions were relatively important in the concentration distribution calculations; at these positions, the flux scattered by the blanks was low.

With the two upstream half traverses, two calculations of C_E/C_U could be made and an average taken. In some cases, the computed drop concentrations in one of the upstream cells were out of line and the data for that half traverse was discarded. The ratio of detector factors usually changed slightly from run to run.

Calculation of Inherent Fractional Non-Coalescence

The inherent non-coalescence on the supports and in the flow channels was obtained from the runs with the support screens. It was the quotient of the downstream over the upstream drop concentration for each drop size. The downstream concentration was brought to the same relative level as the upstream concentration by multiplying by the ratio of detector factors, C_E/C_U .

$$1 - f_{s_i} = \frac{\phi_{E_i}}{\phi_{U_i}} \cdot \frac{C_E}{C_U} \qquad (87)$$

The term, $1 - f_{s_i}$, represents the fraction of drops of size i not coalescing on the supports and in the flow channel. The measurements with the support screens, which are discussed in the section on data interpretation, showed that the number of supports had no significant effect on the extent of inherent coalescence. It was found that inherent coalescence could be attributed largely to drop settling.

Calculation of Net Fractional Coalescence

Suppose that a fraction, η , of the total inherent coalescence occurred between the upstream flow cell and the coalescer. The net inlet concentration at the coalescer would be $\phi_{U_i}(1-f_{s_i}\eta)$; the concentration of the efflux relative to the concentration seen by the downstream cell would be $\frac{\phi_{E_i}}{1-f_{s_i}(1-\eta)}$. The net fractional change in drop concentration due to coalescence, $1-f_i$, would be:

$$1-f_i = \frac{\phi_{E_i} \cdot C_E/C_U}{\phi_{U_i}(1-f_{s_i}\eta)[1-f_{s_i}(1-\eta)]} = \frac{\phi_{E_i} \cdot C_E/C_U}{\phi_{U_i}[1-f_{s_i}+\eta(1-\eta)f_{s_i}^2]} \qquad (88)$$

Since 20 percent of the cell-to-cell holdup was between the coalescer and the downstream cell, $1-\eta$ would be expected to be small. The fractional coalescence, f_{s_i}, was of the order of 0.2 or less. Thus, the third term in the parentheses of the denominator would be negligible. The net fractional coalescence could be computed as:

$$f_i = 1 - \frac{\phi_{E_i} \cdot C_E/C_U}{\phi_{U_i}(1-f_{s_i})} \qquad (89)$$

This treatment assumed that there was no coalescence on the support screens. This was a good assumption since the interstitial distance in the supports was 475 microns.

Sample calculations of the ratio of detector factors and of net coalescence are given in Appendix C. A logic diagram for the automatic computation of drop concentrations is shown.

PART III

DATA APPRAISAL

INTRODUCTION

The objectives of this work were to ascertain the controlling mechanisms in the coalescence of drops on fibrous media and to obtain relationships which would assist in the design of filament-packed coalescers. Correlations relating coalescence to either dimensional or dimensionless combinations of the measured independent variables were attempted. Correlations involving dimensionless groups are to be preferred. However, since spreading, adhesive and film thinning forces embrace variables which cannot be measured, there is the possibility that a dimensional correlation will be unavoidable. When properly constructed, the dimensional groups would have the dimensions of the variables which cannot be measured. Such groups would indicate competing phenomena and would have the same informational value as a dimensionless group. Any correlation developed would in the strictest sense be limited to the range of the variables of this experiment. However, there would be a more rational basis for extrapolation to other regions of interest were the correlation expressed in dimensionless or appropriate dimensional terms.

Interactions Between Variables

The fruition of the events leading to the coalescence of the drops in the filaments depends upon the interaction of the contributing forces and the forces of shear. Since it was most widely varied, flow velocity should give the best indication of the competition of shear. Interactions between velocity and other independent variables were examined in detail.

Perhaps the most interesting interactions which did not involve velocity were those involving drop size and screen dimension. For reasons previously stated, the experiment was confined chiefly to dispersions which contained drops in the range of two to four microns. The measurement of the concentration of each drop size in the distribution was blurred because of the tendency of the drop distributions to be broadened by the transformation. Although inaccurate in shape, the computed distributions did define the limits of the size range. For the fixed distribution, the interaction between drop size and screen dimension was studied by varying the screen dimensions. In Appendix B, it is shown that the computed drop distributions most nearly represented three-micron drops. Cross correlation were formed under the assumption that the coalescence measurements were depicting the behavior of three-micron drops.

Second order interactions between other variables were not examined.

The effect of screen wettability was not studied because the surface state of the screen could not be quantified. The screens were treated to allow the preferential wetting by the drops. The affinity of the screens and the drops was believed to be sufficiently great to mask any effect of the micro-structure of the screens.

In order to avoid multiple scattering, the concentration of the feed dispersion was limited to a maximum of 0.01 volume percent. At this level, no effect of concentration was expected.

Presentation of Data

The coalescence measurements were performed in a number of parts. In each part, the effect of one of the variables on the relation between coalescence and flow velocity was measured by changing the level of the variable from run to run. Most of the runs were conducted with three or five layers of screen present. With this many layers, net coalescence was usually appreciable and exceeded the error of the measurement several fold. Net fractional coalescence was in a range in which the result of a change in variables could be readily preceived. Except for two runs with downward flow, all runs were performed with the dispersion flowing horizontally through the coalescer.

Since flow velocity was the primary variable, the results for each part of the experiment are presented on plots of net fractional coalescence against the logarithm of the upstream velocity. The data on inherent coalescence were plotted as the fraction of material not coalesced, $1 - f_s$, against the logarithm of the upstream velocity. In many cases these plots were nearly linear.

The data of net fractional non-coalescence for each plot and correlation are given in Appendix C.

Data Correlation

The facilities and "Regression Analysis Program" of the University of Michigan Computing Center were used for data analysis. The details of this program are given in a report by Dallemand.(16)

At each level of variation of one of the variables either the net fraction of drops coalesced or the fraction not coalesced was correlated against simple functions of the upstream velocity. The acceptability of a computed correlation was judged by the multiple correlation coefficient and the standard error of the dependent variable. The standard error of the dependent variable is the square root of the average squared deviation. When the multiple correlation coefficient was in the vicinity of 0.95, the correlation was considered satisfactory. If the introduction of additional terms gave little further improvement in the multiple correlation coefficient, the correlations containing these additional terms were not used. The scatter and limited scope of the data favored the use of a minimum of computed coefficients.

Since the screens were in a uniform condition, the errors in each part of the experiment were mostly random. Significant differences between correlations at various levels of one of the variables were appraised at the 95 percent confidence level, which was approximately two standard errors above and below the correlating line. In some cases, particularly in correlations of fractional inherent non-coalescence, a parametric variation of a variable caused a gradual change in the correlations. Correlations for consecutive values of the parameter were often not different at the 95 percent level of confidence. However, the correlations at bounding values of the parameter had a significant difference. In such cases, the correlation at each level of the parameter was assumed to be significant. Wherever screen wettability was at a steady level, cross correlation of a series of runs was possible. The cross correlations were formed from functional combinations of velocity and the variable under study.

CORRELATION OF ROTAMETER CALIBRATION

The preliminary coalescence measurements were performed with a rotameter to measure the rate of flow. The clear-fluid calibration of the rotameter was later found to be unreliable in measuring the flow rates of the dispersions because of the effect of the dispersed drops on the surfaces of the float and bore. The extent of the discrepancy depended upon the period of exposure of the rotameter to the dispersion and on the drop concentration. After a period of exposure to a certain dispersion, the rotameter reached a state of quasi-equilibrium in which the float levels were reasonably reproducible. In the final series of runs, the rate of flow was measured both directly and with the rotameter. The float-level data were correlated against flow rate for the cyclohexane-in-water runs of this series. These data differ appreciably from the clear fluid calibration as Figure 25 shows.

The runs at low interfacial tension were performed using the rotameter to measure the rate of flow. In these runs, the water was saturated with the alcohol used to reduce the interfacial tension. Float-level versus flow-rate data were obtained for an aqueous cyclohexanol solution containing dispersed drops of ten percent cyclohexanol and 90 percent cyclohexane. These data are shown as

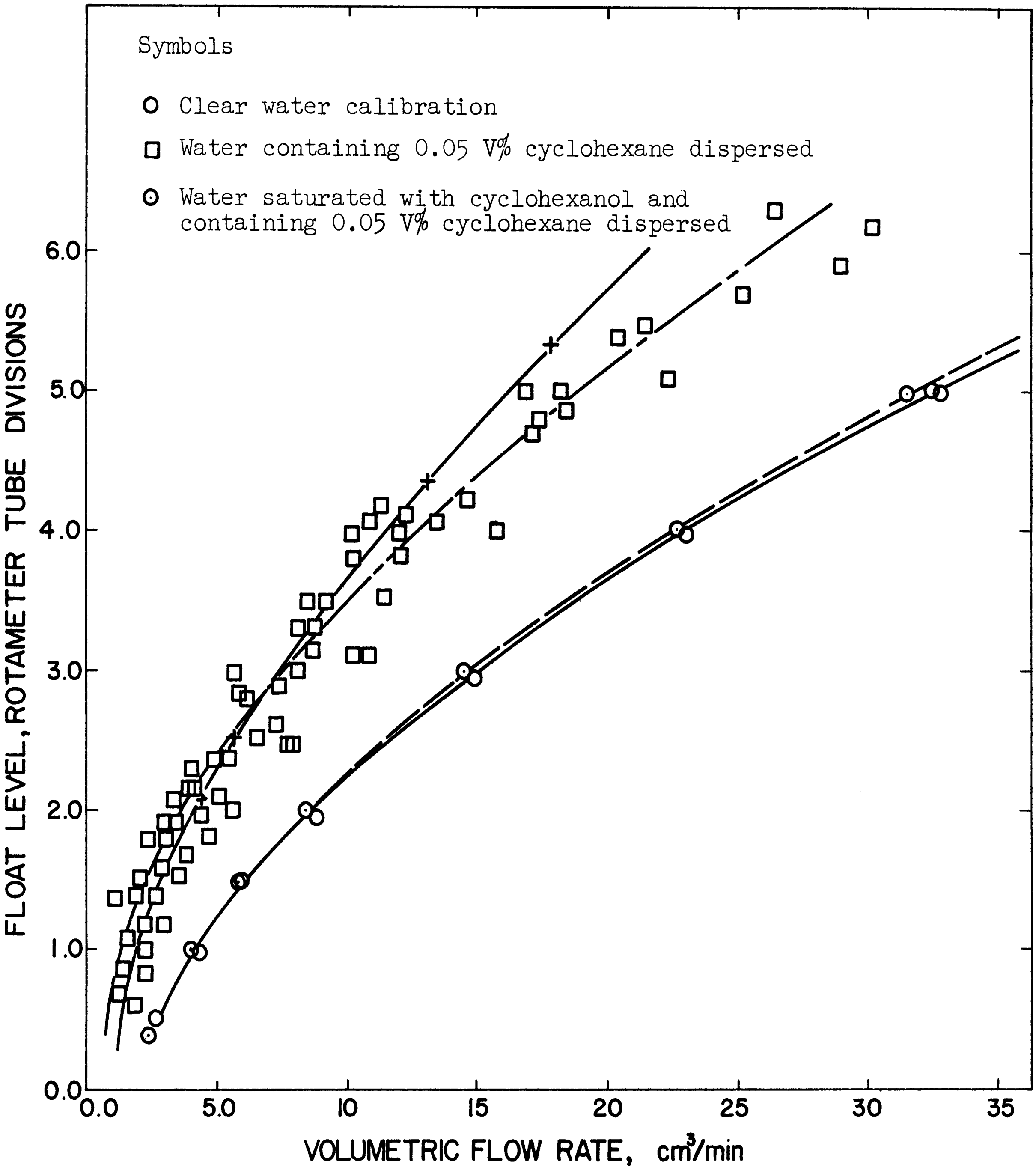

Correlations

——— Clear water: $L = -.619 + .934 \ln q + .072q + 6.8 \times 10^{-7} q^3$

—·— Water with .05 V% cyclohexane dispersed
$L = .241 + .946 \ln q + .104\, q$

— — — Water saturated with cyclohexanol and containing cyclohexane dispersed $L = -.637 + .953 \ln q + .072\, q$

—+— Clear water calibration halved

Figure 25. Relation Between Rotameter Float Level and Flow Rate.

circles with dots in Figure 25. No appreciable difference from the clear water calibration is noted. Evidently, the alcohol adsorbed on the rotameter surfaces and prevented contamination by the drop phase. The same effect was noted for dispersions in aqueous glycerol solutions which contained more than 30 volume percent glycerol.

The scatter of the float-level versus flow-rate data created uncertainty in the relation between the actual flow rates and the flow rates calculated for the preliminary runs, in which the rotameter was the only measuring device. The average relative deviation in the float-level versus flow-rate data was estimated by correlating the logarithm of the flow rate against the float level for the cyclohexane-in-water runs, Appendix A. The average relative error was 24 percent. Although sizeable, this error was not considered so imposing that it precluded analysis of the preliminary runs.

In most cases, a correction of the velocity was unnecessary because the rotameter was used exclusively in the parametric variation of one of the variables. In two cases, parametric variations were conducted with both the rotameter and direct flow measurement. Adjustment was required.

The starred curve in Figure 25 shows the clear fluid calibration with the flow rates reduced by a factor of two. The starred curve follows the correlation for cyclohexane-in-water dispersions up to a float level of 3.0 and does not become significantly different until a float level of 5.0 is reached. Most of the coalescence measurements were performed at float levels less than 5.0. At higher flow rates, coalescence was usually low and the errors of the measurement were equal in magnitude to the measured net fractional coalesence. A more accurate adjustment at high flow rates was of marginal utility. All rotameter measured flow rates for the cyclohexane-in-water dispersions have halved. The correspondence between the clear fluid calibration and the cyclohexanol-containing binary shows that no adjustment of rotameter flow rates was required for dispersions in which the interfacial tension was less than 11 dynes per centimeter.

Because of the change in screen wettability from one part of the experiment to the next, there were only a few examples showing the suitability of the correction. Figures 26 and 27 give a comparison between net fractional coalescence of two-micron drops obtained with and without direct measurement of flow rate. Figures 26 and 27 compare three layers of 1500-mesh and three layers of 1000-mesh screen, respectively. The correlations are not significantly different over most of the range.

In subsequent plots and correlations, a notation is made whenever flow rates were adjusted.

INHERENT COALESCENCE

As the dispersion flowed between the optical cells, some coalescence occurred in the walls of the flow channel and between the drops themselves. In view of the rather large density difference of this experiment, settling was the suspected cause of much of the inherent coalescence. Assuming plug flow and no interactions between

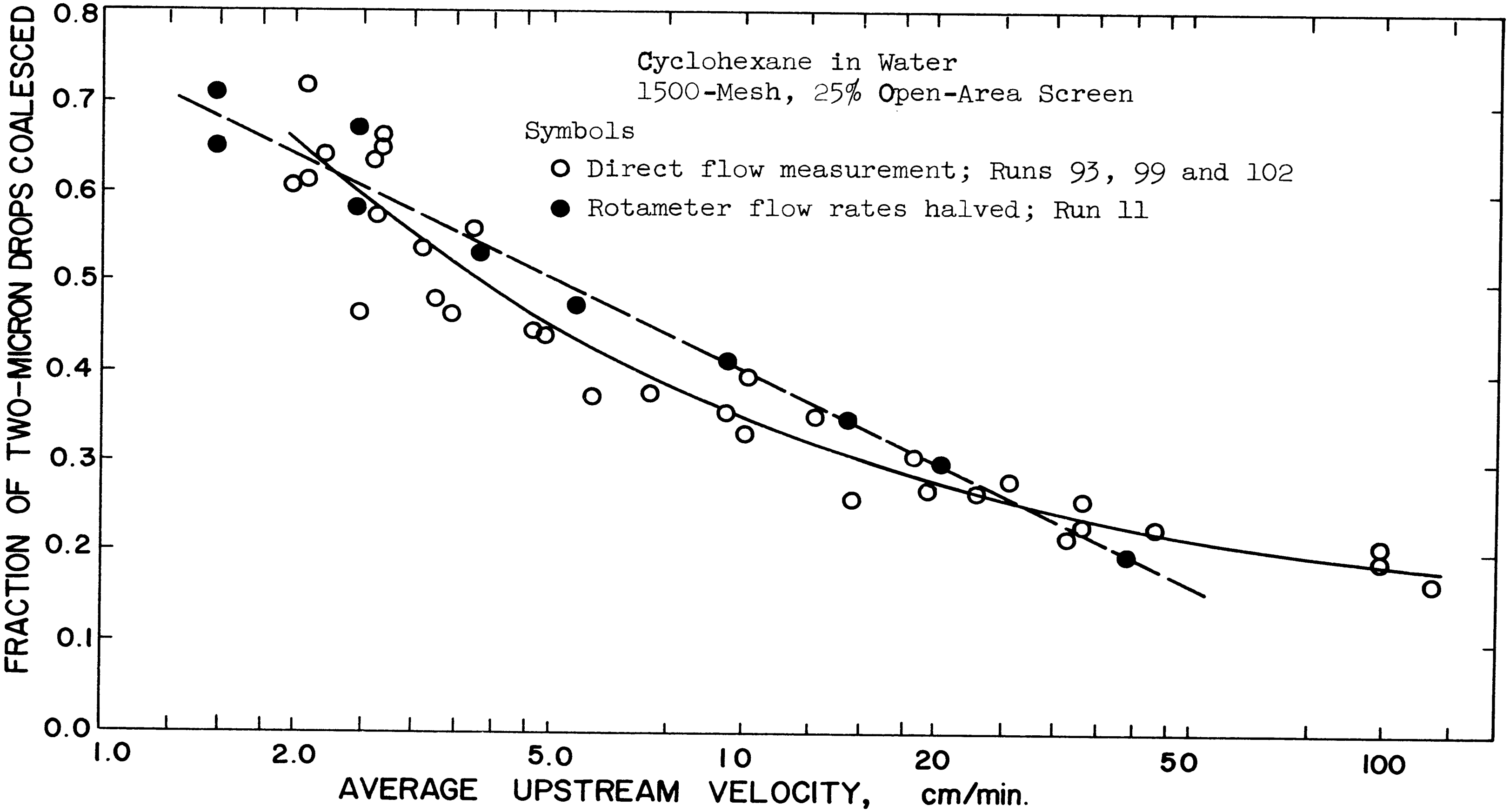

Correlations

——— Direct flow measurement: $f = .108 + .772\ U_\infty$; Standard error = .044

— — — Rotameter: $f = .745 - .149 \ln U_\infty$; Standard error = .027

Figure 26. Test of Adjustment of Rotameter Flow Rates.

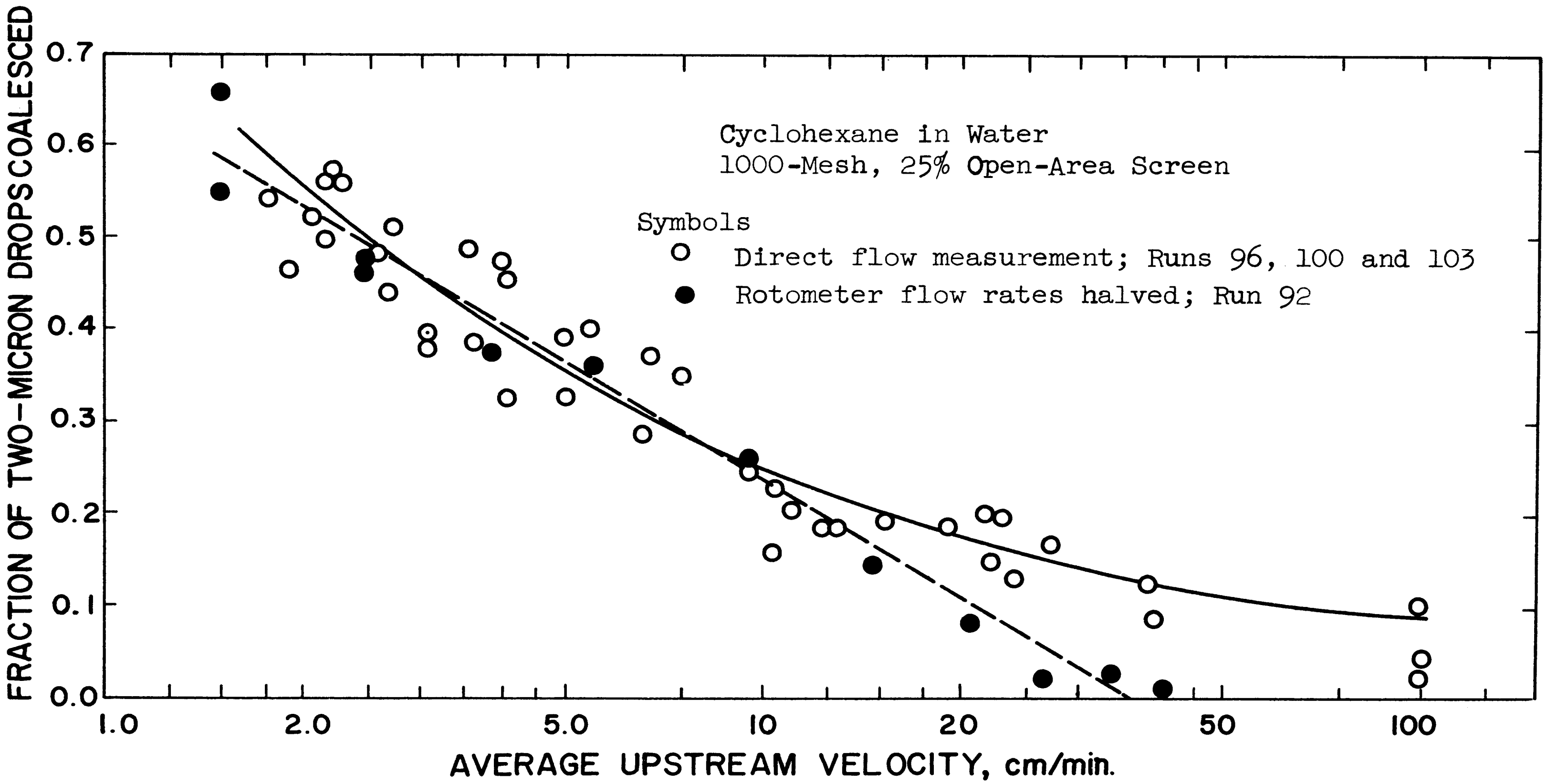

Correlations

——— Direct flow measurement: $f = .007 + .790\ U_\infty^{-.5}$; Standard error = .047

– – – Rotameter: $f = .660 - .185\ \ln U_\infty$; Standard error = .034.

Figure 27. Test of Adjustment of Rotameter Flow Rates.

drops, the settling distance of the drops is given by the Stokes settling velocity times the available time.

$$y_s = U_s \frac{V_H}{q} = \frac{1}{18} \frac{V_H}{q} |\rho_D - \rho_C| \frac{d_p^2 g}{\mu_C} \qquad (90)$$

In Equation (90), V_H is the holdup volume between flow cells, q is the volumetric rate of flow, U_s is the settling velocity and y_s is the distance through which the drop settles. For micron-diameter cyclohexane drops in water, this relation becomes:

$$y_s = 7.2 \times 10^{-4} \frac{V_H d_p^2}{q} \frac{\text{cm.}}{\text{micron}^2 \text{ min.}} \qquad (91)$$

Two-micron drops in a suspension flowing at 2.0 cubic centimeters per minute would settle a distance of 0.036 centimeters in moving through the 25 cubic centimeter holdup volume between the optical cells. For a circular flow channel, the fraction of the two-micron drops which settle to the wall between the two optical cells is given by twice the area of a circular segment whose chord height is the channel radius less 0.018 centimeters relative to the cross sectional area of the channel. For a flow channel having a diamter of 3/16 inch or 0.476 centimeter, the fraction of the two-micron drops not reaching the wall is 0.892. At the same rate of flow, the fractions of the three- and four-micron drops not reaching the wall are 0.787 and 0.622 respectively. Although this idealization overestimates the inherent coalescence which occurred at the conditions in question, it shows that a substantial amount of inherent coalescence can be ascribed to settling. In spite of the broadening effect of the transformation, the inherent coalescence results indicate a gradation in the extent of settling of each of the drop size present in the feed dispersion.

In the discussion to follow, the terms "inherent fractional coalescence" and "inherent fractional non-coalescence" are used interchangeably. They are the complementary fractions f_{s_i} and $1 - f_{s_i}$. The subscript, i , denotes the drop diameter inferred from the computed distributions rather than the actual diameter.

Effect of Temperature

Ambient temperature changes of the order of 10°C were expected to have little effect on the inherent coalescence of cyclohexane drops in water because of the relatively small change of viscosity of water within that range. Figure 28 shows the effect of a 6°C temperature change on the fraction of two-, three- and four-micron cyclohexane drops in water not undergoing inherent coalescence. From the few data shown, it can be judged that temperature had no significant effect. The one aberrant point for four-micron drops at 18°C was probably caused by the sensitivity of the calculated concentration of the four-micron drops to the exact nature of the scattering patterns.

Equation (90) shows that temperature could have an effect on settling distance through the variation of viscosity. The range of temperature over the entire course of the experiment was 16°C to 27°C. In this range the viscosity of water varies between 1.11 and 0.85 centipoise.(48) If the fraction of inherent coalescence averages ten percent of all drops, a 25 percent change in viscosity would be expected to cause a total change of 2.5 percent in the fraction of drops experiencing inherent coalescence. Such a slight change would be difficult to determine in the presence of experimental error. It was concluded that temperature had no significant effect

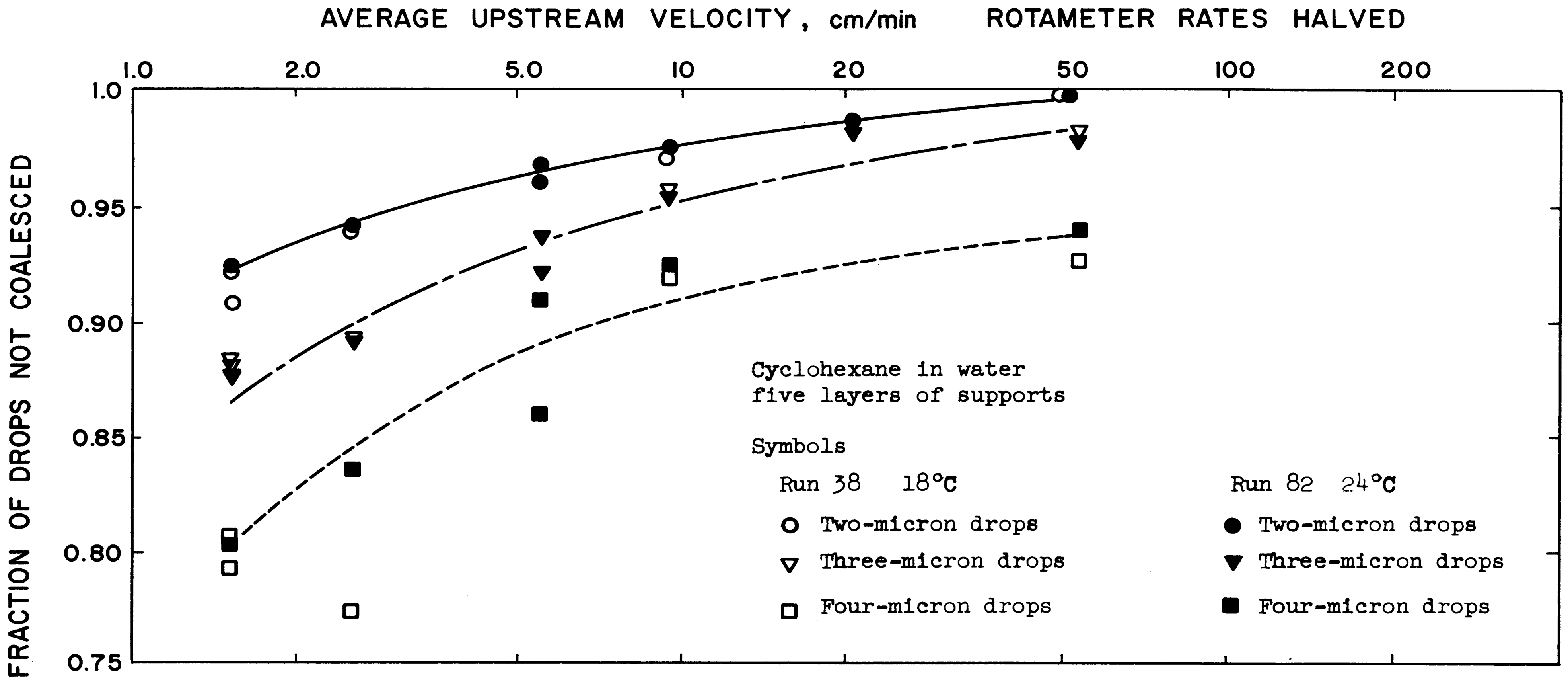

Correlations for run 82

————	Two-micron drops	$1-f_s = 1.013 - .114\ U_\infty^{-.5}$;	Standard error = .003
— - —	Three-micron drops	$1-f_s = 1.007 - .175\ U_\infty^{-.5}$;	Standard error = .010
- - - - -	Four-micron drops	$1-f_s = .997 - .213\ U_\infty^{-.5}$;	Standard error = .020

Figure 28. Effect of Temperature on Inherent Coalescence.

on inherent coalescence in all aqueous solutions used which had a nominal viscosity of one centipoise. An effect of temperature on inherent coalescence was noted for aqueous glycerol solutions having a viscosity of three centipoises or larger. Elevated continuum viscosities were measured at the temperature of the run.

Effect of Number of Layers of Supports

The intersititial distance of the supports was relatively large, 0.045 centimeters. The number of layers of supports would be expected to have little effect. The fraction of two-, three- and four-micron cyclohexane drops in water not coalesced on various numbers of layers of supports is given in Figures 29, 30, and 31, respectively. The flow rate was measured with the rotameter. A comparison of the figures shows no consistent trend of differentiation between the number of layers. The existing differences are small and are comparable with the error of the measurements. The greater scatter of the data for the inherent coalescence of the three- and four-micron drops was caused by a combination of their lower concentration in the dispersions and the greater sensitivity of the computed concentrations to variations in the scattering patterns.

Since it appeared that the number of supports had no significant effect, composite correlations were computed for each drop size. These composite correlations were used to compute fractional inherent non-coalescence in all cyclohexane-in-water runs in which the rotameter was used alone. The apparent lack of an effect of the number

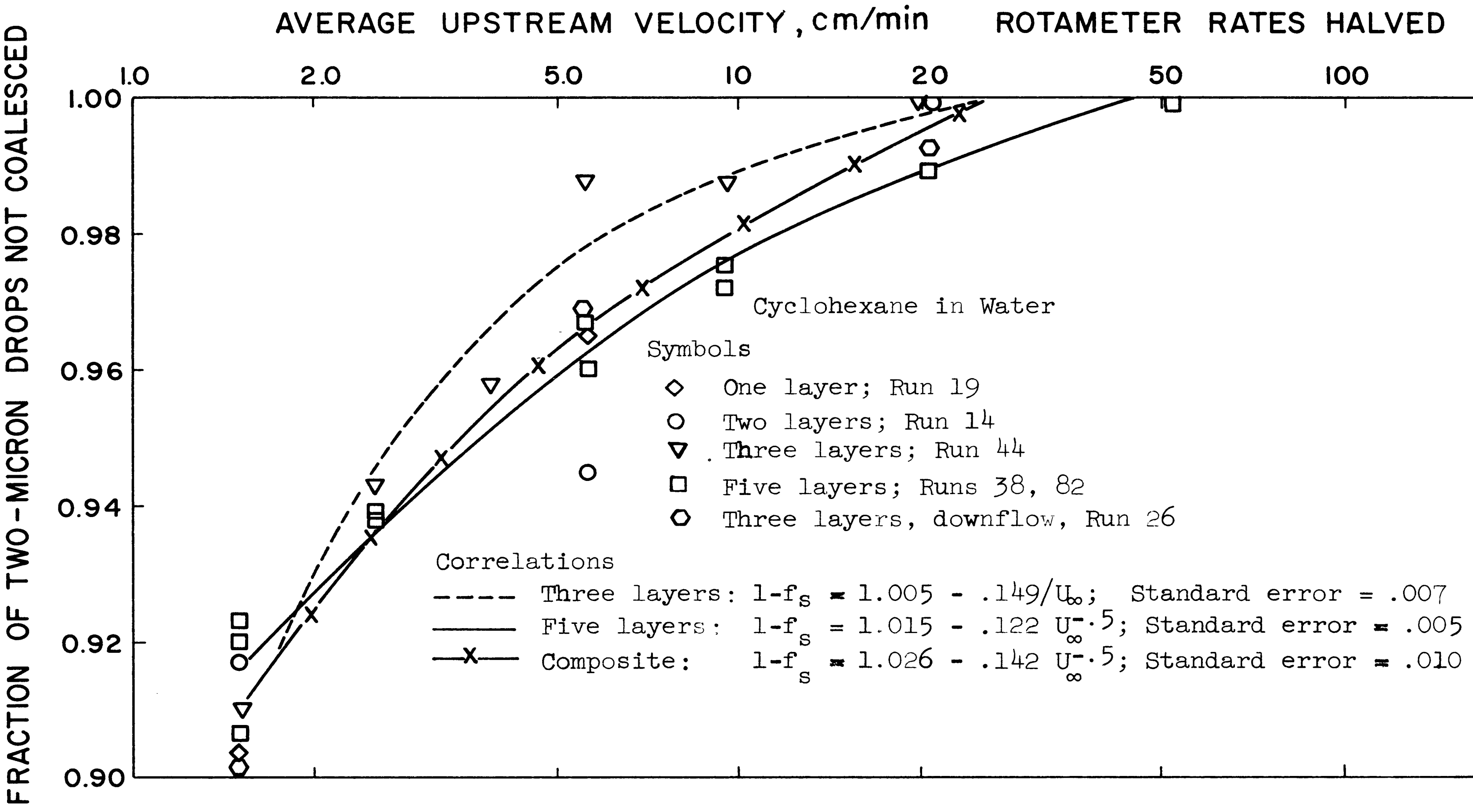

Figure 29. Effect of Number of Supports on Inherent Coalescence of Two-Micron Drops.

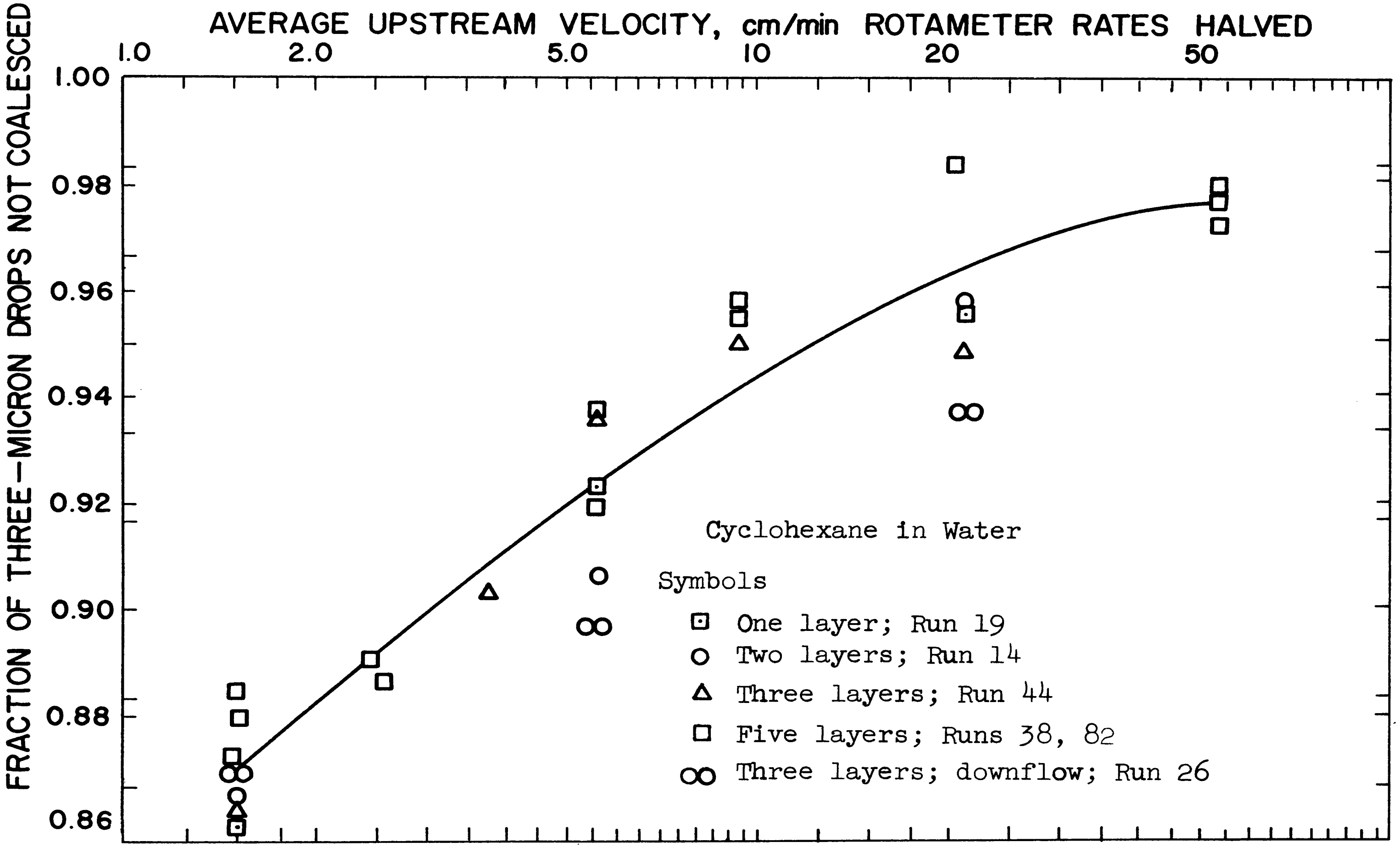

Correlation

——— $1\text{-}f_s = .826 + .042 \ln U_\infty - 4.5 \times 10^{-4} U_\infty$; Standard error = .015

Figure 30. Effect of Number of Supports on Inherent Coalescence of Three-Micron Drops.

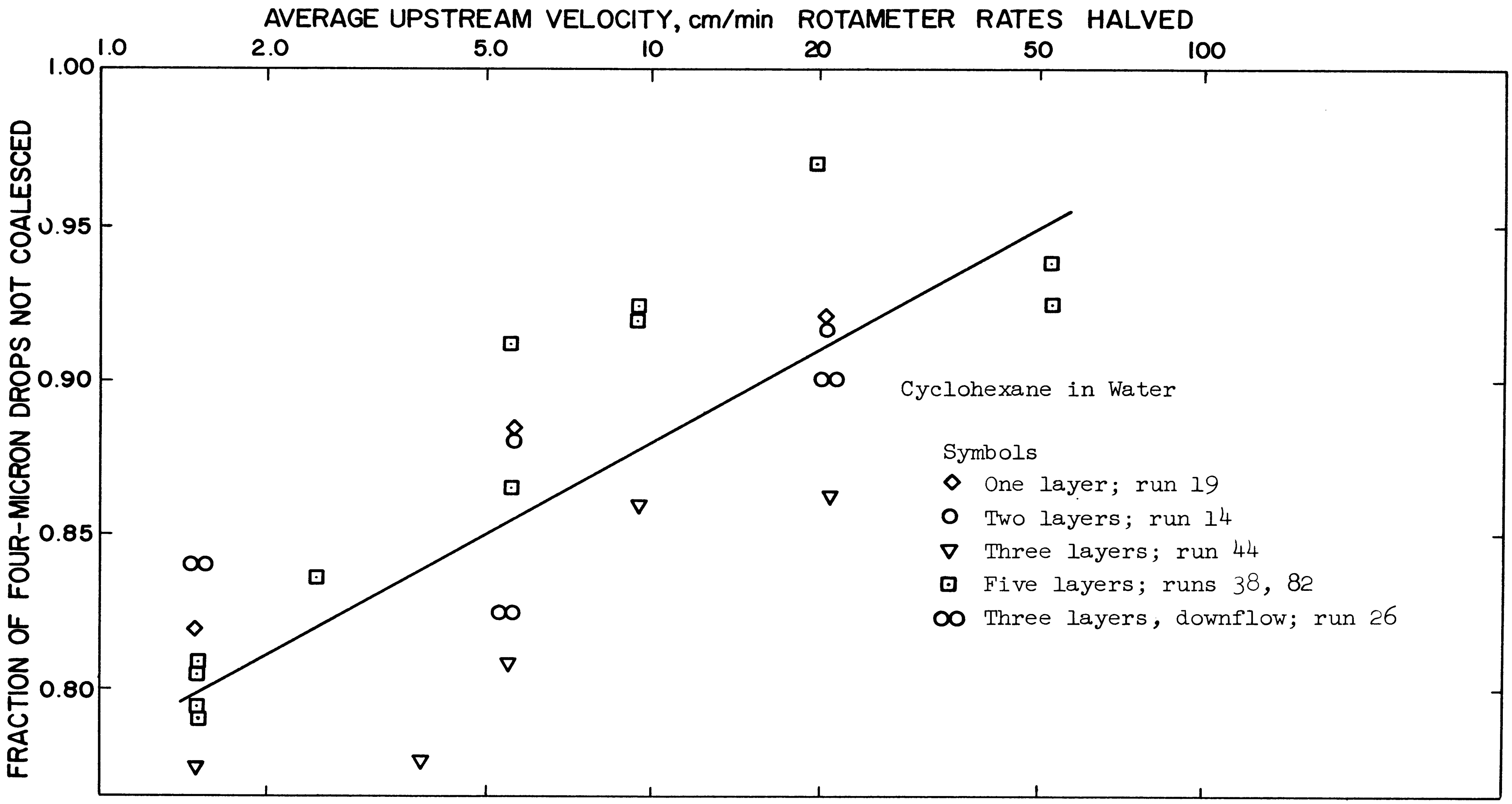

——— $1 - f_s = .782 + .043 \ln U_\infty$; Standard error = .034.

Figure 31. Effect of Number of Supports on Inherent Coalescence of Four-Micron Drops.

of supports confirms the method of computing net fractional coalescence, Equations (88 and 89).

No interactions between the number of supports and the physical properties of the dispersion were expected. Inherent coalescence data for other systems was obtained with five supports.

Effect of Flow Direction

The few inherent fractional coalescence data obtained for downward flow through three layers of supports are also shown in Figures 29, 30 and 31. Because of the longer flow path in the tubing arrangement for downward flow, more coalescence was expected. This effect appeared only for the three- and four-micron drops. Since none of the points for downward flow fell outside the 95 percent confidence limits of the composite correlations, the composite correlations were used to estimate inherent coalescence in the downward flow runs.

Inherent Coalescence and Direct Flow Measurement

In the series of runs with direct flow measurement, two inherent coalescence runs for cyclohexane drops in water were performed. Although they differ by about two percent, the non-coalescence data for the two runs were correlated jointly, Figures 32, 33 and 34. These correlations were used to compute the inherent coalescence in the cyclohexane-in-water system for the direct flow measurement series. For direct flow measurement, four-micron data were available from only one of the inherent coalescence runs. The concentration of the four-micron drops was too small in the other run to yield reliable results.

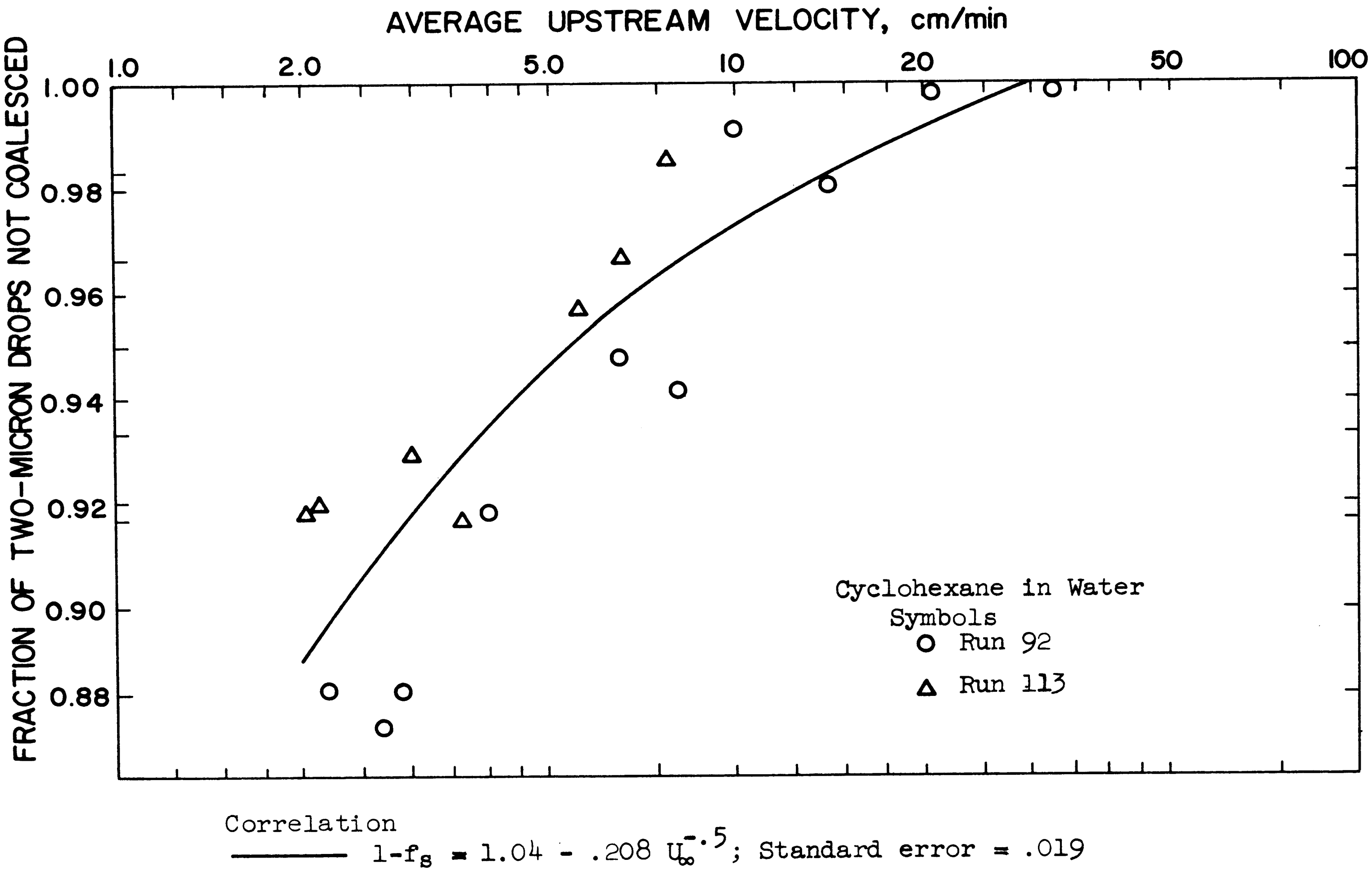

Figure 32. Inherent Coalescence of Two-Micron Drops: Direct Flow Measurement.

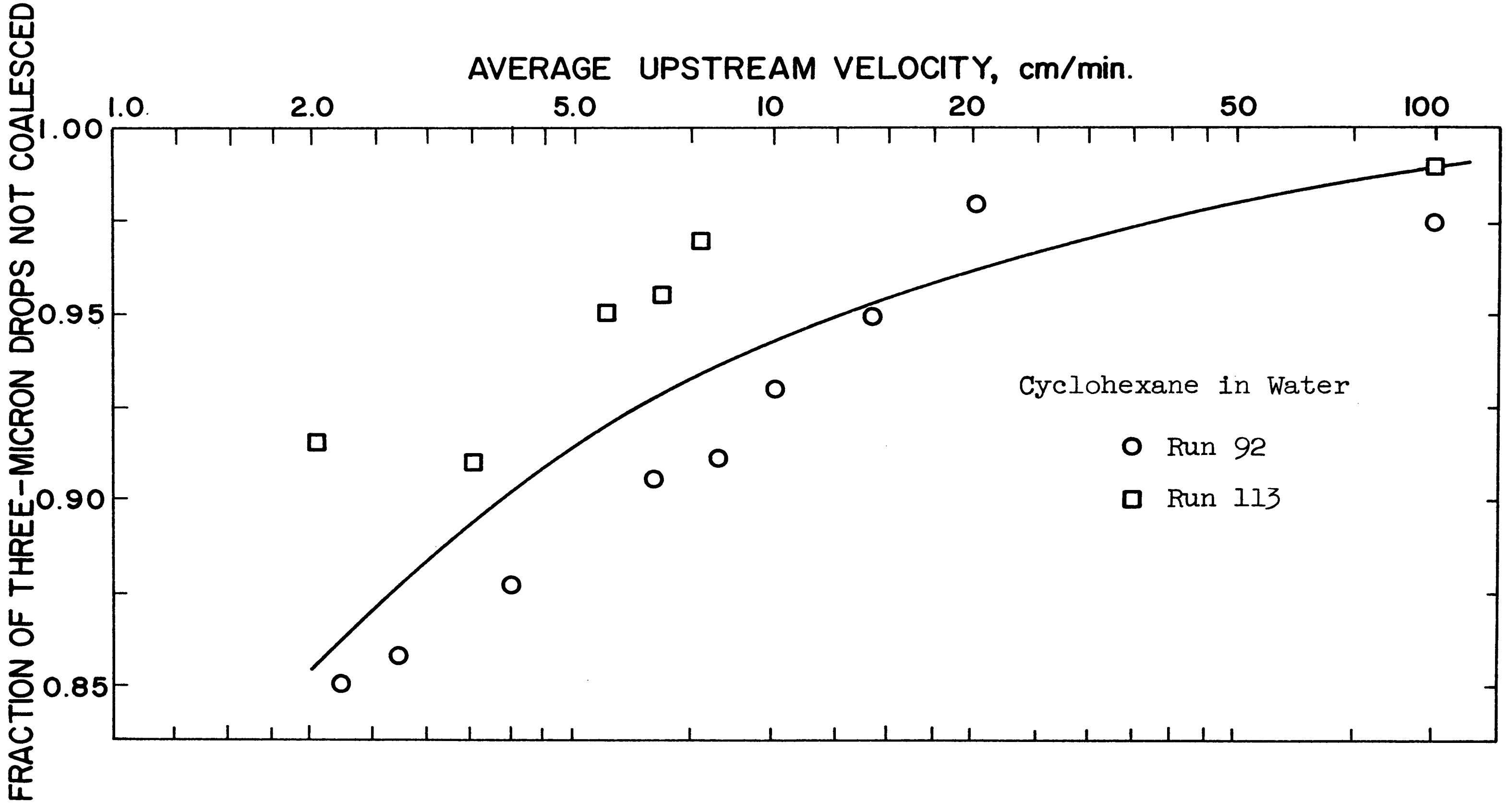

Correlation

——— $1-f_s = 1.011 - .22\ U_\infty^{-.5}$; Standard error = .030

Figure 33. Inherent Coalescence of Three-Micron Drops: Direct Flow Measurement.

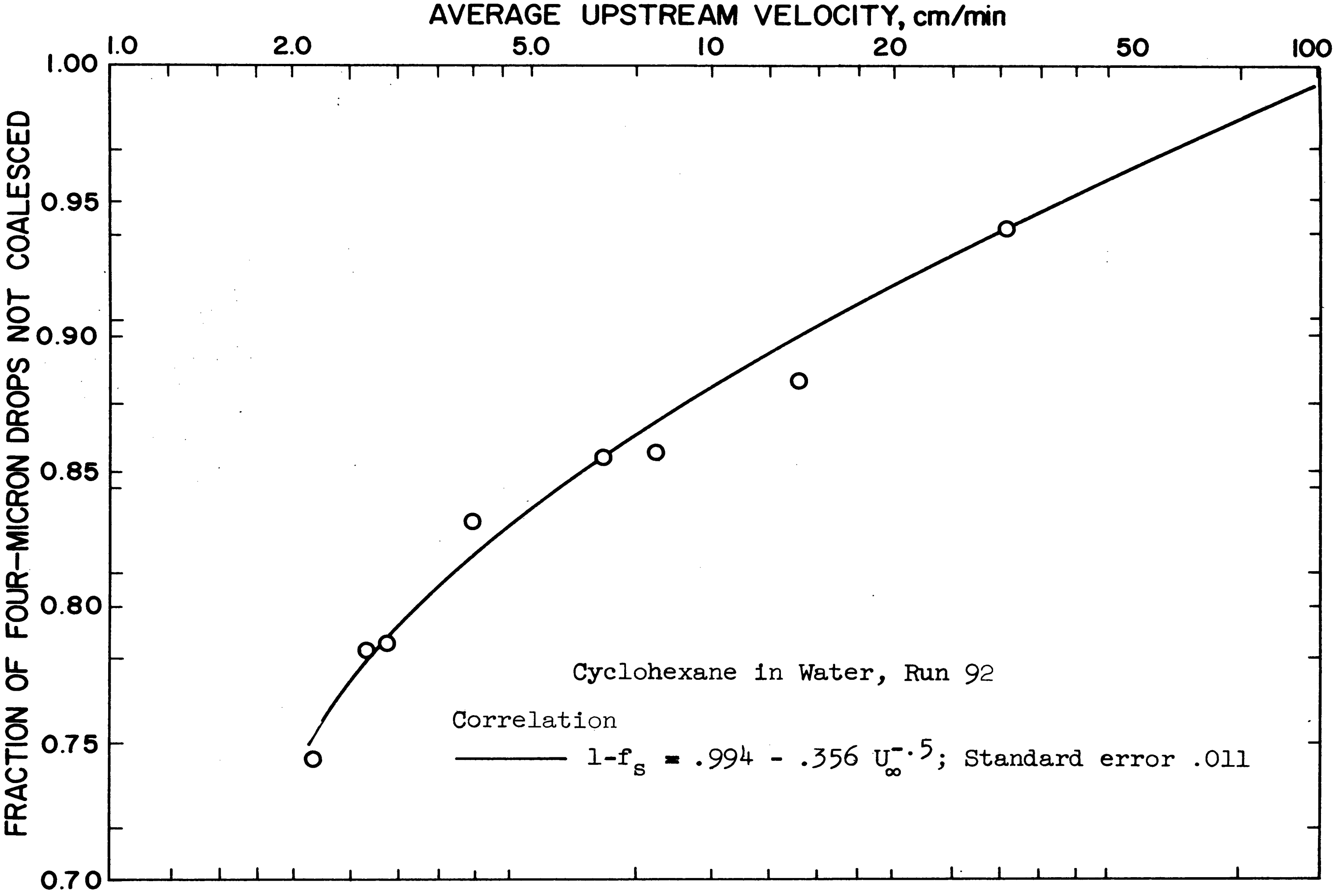

Figure 34. **Inherent Coalescence of Four-Micron Drops: Direct Flow Measurement.**

Comparison of the inherent coalescence correlation with and without direct flow measurement shows that the correlations with direct flow measurement predict that several percent more of the drops are inherently coalesced at low rates of flow. The causes of the differences in the inherent coalescence data with and without direct flow measurement are not wholly known. The small number of runs with direct flow measurement might have resulted in a biased correlation. The inherent coalescence correlations with and without direct flow measurement were not brought into harmony. Each was used to compute net fractional coalescence for the respective condition of flow measurement.

Special Physical Properties

According to Equation (90), continuum viscosity and the density difference are the only physical properties which influence inherent coalescence through their effect on settling. In the runs with an elevated drop viscosity, the density decrease was minor and there was no change in continuum viscosity. The inherent coalescence correlations for the cyclohexane-in-water system were used.

In the low interfacial tension systems, continuous phase viscosity was slightly greater than that of water. A few inherent coalescence traverses were performed for these systems. The data obtained are compared with the direct flow correlations of inherent coalescence for the cyclohexane-in-water system, Figures 35 and 36. For the two-micron drops, Figure 35, the data for $\gamma_{CD} = 11.1$ dynes

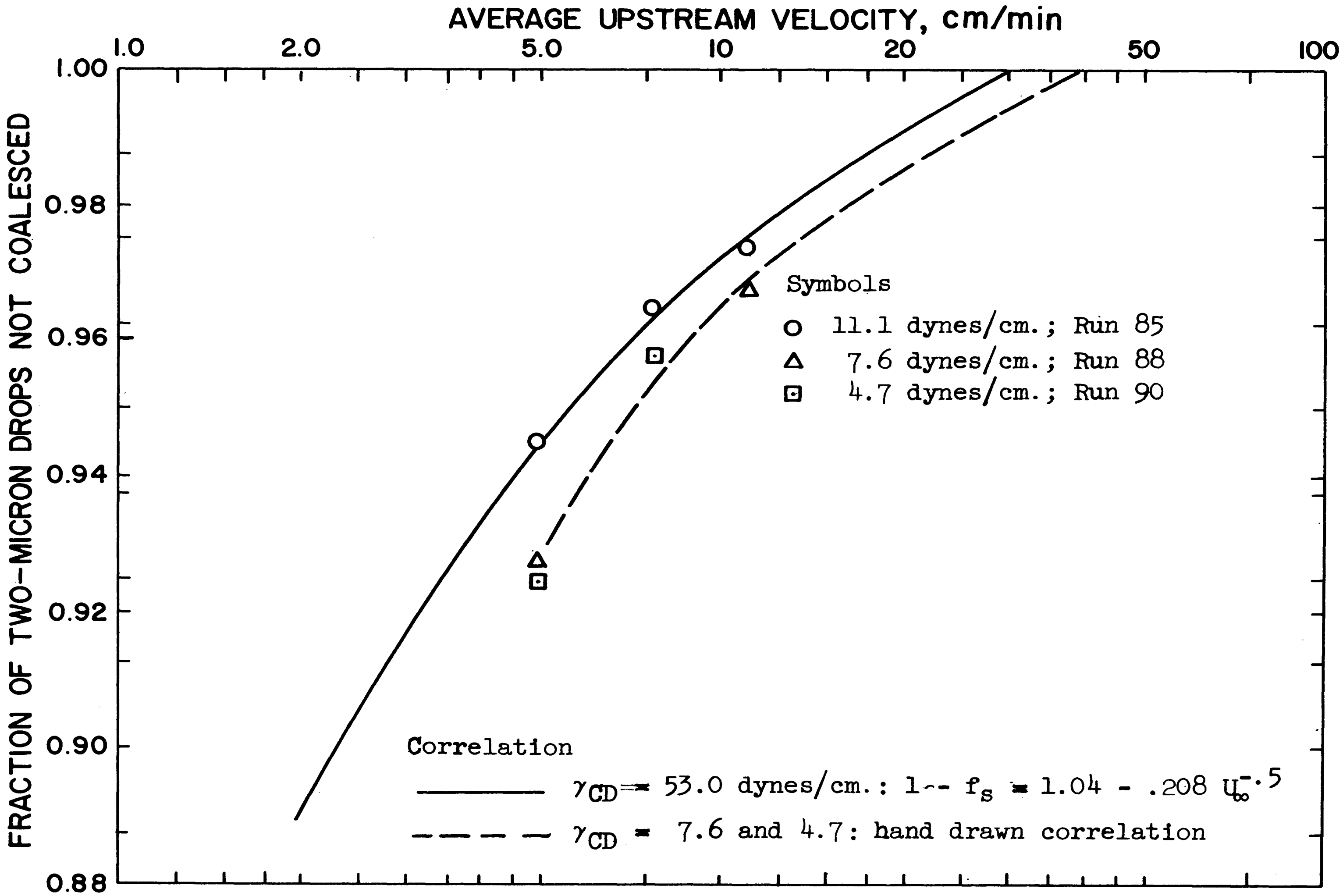

Figure 35. Effect of Interfacial Tension on Inherent Coalescence of Two-Micron Drops.

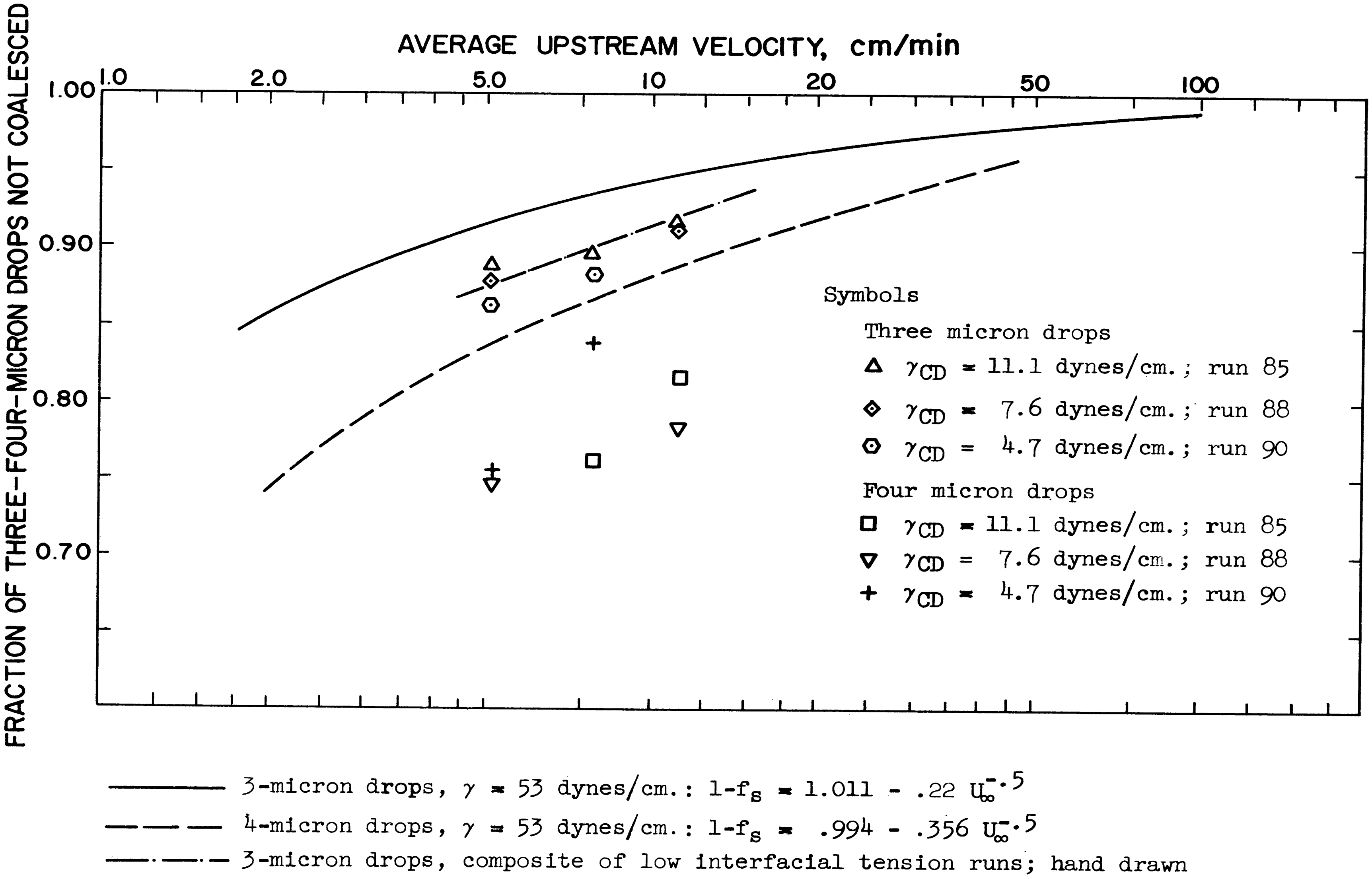

——— 3-micron drops, $\gamma = 53$ dynes/cm.: $1-f_s = 1.011 - .22\ U_\infty^{-.5}$

— — — 4-micron drops, $\gamma = 53$ dynes/cm.: $1-f_s = .994 - .356\ U_\infty^{-.5}$

—·—·— 3-micron drops, composite of low interfacial tension runs; hand drawn

Figure 36. Effect of Interfacial Tension on Inherent Coalescence of Three- and Four-Micron Drops.

per centimeter are indistinguishable from the cyclohexane-in-water correlation. The two other low interfacial tension systems show slightly more inherent coalescence. These data are correlated as a single line drawn by hand. For the three-micron drops, Figure 36, the data for the low interfacial tension systems were correlated with a single straight line which was extended to intersect the cyclohexane-in-water correlation. Figure 36 also shows the four-micron data for low interfacial tension systems. These data were considered too ambiguous to permit a correlating curve. No net coalescence calculations were performed for the four-micron drops in the low interfacial tension systems. The inherent coalescence curves for 4.7 dynes per centimeter were used to compute net coalescence in the run at 2.7 dynes per centimeter. The apparent slight increase in inherent coalescence with decreasing interfacial tension was probably caused by the increased ability of the drops to wet the flow channel.

Figure 37 shows the progressive decline in inherent coalescence of two-micron drops with increasing continuous phase viscosity. The difference between the data at 2.8 and 5.2 centipoises lacks statistical significance. However, the trend of the decrease in fractional inherent coalescence is significant. In view of the trend, the difference between the data at 2.8 and 5.2 centipoises was taken to be real. In order to obtain inherent fractional coalescence at intermediate viscosities, interpolation between the correlations was performed.

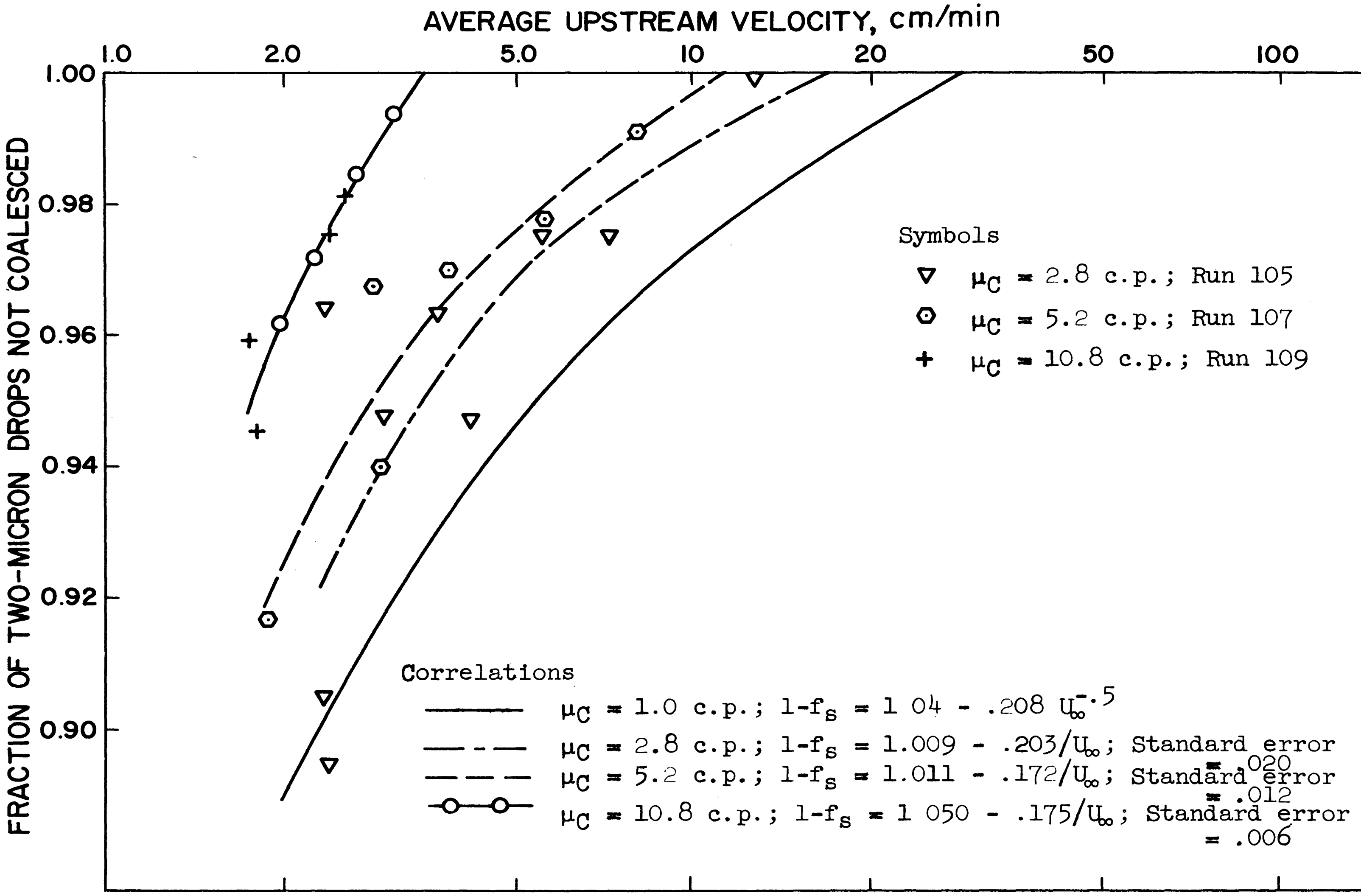

Figure 37. Effect of Continuum Viscosity on Inherent Coalescence of Two-Micron Drops.

In systems of elevated continuum viscosity, it was difficult to prepare dispersions containing predominantly two-micron drops. In the case of the run at 5.2 centipoises, the dispersion was quite heterodisperse. The larger drops showed less inherent coalescence than the two-micron drops. Since this was contrary to theory and was not substantiated by the other runs at elevated continuum viscosity, the data for the three- and four-micron drops were neither used nor included in the inherent coalescence correlations.

Figures 38 and 39 show the decreasing inherent coalescence with increasing continuum viscosity for the three- and four-micron drops, respectively. The indication of the effect of μ_C is less clear because of the greater data scatter. Because of their limited range of velocity, the data at 10.8 centipoises were difficult to extrapolate to $1 - f_s = 1.0$. Since the data for the two-micron drops were more reliable and seemed sufficiently indicative, no net coalescence calculations were performed for the three- and four-micron drops at viscosity levels above three centipoises. The scatter of the four-micron data at 2.8 centipoises seemed too great to admit a reliable correlation. The three-micron correlation at 2.8 centipoises was considered satisfactory for the computation of fractional net coalescence.

NET COALESCENCE ON FINE-MESH SCREEN

Net fractional coalescence on fine-mesh screen was computed according to Equation (89) with the aid of the inherent coalescence

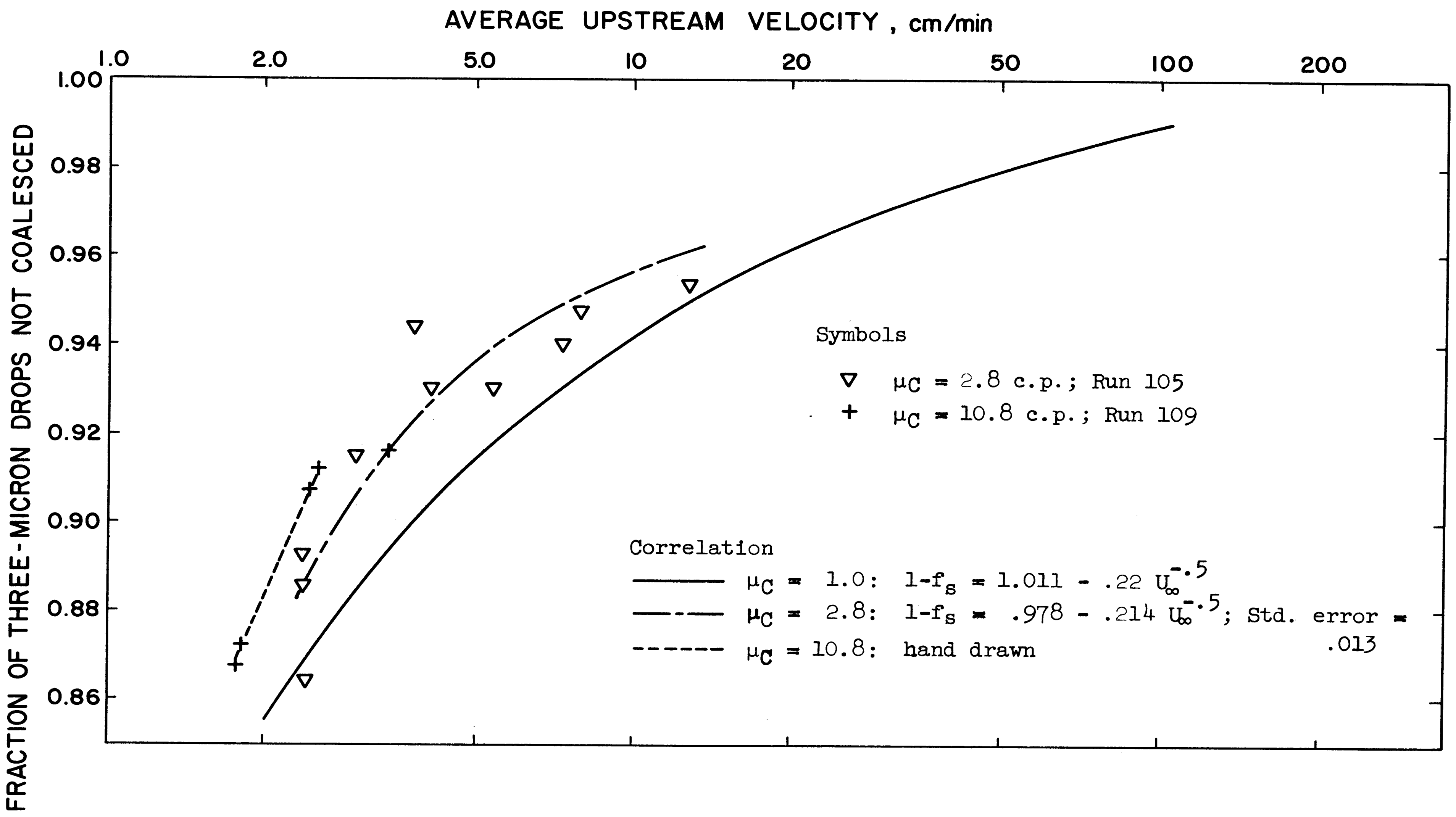

Figure 38. Effect of Continuum Viscosity on Inherent Coalescence of Three-Micron Drops.

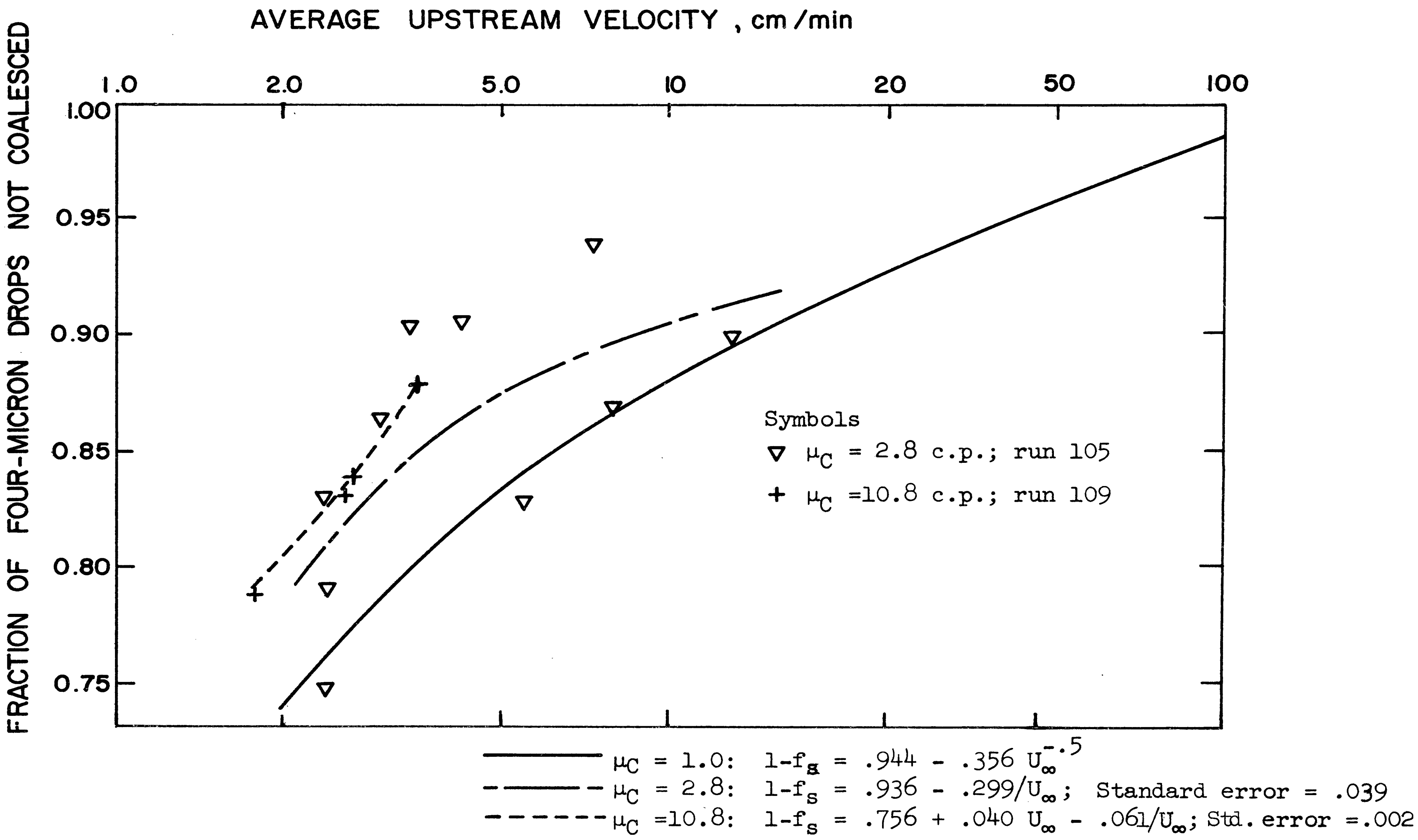

Figure 39. Effect of Continuum Viscosity on Inherent Coalescence of Four-Micron Drops.

correlations. In the following discussion, the terms, "coalescence," "fractional coalescence" and "net fractional coalescence" are synonymous. In each part of the experiment, in which the effect of one of the variables was being examined, the correspondence of duplicate runs and the consistency of the trends of change were taken as evidence of the fixed level of screen wettability. Screen wettability did vary from part to part. The major correlation of this work was drawn from the data of the variable screen geometry and variable continuum viscosity parts. In these parts the screen wettability was subject to the best control and appeared to be uniform.

Effect of Drop Size

Figure 2 predicts the effect of the ratio of drop size to interstitial distance on fractional interception. At a fixed interstitial distance, a substantial increase in coalescence would be expected with an increase in drop size. Figure 40 gives an example of the gradation in coalescence for the various drops of the computed distributions. Although total coalescence differed, the net coalescence showed no significant difference for the various drop sizes in the computed distribution. When it occurred, a distinction in the fractional coalescence was usually accompanied by a change in the characteristic drop size distribution computed for the feed dispersion. However, at an elevated drop viscosity, the screens showed significantly more coalescence of the large drops with the usual feed distribution. On the other hand, elevated continuum viscosity did not produce any gradation.

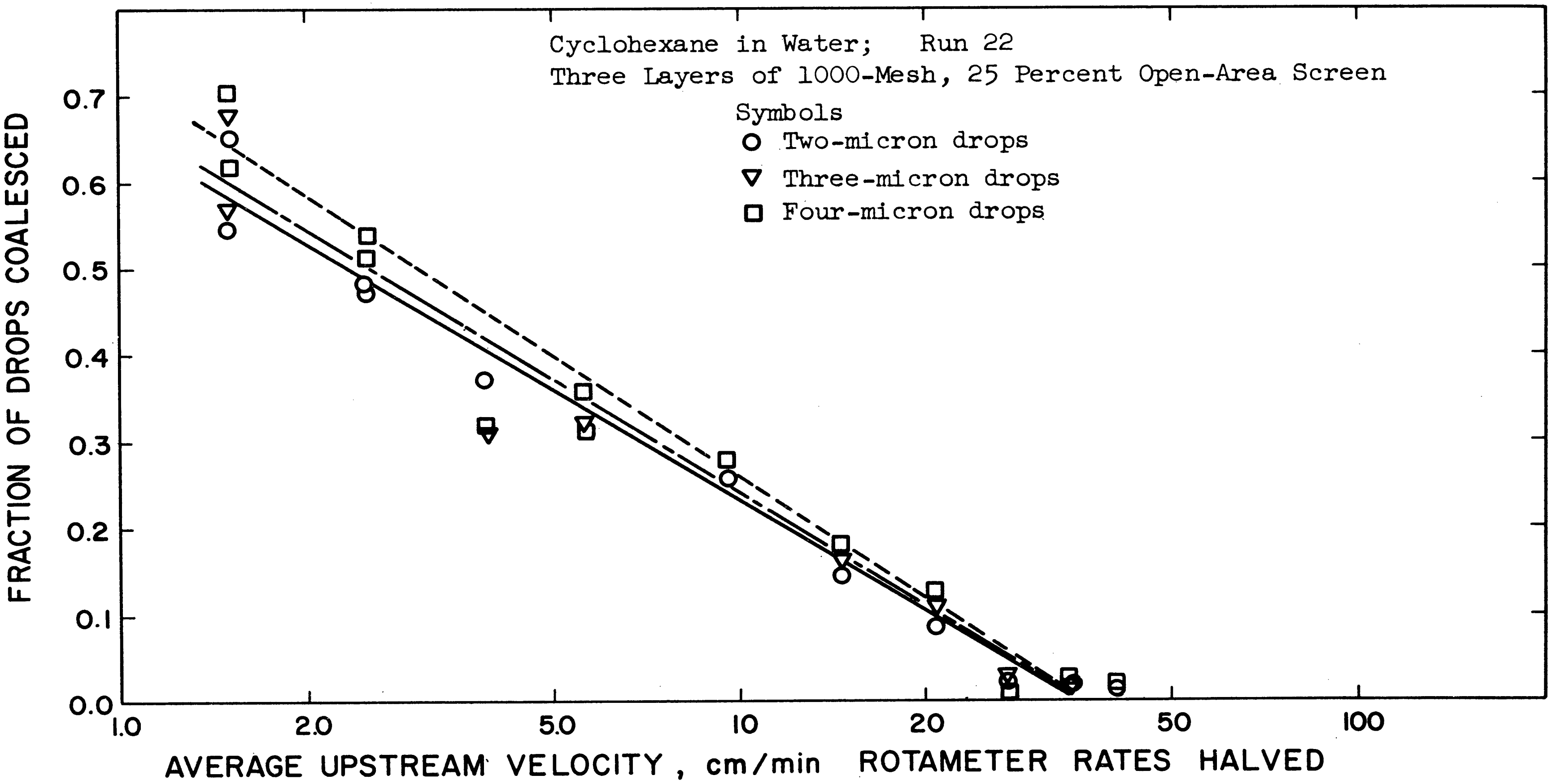

Correlations

——— 2-micron drops: $f = .660 - .185 \ln U_\infty$; Standard error = .034 .

—·— 3-micron drops: $f = .678 - .188 \ln U_\infty$; Standard error = .036 .

- - - 4-micron drops: $f = .728 - .202 \ln U_\infty$; Standard error = .035 .

Figure 40. Variation of Net Coalescence with Drop Size.

The lack of distinction in net coalescence of the drops of various sizes is primarily a reflection of the diffusing effect of the Mellin transformation. This effect was demonstrated by performing calculations on a theoretical Rayleigh flux pattern for particles of a single size, Appendix B. For three- and four-micron particles, spurious maxima appeared at two and three microns, respectively. Finite concentrations of four- and five-micron particles also appeared. Since the various points on the computed distributions represent overlaping size ranges, each part of the distribution would change in a similar fashion as coalescence proceeded. Since the transformation failed to accurately reproduce prescribed distributions for which Rayleigh theory was assumed, the accurate reproduction of a distribution for which Mie scattering prevailed would be fortuitous.

Since inherent and total coalescence did show significant differences for the various drop sizes, it is likely that the blurring effect of the transformation was not the sole factor. The film thinning resistance could have been important. Film thinning by the Stokes stress and molecular forces is more rapid for small drops.

The results for heterodisperse dispersions and for elevated drop viscosity show that the calculations were somewhat sensitive to changes in the drop distributions, although the exact change was not represented. The greater coalescence of large drops when the drop viscosity was large shows that a decrease in the rate of strain in the dispersed phase allowed the accumulation of larger packets of coalesced material before stripping occurred. This suggests that, for a μ_D of one centipoise, the production of enlarged drops by the coalescence of small competed with the removal of large drops by their coalescence. Since the coalescence of the smallest drops would not be confounded by the production of drops of the same size, the extent of coalescence was reckoned exclusively from the concentrations computed for the two-micron drops. The two-microns concentrations were the most sensitive to changes in the concentration of the smallest drops in the dispersions. The numerical representation of the first half-cycle of the Mellin kernel was also the best. All net coalescence results were presented in terms of the fractional coalescence computed for the two-micron drops. In reality, the two-micron calculations indicated the coalescence of drops over a narrow rather than an infinitesimal range of drop size.

Effect of Temperature

Moderate differences of temperature affected coalescence only in systems of elevated viscosity. Figure 41 gives an example of the lack of any significant temperature effect in the coalescence of cyclohexane drops in water.

Effect of Flow Direction

It was unlikely that flow would have an effect on coalescence at the flow velocities used. For a two-micron cyclohexane drop in water, the Stokes settling velocity is 3×10^{-3} centimeter per minute compared with a minimum average upstream velocity of two centimeters per minute. In vertical flow through the coalescer at velocities of the order of 0.1 centimeter per minute or 0.003 foot per minute, settling could become important. Figure 42 compares the effect of downward and horizontal flow on settling for two-micron drops. Although coalescence in downward flow tended to be somewhat greater than for horizontal flow, the difference was not significant as the correlations of Figure 42 show. The same conclusion held for the three- and four-micron drops.

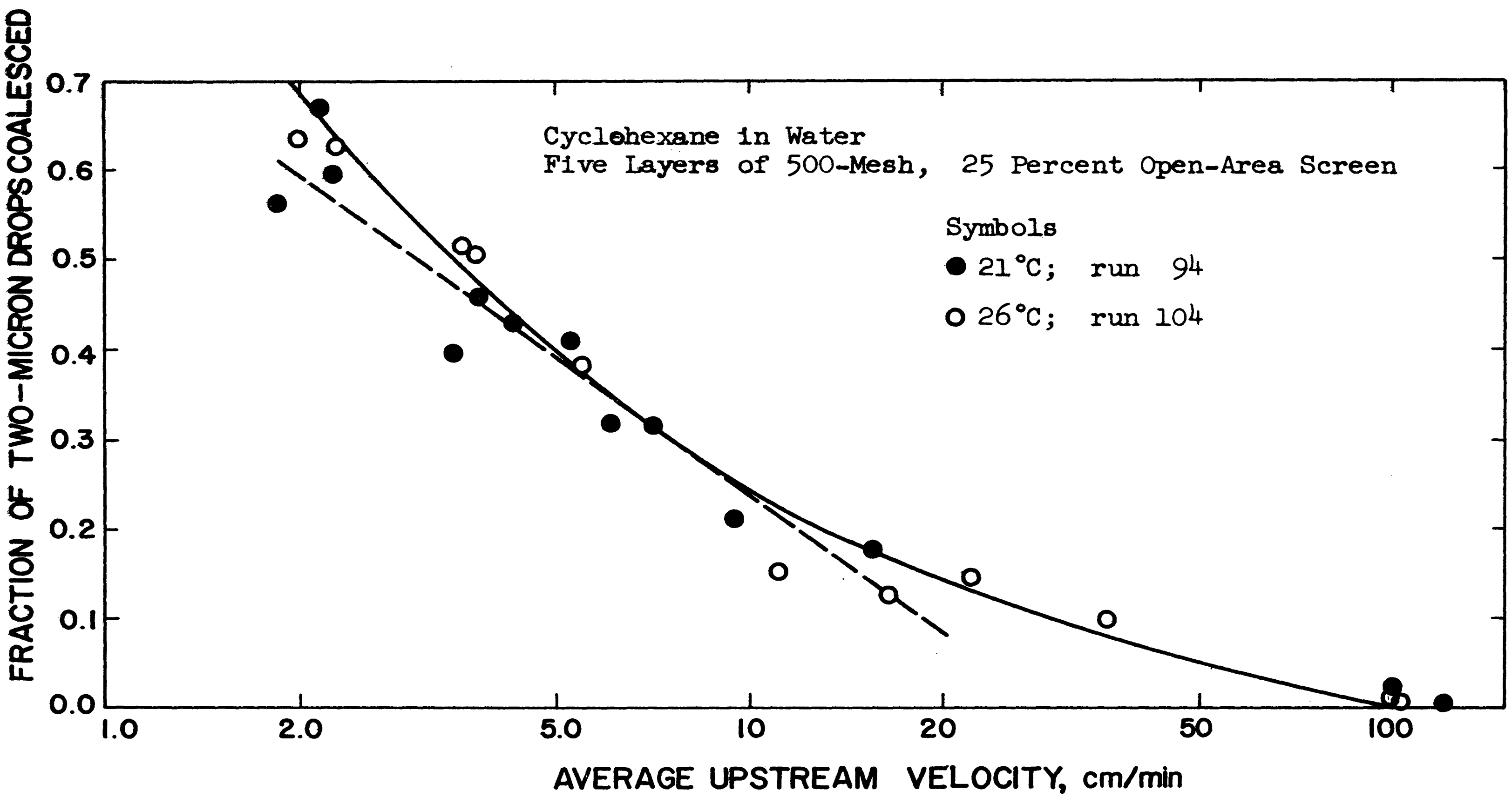

Correlations

– – – 21°C: $f = .750 - .222 \ln U_\infty$; Standard error .050 .

——— 26°C: $f = -.114 + 1.134\, U_\infty^{-.5}$, $U_\infty < 20$ cm./min.; Standard error = .036 .

Figure 41. Effect of Temperature on Coalescence.

Effect of Number of Layers of Screen

Langmuir proposed a depreciation equation to describe the behavior of a multi-layer aerosol filter.(41)

$$1 - f_N = (1 - f_1)^N \qquad (92)$$

The variable N is the number of non-interacting layers present, f_1 is the fractional removal from one layer and f_N is the fractional removal from N layers. Since the screens were widely spaced relative to the filament size, they were expected to follow Equation (92) as long as the accumulation of coalesced material did not interfere with the performance of the downstream screens. Figure 43 compares the performance of one, two, three and four layers of screen. The fractional non-coalescence was forced to a basis of three layers of screen by using the computed dependent variable, $1 - (1 - f_N)^{3/N}$. The agreement is fair. The data for two and four layers are high. These correlations are not significantly different at the 95 percent

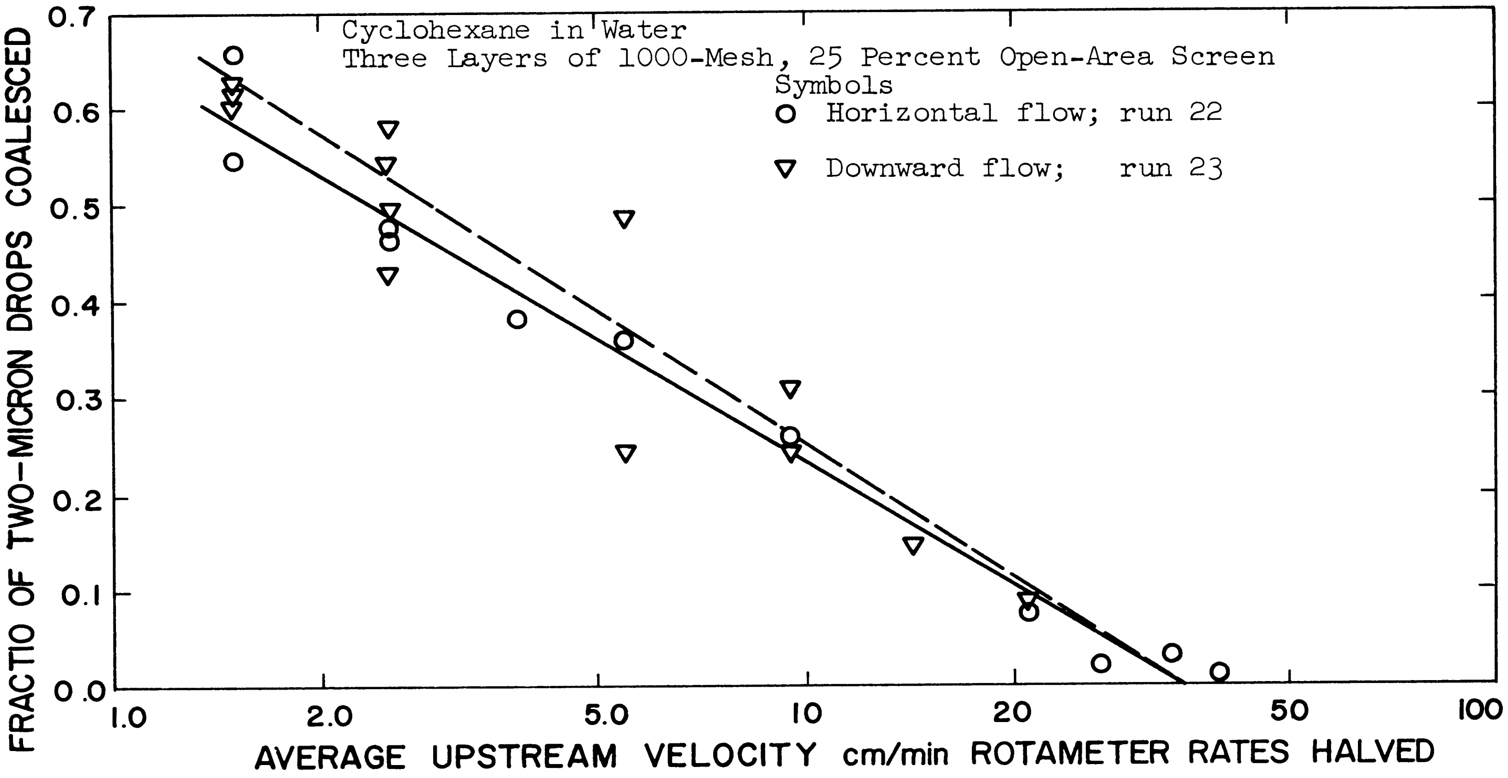

Correlations

——— Horizontal flow: $f = .660 - .185 \ln U_\infty$; Standard error = .034

— — — Downward flow: $f = .717 - .203 \ln U_\infty$; Standard error = .065

Figure 42. Effect of Downward Flow on Coalescence.

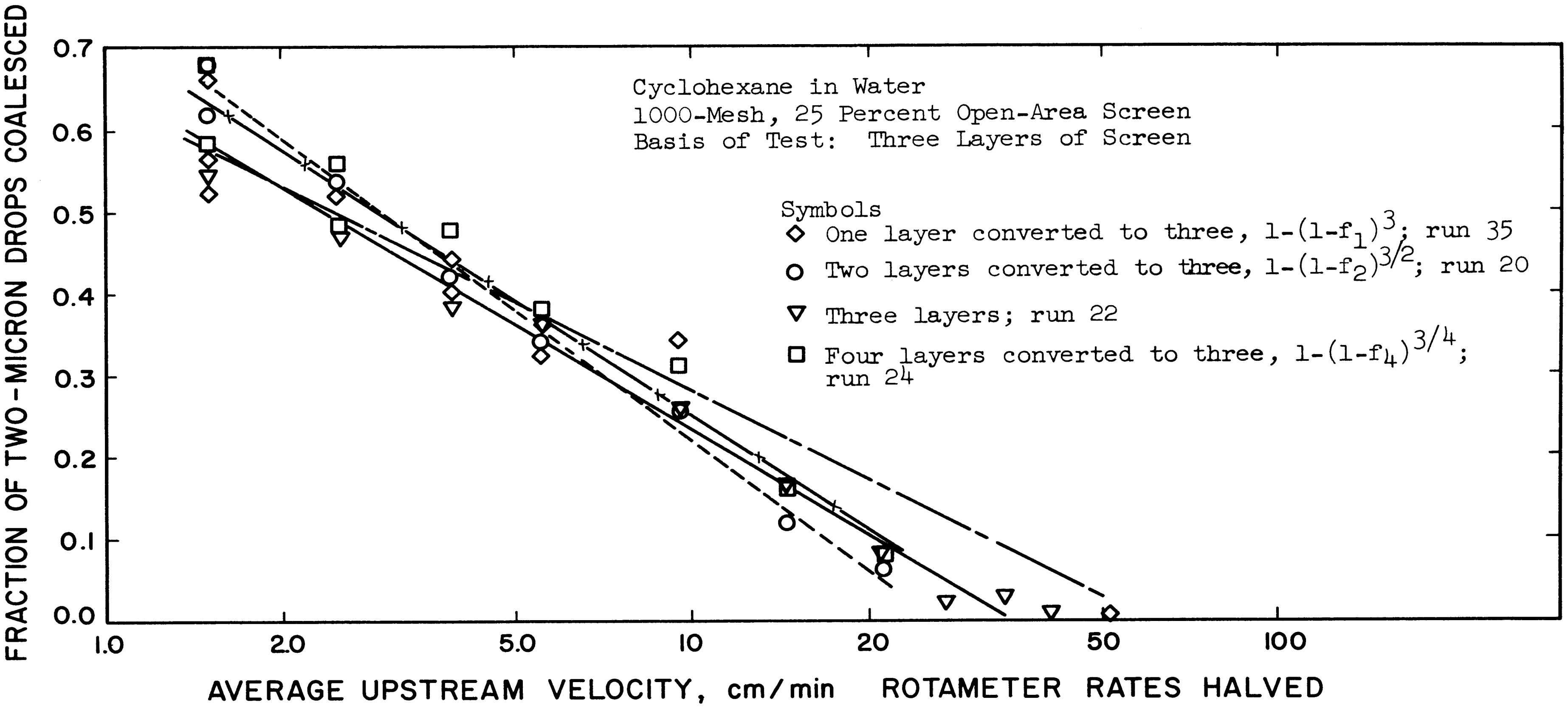

Correlations

— - — One layer: $1-(1-f_1)^3 = .641-.155 \ln U_\infty$; Standard error = .042

- - - - Two layers: $1-(1-f_2)^{3/2} = .748-.229 \ln U_\infty$; Standard error = .025

——— Three layers: $f = .660-.185 \ln U_\infty$; Standard error = .034

—x— Four layers: $1-(1-f_4)^{3/4} = .718-.203 \ln U_\infty$; Standard error = .044

Figure 43. Test of Relation Between Coalescence and Number of Layers of Screen.

confidence level over most of the velocity range. Runs were performed with varying numbers of layers for three of the other screens. These data are shown in Figures 44, 45 and 46 in support of Equation (92). In each curve, the data for one of the layers was forced to be compatible with the data for the other by using Equation (92). The adjustment appeared to bring the data for the different number of layers into general harmony. When they appeared, significant differences were usually at higher velocities, at which the measurements were less accurate. The Langmuir model was accepted for making comparisons of data from differing numbers of layers of screen. The general confirmation of the Langmuir model implies either that the performance of each layer of screen was not affected by the incident velocity profile or that the incident profiles were uniform.

Effect of Drop Viscosity

The runs at elevated viscosity were carried out by constituting the drops from mixtures of cyclohexane and fin oil. Three layers of 1000-mesh screen were used. Although uniform throughout this series of runs, the surface of the screen had less affinity for the hydrocarbon phase than in the runs dealing with the effect of screen geometry and number of layers. Since fin oil is a hydrocarbon, it was assumed that the inherent coalescence correlations and rotameter calibration for cyclohexane in water applied. The drop viscosity was increased up to 24 centipoises. Figure 47 shows that coalescence was slightly greater above ten centipoises and significantly greater

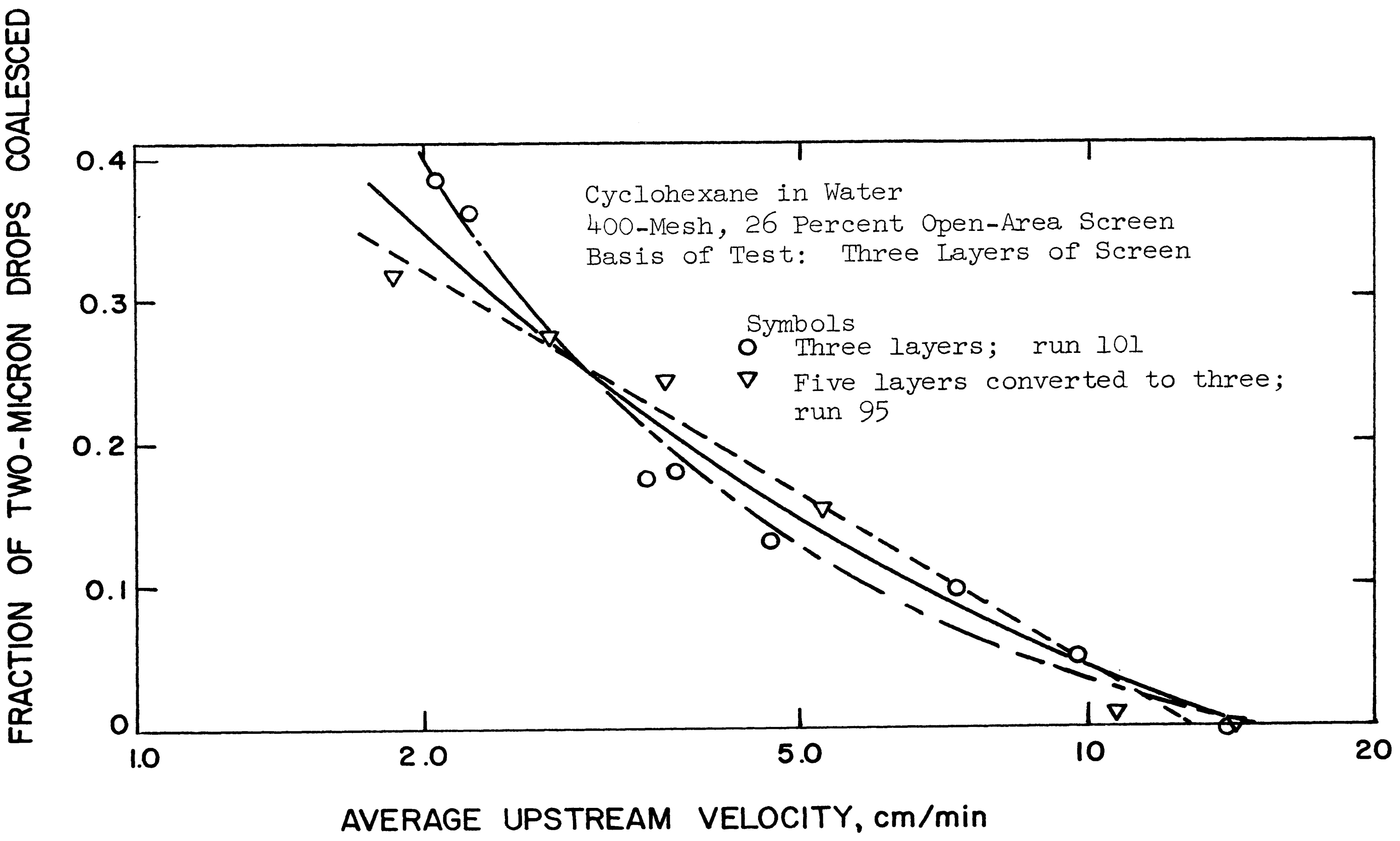

Correlation

—·— Three layers: $f = -.060 + .929/U_\infty$; Standard error = .016

- - - - Five layers converted to three: $1-(1-f_5)^{3/5} = .444 - .172 \ln U_\infty$; Standard error = .017

——— Correlation of combined data: $f_3 = -.207 + .748\, U_\infty^{-.5}$; Standard error = .038

Figure 44. Test of Relation Between Coalescence and Number of Layers of Screen.

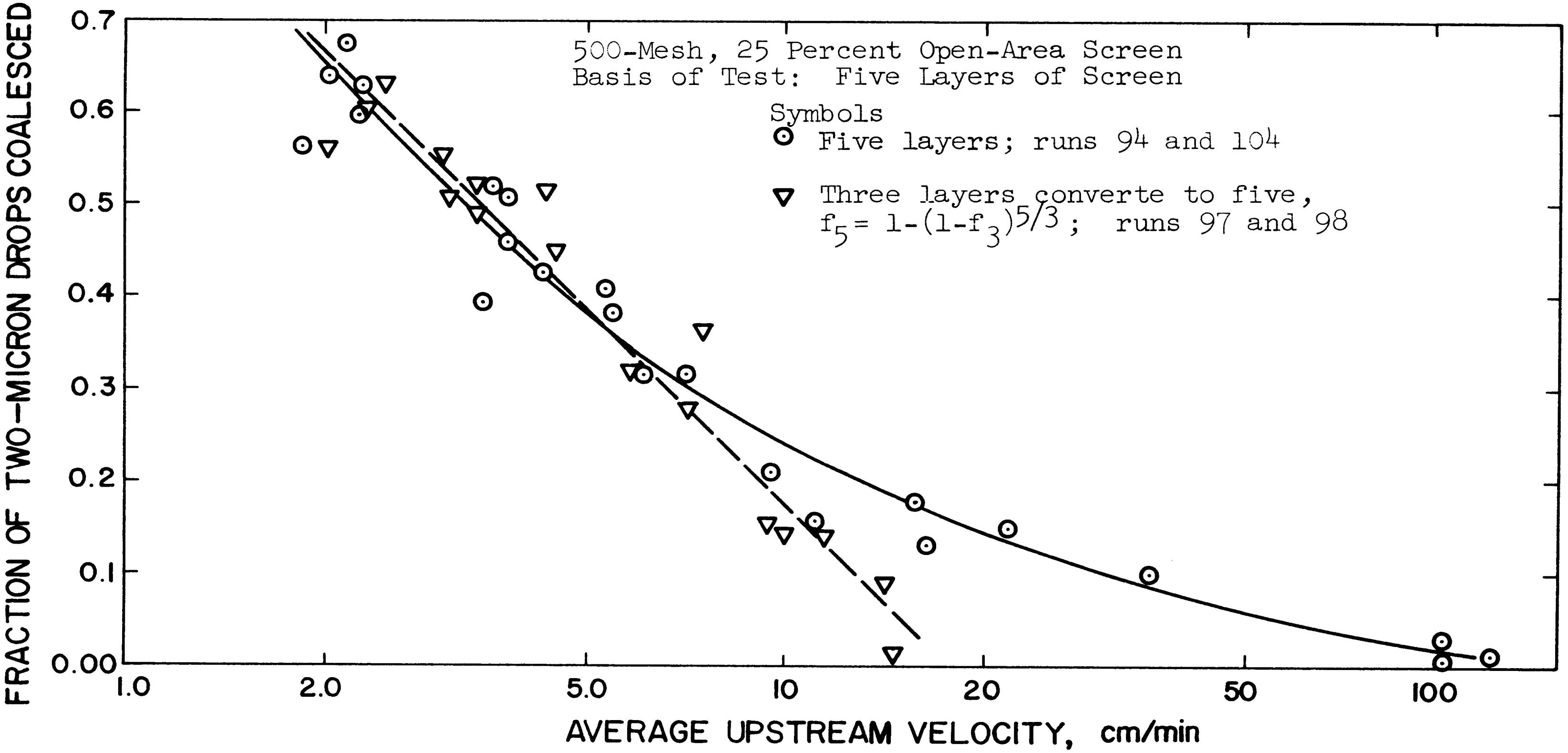

Correlations

——— Five layers: $f = -.09+1.046\ U_\infty^{-.5}$; Standard error = .046

— — — Three layers converted to five: $1-(1-f_3)^{5/3} = .87 - .304 \ln U_\infty$; Standard error =.042

Figure 45. Test of Relation Between Coalescence and Number of Layers of Screen.

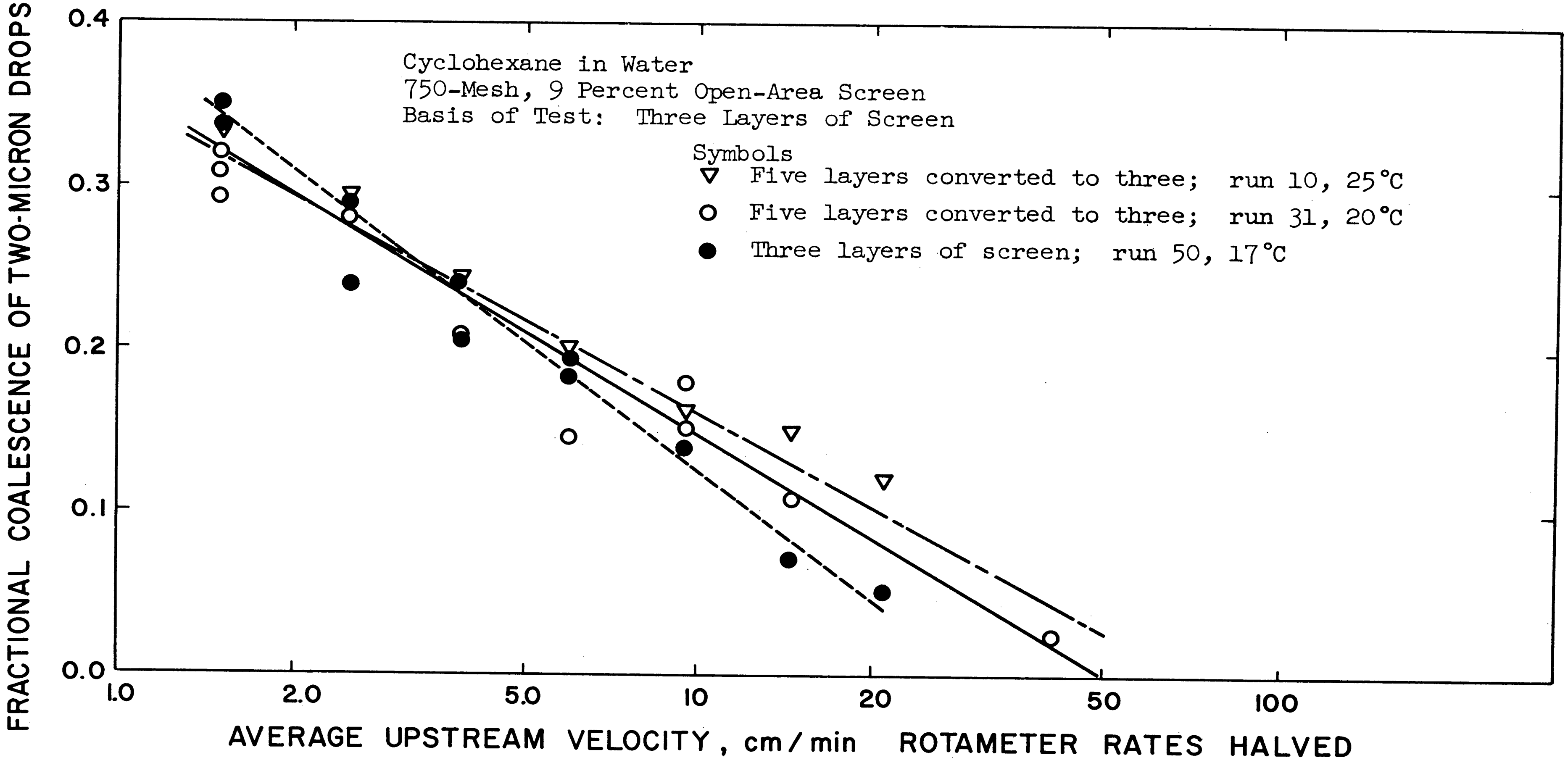

Correlations

------ Three layers: $f = .389-.115 \ln U_\infty$; Standard error = .025

— - — Five layers converted to three: $1-(1-f_5)^{3/5} = .350-.083 \ln U_\infty$; Standard error = .025

——— Correlation of combined data: $f_3 = .358-.092 \ln U_\infty$; Standard error = .026

Figure 46. Test of Relation Between Coalescence and Number of Layers of Screen.

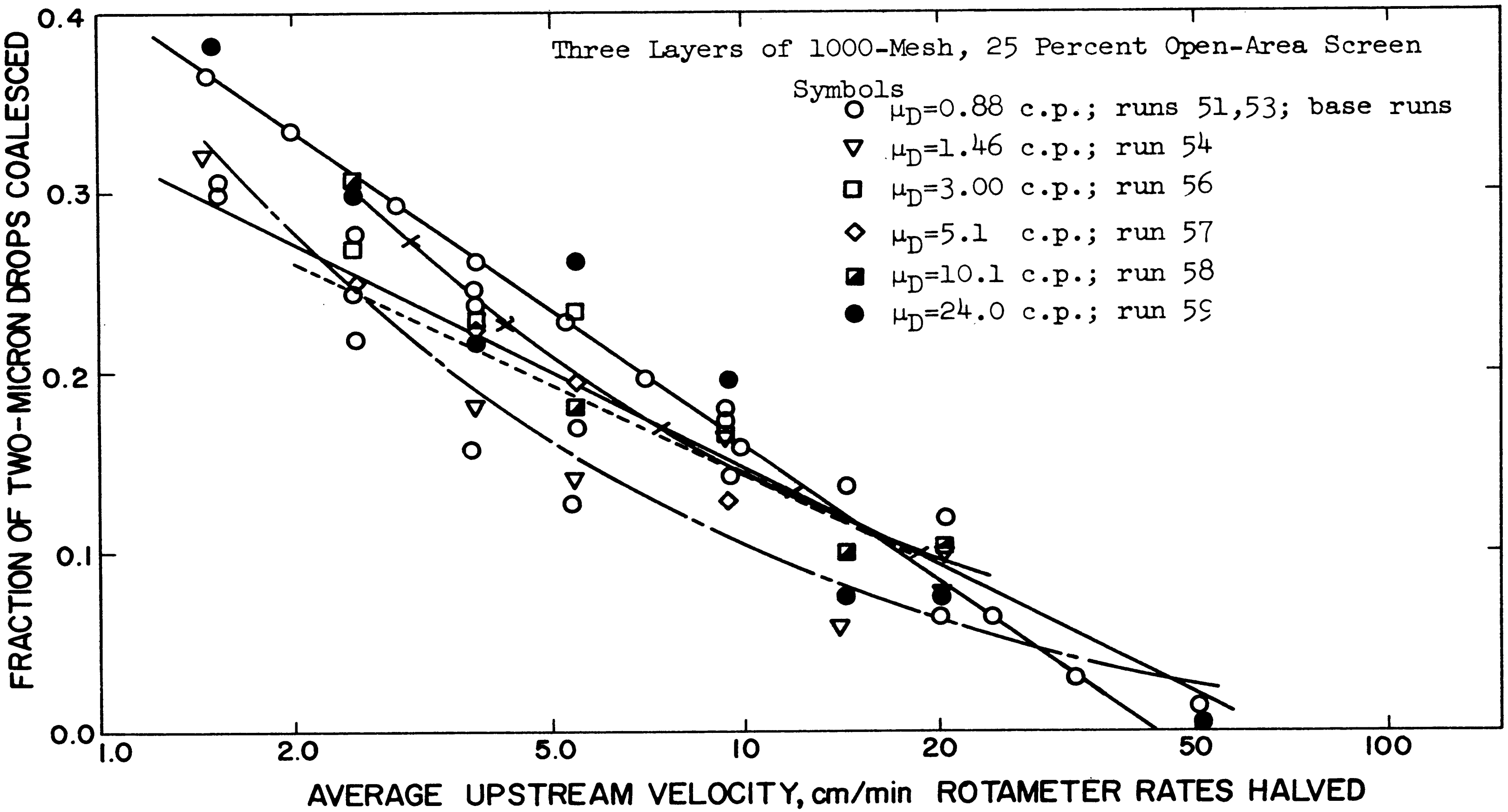

Correlations

———	μ_D = 0.88 c.p.	$f = .324 - .077 \ln U_\infty$	Standard error = .024
—·—	μ_D = 1.46 c.p.	$f = -.037 + .443 U_\infty^{-.5}$	Standard error = .031
- - -	μ_D = 5.1 c.p.	$f = .315 - .076 \ln U_\infty$	Standard error = .012
—x—	μ_D = 10.1 c.p.	$f = -.017 + .503 U_\infty^{-.5}$	Standard error = .016
—○—	μ_D = 24.0 c.p.	$f = .409 - .108 \ln U_\infty$	Standard error = .035

Figure 47. Effect of Dispersed Phase Viscosity on Coalescence.

at 24 centipoises. The trend was not sufficiently developed to support a correlation of coalescence versus drop viscosity. The coalescence of the four-micron drops was substantially greater than that of the two-micron drops above three centipoises. Figure 48 shows the distinction between various drop sizes for a drop viscosity of 24.0 centipoises. The increase in drop viscosity might have increased the retaining capacity of the filaments for the dispersed phase. The relatively low affinity between the dispersed phase and the screens might have been a factor.

Effect of Continuum Viscosity

Continuum viscosity influenced the shearing forces of laminar flow and was expected to have a bearing on the ease of film thinning to the point of rupture. Glycerol-in-water solutions were used for this phase of the study. The most concentrated solution contained 60 percent by volume glycerol. Its interfacial tension against n-octane was 33 dynes per centimeter. At this level of interfacial tension, the two phases were quite dissimilar. The surface of the solid was probably not altered by the presence of the glycerol in the continuous phase. Figure 49 shows the effect of continuum viscosity on the coalescence on five layers of 500-mesh screen. Coalescence declined progressively with an increase in viscosity. The scatter in the run at the highest viscosity was caused by the relatively large experimental error at low levels of coalescence. The data suggested that coalescence could be related

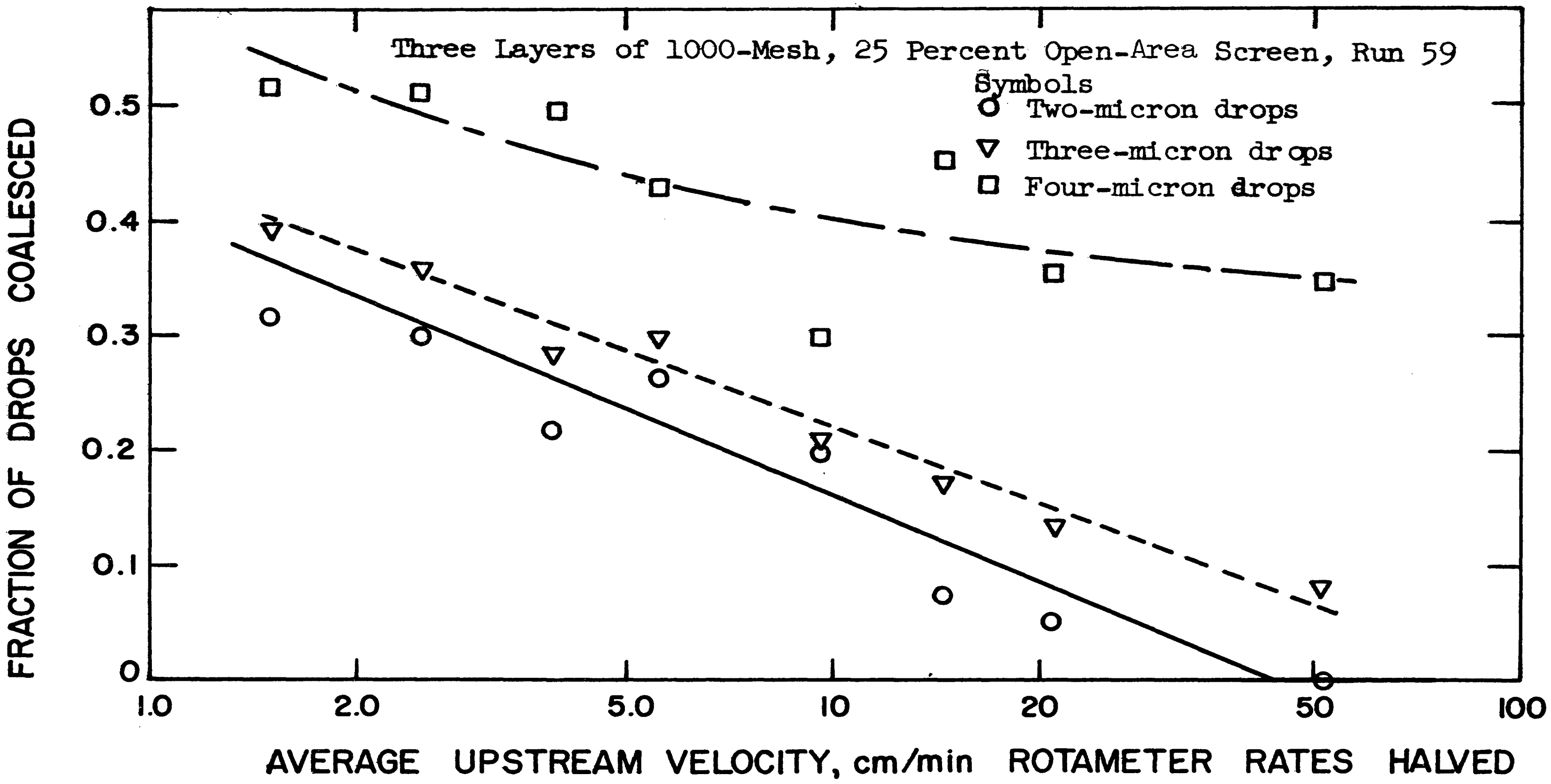

Correlations

——— Two-micron drops: $f = .409 - .108 \ln U_\infty$; Standard error = .035

- - - - Three-micron drops: $f = .438 - .095 \ln U_\infty$; Standard error = .020

—·— Four-micron drops: $f = .306 + .288\, U_\infty^{-.5}$; Standard error = .056

Figure 48. Variation of Coalescence with Drop Size at a Drop Viscosity of 24.0 Centipoises.

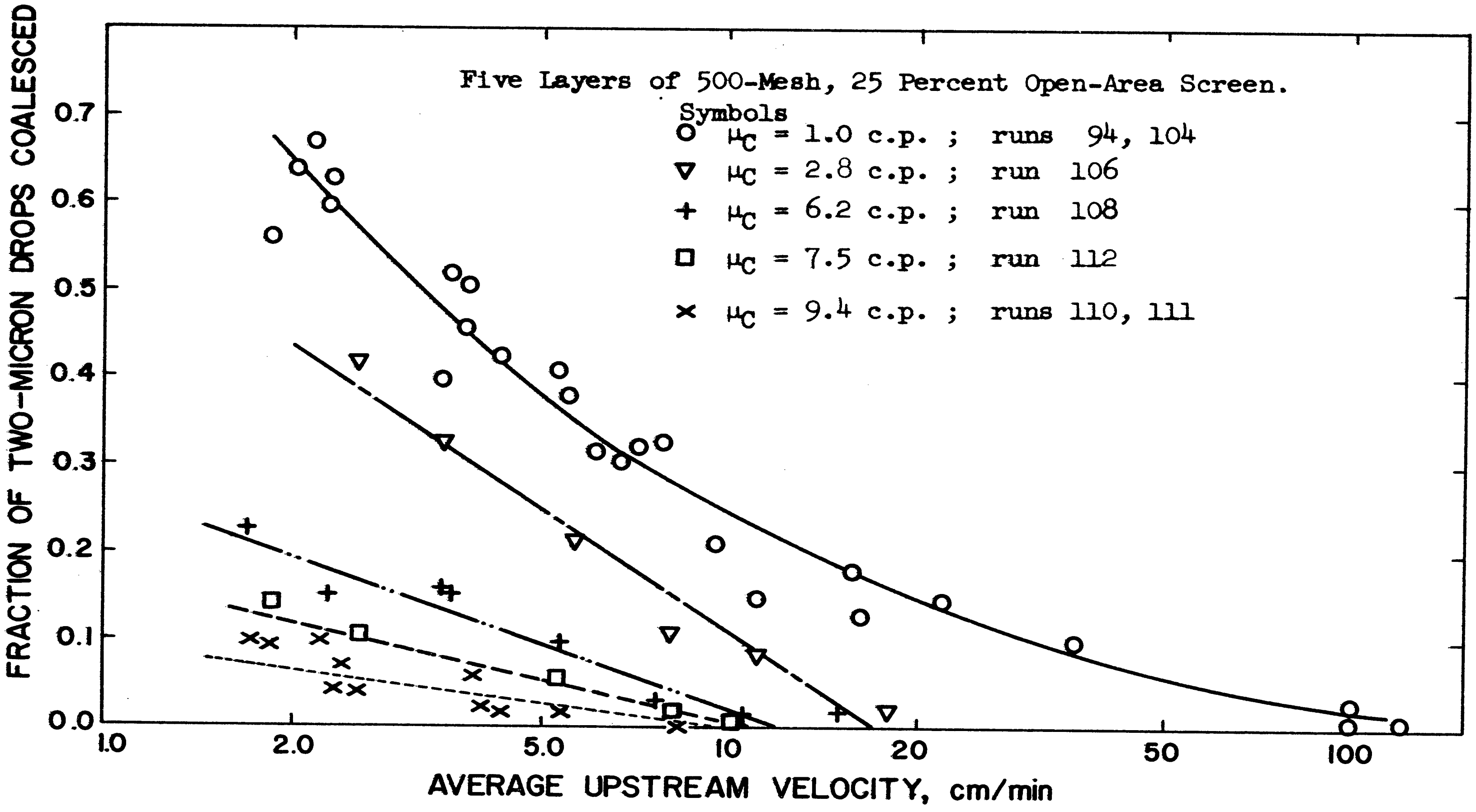

Correlation

—— μ_C = 1.0 c.p. $f = -.09 + 1.046\, U_\infty^{-.5}$; Standard error = .046

— — — μ_C = 2.8 d.p. $f = .58 - .204 \ln U_\infty$; Standard error = .026

—··— μ_C = 6.2 c.p. $f = .248 - .108 \ln U_\infty$; Standard error = .033

– – – μ_C = 7.5 c.p. $f = .17 - .074 \ln U_\infty$; Standard error = .011

------ μ_C = 9.4 c.p. $f = .095 - .043 \ln U_\infty$; Standard error = .022

Figure 49. Coalescence in High Viscosity Systems.

to the product of upstream velocity and continuum viscosity raised to a negative power. The following form of correlation was sutiable:

$$f = A + B(U_\infty \mu_C)^{-0.5} \tag{93}$$

The constant, A , had a value of approximately -0.1. This constant accounts for the cessation of coalescence which was observed in this experiment and elsewhere.(58) Figure 50 is a log-log plot of $f + 0.1$ versus $(U_\infty \mu_C)^{-0.5}$ showing the compatibility of the data when correlated in this manner.

Effect of Interfacial Tension

According to the argument of the Theory section, the direct effect of interfacial tension is expected to be small. Interfacial tension is a measure of the similarity of the liquids. The surface of the solid could be adversely affected if the continuum were similar to the dispersed phase.

Systems of low interfacial tension were prepared by adding alcohols to the water-hydrocarbon binary. The water phase was saturated with the alcohol. The runs with low interfacial systems were characterized by an erratic coalescence behavior. The screens appeared to decrease in activity with prolonged exposure. Because of the apparent desorption of the octadecylamine, only the coalescence measurements of the first several traverses in each run were considered to be representative. The initial coalescence data are

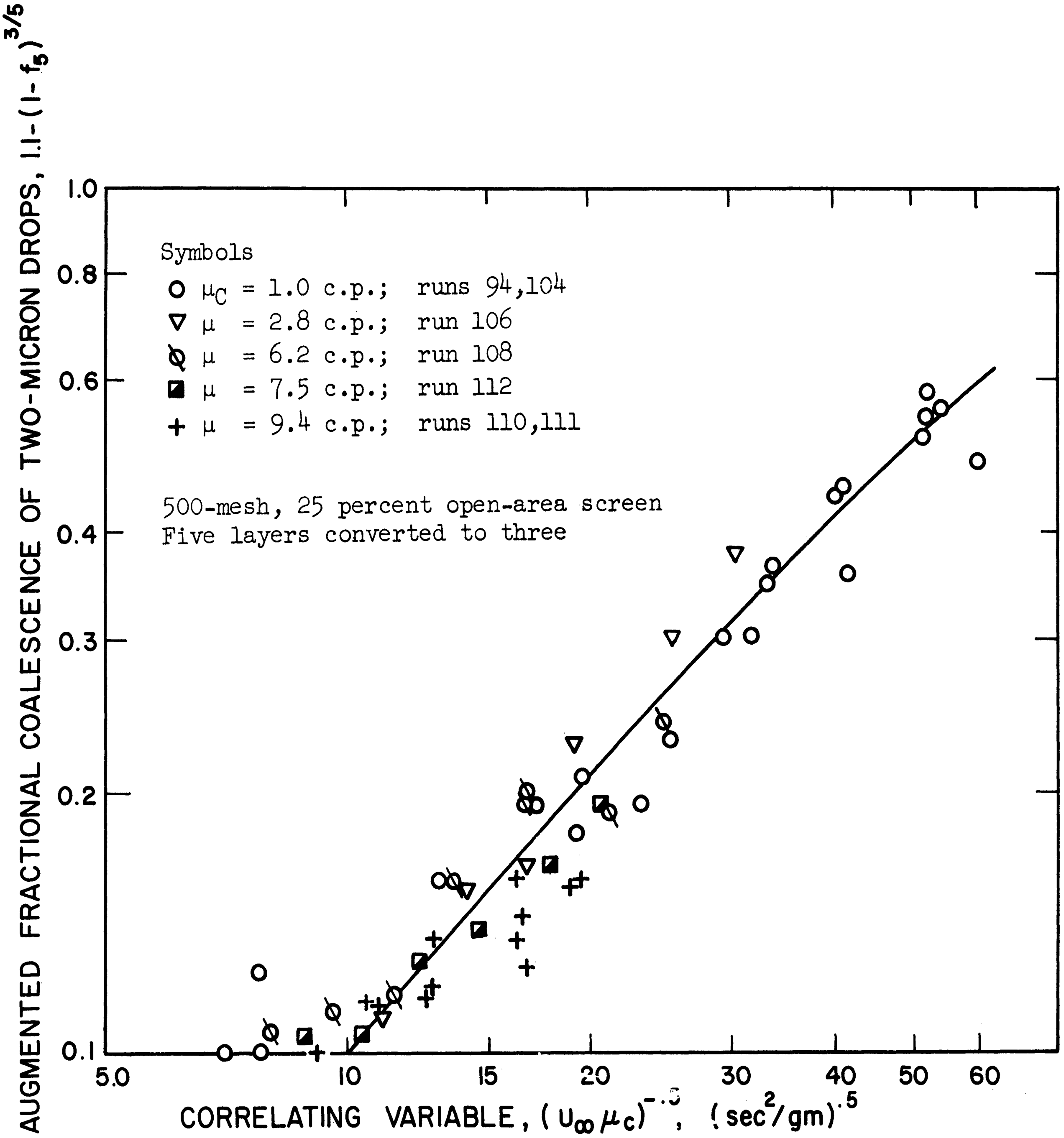

Correlation

——— $1.1-(1-f_5)^{3/5} = -.004 + .0104(U_{\infty}\mu_C)^{-.5}$; Standard
Standard error = .031

Figure 50. Joint Correlation of Coalescence in High Viscosity Systems.

plotted in Figure 51. The initial data at 11.1 dynes per centimeter are not appreciably different from the base run at about 50 dynes per centimeter. The decline in coalescence accompanying a further decrease in interfacial tension could have been caused by a faster rate of desorption. At 2.7 dynes per centimeter, the screens are totally ineffective. Figure 52 shows the detrimental effect of the prolonged exposure of the screens to the cyclohexanol-containing continuum in one run at 11 dynes per centimeter. The lower points are for a second sequence of velocity traverses after the first were completed.

The initial net coalescence in the system at 11.1 dynes per centimeter suggests that, were there no desorption, the performance of the screens would have been comparable with their performance at 50 dynes per centimeter. A coalescing medium having an inherent affinity for the material being coalesced would be preferred over a medium with an artificial affinity.

Since the effect of interfacial tension on coalescence was unclear, no correlation between interfacial tension and coalescence was attempted. All other parts of the experiment were performed with liquid-liquid systems having an interfacial tension above 30 dynes per centimeter. No deactivation of the filaments was noted for these systems.

Effect of Screen Geometry

Screen geometry was expected to be important because it governs the nature of the flow in the vicinity of the coalescing surface and determines the fraction of drops in the flow which come

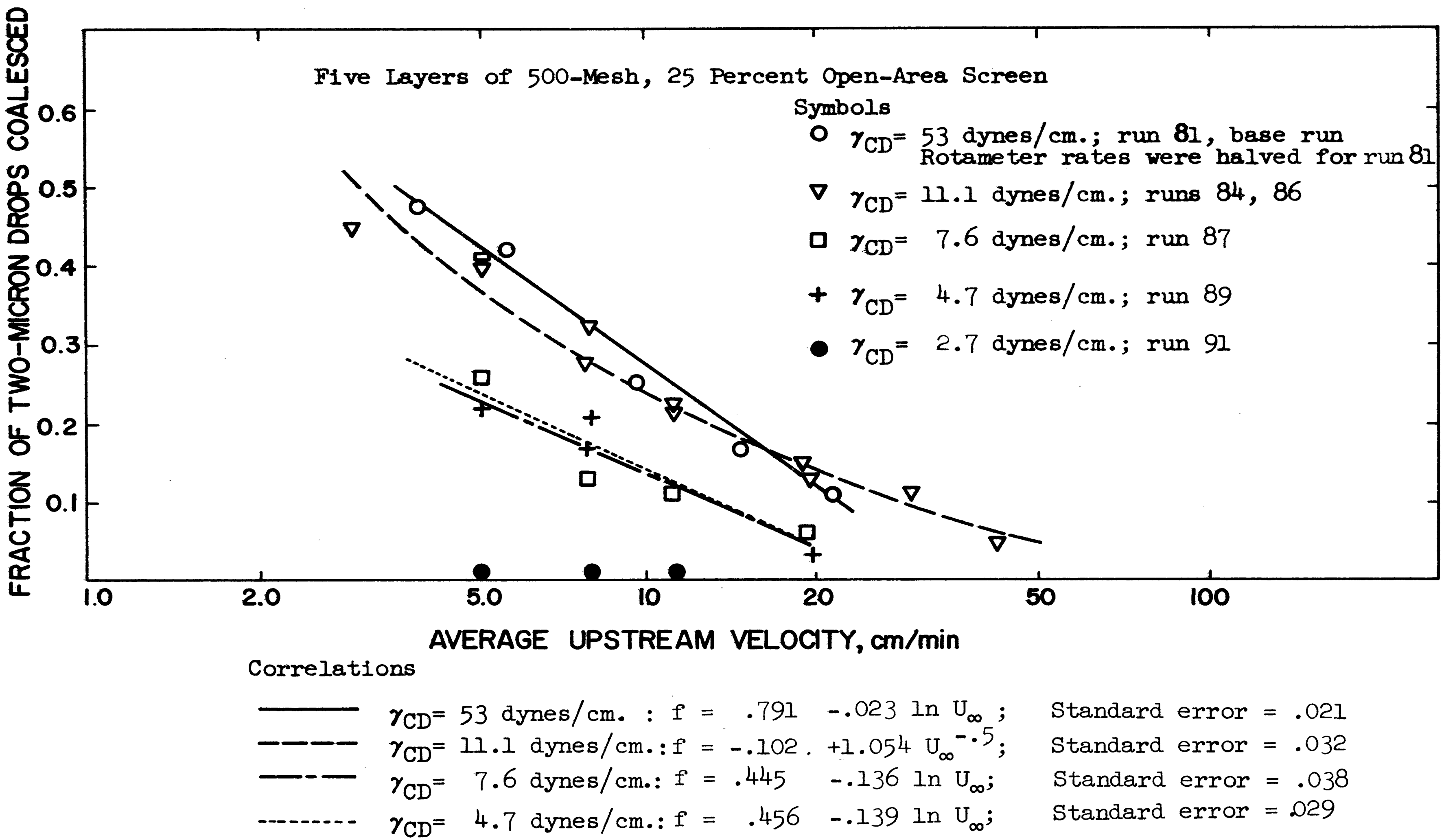

Correlations

γ_{CD}= 53 dynes/cm. : f = .791 −.023 ln U_∞ ; Standard error = .021

γ_{CD}= 11.1 dynes/cm.: f = −.102 , +1.054 $U_\infty^{-.5}$; Standard error = .032

γ_{CD}= 7.6 dynes/cm.: f = .445 −.136 ln U_∞; Standard error = .038

γ_{CD}= 4.7 dynes/cm.: f = .456 −.139 ln U_∞; Standard error = .029

Figure 51. Effect of Interfacial Tension on Coalescence.

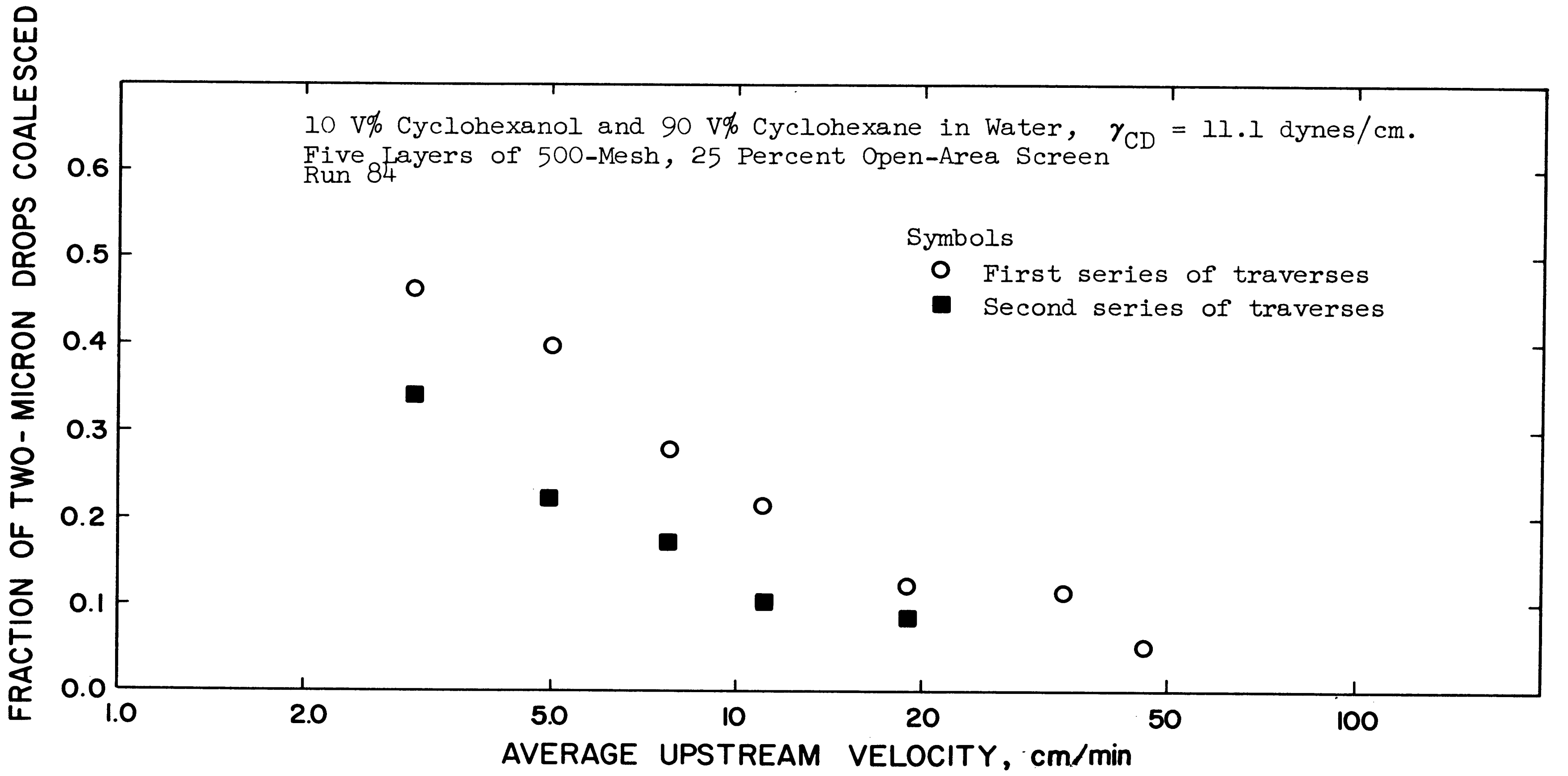

Figure 52. Decline in Performance of Screen After Extended Exposure in Low Interfacial Tension.

within a drop radius of the surface. It was of interest to distinguish the effects of filament width, interstitial distance and drop size. Six screens of varying dimensions were used for this purpose. The performance comparisons were based on data of the cyclohexane-in-water system and of three layers of screen. Whenever the number of layers differed, Equation (92) was used to bring the fractional coalescence to the level of three layers. No interaction between the supports and the coalescing screens was expected. Because of their 50 percent open area, the supports probably blocked off about half of the interstices in the coalescing screens and doubled the flow velocity through the remainder.

The data for the six screens and the correlations are shown in Figures 44, 46 and 53 through 56. The comparative narrowness of the scatter for the five screens for which duplicate runs were made attests to the reproducibility of the surface. The data for the 1500-, 1000- and 500-mesh, 25 percent open-area screens and for the 400-mesh, 26 percent open-area screen were obtained during the same series of runs within a period of one week. The screen surfaces were controlled by keeping the octadecylamine solutions saturated. The data for the 750-mesh and the 400-mesh, 16 percent open-area screen were obtained at various other times. For these two screens, the rotameter was used to measure the rate of flow. The data for the 750-mesh screen were gratifying. Although the screen was used in a variety of ambient conditions, the screen performance remained uniform. It is likely that the treating solution for the

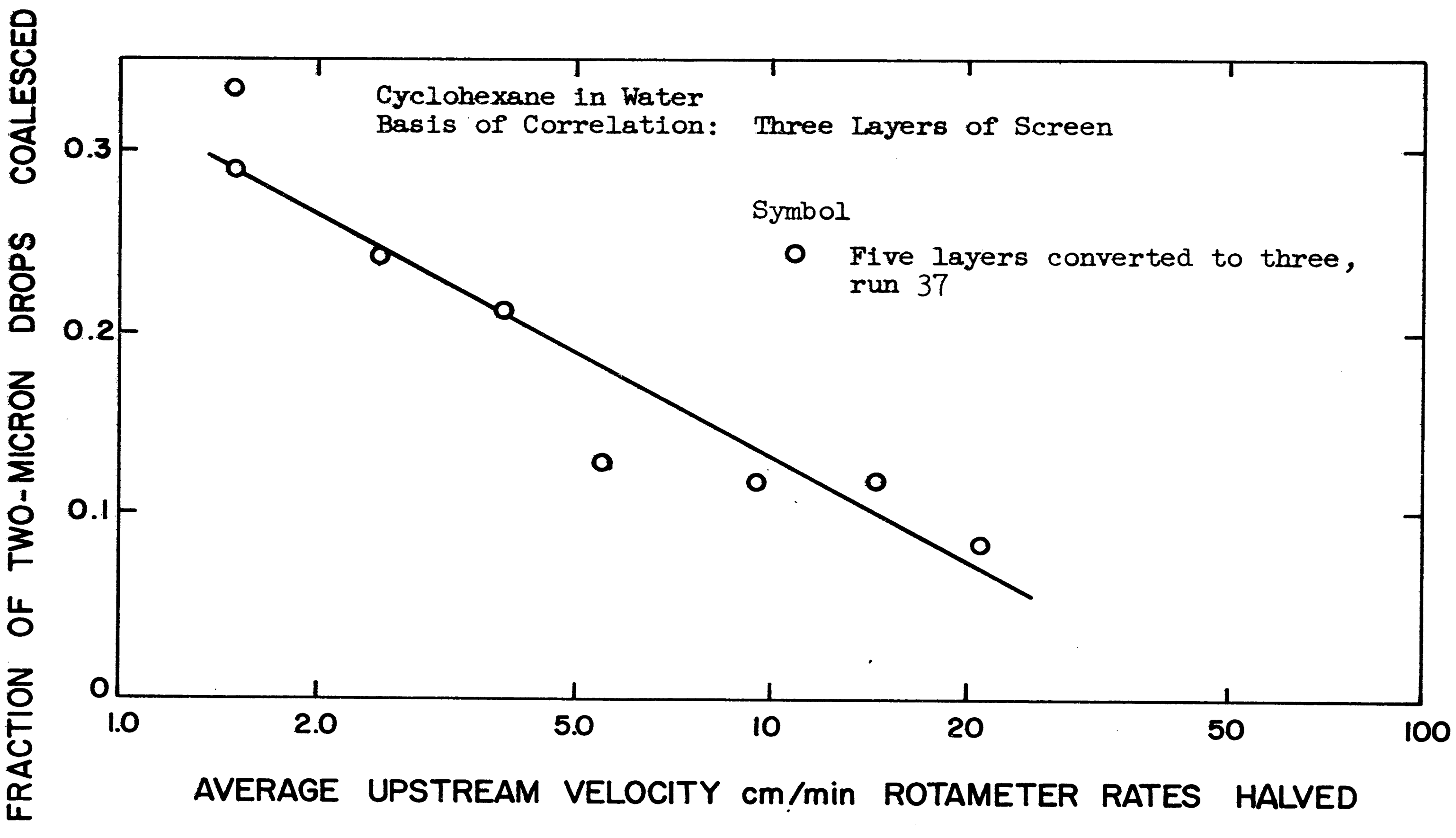

Correlation

——— $1-(1-f_5)^{3/5} = .324-.151 \ln U_{\infty}$; Standard error = .031

Figure 53. Coalescence on 400-Mesh, 16 Percent Open-Area Screen.

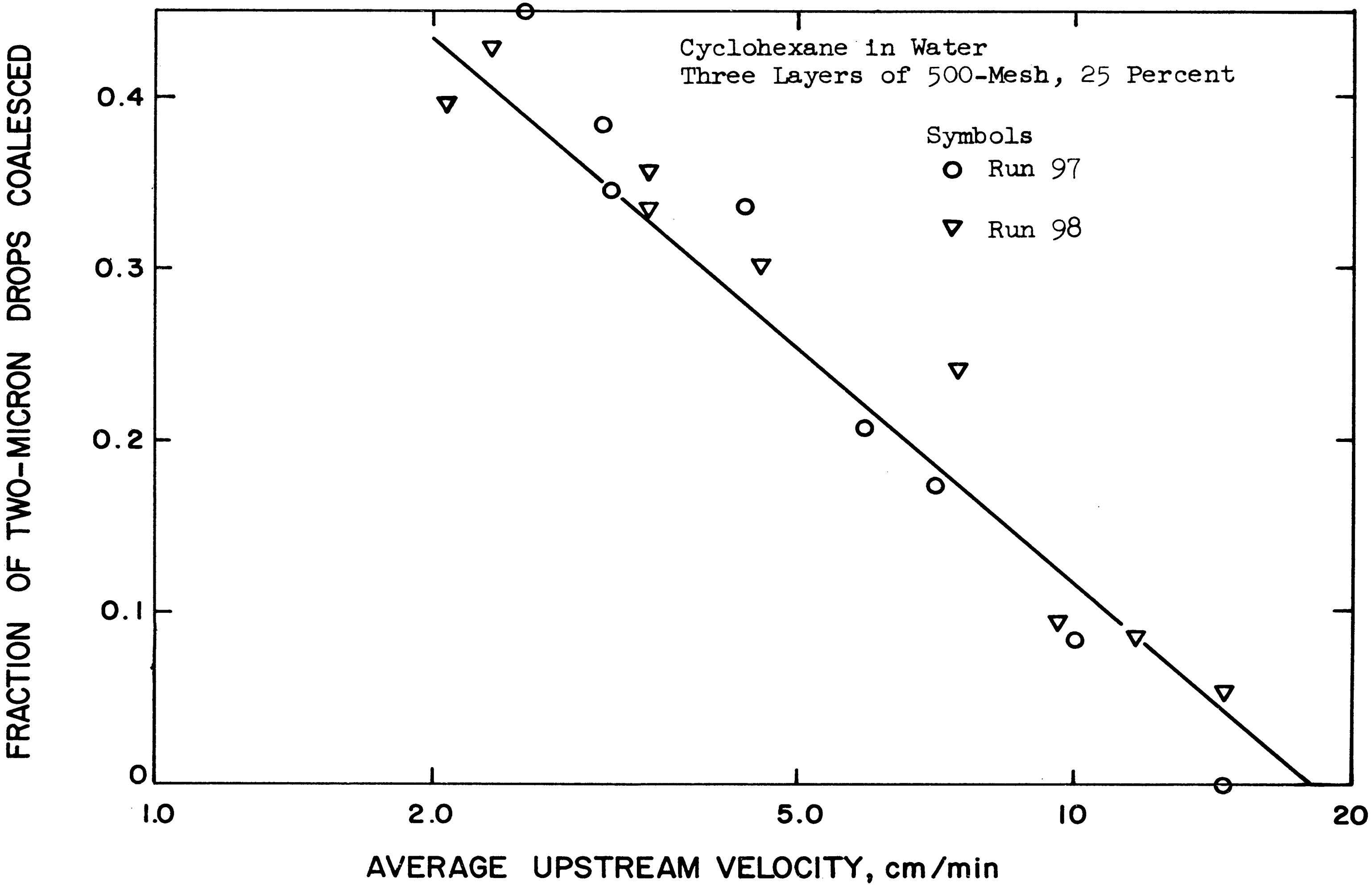

Correlation

——— $f = .569-.198 \ln U_{\infty}$; Standard error = .040

Figure 54. Coalescence on 500-Mesh, 25 Percent Open-Area Screen.

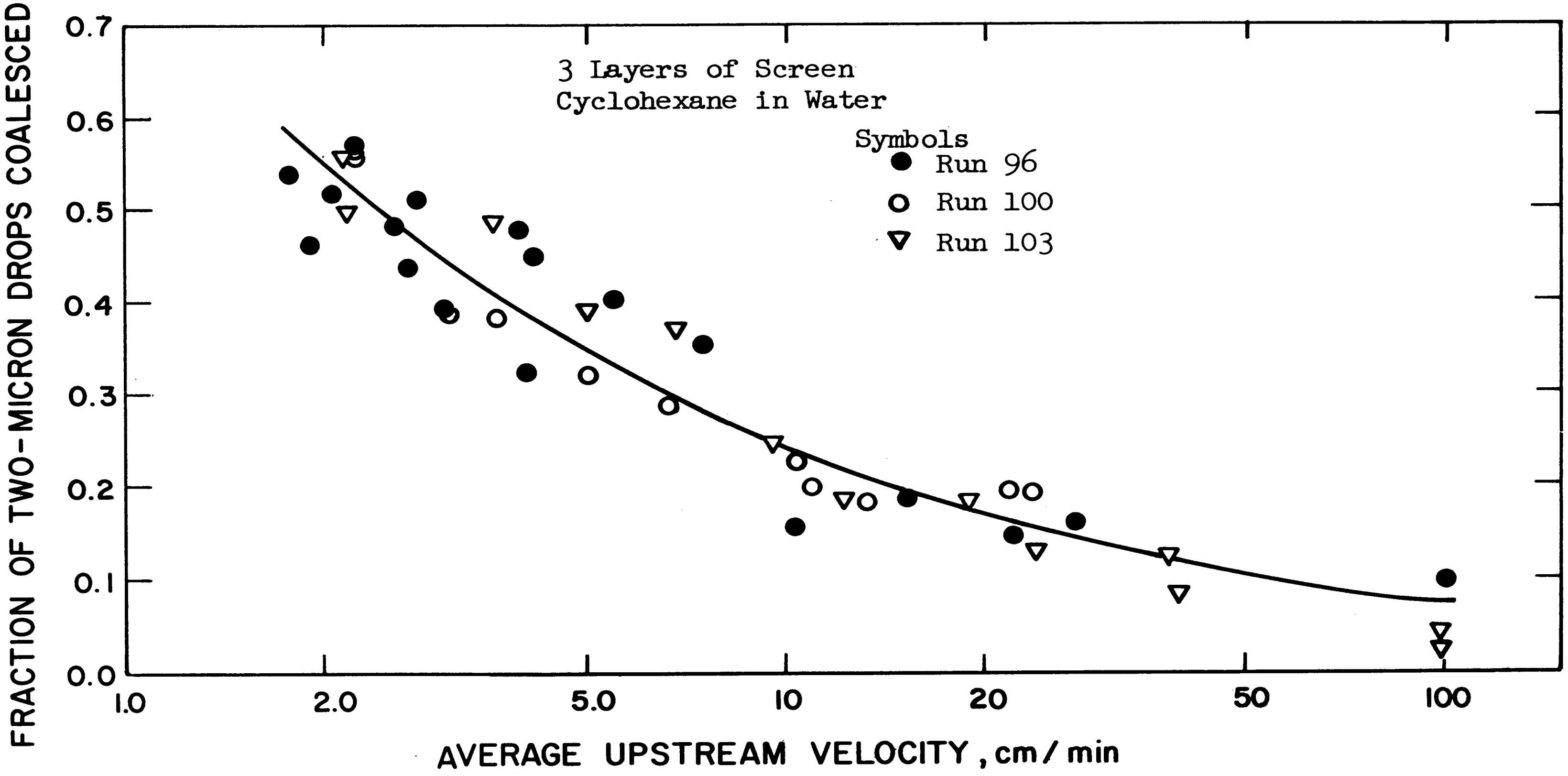

Correlation

——— $f = -.007 + .790\ U_{\infty}^{-.5}$; Standard error = .047

Figure 55. Coalescence on 1000-Mesh, 25 Percent Open-Area Screen.

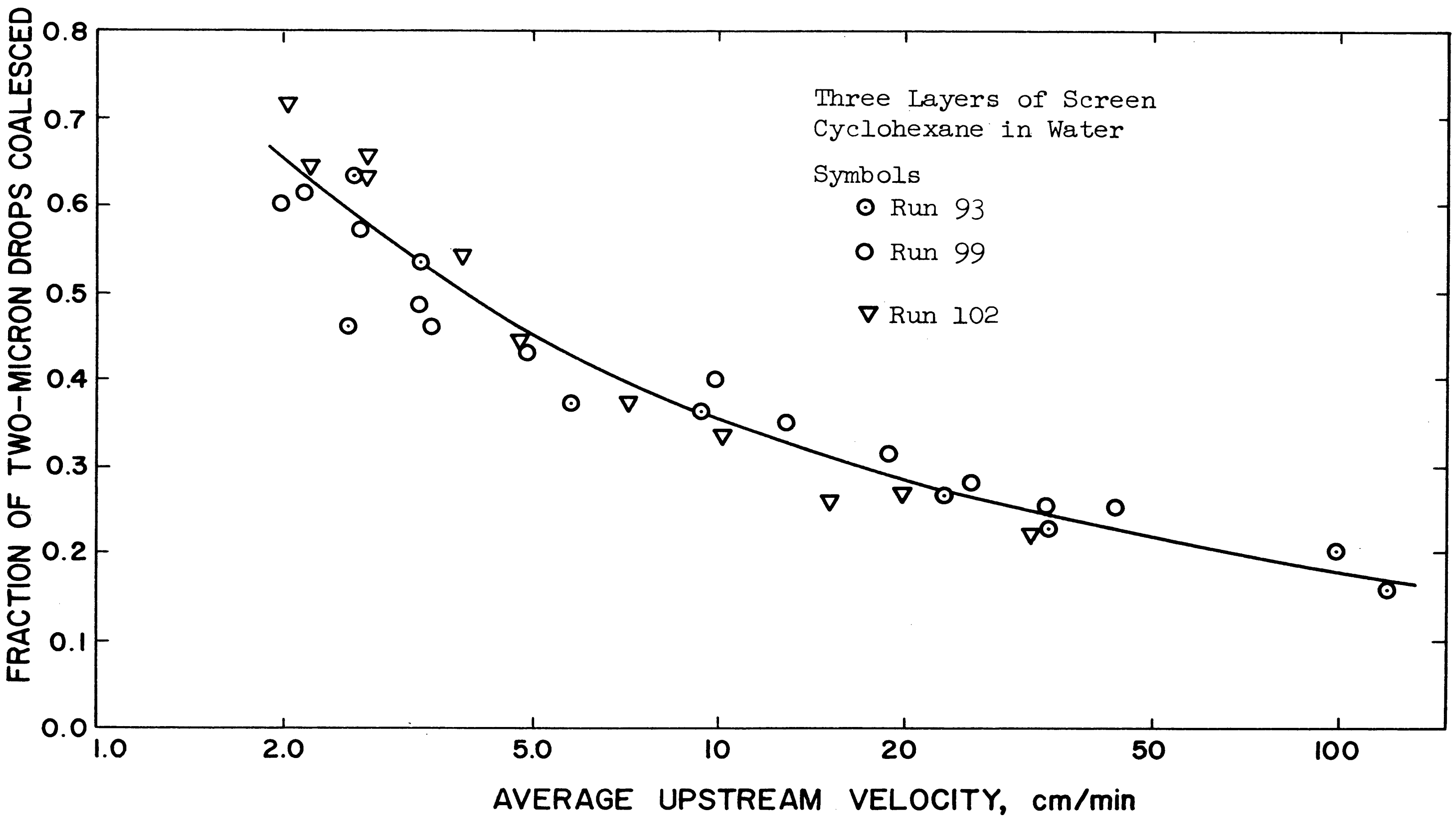

Correlation

——— $f = .108 + .772\ U_{\infty}^{-.5}$; Standard error = .044

Figure 56. Coalescence on 1500-Mesh, 25 Percent Open-Area Screen.

750-mesh screen was fully saturated with amine. If the solution were not saturated, an effect of temperature on screen performance would have appeared. Only one run was acceptable for the 400-mesh, 16 percent open-area screen. Since there was no check on surface uniformity, these data were included for visual comparison but were not inserted in the overall correlation of the effect of screen geometry. A comparison of the figures shows that coalescence on the finer screens was more complete and seems to have continued to higher rates of flow. This indicates the importance of the relation between drop size and screen dimensions.

DATA CORRELATION

The significant changes in the net fractional coalescence of the two-micron drops with changes in screen geometry and continuum viscosity create a need for a cross correlation. The dimensionless groups used in the correlation of screen performance were selected with regard to dimensional analysis and the projections of theory. The pertinent variables were considered to be: d_F , d_I , d_P , μ_D , μ_C , ρ_D , ρ_C , g , U_∞ and z , where z is the thickness of the screen in the direction of flow. At a fixed temperature, the Brownian diffusion coefficient was a function of these variables. Other pertinent variables which were not directly measurable were γ^* and a variable related to the force necessary for the thinning and rupture of the continuum film between an intercepted drop and the filament. The force embraces the short range forces of molecular attraction between the drop and the filament and the relation between the force of molecular motion and retarding forces near the liquid-liquid interface. From the discussion of film thinning, the normal forces, when divided by the projected area, are proportional to $1/d_P$. The force-over-area ratio is equivalent to a normal stress, σ_n . Removal of the $1/d_P$ yields dimensions of force per unit length. The presence of the film thinning stress would be inferred whenever a group in the correlation had the units of force per unit length and had d_P in the denominator. The required form of the film thinning stress would be $\sigma_n L$, where L is a length not related to drop diameter. The γ^* is the lateral force of adhesion of the dispersed phase which acts on the liquid-liquid-solid boundary. The presence of γ^* would be indicated whenever a correlating group had the units of force per unit length.

The dimensions indicative of γ^* and $\sigma_n L$ are identical. Since it was not possible to vary d_P , a clear distinction between the importance of film thinning and adhesion cannot be gained from the appearance of the dimensional terms in a correlation.

The variables which were considered unimportant over their range of variation were drop concentration, shape of the filament cross section and pressure level. Since the systems for which the correlation was developed had interfacial tensions in excess of 30 dynes per centimeter, interfacial tension was not included.

The twelve pertinent variables generate nine dimensionless groups. Three are ratios of dimensions: d_F/d_I , d_P/d_I , and z/d_F . Two involve physical properties: ρ_D/ρ_C , and μ_D/μ_C . Two others are the modified intertial parameter, $\left(\frac{\rho_C d_P^2 U_o}{\pi \mu_C d_I}\right)^{1/2}$, and the drag, $\frac{1}{18} \frac{|\rho_D - \rho_C| g d_P^2}{U_o \mu_C}$. For the square interstices of the screens and the expected blockage of 50 percent of the interstices by the supports, the interstitial velocity was computed as $2(1 + d_F/d_I)^2 U_\infty$. The film thinning group has the form $\sigma_n L d_F/U_o \mu_C$, where d_F/U_o is related to the time of contact between the drop and the filament. The final group is the ratio of the forces of adhesion to the shear stress in the interstice, $\gamma^* d_I/U_o d_F \mu_C$.

The film thinning group is similar in form to the Brownian diffusion group, Equation (47). The film thinning group is considered to include the effect of Brownian diffusion, since the dimensional analysis does not permit a distinction.

Since the term $(U_\infty \mu_C)^{-0.5}$ correlated the fractional coalescence data for the elevated continuum viscosity runs, it appeared that a composite correlation could be formed if $U_\infty^{-0.5}$ were important in aligning the fractional coalescence versus velocity relations of the various screens. One method of alignment was to cause the various correlations to be parallel and to find a parametric relation between them. A function of d_I was desirable for the parameter because it would indicate the presence of the inertial parameter, d_P/d_I, the interception parameter should have been responsible for the differences between the screens. Following this reasoning, the best correlation was:

$$f = -0.25 + 2.17\ (d_I/U_o d_F)^{0.5} + 3.10/d_I \qquad (94)$$

where U_O is in centimeters per minute and d_I is in microns. Figure 57 compares Equation (94) with the data of the various screens. The data for the 500-mesh screen are somewhat above their predicted parametric line while the data for the 400-mesh, 26 percent open-area screen are below their predicted line. The seven points for the 400-mesh, 16 percent open-area screen are out of place at all but the lowest velocity. The runs at an elevated continuum viscosity could be successfully included in a correlation of this type.

Equation (94) has several disadvantages. If d_I were less than 12 microns, the third term on the right would exceed the constant and coalescence would be predicted at an infinite velocity. When the second term is made dimensionless by forming the group, $\gamma^* d_I / U_O d_F \mu_C$, the second term does not vanish as the drop size goes to zero. These defects show that Equation (94) would be strictly limited to the experimental range of variables. In addition, the effect of d_I in the third term on the right is contrary to the effect of d_I in the second term. An excess of correlating terms is indicated.

A correlation which brought the data for the various screens into a single line was tried. The term $(U_O d_F)^{-0.5}$ was used. Figure 58 is a log-log plot of $f_3 + 0.1$ versus $(U_O d_F)^{-0.5}$ for the six types of screen. It is the sequel of Figure 50 for the fractional coalescence at elevated continuum viscosities. At high values of the correlating group, the data seem to converge to a single line.

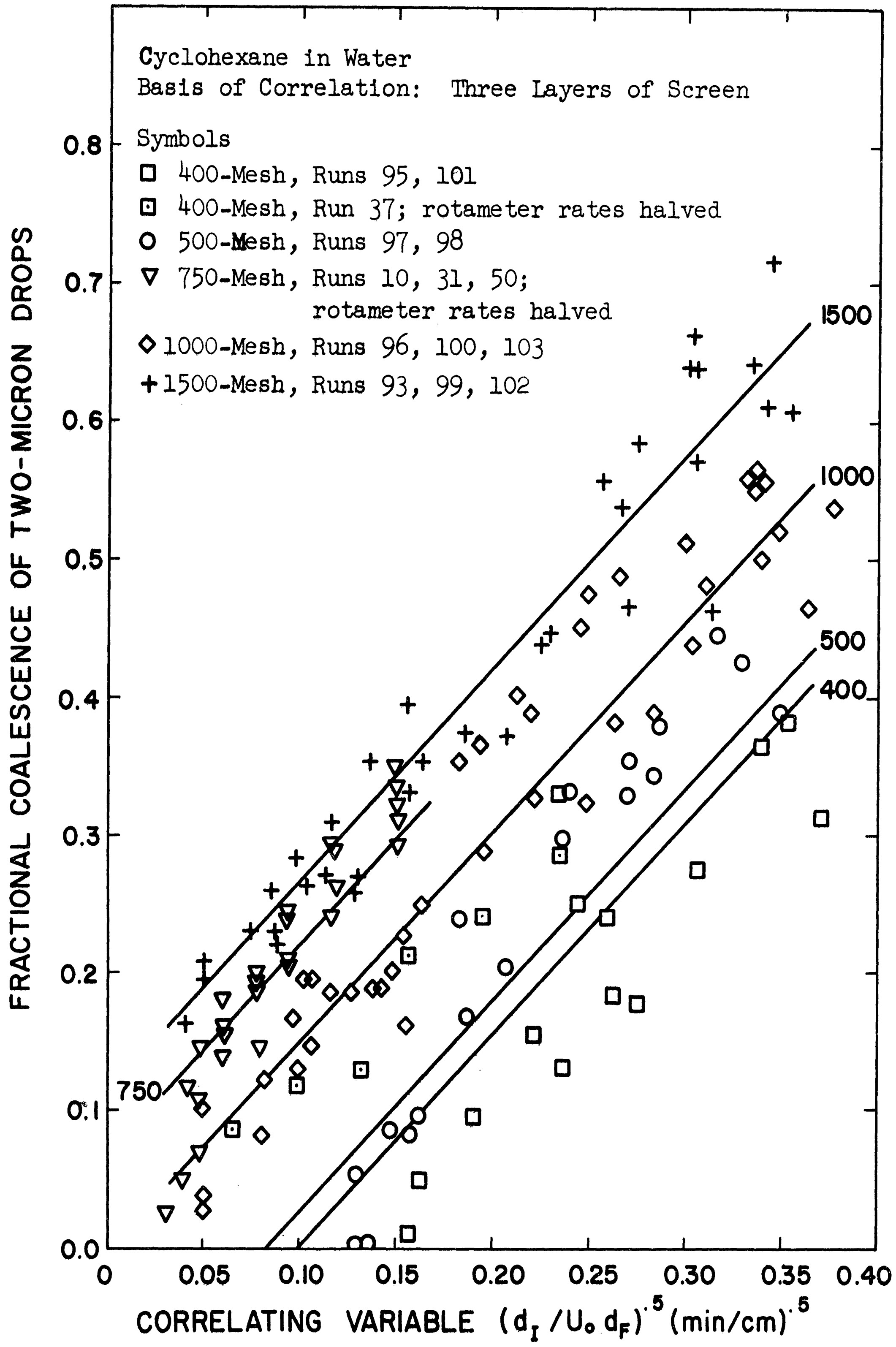

Correlation

——— $f = -.25 + 2.17\,(d_I/U_0 d_F)^{.5} + 3.10(1/d_I)$

Standard error = .049

Figure 57. Prediction of Effect of Screen Geometry by Two-Variable Correlation.

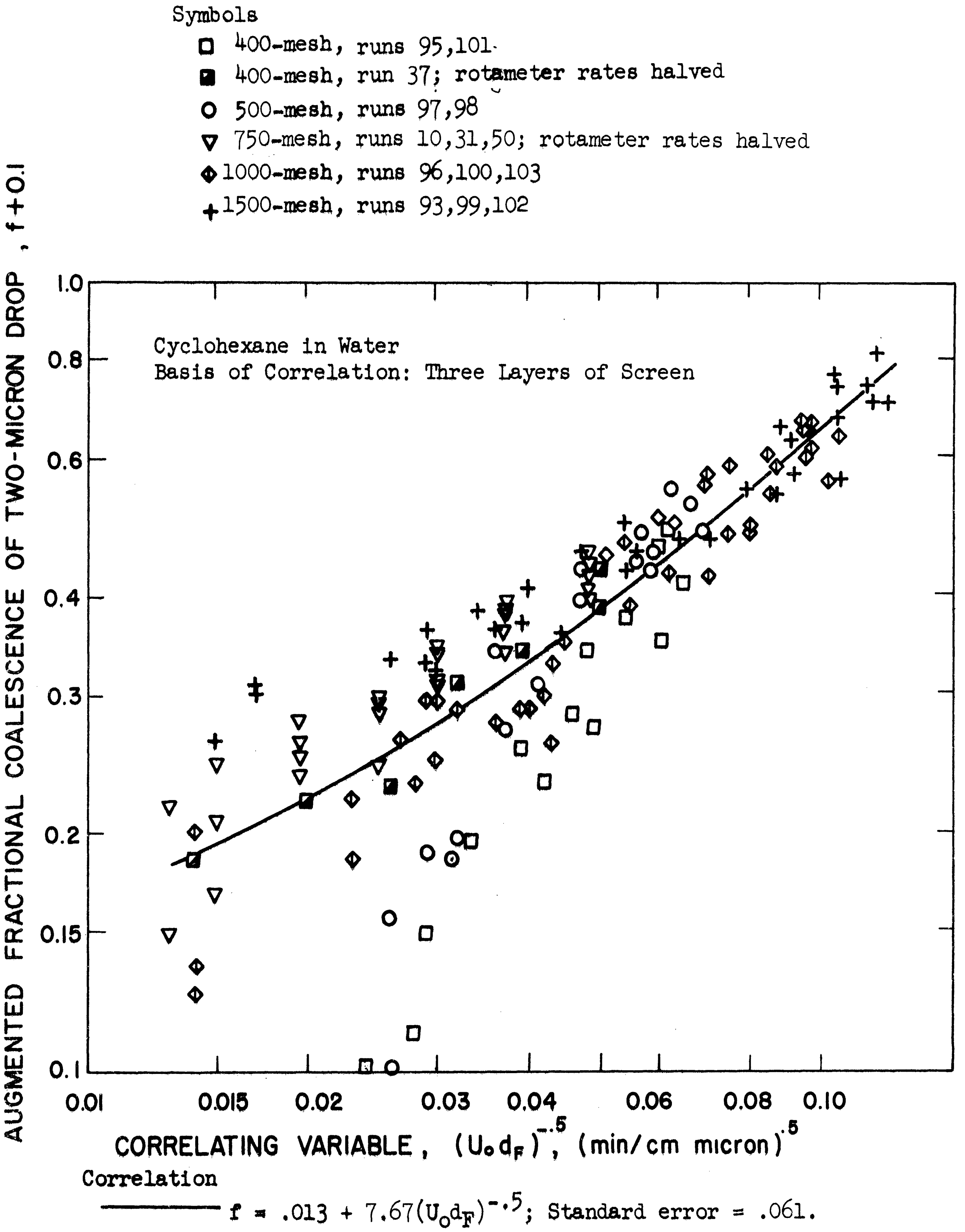

Figure 58. Prediction of Effect of Screen Geometry by Single-Variable Correlation.

At low values the screens diverge. Interstitial distance appears to be significant at low values of $(U_O d_F)^{-0.5}$. However, where $(U_O d_F)^{-0.5}$ was low, the relative and absolute errors of the measurements were high. These errors are discussed in a subsequent section. In view of the error, no terms were added to predict the divergence. The tendency to diverge is emphasized by the log-log plot.

The data of Figures 50 and 58 were combined in a single correlation. The term, $U_O d_F \mu_C$, raised to a negative power close to -0.5, was used as the correlating variable. The best correlation for the combined effects of screen geometry and elevated continuum viscosity was:

$$f = -0.089 + 0.168(U_O d_F \mu_C)^{-0.4} \qquad (95)$$

In Equation (95), U_O was in centimeters per second, d_F in microns and μ_C in poises. The composite data are plotted on cartesian coordinates against $(U_O d_F \mu_C)^{-0.4}$, Figure 59. Equation (95) is specific to two-micron drops. Because of the variation in the ratios d_P/d_I and d_P/d_F in the experiment, Equation (95) can be generalized to other drops sizes with these groups. Since coalescence was inversely related to filament size, the results support a relation between f and d_P/d_F or d_P/d_I. Comparison of the usual computed distribution for the feed dispersion with the distributions computed from Rayleigh theory for specified particle sizes suggests that the three-micron drop is the most representative single size for the dispersions. Assuming that the feed comprised only three-micron drops, the effect of d_P/d_I was formally introduced by multiplying the term within the brackets in

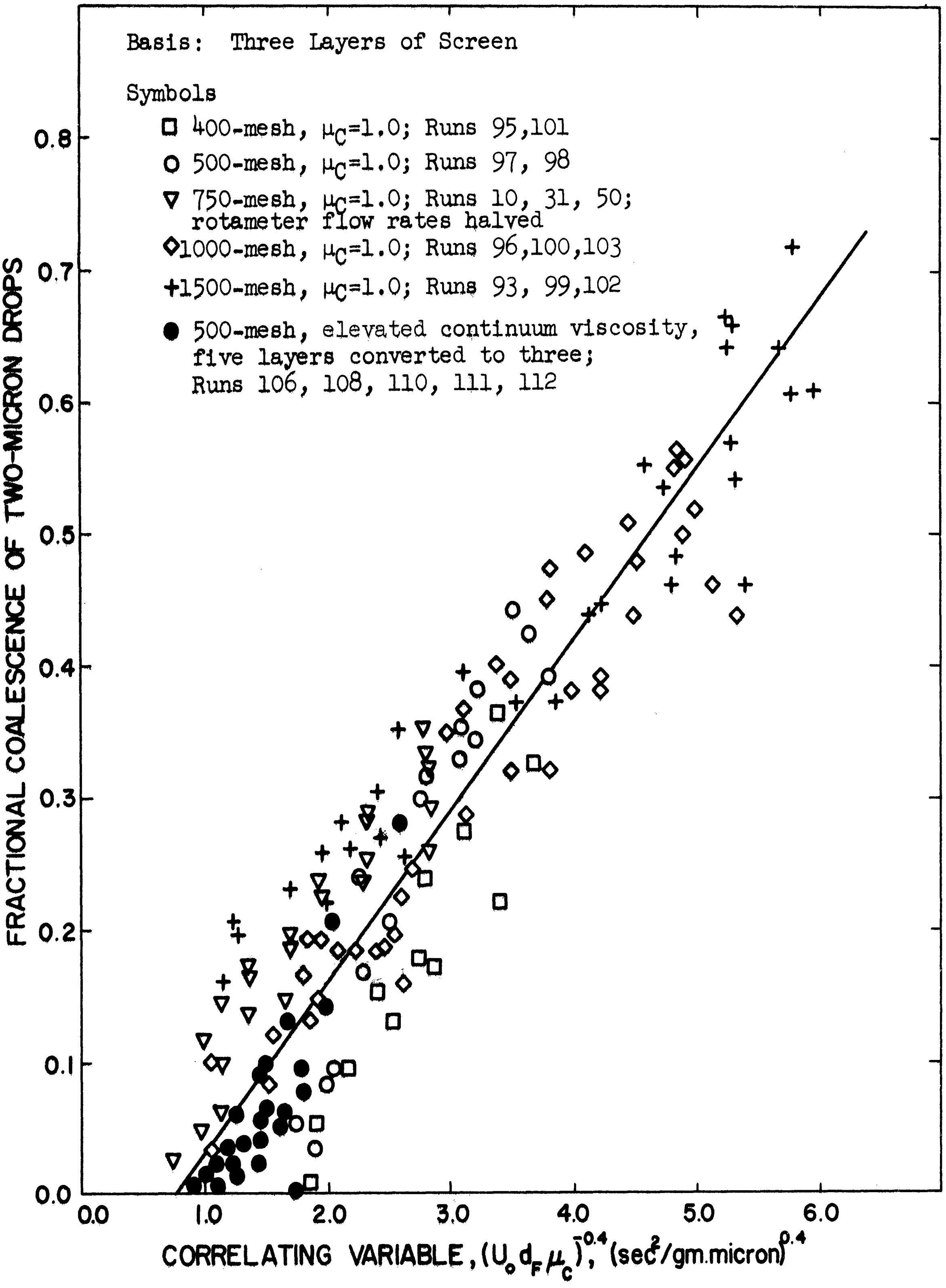

Correlation

———— $f = -.089 + .168(U_0 d_F \mu_C)^{-.4}$; Standard error = .057

Figure 59. Prediction of Effect of Screen Geometry and Continuum Viscosity by Single-Variable Correlation.

Equation (95) by $d_P/3$ microns and by d_I/d_I . The resulting expression was:

$$f = -0.089 + (0.0039\ d_I/U_o\mu_C d_F)^{0.4}\ (d_P/d_I)^{0.4} \qquad (96)$$

When moved inside the brackets, the coefficient of the second term on the right has dimensions in a convenient form.

Indicated Mechanisms of Coalescence

The coefficient inside the brackets of Equation (96) has the dimensions of dynes per centimeter. Either γ^* or $\sigma_n L$ can be considered proportional to the coefficient and can be introduced in order to yield a dimensionless independent variable. Both γ^* and $\sigma_n L$ should probably be present to complementary powers of 1.0. However, in Rose's work with a variety of fibrous media, wettability was the major variable.(50) Decisive variations in wettability were observed in this work. Since cyclohexane did not spread on an amine treated metal plate immersed in water, adhesion was probably important. Moreover, the association between d_F and the product $U_o\mu_C$ in the independent variable is suggestive of the group relating adhesion and Stokes stresses. When the γ^* is introduced alone in Equation (96), the resulting equation has the following form:

$$f = A + B\left(\frac{\gamma^* d_I}{U_o d_F \mu_C}\right)^{0.4}\left(\frac{d_P}{d_I}\right)^{0.4} \qquad (97)$$

where A and B are a dimensionless constant and coefficient, respectively. Equation (97) explicitly represents adhesion, viscous shear and interception as being important. The significance of interception and viscous shear was demonstrated by the experimental results which led to Equation (95). Over the range of variables studied, the effect of film thinning was not made explicit. However, film thinning was probably one of the factors which caused the usual lack of distinction in the coalescence of drops of different sizes in the computed distributions.

The divergence of the coalescence performance of the various screens from the prediction of Equation (95) at low values of the correlating parameter, $(U_O d_F \mu_C)^{-0.4}$, indicates the presence of inertia. This can be ascertained by computing the modified inertial parameter, β' . The values of β' at the maximum experimental velocities for the 400- and 1500-mesh screens and the three-micron drops were 0.168 and 0.330, respectively. Since 0.125 is regarded as a threshold value for inertia, it is likely that inertial impaction at high flow rates significantly augmented the performance of the screens having the smaller interstices. Inertia would explain the tendency of coalescence on the 1000- and 1500-mesh screens to level off at a non-zero value with an increase in velocity. Unfortunately, the lack of coalescence data at high rates of flow and the larger error of measurement at the accompanying low levels of coalescence prevent a verification of the inertial effect.

Voyutskii *et al.* state that coalescence is affected by the total surface area of the solid medium rather than by interstitial distance.(50,58) This statement can be tested by computing the surface areas of the screens. A screen can be partitioned into a series of equal square cells, each enclosing one interstice. These cells would have the length p_F on a side. The total surface area of each cell comprises the projected filament area on the front and back of the

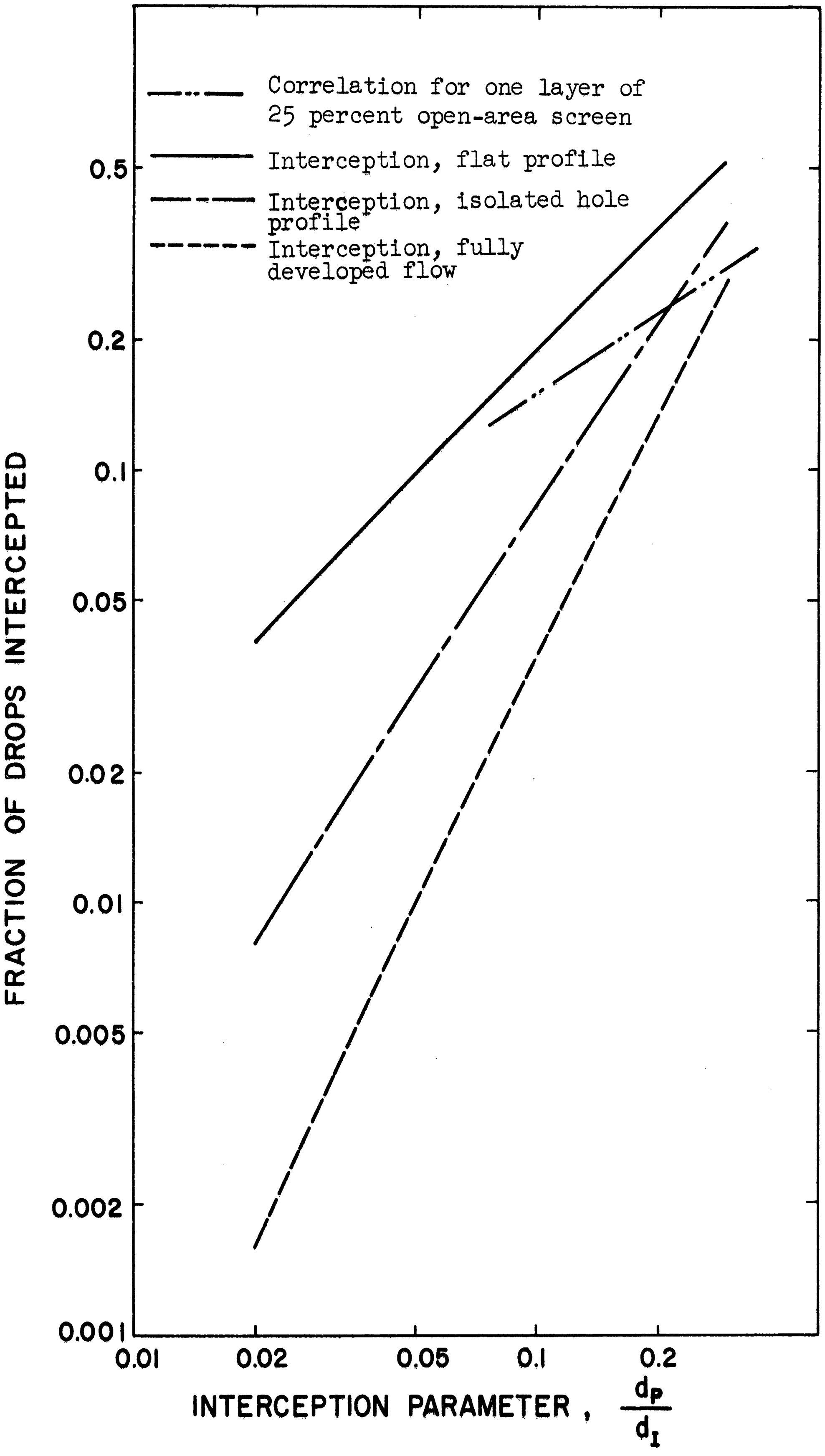

Figure 60. Comparison of Correlation with Interception Theory.

screen and the area in the interstice. The total area is approximately $2(p_F^2 - d_I^2) + 4d_Iz$. The ratio of the surface area of the cell to its projected area is identical with the ratio between the surface area of the screen and its projected area. This ratio is given by:

$$\frac{2(p_F^2-d_I^2) + 4d_Iz}{p_F^2} = 2(1-\epsilon) + 4 \frac{z}{p_F} \epsilon^{0.5} \qquad (98)$$

where ϵ is the percent free area or planar void fraction of the screen. If z/p_F is constant, Equation (98) shows that the total surface area of a screen depends only on the percent free area. In this work, the four screens having 25 percent open area differed substantially in their ability to cause coalescence. It appears that when the percent free area of the fibrous bed is low, the micro-dimensions of the bed are important.

It is of interest to compare the composite correlation in the form of Equation (96) with the prediction of drop interception in a single interstice. Most of the data in the correlation were taken from the four screens which had about 25 percent open area, or for which d_F and d_I were nearly equal. If only these screens are considered, d_I may be substituted for d_F in Equation (96). In this form, the equation may be used to predict the effect of the d_P/d_I on the coalescence of three-micron drops in an aqueous continuum which has the lowest experimental U_o , 16 centimeters per second. The prediction may be converted to a single layer of screen by Equation (92). The results of this calculation are plotted along with the prediction of Equations (33), (34) and (35) for interception theory, Figure 60. The correlation for the assumed representative drop diameter of three microns tends to straddle the curve for drop interception in the velocity profile of an isolated hole. The three-micron average drop diameter and the velocity profile of an isolated hole seem to be the most reasonable assumptions regarding microscopic experimental conditions. The disparity between the slopes of the curves for interception theory and the correlation indicates that the other steps in coalescence varied in importance relative to interception. It is also possible that the interstitial velocity profiles changed over the range of the correlation.

TABLE V

RANGE OF EXPERIMENTAL VARIABLES COVERED BY CORRELATION GIVEN BY EQUATIONS (96) AND (97)

Representative drop diameter, d_P	3 microns
Drop concentration, ϕ	0.01 V%
Screen filament width, d_F	8.5 - 31.4 microns
Screen interstice size, d_I	8.5 - 32.1 microns
Screen thickness, z	2.5 - 19 microns
Ratio of drop size to interstice*, d_P/d_I	0.093 - 0.35
Ratio of filament size to interstice, d_F/d_I	1.0 - 2.46
Average upstream velocity, U_∞	2 - 125 cm./min.
Average interstitial velocity, U_o	16 - 1000 cm./min.
Drop density, ρ_D	0.70 - 0.84 gm./cm.^{3}
Continuum density, ρ_C	0.98 - 1.16 gm./cm.^{3}
Viscosity of drops, μ_D	0.95 centipoise
Viscosity of continuum, μ_C	1.0 - 9.4 centipoise
Interfacial tension, γ_{CD}	33 - 53 dynes/cm.
Drop Reynolds number*, $\rho_D U_o d_P/\mu_C$	0.0007 - 0.40
Continuum Reynolds number, $\rho_C U_o d_I/\mu_C$	0.008 - 5.1
Correlating parameter, $U_o d_F \mu_C$	0.023 - 5.0 gm. micron/sec.^{2}
Inertial parameter*, $(2\rho_C U_o d_P/\pi\mu_C d_I)$	0.011 - 0.330

* Based on d_P of 3 microns

Range of Application of Correlation

Table V gives the range of experimental variable upon which Equations (96) and (97) are based. Equations (96) and (97) predict the coalescence of drops in dilute dispersions in the absence of the production of drops of the same size from the coalesced material. Because the contribution of Brownian motion and inertia become important near the ends of the ranges of the experimental variables, the correlation is largely limited to the experimental range of the product, $U_o d_F \mu_C$, and the ratio d_P/d_I . The upper limit on $U_o d_F \mu_C$ corresponds to the point at which coalescence is predicted to cease. Since the combination of variables differs for the various influential mechanisms, the restrictions on the range of each variable must be examined independently.

The force of adhesion was introduced in Equation (97) because of theoretical and empirical considerations. Although it cannot be measured, its presence emphasizes that a new correlation must be obtained experimentally for each type of filter medium and surface preparation. For a given medium, the correlation predicts the effect of a change of measurable variables over the experimental range.

The correlation is considered to predict the coalescence of drops between two and four microns in diameter. Drops below two microns in diameter are expected to show appreciable Brownian motion at low values of the $U_O \mu_C$ product. At four microns, the film thinning resistance and inertia might appear more strongly than represented by the correlation. The prediction of the correlation becomes poorer at the limiting ratios of d_P/d_I . A variation of d_P appears acceptable only as long as the d_P/d_I ratio is held within the experimental limits. If d_P/d_I grows above 0.35, the flow in the interstice would be noticeably affected by the passage of a drop. If d_P/d_I declines below 0.08, interception is likely to become the dominant factor. Coalescence would probably become related to d_P/d_I according to the prediction of interception for one of the velocity profiles.

The appearance of the filament diameter in the group, $U_o d_F \mu_C$, is a reflection of the importance of the work done by viscous shear on the filament. As long as viscous shear is a controlling factor, the effect of filament size should be correctly represented by the correlation. At low values of $U_o \mu_C$, a large value of d_F would emphasize Brownian diffusion. The d_F should be confined to values below 40 microns. No lower limit is apparent. Although the screens did not have a circular cross section, screen thickness was not a significant variable.

Continuum viscosity primarily reflects the presence of viscous shear. Since viscous shear was a major factor over the range of variables studied, the effect of viscosity should be reliably represented by the correlation over a wide range. There seems to be no upper limit on the variation of viscosity. However, the correlation is not expected to predict the consequences of a reduction of μ_C below the lower end of the range of $U_o d_F \mu_C$ because of the importance of Brownian motion.

The correlation probably gives a moderate representation of the effects of Brownian motion and inertia. Since these effects did not have an equal influence on all of the screens, the correlation gives a good representation of the performance of only the 1000-mesh and perhaps the 500-mesh screens. The 400-mesh screen deviates at high U_o because of little inertia and the 750- and 1500-mesh screens deviate because of considerable inertia. If data were available for them, the 400-, 500- and 750-mesh screens would probably show deviations from the correlation at the upper limit of the variable $(U_O d_F \mu_C)^{-0.4}$ because of Brownian motion. These considerations indicate that the correlation should not be used for interstitial velocities outside of the range of 16 to 800 centimeters per minute. Since the interstitial velocity influences the processes which occur in the vicinity of the screen, the upstream velocity was not considered in the formulation of the correlation.

The modified inertial parameter shows that continuum density is of major importance in determining the appearance of inertial effects. Continuum density was not amenable to experimental variation. In practice, no liquid density term would be needed in a coalescence correlation since most common liquids have a specific gravity close to one. In a liquid medium, the effect of drop inertia cannot be ascertained by varying the drop density.

Drop viscosity caused a slight increase in coalescence over the experimental range. In view of the effect of drop viscosity on the rate of strain, coalescence might increase above the prediction of the correlation for μ_D in excess of 25 centipoise. Coalescence was unaffected by a change in the ratio, μ_D/μ_C, over the range of 0.09 to 24. However, μ_D/μ_C might affect the size of the packets of liquid carried away from the filaments.

The correlation is confined to liquid-liquid systems having interfacial tensions above 30 dynes per centimeter, since the experiment did not give a quantitative indication of the effect of low interfacial tension. The high initial coalescence at 11 dynes per centimeter suggests that the correlation would be valid at this level if the properties of the surface could be maintained.

The cyclohexanol employed for the system at 11 dynes per centimeter was probably oriented at the interface. It has a dielectric constant of 15. The initial coalescence for this system indicates that moderate interfacial orientation does not retard coalescence. The same mechanisms are expected to govern coalescence in water-in-oil systems as in oil-in-water systems. The form of Equations (96) and (97) should be applicable to both kinds of systems.

The presence of the support screens is not considered to have any synergistic or antagonistic effect on the coalescing ability of the fine mesh screen. The supports probably aided in the retention of the coalesced material. The interstice blocking effect was recognized in the computation of the average interstitial velocity.

The range of Reynolds numbers in the tubing upstream from the coalescing filter was between five and 400. It is believed that the length of the upstream section of the filter flange, which was equivalent to 20 tube diameters, was sufficient to diffuse any non-uniformity in the flow resulting from the geometry or an irregularity in the upstream flow channel. At the upper limiting Reynolds number, an irregularity in the flow might have reached the screen. However, the coalescence was low at high upstream Reynolds numbers. If any effect of flow non-uniformity produced a percentage change in coalescence, the change would have a small absolute effect and would not alter the indications of the data. Since the Langmuir relation between coalescence and the number of layers of screen implies an identical flow at each layer of screen, the fact that the Langmuir relation was verified for one layer of screen as well as for multiple layers of screen, within the accuracy of the data, shows that the geometry of the upstream section was not a variable.

The data for the correlation were obtained at a total dispersed phase concentration of 0.01 volume percent or less. The correlations should apply to dispersions in which interactions between drops are minor. A dispersed phase concentration of 0.5 volume percent is perhaps the upper limit of validity. At this concentration, the bulk viscosity would be increased by about one percent by the presence of the drops.(23) The average distance between drop centers would be between four and five diameters.

Application of Correlation to Fibrous Beds

Since the fine-mesh screens preserve the filament and pore features of a fibrous bed, the form of Equations (96) and (97) is considered applicable to fibrous media. The same mechanisms should prevail irrespective of a difference in the projected filament cross sectional area of a given plane. The d_F would be a characteristic dimension of the filament cross section. The d_I can be calculated from the volumetric void fraction of the bed and an assumed alignment of the fibers. The interstitial velocity would be equivalent to the upstream velocity divided by the volumetric void fraction of the bed. Interactions between layers of filaments in a fibrous bed would obscure any bed entry effect. Were the bed uniformly packed, the Langmuir relation, Equation (92), should be applicable in relating coalescence at various bed thicknesses.

ERRORS IN CALCULATED NET FRACTIONAL COALESCENCE

The error in each net fractional coalescence calculation arose from the error in the calculated ratio of drop concentrations in the downstream and upstream cells, from the ratio of detector coefficients, C_E/C_U , and from the error in the correlation of inherent coalescence. The errors in ϕ_{E_i}/ϕ_{U_i} were random from traverse to traverse. Although random from run to run, the error in C_E/C_U biased all the data of a particular run. The error in each inherent coalescence correlation biased all of the data in a particular liquid-liquid system to the same extent.

The errors in the ratios ϕ_{E_i}/ϕ_{U_i} arose from the error in recording the scattering distributions, undetected fluctuations in feed concentrations during the time allowed for the attainment of equilibrium, surging discharge of dispersed material from the screens, partial blockage of screens by accumulations of coalesced material, fog on the windows of the optical cells, and errors in recording the scattered flux. The feed concentration normally changed gradually because of settling and coalescence. Window fog and accumulations of dispersed phase between the screens were minimized by the surge of fast flow between traverses. The departure of $dR(\theta)/d\theta$ from Mie theory was not a factor. For similar concentration distributions, the error in $dR(\theta)/d\theta$ essentially cancelled when the ratio of drop concentration in the upstream and downstream cells was formed. An estimate of the average error in ϕ_{E_i}/ϕ_{U_i} could be obtained from the standard error of the correlations for the system in question.

The source and extent of the error in C_E/C_U were identical with that of recording the distribution of scattered flux. This was three percent per half traverse. Since two half traverses were necessary, the average bias in C_E/C_U was six percent. The average bias in C_E/C_U was considered equivalent to the standard deviation caused by the random error in the measurement of C_E/C_U. When several runs were included in a correlation, several samples of the random error were available. The average bias in C_E/C_U was estimated from the standard deviation of the sample mean, $0.06/(n)^{0.5}$. Since 0.8 was an average value of the product, $(\phi_{E_i}/\phi_{U_i})(C_E/C_U)(1/(1 - f_{s_i}))$, the average bias caused by C_E/C_U was computed as $0.048/(n)^{0.5}$.

The bias in C_E/C_U could be added to the standard error of the inherent coalescence correlation as well as to that of net coalescence. However, this practice was considered to yield an excessive error estimate. The C_E/C_U ratio was measured by performing two half traverses in one detector and the third in the other. The duplicate traverses diminished the average bias of each run from six to about five percent. During each inherent coalescence run, several high velocity traverses were usually made. In these, the drop concentrations were identical in both flow cells. In effect, the high velocity traverses served to check the C_E/C_U . In view of the several assays of C_E/C_U , the possible bias of C_E/C_U in an inherent coalescence run was substantially reduced. It was neglected. The net bias in the inherent coalescence correlation was considered to be equivalent to the standard error of the correlation.

The effect of the variation of C_E/C_U was evident when correlations which were formed from a single run and several runs were compared. The correlations formed from several runs usually had larger standard errors of predicted fractional coalescence. It was possible that slight variations in screen wettability were also a cause of the larger standard errors. The reduction of the bias in C_E/C_U for correlations of several runs partially compensated for the larger standard error.

The total average error in the data points in each correlation was estimated from the sum of the standard error of the net coalescence correlation, the average bias of C_E/C_U and the bias of the inherent coalescence correlation. Table VI shows the calculation of the above sum for each of the correlations discussed. The inherent coalescence data for the low interfacial tension runs were too scarce to yield an adequate measure of the standard error. Since the data were close to those for cyclohexane-in-water with direct flow measurement, the standard error of the later was used. An estimate of the average error of inherent coalescence at a continuum viscosity of 7.5 centipoises was taken from the standard error of the inherent coalescence run at 5.2 centipoises.

Table VI shows that the average of the total error in the data points of most of the correlations was between 0.080 and 0.100. The random error in the measurement of ϕ_{E_i}/ϕ_{U_i} and the bias in C_E/C_U were the major sources of error. The average total error of the data for the composite geometry and the composite geometry and continuum viscosity correlations, Equations (94) and (96), was approximately 0.090. The largest bias of the inherent coalescence correlations for the included systems was used to compute the total error in the composite correlations. The total error in ϕ_E/ϕ_U increased with drop size because the smaller concentration of the larger drops produced a greater sensitivity of the numerical integration to changes in the angular distributions of scattered flux.

The average error in the correlations created a larger relative uncertainty in lower values of fractional coalescence. The absolute error was also larger. The percentage bias in C_E/C_U was applied to a larger value of $1 - f_i$ to yield a larger absolute bias in fractional coalescence. Table VI was based on an average value of $1 - f$ of 0.8. In Figure 39, $1 - f$ varied from 0.3 to 1.0. The absolute bias from the C_E/C_U was correspondingly smaller at the lower limit $(f = 0.7)$ and gave rise to less scatter at high fractional coalescence.

TABLE VI

AVERAGE ERROR OF THE DATA OF COALESCENCE CORRELATIONS

Comparison for which Correlation Was Formed	Description of Correlation		No. of Runs	Standard Error of Net Coalescence	Probable Bias		Estimated Average Error in Net Fractional Coalescence
	Mesh, Open Area, No. of Layers				Inherent Coalescence	C_E/C_U	
Effect of Temperature	500, 25%, 5	21°C	1	.050	.019	.048	.117
	500, 25%, 5	26°C	1	.036	.019	.048	.103
Effect of Drop Size		Drop Size					
	1000, 25%, 3	2 micron	1	.034	.010	.048	.092
	1000, 25%, 3	3 micron	1	.036	.014	.048	.098
	1000, 25%, 3	4 micron	1	.035	.034	.048	.117
Effect of Flow Direction	1000, 25%, 3	horizontal	1	.034	.010	.048	.092
	1000, 25%, 3	down	1	.065	.010	.048	.123
Effect of Number of Layers		conversion					
	1000, 25%, 1	$(1-f)^3$	1	.044	.010	.048	.102
	1000, 25%, 2	$(1-f)^{3/2}$	1	.025	.010	.048	.083
	1000, 25%, 3		1	.034	.010	.048	.092
	1000, 25%, 4	$(1-f)^{3/4}$	1	.044	.010	.048	.102
	750, 9%, 3		1	.025	.010	.048	.083
	750, 9%, 5	$(1-f)^{3/5}$	2	.025	.010	.034	.069
	500, 25%, 3	$(1-f)^{5/3}$	2	.058	.019	.034	.111
	500, 25%, 5		2	.046	.019	.034	.099
	400, 26%, 3		1	.017	.019	.048	.084
	400, 26%, 5	$(1-f)^{3/5}$	1	.017	.019	.048	.084
Elevated Drop Viscosity		μ_D					
	1000, 25%, 3	0.85 c.p.	2	.024	.010	.034	.068
	1000, 25%, 3	1.5 c.p.	1	.031	.010	.048	.089
	1000, 25%, 3	3.0 c.p.	1	.026	.010	.048	.084
	1000, 25%, 3	5.1 c.p.	1	.012	.010	.048	.070
	1000, 25%, 3	10.1 c.p.	1	.016	.010	.048	.074
	1000, 25%, 3	24. c.p.	1	.035	.010	.048	.093
Elevated Continuum Viscosity		μ_C					
	500, 25%, 5	1.0 c.p.	2	.046	.019	.034	.099
	500, 25%, 5	2.8 c.p.	1	.026	.013	.048	.077
	500, 25%, 5	6.2 c.p.	1	.033	.012	.048	.093
	500, 25%, 5	7.5 c.p.	1	.011	.012	.048	.071
	500, 25%, 5	9.4 c.p.	2	.023	.009	.034	.066
Reduction of Interfacial Tension		γ dyne/cm.					
	500, 25%, 5	53.0	1	.021	.010	.048	.079
	500, 25%, 5	11.1	2	.032	.019	.034	.085
	500, 25%, 5	7.6	1	.038	.019	.048	.105
	500, 25%, 5	4.7	1	.029	.019	.048	.096
	500, 25%, 5	2.7	1	.000	.019	.048	.067
Variation of Screen Geometry	400, 26%, 3		2	.038	.019	.034	.091
	400, 16%, 3		1	.031	.010	.048	.089
	500, 25%, 3		2	.040	.019	.034	.093
	750, 9%, 3		3	.026	.010	.028	.064
	1000, 25%, 3		3	.045	.019	.028	.092
	1500, 25%, 3		3	.043	.019	.028	.090
Equation (94)	All geometry data		5	.049	.019	.021	.089
Equation (96)	All geometry and μ_C data		11	.057	.019	.015	.091

CONCLUSIONS

Quantitative measurements of the extent of coalescence of dispersions of organic solvents in water in flow past fine mesh screen have given information on the variables which govern this process. The drop size distribution was fixed and was in the range between two and four microns. The measurements were performed over a range of the dimensional viscous shear parameter, $U_0 d_F \mu_C$, of 0.02 to 5.0 gm. micron/sec.^{2} and a range of the interception parameter, d_P/d_I , of 0.09 to 0.35. The Reynolds number, $\rho_C U_0 d_I/\mu_C$, ranged between 0.008 and 5.1. The factors exerting primary control were the probability of drop interception by the screen filaments, the ability of the captured drops to adhere to the filaments long enough for multiple coalescence to occur and the competing effect of viscous shear. At the highest experimental interstitial velocity, 1000 centimeters per minute, coalescence appeared to increase because of inertial impaction. At the lowest interstitial velocity, Brownian motion might have been important. The film thinning resistance may have become important as the viscous shear in the interstice increased. An increase in drop viscosity up to 24 centipoises gave a slight increase in coalescence probably because of the decreased rate of strain on the coalesced material. The effect of interfacial tension was unclear. Above 30 dynes per centimeter, coalescence was not affected. Below 11 dynes per centimeter, a decline in coalescence appeared to be related to a gradual destruction of the affinity of the filament surface for the drops. Initially, the coalescence at 11 dynes per centimeter was equivalent to that at 50 dynes per centimeter.

The experimental data yielded a correlation which relates the coalescence of the two- to four-micron drops to the dimensional viscous shear parameter. Over the range of experimental variables, the form of the correlation should apply to a variety of fibrous media since the mechanisms of coalescence are identical. Since moderate interfacial polarization appeared to have no effect, the form of the correlation is valid for both oil-in-water and water-in-oil dispersions. The correlation shows the advantage of small filaments and of an increase in temperature when continuum viscosity is high. Langmuir's equation was found satisfactory for relating the performance of differing numbers of layers of screen.

The size distribution of the coalesced material broken off of the filaments was not measured. Visco-elastic and electrical double layer effects were not studied.

Drop concentration distributions within the range of two to four microns were obtained by measuring forward-angle light scattering with moving lens-pinhole detectors. For fixed drop distributions, the measurements accurately followed concentration changes and gave an indication of the drop distribution. The transformation of the patterns of scattered flux to concentration appeared to broaden and smooth the actual distribution. Because of the broadening, the computed point values of the distribution represented the concentration of drops whose diameters were within a range of one to two microns. The diffusing effect could have been reduced by the use of ultraviolet wave lengths in the examination of the two- to four-micron drops.

RECOMMENDATIONS

A factor of economic significance which was not fully clarified is the effect of inertia. If it is possible to cause drops to coalesce by high velocity impaction on filaments, then smaller coalescing vessels could be designed. An exploration of coalescence at high velocity would have merit.

If coalescence on fibrous media is to be effective, the size of the drops shorn off of the filament must be larger than the size of the incident drops. Future studies should include an examination of the breakaway of coalesced material from a filament. An isolated filament could be continuously wetted by a liquid which is immiscible in a second liquid which flows past. The break-off process and the size distribution of the drops which are shorn off could be recorded with microphotography. The coalescence of incident drops on an isolated filament could also be observed. The effects of low interfacial tension, strong interfacial polarization and an electrical double layer could be examined in detail.

APPENDIX A

EQUIPMENT CALIBRATION

It was necessary to calibrate the rotameter and to check the linearity of the response of the photomultiplier.

The linearity of the photomultiplier was tested by measuring its output as a function of the distance from a point source of light to the photocathode. If it were linear, then the response would be proportional to the inverse square of the distance. The housing containing the photomultiplier was mounted at one end of an optical bench in a dark room. Following Clark,(15) a neon glow lamp, type NE-51, was used as the effective point source of radiation. The glow lamp was moved along the optical bench directly opposite the aperture. A constant voltage transformer controlled the lamp voltage. The photomultiplier was excited at the desired voltage level by using the high voltage switch to throttle the output of the high voltage power supply. The photomultiplier output was measured with a Leeds and Northrop type K-3 potentiometer. Prior to the measurements, the most sensitive location of the photocathode was found and the aperture was moved into that position. Test data are given in Table VII and Figure 61. Linearity was checked on the three highest voltage scales or positions of the high voltage switch. The slopes of the log-log plots of output versus distance varied between -1.97 and -2.07. This was taken as proof that the photomultiplier was also linear on the lower voltage scales within the error of the measurements.

The data correlations for the rotameter calibrations are given in Figure 26. The data are repeated here in tabular form. Table VIII gives data for clear water and for a dispersion of 10 per cent cyclohexahol and 90 per cent cyclohexane in saturated water, which had an

TABLE VII

TEST OF PHOTOMULTIPLIER LINEARITY

Distance between Pinhole and Lamp Filament cm.	Net Response with Series Resistance millivolts		
	0 megohms	0.5 megohms	1.2 megohms
104	0.50	--	--
94	0.62	0.12	--
84	0.78	0.15	--
74	0.98	0.19	--
64	1.31	0.25	--
54	1.82	0.36	--
44	2.68	0.52	0.09
39	3.38	--	--
34	4.42	0.90	0.16
29	6.03	1.23	0.22
26	7.52	--	--
24	--	1.80	0.33
23	9.55	--	--
21	11.48	--	--
19	14.07	2.80	0.53
18	15.67	--	--
dark current output	0.26	0.12	0.10

TABLE VIII

ROTAMETER CALIBRATIONS FOR CLEAR WATER AND FOR DISPERSION HAVING LOW INTERFACIAL TENSION

Float Level	Volumetric Water Rate (2 measurements, 24° & 20°C) cm.^{3}/min.	Volumetric Dispersion Rate γ_{CD} = 11.1 dynes/cm., 25°C cm.^{3}/min.
0.4	2.37	2.45
0.5	2.80	--
1.0	4.27	4.03
	3.92	--
1.5	6.08	6.06
2.0	8.65	8.52
	8.69	--
3.0	15.04	14.6
	15.05	--
4.0	23.05	22.8
	22.8	--
5.0	32.8	31.7
	32.35	--
6.0	42.5	41.6
	42.4	--
7.0	53.0	52.7
	53.3	--
8.0	63.8	62.2
	62.7	--
9.0	73.8	72.9
10.0	84.1	83.3
	84.3	--

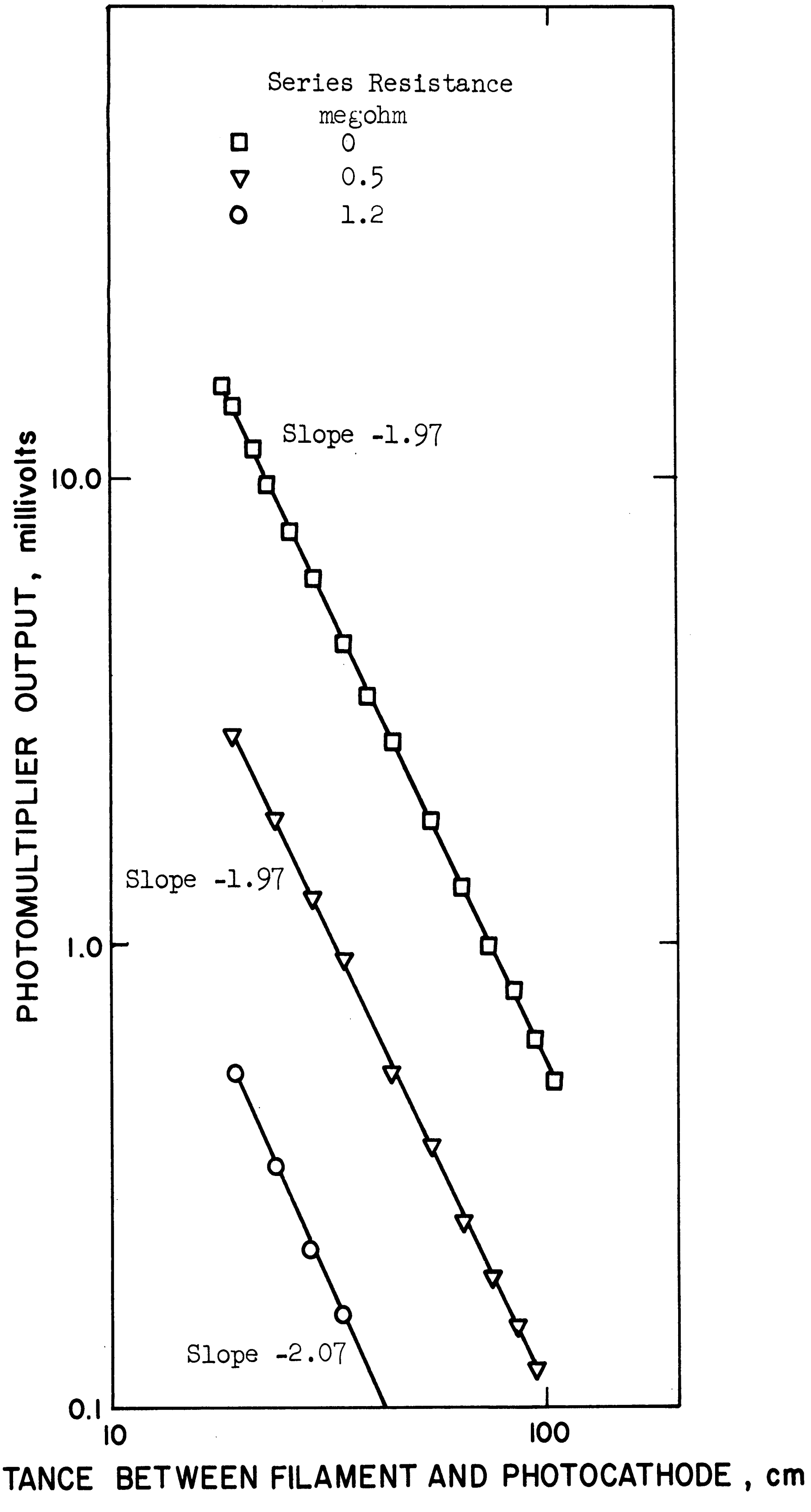

Figure 61. Test of Photomultiplier Linearity.

interfacial tension of 11.1 dynes per centimeter. Table IX presents data of float level versus flow rate for all cyclohexane-in-water runs in which the flow rate was measured directly. The correlation giving the relative error in the flow rate for these runs was:

$$\ln q = 0.517 + 0.414 \ln L + 0.176 L^2 - 0.0204 L^3 \qquad (99)$$

where L is the float level. The standard error in ln q was 0.2127. This gives an estimate of the average relative error in q. The antilog is 1.24 and indicates relative error of 24 per cent.

TABLE IX

ROTAMETER PERFORMANCE DATA FOR CYCLOHEXANE-IN-WATER DISPERSIONS

Temperature: 20° to 26°C

Volumetric Rate cm.^{3}/min.	Float Level	Volumetric Rate cm.^{3}/min.	Float Level	Volumetric Rate cm.^{3}/min.	Float Level
2.00	0.9	8.40	3.5	21.5	5.5
2.63	1.4	10.9	4.1	27.8	6.5
4.60	1.9	1.72	0.7	1.97	1.0
7.40	2.6	2.90	1.5	2.47	1.3
12.1	3.8	1.55	0.7	2.40	1.3
18.3	5.0	1.65	1.1	3.42	1.6
26.6	6.3	2.13	1.4	4.55	2.0
2.08	1.5	2.42	1.4	5.60	2.4
1.40	0.9	3.20	1.8	7.83	3.0
1.70	1.1	4.50	2.0	11.52	3.5
3.0	1.5	1.95	1.0	1.80	1.0
2.75	1.8	6.23	2.5	1.70	1.0
1.65	1.4	8.76	3.1	2.68	1.5
4.83	2.3	1.35	0.7	2.68	1.7
7.50	2.9	1.73	1.0	3.53	2.1
12.4	4.1	2.08	1.3	5.85	3.0
3.43	1.5	3.16	1.9	9.02	3.5
4.21	2.2	2.04	1.5	11.38	4.2
5.81	2.9	3.27	1.9	16.7	5.0
1.50	0.7	4.37	2.2	25.3	5.7
2.20	1.2	5.97	2.8	30.2	6.2
2.83	1.7	8.18	3.3	13.58	4.1
4.14	2.3	12.18	4.0	1.68	0.7
5.93	2.8	17.42	4.8	1.65	0.7
2.33	1.0	2.70	1.4	2.18	1.0
3.69	1.7	2.70	1.2	5.73	2.0
3.83	1.6	7.77	2.5	5.30	2.1
10.88	3.1	7.98	2.5	15.9	4.0
10.25	3.1	22.4	5.1	14.80	4.2
28.9	5.9	20.5	5.4	26.9	6.5
34.9	7.6	1.75	0.7	1.77	0.9
2.43	1.2	2.84	1.6	5.19	2.1
8.28	3.0	10.3	3.8	17.15	4.7
8.72	3.3	10.26	4.0	18.4	4.9
1.67	0.7	1.77	0.7	3.00	1.4

APPENDIX B

CALIBRATION OF LENS-PINHOLE DETECTORS

Calibration of the light scattering detectors was necessary in order to demonstrate their ability to measure the concentration distributions of spherical particles in the micron-size range. Figures 28 and 29 and Table III compare relative concentration distributions of Pyrex spheres with distributions from assays. The supporting data are presented in this appendix. A sample calculation is given. The adequacy of the angular interval in the numerical integration is tested. Calculations which show the effect of a change in the angle of truncation are made. Mellin kernels and light scattering coefficients are tabulated.

Table III shows calculated size distribution for the two- to three-micron fraction of spheres and the effect of dilution. The microscope assay was obtained from a photomicrograph, Figure 21, of spheres which were deposited from an alcohol suspension onto a microscope slide. The average sphere diameter was four millimeters at 1800 magnification, or about 2.2 microns. A suspension of spheres of this size should give positive values at two and three microns on the point-by-point representation of the size distribution. If the spheres are measured in terms of volume concentration, then the presence of a particle of an intermediate size would lead to the following inference of the volume fractions of two particles of bracketing sizes:

$$\phi_1' = \frac{d_{P_2}^3 - \bar{d}_P^3}{d_{P_2}^3 - d_{P_1}^3} \qquad (100)$$

In Equation (102), ϕ_1' is the relative concentration of particles of the first bracketing diameter, d_{P_1}; d_{P_2} is the second bracketing diameter; and, $\bar{d}_P$ is the average diameter of particles of intermediate size. The volume fraction computed for the two-micron spheres was 0.842. A four milliliter fraction of the starting suspension contained 6.2 milligrams of spheres, or 0.069 volume per cent spheres at a density of 2.23 grams per cubic centimeter. The data of Table III are based on two suspensions which were prepared by diluting the starting suspension by factors of 12.25 and 27.6, respectively.

The detector factors, C_U and C_E, were obtained by ratioing the actual concentration of the diluted suspension to the total concentrations calculated from the scattering data of each detector. The C_U and C_E differed because of the distinct characteristics of each detector. For the two levels of concentration shown, each value was approximately constant. They increased at higher concentrations because of the onset of multiple scattering.

Table XI compares the scattering measurements with the microscope assay for the eight- to ten-micron fraction of spheres at a concentration of 0.0146 volume per cent. The comparison is also displayed in Figure 24.

The data for the microscope assay was obtained from Figure 21 and five other photomicrographs of the eight- to ten-micron fraction. The number of spheres in each size interval of 1.8 millimeters, starting at 2.7 millimeters, was counted. The intervals were selected such that the midpoint length corresponded to a whole integer of microns, which was taken as the average diameter of the particles in the fraction. A total of 109 spheres were counted. Table X gives the breakdown by size intervals and shows the calculation for the volume fraction of each size.

TABLE X

PARTICLE SIZE ASSAY FOR EIGHT- TO TEN-MICRON FRACTION OF PYREX SPHERES

Size Range at 1800x mm.	Average d_p micron	d_p^3	Number of Particles	$N \times d_p^3$ x 10^{-3}	Fractional Composition Vol./Vol.
4.5- 6.2	3	27	2	0.05	.001
6.3- 8.0	4	64	6	0.38	.007
8.1- 9.9	5	125	6	0.75	.013
10.0-11.6	6	216	3	0.65	.012
11.7-13.4	7	343	14	4.80	.085
13.5-15.2	8	512	44	22.50	.401
15.3-17.0	9	729	28	20.40	.363
17.1-18.9	10	1000	4	4.00	.071
19.0-20.7	11	1331	2	2.66	.047
Total			109	56.15	1.000

TABLE XI

CALCULATED PARTICLE CONCENTRATION OF EIGHT- TO TEN-MICRON FRACTION OF PYREX SPHERES

Particle Size	Computed Concentration at 0.0146 V%				Microscope Assay
	ϕ_i x 10^5		Volume Fraction		
micron	up-stream	down-stream	up-stream	down-stream	Volume Fraction
3	--	--	--	--	.001
4	--	--	--	--	.007
5	--	--	--	--	.013
6	1.33	1.44	.041	.036	.012
7	5.36	6.27	.162	.158	.085
8	10.59	13.11	.321	.329	.401
9	12.02	12.71	.364	.319	.363
10	3.71	6.27	.112	.158	.071
11	--	--	--	--	.047
Total	33.01	39.80	1.000	1.000	1.000

$C_U = (14.6 \times 10^{-5})/(33.01 \times 10^{-5}) = .442$

$C_E = (14.6 \times 10^{-5})/(39.80 \times 10^{-5}) = .367$

$C_E/C_U = .829$

Calculation of Sphere Size Distributions

The particle concentration distributions were calculated according to Equation (80), which is repeated for convenience.

$$\phi_i = \left(\frac{d\phi}{d(d_p)}\right)_i = \frac{510\ d_{p_i}^{\ 2}}{tK(\alpha_i)F_o} \cdot \frac{\text{inch}}{\text{micron}^3}$$

$$\left\{-JY(\alpha_i\theta_m)\theta_m^{\ 4}F(\theta_m) + \Delta\theta \sum_{j=1}^{m-1} F(\theta_j)\ \theta_j^{\ 3}M(\alpha_i\theta_j)\right.$$

$$\left. + \frac{1}{2}\Delta\theta F(\theta_m)\ \theta_m^{\ 3}\ M(\alpha_i\theta_m)\right\} \qquad (80)$$

The subscripts i and j are the size and angle indices, respectively. The functions in Equation (80) are given by Equations (75) and (76).

$$JY(\alpha_i\theta_j) = J_1(\alpha_i\theta_j)\ Y_1(\alpha_i\theta_j) \qquad (75)$$

$$M(\alpha_i\theta_j) = \alpha_i\theta_j\ [J_o(\alpha_i\theta_j)\ Y_1(\alpha_i\theta_j) + J_1(\alpha_i\theta_j)\ Y_0(\alpha_i\theta_j)]$$

$$- J_1(\alpha_i\theta_j)\ Y_1(\alpha_i\theta_j) \qquad (76)$$

Table XII gives values of $M(\alpha\ \theta)$ and $JY(\alpha\ \theta)$ in intervals of 0.01 radian and one micron, which correspond to the intervals used in most of the calculations. Since $\alpha = 5.75$ for a one-micron sphere ($\alpha = \pi d_p/\lambda$), the table was prepared for integer values of $\alpha\ \theta \div 0.0575$. Values of the functions for intermediate arguments were obtained by interpolation. Table XIII gives the values of the light scattering coefficient for Pyrex spheres in the suspending solvent, m = 0.93, which were obtained from the correlations of Penndorf.(47)

TABLE XII

MELLIN KERNEL FUNCTIONS

$\frac{\alpha\theta}{.0575}$	$\alpha\theta$	$M(\alpha\theta)$	$JY(\alpha\theta)$	$\frac{\alpha\theta}{.0575}$	$\alpha\theta$	$M(\alpha\theta)$	$JY(\alpha\theta)$
1	0.0575	-.3255	-.322	55	3.1625	-.1638	.1002
2	0.115	-.340	-.330	56	3.22	-.2329	.0949
3	0.1725	-.3425	-.328	60	3.45	-.472	.0644
4	0.230	-.3445	-.3335	63	3.6225	-.586	.0354
5	0.2875	-.3672	-.3383	64	3.68	-.6104	.0259
6	0.345	-.3760	-.3445	65	3.7375	-.628	.0159
7	0.4025	-.383	-.350	66	3.795	-.636	.0061
8	0.460	-.3885	-.354	68	3.91	-.6238	-.0127
9	0.5175	-.385	-.3612	70	4.025	-.590	-.0298
10	0.575	-.3842	-.3603	72	4.14	-.5225	-.0445
11	0.6325	-.3775	-.3625	74	4.255	--	-.0563
12	0.690	-.3630	-.363	75	4.3125	-.374	-.0608
14	0.805	-.327	-.360	76	4.37	-.3120	-.0645
15	0.8625	-.298	-.357	77	4.4275	-.2476	-.0674
16	0.920	-.2665	-.3525	78	4.485	-.1707	-.0693
18	1.035	-.191	-.342	80	4.60	-.0383	-.0703
20	1.15	-.0980	-.3195	81	4.6575	.043	-.0694
21	1.2075	-.0475	-.3065	84	4.83	.2430	-.0620
22	1.265	.0045	-.2945	85	4.8875	.308	-.0580
24	1.38	.1166	-.2655	88	5.06	.4765	-.0425
25	1.4375	.1685	-.249	90	5.175	.560	-.0300
26	1.495	.230	-.232	91	5.2325	.590	-.0234
27	1.5525	.284	-.213	92	5.29	.6130	-.0166
28	1.61	.3378	-.1949	94	5.405	.638	-.00462
30	1.725	.433	-.1558	95	5.4625	.636	.0038
31	1.785	--	-.1362	96	5.52	.6272	.01035
32	1.84	.5040	-.1161	98	5.635	.584	.0227
33	1.8975	.5555	-.0965	99	5.6925	.552	.0281
34	1.955	.584	-.0768	100	5.75	.513	.0331
35	2.0125	.608	-.0576	102	5.865	.414	.0416
36	2.07	.6240	-.0389	104	5.98	.2955	.0472
38	2.185	.638	-.00357	105	6.0375	.228	.0520
39	2.2425	.628	.0129	108	6.21	.0165	.0518
40	2.30	.6220	.0282	110	6.325	-.1282	.0498
42	2.415	.579	.0556	112	6.44	-.2653	.0453
44	2.53	.5066	.0789	116	6.67	-.4935	.0305
45	2.5875	.466	.0864	117	6.7275	-.536	.0258
48	2.76	.2990	.1055	120	6.90	-.6206	.0106
49	2.8175	.236	.1088	123	7.0725	-.632	-.0051
50	2.875	.1106	.170	124	7.13	-.621	-.00986
51	2.9325	.1022	.1103	125	7.1875	-.600	-.0149
52	2.99	.0322	.1104	126	7.245	-.573	-.0195
54	3.105	-.1124	.1050	130	7.475	.389	-.0339

TABLE XIII

SCATTERING COEFFICIENTS FOR PYREX SPHERES

dp, micron	1	2	3	4	5	6	7	8	9	10	11	12
K	.265	.995	1.90	2.61	2.90	2.68	2.24	1.722	1.44	1.44	1.69	2.00

Table XIV gives the net flux obtained in the upstream and downstream detectors, respectively, for each of the six sphere size distributions discussed in this appendix. The recorded values of the flux are in the units of one of the scales on the high voltage attenuating switch. The net flux was obtained by subtracting the scattered flux of a blank from the gross scatter. The flux scattered by the blank in each detector is also recorded in the tables.

Sample Calculation

The foregoing tables permit a sample calculation for the volume fraction distribution for the more dilute dispersion of the two- to three-micron spheres in the upstream detector. The initial step is the calculation of Θ_m by a straight line extrapolation from the last two values available from the scattering measurements, F(0.11) and F(0.10). The arguments are in radians. For the two- to three-micron fraction of spheres, the change in $F(\Theta)$ was nearly linear in Θ at the extremity of the available scattering pattern. This was usually the case for the dispersions used in the coalescence measurements. The equation for the straight-line extrapolation is $95.6 - 480\ \Theta$. By Equation (79), Θ_m is the nearest whole hundredth radian to the angle at which

$$\frac{d}{d\Theta}\left(\Theta^2 \frac{dI(\Theta)}{d\Theta}\right) = \frac{d}{d\Theta}\left(\Theta^3 F(\Theta)\right) = 0 \qquad (79)$$

TABLE XIV

SCATTERED FLUX DISTRIBUTIONS OF CALIBRATION MEASUREMENTS

			2- to 3-micron				8- to 10-micron	
	Blank		.0056 V%		.0025 V%		.0146 V%	
θ Radian	up-stream	down-stream	up-stream	down-stream	up-stream	down-stream	up-stream	down-stream
.00	8.50*	8.50*	8.33*	8.33*	8.33*	8.33*	7.8*	8.0*
.01	194.5	310.	143.5	155.	64.5	54.0	692.	900.
.015	95.0	126.	--	--	60.4	68.5	635.	836.
.02	60.0	73.1	154.1	187.	66.2	76.5	530.	704.
.025	41.5	49.4	--	--	70.7	78.6	433.	568.
.03	37.8	38.1	160.	193.	70.0	80.8	345.	458.
.035	28.6	32.4	--	--	70.2	82.6	268.	355.
.04	21.4	23.0	152.	186.	68.7	79.7	212.	282.
.045	18.0	19.6	--	--	67.6	77.8	167.6	218.
.05	15.3	17.0	146.7	178.	66.7	75.8	126.4	165.
.055	13.3	15.0	--	--	65.3	73.7	94.8	122.8
.06	11.6	13.3	139.2	168.7	63.6	71.6	70.8	90.6
.065	10.4	11.9	--	--	62.0	69.4	52.2	66.0
.07	9.1	10.8	132.3	157.2	60.5	67.2	40.5	51.3
.075	7.9	9.3	--	--	58.9	65.1	32.5	42.1
.08	7.1	8.6	123.9	146.4	56.9	63.2	27.6	35.5
.085	6.3	8.0	--	--	54.9	61.0	24.6	32.6
.09	5.7	7.4	115.5	135.6	52.7	58.9	23.1	31.2
.095	5.0	6.8	--	--	50.2	56.7	22.4	30.0
.10	4.6	6.2	106.4	124.8	47.6	54.6	21.7	29.2
.105	4.2	5.7	--	--	45.2	52.0	20.6	27.8
.11	3.8	5.1	96.2	113.4	42.8	49.4	19.6	25.6
.115	--	4.5	--	--	--	46.8	--	23.4
.12	--	4.0	--	102.0	--	44.2	--	21.2

* x 10^5

where I is the total flux contained within the polar angle Θ. As a result, $\Theta_m = \frac{3}{4} \cdot \frac{95.6}{480} \approx 0.15$ radian. The additional required values of the scattered flux are supplied by straight-line extrapolation to $\Theta = 0.15$: $F(0.12) = 38.0$; $F(0.13) = 33.2$; $F(0.14) = 28.4$; $F(0.15) = 23.6$.

The quantity within the brackets in Equation (80) is conveniently calculated in tabular form. In Table XV, two columns are allocated to each particle diameter. The first contains the appropriate value of $M(\alpha_i\Theta_j)$. The second gives the product $\Theta_j^3 M(\alpha_i\Theta_j)\,F(\Theta_j)$. In the row for Θ_m, the product is halved in accordance with the requirements of the trapezoidal rule of numerical integration. The sum of the second columns under each sphere diameter, SUM(i), is equivalent to

$$\sum_{j=1}^{m-1} F(\Theta_j)\Theta_j^3\ M(\alpha_i\Theta_j) + \frac{1}{2}\,F(\Theta_m)\Theta_m^3\ M(\alpha_i\Theta_m)\ .$$

The sum must be multiplied by $\Delta\,\Theta = 0.01$ and added to $-F(\Theta_m)\Theta_m^4 JY(\Theta_m)$. These operations are performed in the next four lines of the table. The value within the brackets in Equation (80) is termed INT(i). The calculation is completed by multiplying by the coefficient in front of the brackets. Since none of the individual terms in SUM(1) are positive, the concentration distribution function and the particle concentration for the one-micron spheres are equated to zero by convention. The convention was necessary to exclude the one-micron particles from appearing in the numerical approximation when they were actually not present. Since INT(5) was negative, the concentration of the five micron particles is equated to zero. The particle size distribution was assumed to be mono-nodal. It was truncated at the two- and four-micron intervals.

TABLE XV

SAMPLE CALCULATION OF SPHERE CONCENTRATIONS FROM SCATTERING PATTERNS OBTAINED IN UPSTREAM DETECTOR

			$d_p = 1\mu$		$d_p = 2\mu$		$d_p = 3\mu$		$d_p = 4\mu$		$d_p = 5\mu$	
θ radians	θ^3 x 10^3	F(θ)	M(αθ)	θ^3FM x 10^3	M(αθ)	θ^3FM x 10^3	M(αθ)	θ^3FM x 10^3	M(αθ)	θ^3FM x 10^3	M(αθ)	θ^3FM x 10^3
.01	0.001	64.5	-.3255	- 0.02	-.340	- 0.02	-.3425	- 0.02	-.3445	- 0.02	-.3672	- 0.02
.015	0.003	60.4			-.3425		-.3558		-.3760			
.02	0.008	66.2	-.340	- 0.18	-.3445	- 0.18	-.3760	- 0.20	-.3885	- 0.20	-.3842	- 0.20
.025	0.016	70.7			-.3672		-.386		-.3842			
.03	0.027	70.0	-.3425	- 0.65	-.3760	- 0.71	-.385	- 0.73	-.3630	- 0.69	-.298	- 0.55
.035	0.043	70.2			-.383		-.3808		-.327			
.04	0.064	68.7	-.3445	- 1.51	-.3885	- 1.71	-.3630	- 1.59	-.2665	- 1.17	-.0980	- 0.43
.045	0.091	67.6			-.385		-.336		-.191			
.05	0.125	66.7	-.3672	- 3.07	-.3842	- 3.20	-.298	- 2.43	-.0980	- 0.82	.1685	1.43
.055	0.166	65.3			-.3775		-.2577		.0045			
.06	0.216	63.6	-.3760	- 5.17	-.3630	- 5.00	-.191	- 2.50	.1166	1.60	.433	5.80
.065	0.275	62.0			-.345		-.1212		.230			
.07	0.343	60.5	-.383	- 7.95	-.327	- 6.44	-.0475	- 0.97	.3378	7.00	.608	12.24
.075	0.421	58.9			-.298		.0324		.433			
.08	0.512	56.9	-.3885	- 11.32	-.2665	- 7.76	.1166	3.40	.5040	14.7	.6220	18.10
.085	0.614	54.9			-.2288		.1992		.584			
.09	0.729	52.7	-.385	- 14.78	-.191	- 7.01	.284	10.86	.6240	24.0	.466	17.43
.095	0.859	50.2			-.1445		.3616		.638			
.10	1.00	47.6	-.3842	- 18.28	-.0980	- 4.66	.433	20.10	.6220	29.6	.1106	7.89
.105	1.155	45.2			-.0475		.4865		.579			
.11	1.331	42.8	-.3775	- 21.40	.0045	0.03	.5555	31.65	.5066	28.8	-.1638	- 9.3
.115	1.52	40.4			.0603		.596		.4028			
.12	1.728	38.0	-.3630	- 23.80	.1166	7.66	.6240	41.00	.2990	19.6	-.472	-31.0
.125	1.95	35.6			.1685		.6345		.170			
.13	2.197	33.2	-.345	- 24.75	.230	16.60	.660	46.00	.0322	2.4	-.628	-45.5
.135	2.455	30.8			.284		.611		-.1124			
.14	2.744	28.4	-.327	- 24.55	.3378	26.40	.579	44.00	-.2329	-18.7	-.590	-44.7
.145	3.05	26.0			.3854		.525		-.356			
.15	3.375	23.6	-.298	- 23.15	.433	16.79	.466	18.11	-.472	-18.8	-.374	-14.6
SUM(i) x 10^3				-180.58		30.79		206.66		87.3		-83.4
.01 SUM(i) x 10^3						0.3079		2.067		0.873		- 0.834
JY($\alpha\theta_m$)					-.156		.087		.0644		-.0605	
θ_m^4 F(θ_m) JY x 10^3						1.865		- 1.04		- 0.771		0.728
INT(i) x 10^3						2.173		1.027		0.102		- 0.106

$\phi_i = [d\phi/d(d_P)]_i = (510\ d_{P_i}^2/tK(\alpha i)F_o)(\text{inch/micron}^2)\ \text{INT}(i)$

$\phi_1 = 0$, since no term in SUM(i) is positive

$\phi_2 = (510 \times 4 \times 2.173 \times 10^{-3})/(0.050 \times 0.995 \times 8.33 \times 10^5) = 1.071 \times 10^{-4}$

$\phi_3 = (510 \times 9 \times 1.027 \times 10^{-3})/(0.050 \times 1.90 \times 8.33 \times 10^5) = 0.597 \times 10^{-4}$

$\phi_4 = (510 \times 16 \times 1.02 \times 10^{-4})/(0.050 \times 2.61 \times 8.33 \times 10^5) = 0.077 \times 10^{-4}$

$\phi_5 = 0$, since INT(5) < 0

Effect of Changing Point of Truncation

The typical effect of changing the point of truncation by 0.01 radian can be ascertained from Table XVI. If the integral is truncated at $\Theta_m = 0.14$, the values of SUM(i) are added to $-\frac{1}{2}[F(0.14)(0.14)^3 M(0.14\ \alpha_i) + F(0.15)(0.15)^3 M(0.15\ \alpha_i)]$. The new values of SUM(i) are added to $-F(0.14)(0.14)^4 JY(0.14\ \alpha_i)$. A similar calculation gives values of INT(i) for $\Theta_m = 0.16$. For this, the function of $F(\Theta)$ must be extrapolated an additional 0.01 radian. The angle of truncation has some effect, particularly on the tails of the distribution. The effect increases with increasing distance from the angle at which the derivative, $\frac{d}{d\Theta}(\Theta^3 F(\Theta))$, appears to go to zero.

Effect of Changing the Slope of the Extrapolating Line

Whenever it was necessary to extrapolate the flux distribution to the point of truncation, there was the possibility that the extrapolation would be in error. The possibility of error was increased as the extrapolation was lengthened. In order to appraise this error, the slope of the extrapolating line for the upstream flux distribution of the two- to three-micron fraction having a total particle concentration of 0.0025 volume per cent is increased in magnitude by ten per cent. The new slope was -528/radian and the extrapolating line continues to pass through F(0.11). The equation of the line required a shift of the point of truncation to $\Theta_m = 0.14$ radian. The values of the scattered flux obtained by extrapolation were: $F(0.12) = 37.5$, $F(0.13) = 32.2$, $F(0.14) = 27.0$. New concentration calculations were performed. Table XVII compares the result of the slope

TABLE XVI

EFFECT OF SHIFTING POINT OF TRUNCATION

θ_m radian	$\phi_1 \times 10^5$	$\phi_2 \times 10^5$	$\phi_3 \times 10^5$	$\phi_4 \times 10^5$	$\phi_5 \times 10^5$
0.14	0	10.54	6.15	0.89	0
0.15	0	10.71	5.97	0.77	0
0.16	0	10.83	6.20	1.01	0

TABLE XVII

EFFECT OF TEN PER CENT CHANGE IN SLOPE OF EXTRAPOLATING LINE

Two- to Three-Micron Fraction, 0.0025 V%, Upstream

Extrapolation	$\phi_1 \times 10^5$	$\phi_2 \times 10^5$	$\phi_3 \times 10^5$	$\phi_4 \times 10^5$	$\phi_5 \times 10^5$
Unaltered	0	10.71	5.97	0.77	0
10% Change in Slope	0	9.94	6.16	1.29	0

TABLE XVIII

EFFECT OF INTERVAL HALVING

$\Delta\theta$	$\phi_2 \times 10^5$	$\phi_3 \times 10^5$	$\phi_4 \times 10^5$	$\phi_8 \times 10^5$
0.01	10.71	5.97	0.77	--
0.005	10.69	5.91	0.85	13.11
0.0025	--	--	--	12.71

change with the calculation of Table XV. The percentage concentration changes for the two-, three- and four-micron particles were eight, three and 68, respectively. The concentrations of the three- and four-micron particles increase at the expense of the two-micron particle.

As the size distribution shifted to coarser particles, the angle of truncation became smaller and the slope of the extrapolating line to the point of truncation became steeper. Table XVII shows that the calculations were sensitive to these changes.

Effect of Halving of Interval

The smaller the interval, $\Delta\ \Theta$, in the numerical integration, the better the approximation of the kernel $M(\alpha_i\Theta)$. The larger the α_i, the greater the frequency of oscillation with Θ, and the smaller $\Delta\ \Theta$ should be. An interval of 0.01 radian was used for particles up to five microns. An interval of 0.005 radian was used for larger particles. The SUM(i) of Table XVI involves twice as many terms when the interval is halved. Twice as many values of $F(\Theta_j)$ are required. Table XVIII summarizes the effect of interval halving for the calculation of the concentrations in the two- to three-micron fraction at 0.0025 volume per cent for the upstream detector. The downstream eight-micron concentration of the eight- to ten-micron fraction, whose total concentration was 0.0146 volume per cent, was also included. The additional $F(\Theta_j)$ data for the two- to three-micron fraction are given in Table XV. The additional data for the eight-micron calculation were obtained with sufficient accuracy by interpolation. Table XVIII shows that the 0.01 radian approximating interval was adequate for the two- and three-micron spheres. The number of points used per cycle of the Mellin kernel was the same for the eight-micron and four-micron particles. Halving the interval for the eight-micron spheres caused a three per cent change compared with a ten per cent change for the four-micron particles. At the tail of the distribution, a change in the interval can have a substantial effect as the results for the four-micron drops show.

Broadening of the Distribution by the Mellin Transformation

Since the Mellin transformation was truncated at a finite polar angle, it was expected that the concentration distributions derived from the calculations would be somewhat more diffuse than the distribution of the particles causing the scattering. The diffusion was expected to be particularly apparent for particles up to four microns in diameter. The use of only the first positive half-cycle of the Mellin kernel prevented an accurate screening of particles which were smaller than those actually present in the distributions. Screening on the basis of no positive terms in the summation of Equation (80) was clearly an approximation.

Although some diffusion is apparent in the distributions calculated for the two- to three-micron fraction of Pyrex spheres, Figure 23, it was desireable to investigate the broadening in greater detail by transforming the Rayleigh scattering patterns for monodisperse dispersions of two-, three- and four-micron spheres. A relative index of refraction of 0.93 was assumed for the calculations. Figure 62 shows the respective derived distributions in terms of the volume percent of all spheres present. Considerable broadening appears for the three- and four-micron spheres. In both cases, the peak of the distribution is one micron lower than the size of the spheres which were used in the computation of the scattering pattern. Were there no criterion for subtending the distriburion, large concentration of smaller spheres would have appeared.

The concentration distributions normally encountered in the experiment were similar to that generated by the Rayleigh flux distribution for the three-micron particle. A drop size of three microns was chosen as the most representative in the formation of cross correlations.

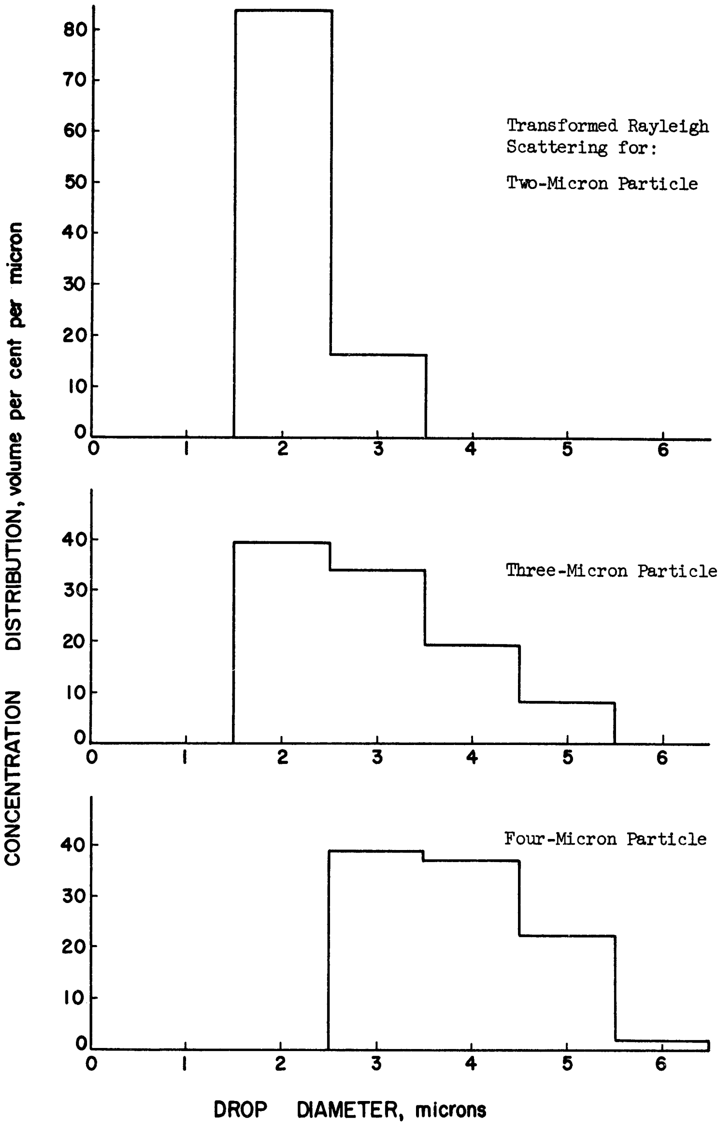

Figure 62. Size Distribution Broadening by Mellin Transformation.

APPENDIX C

COALESCENCE DATA

The method of calculation of fractional coalescence was discussed in the Experimental section. This appendix presents sample calculations. The calculated fractional coalescence is tabulated for each data point used in the various figures and correlations. A logic diagram for the automatic computation of drop concentration is given.

Light Scattering Coefficients

The light scattering coefficient, K, appears as a constant in Equation (80) for each drop size. The light scattering coefficient depends on the relative index of refraction as well as the reduced particle diameter. The light scattering coefficients were computed from the correlations of Penndorf.(47) The measured relative indices of refraction for each liquid system are recorded in Table IV. Table XIX gives the values of K for the liquid-liquid systems used at particle diameters of two, three, four, five and six microns.

Inherent Coalescence

Both total and inherent coalescence of drops of each size were computed by forming the ratio of the concentration in the downstream and upstream optical cells. The concentrations were brought to the same relative level by multiplying the ratio by the ratio of the detector factors, C_E/C_U.

The following example from run 38 with five layers of supports gives the details of the calculation. Table XX contains the pattern of net scattering of the pre-run calibrations. According to the averaging procedure, which was used in conjunction with Equation (86), C_E/C_U was calculated by:

TABLE XIX

LIGHT SCATTERING COEFFICIENTS

Phase of Experiment	System	Relative Refractive Index	K for Various d_p, micron				
			2	3	4	5	6
Calibration	Pyrex in Solvent	0.93	0.995	1.90	2.61	2.90	2.68
Base Points of All Parts	Cyclohexane in Water	1.067	1.07	2.07	2.91	3.30	3.10
Elevated Drop Viscosity	μ_D, c.p.						
	1.46	1.076	1.30	2.34	3.04	3.17	2.84
	2.15	1.081	1.46	2.65	3.18	3.12	2.62
	3.00	1.084	1.61	2.84	3.29	3.00	2.36
	5.13	1.089	1.76	2.97	3.35	2.86	2.28
	10.14	1.092	1.85	3.03	3.32	2.77	2.13
	24.0	1.10	2.10	2.23	3.24	2.50	1.70
Reduced Interfacial Tension	γ, dyne/cm.						
	11.1	1.070	1.16	2.20	2.95	3.19	2.95
	7.6	1.069	1.14	2.16	2.93	3.23	3.00
	4.7	1.045	0.504	1.09	1.725	2.38	2.87
	2.7	1.044	0.504	1.09	1.725	2.38	2.87
Elevated Continuum Viscosity	μ_C, c.p.						
	2.8	1.03	0.24	0.50	0.87	1.297	1.81
	6.2	1.014	0.061	0.140	0.240	0.350	0.481
	7.5	0.984	0.069	0.160	0.262	0.400	0.550
	9.4	0.981	0.103	0.223	0.37	0.582	0.80

TABLE XX

CALIBRATION DATA OF RUN 38

Cell	θ												
	0.0 x10^{-4}	.01	.02	.03	.04	.05	.06	.07	.08	.09	.10	.11	.12
upstream	9.14	53.0	61.9	59.9	56.7	52.6	48.7	44.4	40.8	37.0	33.1	29.2	—
downstream	9.88	81.6	93.3	91.3	86.9	81.4	74.9	68.6	61.8	55.5	48.7	43.8	38.3
upstream	9.32	53.0	66.2	64.2	61.0	56.9	52.5	47.5	43.1	38.7	34.4	30.3	—

$$\frac{C_E}{C_U} = \frac{1}{3}\,\frac{F_E(0)}{F_U(0)}\;\frac{F_U(.09)}{F_E(.09)} + \frac{F_U(.10)}{F_E(.10)} + \frac{F_U(.11)}{F_E(.11)} \qquad (103)$$

Two values of C_E/C_U were computed from the data of Table XX. The average was used.

$$(C_E/C_U)_1 = (1/3)(9.88/9.14)[(37.0/55.5)+(33.1/48.7)+(29.2/43.8)]$$

$$= (1/3)\ 1.08\ (.667 + .680 + .667) = .725$$

$$(C_E/C_U)_2 = (1/3)(9.88/9.32)[(38.7/55.5)+(34.4/48.7)+(30.3/43.8)]$$

$$= (1/3)\ 1.06\ (.698 + .707 + .692) = .742$$

$$(C_E/C_U)_{\text{average}} = .734$$

The non-uniformity of the ratios $F_U(\theta_j)/F_E(\theta_j)$, shows that a slight amount of settling occurred during the measurements.

Table XXI completes the calculation according to Equation (87).

$$1 - f_{s_i} = (\phi_{E_i}/\phi_{U_i})(C_E/C_U) \qquad (87)$$

The data of the traverse at a flow rate of 9.58 cubic centimeters per minute are given as an example. Because of the small concentration, the data for the five-micron drops were not used.

Net Coalescence

Net coalescence was calculated according to Equation (89).

$$f_i = 1 - \frac{1 - f_{t_i}}{1 - f_{s_i}} = 1 - \frac{\phi_{E_i}\,\frac{C_E}{C_U}}{\phi_{U_i}(1 - f_{s_i})} \qquad (89)$$

The f_t is the gross fractional coalescence. The example is taken from Run 22 for three layers of 1000-mesh screen. The C_E/C_U was 0.745. The calculations for the data of the 1-1/2 traverses at a

TABLE XXI

INHERENT COALESCENCE CALCULATION FOR RUN 38

Drop Size micron	ϕ_{E_i} x 10^5	ϕ_{U_i} x 10^5	C_E/C_U	$1 - f_{s_i} = (\phi_E/\phi_U)_i(C_E/C_U)$
2	10.38	7.80	.734	.972
3	8.15	6.24	.734	.957
4	4.03	3.21	.734	.919
5	0.801	0.721	.734	.813
6	--	--	.734	--

TABLE XXII

NET COALESCENCE CALCULATION FOR RUN 22

Traverse	Drop Size micron	ϕ_{E_i} x 10^5	ϕ_{U_i} x 10^5	C_E/C_U	$1-f_{t_i}$	$1-f_{s_i}$	$f_i = 1 - \frac{1-f_{t_i}}{1-f_{s_i}}$
First Upstream	2	2.488	3.82	.745	.484	.936	.480
	3	2.052	3.33	.745	.459	.891	.484
	4	1.167	2.16	.745	.402	.821	.515
	5	0.341	0.918	.745	.277	--	--
Second Upstream	2	2.488	3.67	.745	.505	.936	.460
	3	2.052	3.22	.745	.475	.891	.466
	4	1.167	2.11	.745	.412	.821	.499
	5	0.341	0.932	.745	.273	--	--

velocity of 2.5 centimeters per minute are given in Table XXII. The $1-f_{s_i}$ for the two-, three- and four-micron drops were read from Figures 29, 30 and 31. The $1-f_{s_i}$ are, respectively, .936, .891 and .821. Advanced and final upstream half traverses were performed. At the velocity of 2.5 centimeters per minute, the first upstream and the final downstream half traverses were in the correct time relation. The first group of coalescence results were used. The second group showed that the drop settling was within acceptable bounds.

Computer Program

A computer program was written in MAD language for the execution of the concentration calculations on the IBM 7090 digital computer at the University of Michigan Computing Center. This program merely performed the repetitive arithmetic operations of converting the light scattering patterns to drop concentrations. The conversion of the raw data to a common scale of the high voltage switch and the extrapolation of the net scatter to the point of truncation were performed manually. Figure 62 is a logic diagram of the program. The program required tables of $M(\alpha\ \Theta)$ and $JY(\alpha\ \Theta)$, which were computed manually. The program also contained short tables of K and blank scattering. These were changed as required.

Briefly, the program read in the data from a half traverse and subtracted the appropriate blank scatter. The appropriate cell thickness and the net scattering patterns were recorded with the input data. Next the drop concentrations were calculated successively according to Equation (80). Concentrations, or the point-by-point size distribution, were calculated at intervals of one micron between

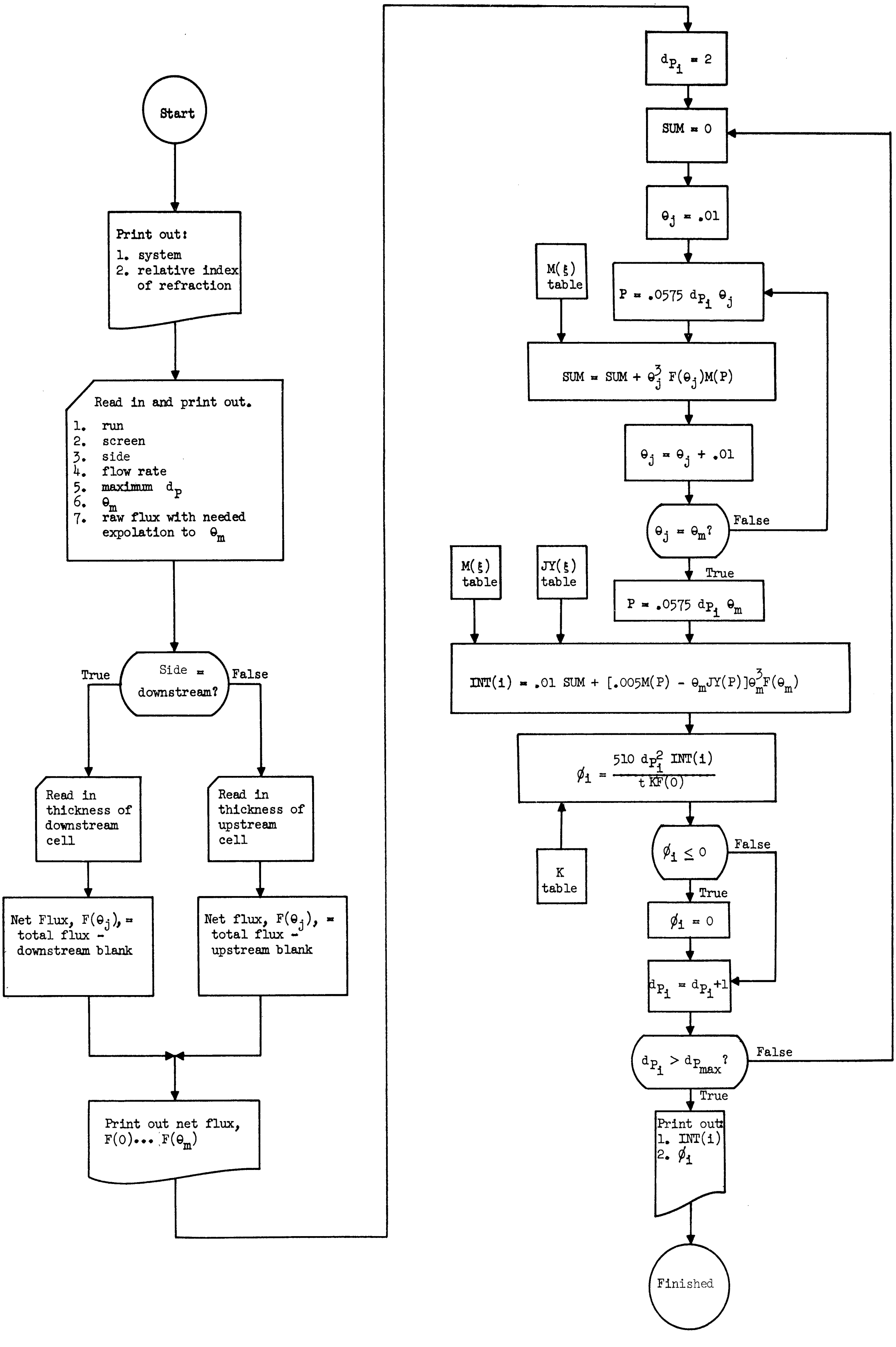

Figure 63. Logic Diagram for Concentration Calculation

two and six microns. The results of the calculation were printed out and the next set of data was read into the computer.

Tables of Data

The coalescence calculations were performed manually for two-, three- and four-micron drops. Inherent fractional non-coalescence data for the support runs and net fractional coalescence for the fine-mesh screen are recorded. Only the data from the runs employed in the correlations are shown. The balance of the runs were culled because of the erratic performance of the screen surface. Table XXIV gives the inherent fractional non-coalescence for the two-, three- and four-micron drops for the various systems employed. Table XXV gives the data for the net fractional coalescence on fine-mesh screen. A description of the various runs is given in Table XXIII. The 40-mesh screen denotes supports or inherent coalescence run. Many of the low velocity measurements were performed with two upstream half traverses. Wherever two were available, the fractional coalescence data computed from the advanced and second upstream half traverse are labeled one and two, respectively, in the upstream half traverse column in Tables XXIV and XXV.

TABLE XXIII

DESCRIPTION OF RUNS

Run No.	Liquid-Liquid System	Temperature °C	Screen Description			Physical Properties		
			Mesh	% Open Area	No. of Layers	μ_C c.p.	μ_D c.p.	γ_{CD} dynes/cm.
10	Cyclohexane in Water	25	750	9	5	1.0	0.885	53.0
11		24	1500	25	3			
14		21	40	50	2			
			1000	25	2			
19		22	40	50	1			
20		22	1000	25	2			
22		22	1000	25	3			
23	(downflow)	22	1000	25	3			
24		22	1000	25	4			
26	(downflow)	22	40	50	3			
31		20	750	9	5			
35		16	1000	25	1			
37		19	400	16	5			
38		19	40	50	5			
44		17	40	50	3			
50		17	750	9	3			
51		17	1000	25	3			
53		20	1000	25	3			
54	25% Fin Oil, 75% Cyclohexane in Water	19	1000	25	3	1.0	1.46	53.0
56	50% Fin Oil, 50% Cyclohexane in Water	18	1000	25	3	1.0	3.0	53.0
57	67% Fin Oil, 33% Cyclohexane in Water	20	1000	25	3	1.0	5.13	53.0
58	80% Fin Oil, 20% Cyclohexane in Water	18	1000	25	3	1.0	10.14	53.0
59	Fin Oil in Water	20	1000	25	3	1.0	24.0	53.0
81	Cyclohexane in Water	21	500	25	5	1.0	0.885	53.0
82		24	40	50	5			
84	10% Cyclohexanol, 90% Cyclohexane in Water Saturated with Cyclohexanol	18	500	25	5	1.026	0.966	11.1
85		20	40	50	5			
86		19	500	25	5			
87	11% Cyclohexanol, 89% Normal Heptane in Water Saturated with Cyclohexanol	20	500	25	5	1.026	0.55	7.6
88		20	40	50	5			
89	50% Cyclohexanol, 50% Normal Heptane in Water Saturated with Cyclohexanol	20	500	25	5	1.026	1.95	4.7
90		20	40	50	5			
91	50% Isobutanol, 50% Normal Heptane in Water Saturated with Isobutanol	24	500	25	5	1.04	0.58	2.7
92	Cyclohexane in Water	21	40	50	5	1.0	0.885	53.0
93		20	1500	25	3			
94		21	500	25	5			
95		20	400	26	5			
96		20	1000	25	3			
97		20	500	25	3			
98		20	500	25	3			
99		23	1500	25	3			
100		21	1000	25	3			
101		21	400	26	3			
102		23	1500	25	3			
103		24	1000	25	3			
104		26	500	25	5			
105	Cyclohexane in 35V% Glycerol, 65V% Water	25	40	50	5	2.8	0.885	--
106		25	500	25	5			
107	Cyclohexane in 50V% Glycerol, 50V% Water	27	40	50	5	5.17	0.885	--
108		22	500	25	5	6.2		
109	Normal Octane in 60V% Glycerol, 40V% Water	23	40	50	5	10.8	0.55	33.
110		27	500	25	5	9.4		
111		27	500	25	5	9.4		
112	Normal Octane in 56.7V% Glycerol, 43.3V% Water	27	500	25	5	7.5	0.55	--
113	Cyclohexane in Water	22	40	50	5	1.0	0.885	53.0

TABLE XXIV

INHERENT FRACTIONAL NON-COALESCENCE

System	Run	U_∞	Upstream Half	Inherent Fractional Non-Coalescence Drop Diameter in Microns		
r = rotameter flow rate measurement		cm./min.	Traverse	2	3	4
Cyclohexane in Water	r 19	1.51	-	.902	.862	.818
		5.56	-	.965	.921	.882
		20.6	-	1.000	.955	.918
	r 14	1.51	-	.917	.865	.796
		5.56	-	.935	.906	.882
		20.6	-	1.000	.956	.920
	r 44	1.51	-	.909	.862	.773
		2.50	-	.943	.874	.710
		3.88	1	.944	.893	.768
			2	.971	.915	.782
		5.56	-	.987	.936	.807
		9.58	-	.987	.952	.860
		20.6	-	1.000	.951	.863
	r 38	53.6	-	1.000	.980	.924
		1.51	-	.906	.881	.809
		2.50	-	.938	.891	.773
		9.58	-	.972	.957	.919
		1.51	-	.919	.884	.792
	r 82	5.56	-	.960	.937	.912
		9.58	-	.975	.955	.924
		20.6	-	.988	.981	.969
		53.6	-	1.000	.977	.938
		1.51	-	.923	.872	.804
		2.50	-	.939	.888	.836
		53.6	-	1.000	.972	.925
		5.56	-	.968	.920	.864
	r 26	1.51	-	.899	.871	.842
		5.56	-	.969	.898	.824
		20.6	-	.992	.938	.901
	92	2.18	-	.885	.843	.745
		2.89	-	.883	.857	.786
		8.15	1	.903	.883	.845
			2	.941	.912	.860
		14.2	-	.980	.948	.885
		32.6	-	1.000	.978	.942
		2.70	1	.876	.830	.777
			2	.874	.825	.762
		3.97	1	.921	.879	.832
			2	.943	.896	.840
		6.66	1	.948	.903	.850
			2	.957	.915	.868
		10.0	-	.991	.929	.838
		100.	-	1.000	.974	.924
	113	2.06	-	.919	--	
		2.04	-	.918	.916	
		5.65	-	.958	.950	
		6.80	1	.973	.953	
			2	.953	.972	
		7.77	-	.986	.970	
		100.	-	.997	.984	
		3.46	-	.917	.911	
Low Interfacial Tension	r 85	5.00	-	.945	.886	.750
γ_{CD} =		7.75	-	.965	.900	.765
11.1 dynes/cm.		11.11	-	.974	.922	.817
		107.3	-	1.000	.922	.770
	r 88	107.3	-	1.000	.940	.826
γ_{CD} =		11.11	-	.968	.915	.787
7.6 dynes/cm.		107.3	-	1.000	.958	.821
		5.00	-	.928	.875	.745
	r 90	5.00	-	.924	.870	.757
γ_{CD} =		7.75	-	.958	.885	.836
4.7 dynes/cm.		107.3	-	1.000	.935	.866
Elevated Continuum Viscosity	105	2.34	-	.905	.885	.830
μ_C =		2.33	-	.964	.894	.749
2.8 c.p.		2.33	-	.896	.864	.792
		3.67	-	.962	.944	.905
		5.41	-	.976	.930	.840
		7.85	-	.976	.948	.869
		12.8	-	1.000	.963	.901
		2.96	-	.947	.915	.865
		4.18	-	.947	.929	.907
		7.31	-	.967	.940	.912
	107	1.88	-	.917		
μ_C =		2.96	-	.942		
5.2 c.p.		2.85	-	.968		
		3.84	-	.969		
		5.65	-	.977		
		8.00	-	.991		
		100.	-	1.000		
	109	1.75	-	.957	.895	.818
μ_C =		1.81	-	.945	.885	.808
10.8 c.p.		2.42	-	.975	.908	.828
		2.48	-	.981	.912	.831
		3.49	-	1.000	.916	.879

TABLE XXV

NET FRACTIONAL COALESCENCE ON FINE-MESH SCREEN

System r = rotameter flow rate measurement	Run	U_∞ cm./min.	Upstream Half Traverse	Net Fractional Coalescence Drop Diameter in Microns		
				2	3	4
Cyclohexane in Water	95	1.91	1	.470	.434	.286
			2	.438	.426	.367
		2.78	1	.415	.406	.371
			2	.319	.330	.332
		3.60	-	.369	.369	.357
		5.28	-	.245	.225	.189
		10.7	-	.020	.024	.057
		13.9	-	.000	.038	.133
		125.	-	.000	.020	.057
	101	2.11	1	.385	.391	.354
			2	.383	.385	.368
		2.25	1	.365	.376	.361
			2	.320	.339	.368
		3.81	1	.182	.179	.160
			2	.151	.156	.154
		3.44	1	.178	.163	.126
			2	.134	.127	.105
		4.70	1	.132	.124	.089
			2	.099	.090	.058
		7.30	-	.096	.085	.058
		9.90	-	.049	.057	.080
		13.85	-	.000	.000	.001
		20.2	-	.000	.028	.093
	r 31	1.51	1	.432	.435	.451
			2	.390	.400	.437
		2.50	1	.368	.385	.397
			2	.340	.356	.369
		3.88	-	.308	.296	.263
		5.56	-	.205	.217	.217
		9.58	-	.192	.197	.175
		14.5	-	.195	.207	.202
		20.6	-	.138	.138	.111
		1.51	1	.491	.497	.497
			2	.491	.500	.501
		53.6	-	.007	.035	.136
	94	100.	-	.024	.047	.099
		1.85	1	.560	.560	.550
			2	.535	.543	.569
		2.18	1	.667	.676	.697
			2	.640	.657	.694
		3.81	1	.456	.455	.459
			2	.441	.443	.447
		2.27	-	.595	.605	.587
		3.50	-	.393	.388	.359
		6.15	1	.313	.310	.294
			2	.311	.296	.255
		9.55	1	.181	.176	.159
			2	.236	.239	.245
		15.8	-	.175	.171	.157
		120.	-	.000	.064	.248
		4.35	1	.428	.439	.406
			2	.418	.433	.404
		5.36	1	.408	.401	.351
			2	.390	.389	.354
		7.22	1	.333	.316	.272
			2	.300	.288	.236

TABLE XXV (CONT'D)

System r = rotameter flow rate measurement	Run	U_∞ cm./min.	Upstream Half Traverse	Net Fractional Coalescence Drop Diameter in Microns		
				2	3	4
	104	100.	-	.000	.000	.015
		2.06	1	.641	.670	.731
			2	.610	.652	.737
		2.30	1	.631	.639	.648
			2	.619	.627	.636
		3.80	1	.508	.514	.514
			2	.469	.473	.470
		3.59	1	.518	.520	.510
			2	.433	.438	.429
		5.52	1	.380	.439	.524
			2	.347	.337	.308
		7.89	-	.353	.384	.425
		11.3	-	.152	.178	.202
		6.73	-	.350	.371	.389
		16.40	-	.130	.178	.242
		22.3	-	.148	.162	.168
		36.7	-	.096	.112	.124
		100.	-	.000	.031	.142
	97	2.52	1	.447	.432	.370
			2	.403	.393	.349
		3.13	1	.346	.346	.312
			2	.353	.340	.289
		3.06	1	.383	.388	.362
			2	.327	.331	.303
		4.35	-	.333	.330	.304
		5.80	1	.207	.213	.188
			2	.149	.136	.087
		7.13	1	.175	.184	.199
			2	.160	.171	.160
		10.0	-	.086	.092	.070
		14.7	-	.000	.000	.000
	98	2.29	1	.427	.403	.288
			2	.402	.397	.354
		2.05	1	.393	.454	.559
			2	.359	.417	.526
		3.41	1	.330	.352	.389
			2	.327	.324	.285
		3.41	1	.356	.355	.341
			2	.287	.287	.271
		4.50	1	.299	.287	.263
			2	.209	.182	.150
		7.45	-	.240	.222	.201
		9.45	-	.096	.122	.177
		14.5	-	.055	.085	.077
		11.5	-	.087	.117	.144
r	10	1.51	-	.494	.498	.529
		2.50	-	.441	.431	.447
		3.88	-	.371	.347	.329
		5.56	-	.310	.316	.267
		9.58	-	.255	.285	.344
		14.5	-	.234	.242	.250
		20.6	-	.087	.193	.202
r	31	1.51	1	.438	.435	.455
			2	.423	.400	.369
		2.50	-	.429	.420	.463
		3.88	-	.324	.329	.357
		5.56	-	.230	.254	.324
		9.58	-	.242	.274	.333
		14.5	-	.189	.188	.211
		1.51	1	.478	.495	.525
			2	.454	.472	.502
		2.50	1	.432	.455	.488
			2	.290	.302	.299
		9.58	-	.282	.308	.335
		1.51	-	.460	.465	.460
		2.50	-	.396	.433	.494
		40.6	-	.043	.081	.193

TABLE XXV (CONT'D)

System r = rotameter flow rate measurement	Run	U_∞ cm./min.	Upstream Half Traverse	Net Fractional Coalescence Drop Diameter in Microns		
				2	3	4
	r 50	1.51	1	.336	.340	.381
			2	.286	.311	.380
		2.50	1	.240	.241	.287
			2	.240	.236	.272
		3.88	1	.207	.194	.182
			2	.188	.168	.146
		5.56	-	.195	.185	.174
		9.58	-	.138	.132	.143
		14.5	-	.069	.071	.105
		20.6	-	.050	.058	.109
		1.51	1	.350	.363	.376
			2	.310	.334	.355
		3.88	1	.240	.242	.226
			2	.223	.224	.223
		5.56	-	.185	.191	.170
	r 35	5.56	-	.137	.154	.207
		9.58	-	.133	.143	.189
		53.6	-	.000	.054	.124
		1.51	1	.241	.249	.282
			2	.236	.235	.260
		2.50	1	.232	.230	.209
			2	.215	.207	.187
		53.6	-	.002	.048	.163
		1.51	1	.238	.250	.312
			2	.204	.215	.301
		2.50	-	.218	.271	.293
		3.88	-	.158	.164	.197
		3.88	1	.201	.218	.249
			2	.174	.194	.232
		5.56	-	.126	.156	.212
	r 20	1.51	1	.474	.480	.527
			2	.447	.469	.544
		2.50	1	.421	.414	.418
			2	.389	.383	.399
		3.88	-	.309	.308	.319
		5.56	-	.241	.265	.310
		9.58	-	.178	.182	.216
		14.5	-	.079	.096	.111
		20.6	-	.038	.050	.079
		1.51	-	.530	.554	.582
		2.50	-	.399	.418	.448
	r 22	1.51	1	.550	.569	.623
			2	.523	.549	.627
		2.50	1	.480	.484	.515
			2	.460	.466	.499
		3.88	-	.376	.382	.418
		5.56	-	.361	.379	.404
		9.58	-	.258	.268	.281
		14.5	-	.144	.154	.182
		20.6	-	.082	.102	.128
		27.0	-	.023	.028	.006
		34.0	-	.028	.029	.017
		40.6	-	.000	.017	.021
		53.6	-	.000	.018	.006
		1.51	1	.657	.677	.709
			2	.636	.655	.690
		2.50	1	.470	.497	.534
			2	.395	.421	.456

TABLE XXV (CONT'D)

System r = rotameter flow rate measurement	Run	U_∞ cm./min.	Upstream Half Traverse	Net Fractional Coalescence Drop Diameter in Microns		
				2	3	4
r	23	1.51	1	.612	.626	.676
			2	.599	.616	.674
		2.50	-	.577	.586	.371
		5.56	-	.477	.491	.505
		9.58	-	.304	.299	.287
		14.5	-	.145	.141	.134
		20.6	-	.087	.082	.078
		1.51	1	.611	.622	.635
			2	.599	.610	.625
		2.50	-	.491	.479	.461
		2.50	-	.542	.545	.548
		5.56	-	.243	.235	.212
		9.58	-	.238	.241	.236
		2.50	-	.436	.430	.405
r	24	1.51	1	.690	.714	.770
			2	.686	.706	.769
		2.50	1	.581	.604	.661
			2	.564	.593	.662
		3.88	-	.494	.509	.547
		5.56	-	.470	.482	.491
		9.58	-	.390	.401	.418
		14.5	-	.207	.208	.210
		20.6	-	.103	.104	.112
		1.51	1	.786	.801	.824
			2	.767	.782	.809
		2.50	1	.667	.686	.718
			2	.655	.666	.684
		3.88	1	.577	.592	.616
			2	.575	.590	.611
	96	1.91	1	.462	.465	.451
			2	.451	.458	.443
		2.09	1	.521	.524	.509
			2	.488	.493	.484
		2.70	1	.437	.430	.399
			2	.404	.408	.406
		100.	-	.101	.100	.100
		3.10	1	.389	.378	.319
			2	.377	.365	.306
		4.06	-	.323	.312	.267
		1.76	-	.537	.527	.468
		2.20	1	.564	.548	.483
			2	.523	.532	.543
		2.78	1	.509	.518	.524
			2	.498	.503	.501
		4.02	-	.475	.459	.412
		2.60	-	.480	.470	.424
		4.16	-	.451	.471	.456
		5.50	-	.401	.413	.409
		7.60	-	.350	.348	.348
		10.42	-	.154	.188	.231
		15.50	-	.188	.180	.163
		22.2	-	.146	.136	.134
		27.4	-	.164	.159	.155
	100	2.23	1	.553	.520	.409
			2	.533	.511	.441
		2.24	-	.556	.528	.429
		3.11	1	.385	.383	.340
			2	.365	.365	.343
		3.62	1	.382	.363	.305
			2	.318	.283	.180
		5.05	-	.325	.314	.272
		6.60	-	.288	.292	.315
		10.52	-	.227	.222	.222
		21.8	-	.194	.182	.163
		11.1	-	.201	.206	.205
		13.07	-	.187	.200	.216
		23.4	-	.196	.190	.181

TABLE XXV (CONT'D)

System r = rotameter flow rate measurement	Run	U_∞ cm./min.	Upstream Half Traverse	Net Fractional Coalescence Drop Diameter in Microns		
				2	3	4
	103	100.	-	.036	.092	.233
		2.18	1	.499	.497	.476
			2	.483	.488	.480
		2.18	-	.557	.550	.517
		3.54	1	.487	.477	.442
			2	.479	.466	.422
		5.08	1	.392	.379	.344
			2	.366	.359	.341
		6.78	1	.368	.351	.305
			2	.308	.282	.215
		9.59	-	.247	.240	.220
		12.32	-	.188	.181	.200
		19.0	-	.185	.177	.164
		24.3	-	.130	.126	.137
		38.2	-	.122	.118	.122
		100.	-	.023	.059	.136
		38.8	-	.083	.107	.143
r	11	1.51	-	.651	.682	.781
		2.50	-	.580	.588	.631
		3.88	-	.530	.530	.549
		5.56	-	.475	.475	.485
		9.58	-	.411	.401	.407
		14.5	-	.347	.352	.358
		20.6	-	.297	.300	.318
		40.6	-	.193	.207	.209
		1.51	-	.708	.711	.712
		2.50	-	.669	.674	.686
		3.88	-	.399	.409	.420
	93	125.	-	.208	.219	.291
		2.56	1	.464	.445	.386
			2	.433	.438	.453
		3.35	1	.537	.482	.278
			2	.495	.463	.357
		5.86	1	.373	.397	.450
			2	.357	.361	.381
		9.42	-	.353	.330	.276
		23.3	-	.263	.246	.236
		33.9	-	.230	.218	.191
		2.65	1	.639	.629	.596
			2	.546	.508	.390
		120.	-	.162	.170	.192
	99	2.14	1	.611	.591	.504
			2	.590	.577	.516
		1.97	1	.608	.614	.596
			2	.556	.573	.593
		3.31	1	.484	.484	.472
			2	.468	.469	.461
		2.68	1	.572	.550	.513
			2	.544	.529	.482
		3.44	1	.466	.456	.405
			2	.411	.389	.297
		4.89	1	.440	.437	.421
			2	.352	.323	.228
		10.19	-	.396	.366	.293
		13.05	-	.353	.341	.315
		18.84	-	.307	.318	.336
		26.1	-	.282	.279	.278
		34.2	-	.260	.262	.274
		44.2	-	.229	.253	.290
	102	2.23	1	.642	.607	.475
			2	.649	.608	.460
		2.10	1	.718	.727	.738
			2	.704	.719	.744
		2.72	1	.664	.666	.667
			2	.649	.657	.674
		2.72	1	.641	.637	.620
			2	.616	.617	.613
		3.78	1	.557	.551	.532
			2	.518	.496	.425
		7.28	1	.385	.391	.402
			2	.351	.334	.288
		4.76	-	.554	.558	.583
		10.21	-	.332	.326	.311
		15.07	-	.259	.245	.211
		19.54	-	.269	.263	.254
		32.6	-	.220	.228	.254

TABLE XXV (CONT'D)

System r = rotameter flow rate measurement	Run	U_∞ cm./min.	Upstream Half Traverse	Net Fractional Coalescence Drop Diameter in Microns		
				2	3	4
Elevated Drop Viscosity, Base Runs	r 51	1.51	1	.303	.318	.317
μ_D = 0.88 c.p.			2	.290	.295	.296
		2.50	1	.219	.215	.197
			2	.202	.199	.182
		3.88	1	.244	.232	.177
			2	.242	.230	.173
		5.56	-	.171	.163	.121
		9.58	-	.182	.170	.132
		14.5	-	.136	.137	.124
		20.6	-	.120	.113	.099
	r 53	1.51	1	.294	.299	.316
			2	.284	.277	.302
		2.50	1	.277	.232	.136
			2	.234	.192	.102
		3.88	-	.240	.222	.196
		5.56	-	.171	.165	.156
		9.58	-	.170	.174	.186
		2.50	1	.258	.267	.264
			2	.244	.240	.246
		3.88	1	.188	.184	.159
			2	.130	.127	.095
		5.56	-	.146	.145	.133
		9.58	-	.143	.143	.141
		20.7	-	.064	.060	.049
		53.7	-	.013	.037	.040
Elevated Drop Viscosity	r 54	1.51	1	.320	.322	.366
μ_D = 1.46 c.p.			2	.348	.388	.375
		3.88	1	.174	.200	.357
			2	.190	.203	.314
		5.56	-	.139	.181	.362
		9.58	-	.163	.169	.252
		14.5	-	.058	.119	.362
		20.6	-	.074	.104	.266
		53.6	-	.000	.048	.217
	r 56	2.50	1	.270	.325	.537
μ_D = 3.0 c.p.			2	.284	.325	.509
		5.56	-	.234	.285	.480
		9.58	-	.166	.228	.458
		14.5	-	.097	.201	.532
		20.6	-	.096	.177	.467
	r 57	2.50	1	.246	.279	.390
μ_D = 5.1 c.p.			2	.260	.283	.366
		3.88	-	.227	.276	.405
		5.56	-	.193	.331	.693
		9.58	-	.130	.228	.482
		20.6	-	.092	.140	.334
	r 58	2.50	-	.309	.336	.446
μ_D = 10.1 c.p.		3.88	1	.244	.332	.563
			2	.223	.321	.574
		5.56	-	.180	.254	.474
		9.58	-	.167	.229	.427
		14.5	-	.102	.172	.399
		20.6	-	.100	.188	.468
	59	2.50	-	.304	.358	.511
μ_D = 24.0 c.p.		3.88	1	.219	.285	.500
			2	.217	.281	.491
		5.56	-	.263	.296	.428
		9.58	-	.196	.208	.300
		14.5	-	.075	.176	.453
		20.6	-	.072	.133	.356
		53.6	-	.000	.087	.345
		1.51	1	.383	.412	.515
			2	.369	.391	.502

TABLE XXV (CONT'D)

System r = rotameter flow rate measurement	Run	U_∞ cm./min.	Upstream Half Traverse	Net Fractional Coalescence Drop Diameter in Microns		
				2	3	4
Elevated Continuum Viscosity μ_C = 2.8 c.p.	106	2.53	1	.420	.379	
			2	.400	.365	
		3.52	-	.320	.275	
		5.83	-	.207	.136	
		8.09	-	.105	.035	
		18.3	-	.019	.000	
		11.15	-	.090	.032	
μ_C = 6.2 c.p.	108	100.	-	.000		
		2.23	1	.147		
			2	.171		
		1.66	1	.231		
			2	.180		
		3.49	1	.150		
			2	.113		
		3.44	-	.158		
		5.30	1	.095		
			2	.139		
		7.58	1	.028		
			2	.000		
		10.45	1	.025		
			2	.020		
		15.03	-	.010		
μ_C = 7.5 c.p.	112	1.86	1	.148		
			2	.108		
		2.57	1	.108		
			2	.060		
		3.81	1	.062		
			2	.061		
		5.37	-	.046		
		7.58	1	.000		
			2	.018		
		10.21	-	.007		
		14.70	-	.000		
μ_C = 9.4 c.p.	110	2.25	-	.100		
		2.32	1	.043		
			2	.048		
		3.94	-	.059		
		3.72	-	.031		
		5.37	-	.020		
		80.	-	.000		
	111	1.72	1	.095		
			2	.122		
		1.81	1	.092		
			2	.066		
		2.41	1	.070		
			2	.109		
		2.42	-	.055		
		2.48	1	.096		
			2	.077		
		4.05	1	.029		
			2	.044		
		5.76	1	.025		
			2	.013		
		7.68	1	.000		
			2	.017		
		80.	-	.000		

TABLE XXV (CONT'D)

System	Run	U_∞	Upstream Half Traverse	Net Fractional Coalescence		
r = rotameter flow rate measurement		cm./min.		Drop Diameter in Microns		
				2	3	4
Low Interfacial Tension, Base Run	r 71	1.51	-	.537	.495	.398
γ_{CD} =		3.88	-	.472	.462	.460
53 dyne/cm.		5.56	-	.426	.420	.415
		9.58	-	.252	.255	.286
		14.5	-	.165	.163	.175
		20.6	-	.110	.126	.169
Low Interfacial Tension	r 84	3.02	1	.464	.322	
γ_{CD} =			2	.409	.315	
11.1 dyne/cm.		5.00	-	.397	.342	
		7.75	1	.273	.255	
			2	.275	.249	
		11.11	-	.212	.231	
		19.16	-	.123	.180	
		29.0	-	.113	.162	
		41.2	-	.050	.146	
		3.02	1	.338	.302	
			2	.264	.233	
		5.00	-	.220	.189	
		7.75	-	.169	.181	
		11.11	-	.105	.140	
		19.16	-	.085	.125	
	r 86	107.3	-	.000	.033	
		5.00	1	.402	.440	
			2	.374	.365	
		7.75	1	.333	.303	
			2	.316	.290	
		11.11	-	.200	.177	
		19.16	-	.143	.153	
γ_{CD} =	r 87	5.00	1	.256	.289	
7.6 dyne/cm.			2	.276	.307	
		7.75	-	.129	.246	
		107.3	-	.000	.063	
		11.11	-	.112	.086	
		19.16	-	.060	.085	
γ_{CD} =	r 89	5.00	1	.212	.299	
4.7 dyne/cm.			2	.192	.272	
		107.3	-	.000	.155	
		7.75	1	.162	.272	
			2	.168	.258	
		7.75	1	.202	.291	
			2	.207	.285	
		19.16	-	.035	.149	
γ_{CD} =	r 91	5.00	1	.005	.088	
2.7 dyne/cm.			2	.000	.058	
		7.75	-	.000	.051	
		107.3	-	.000	.070	
		5.00	-	.000	.039	
		107.3	-	.001	.062	
		11.11	-	.000	.000	

NOMENCLATURE

A = major radius of ellipse; empirical coefficient

$A(\tau)$ = amplitude of oscillation of varicose thread as a function of time

A_o = initial amplitude

a = radius of liquid thread; diameter of aperture in front of light sensitive detector

a_o, a_{2n} = series coefficients in Equations (20) and (21)

B = minor diameter of ellipse; empirical coefficient

$B(\Theta) = \frac{4\pi}{\lambda^2 t} \frac{d}{d\Theta} [\frac{\Theta}{I_t + I(\Theta)} \frac{dI(\Theta)}{d\Theta}]$ = function of scattered flux distribution

b = focal length of lens which converges the light in the collimated beam onto the plane traversed by the aperture of the sensor

b_{2n} = series coefficient in Equation (21)

C, C' = constants

C_E, C_U = detector factors for downstream and upstream detectors, which relate the total measured particle concentration to the actual concentration

c = particle concentration, number per unit volume

$D_{Br} = \frac{kT}{3\pi d_P \mu_C}$ = Brownian diffusion coefficient

d_F = projected width or diameter of filament

d_I = width or diameter of interstice

d_P = diameter of particle, drop or sphere

$\overline{d_P}$ = average particle diameter

E = Faraday of charge = 9.65×10^4 coulombs per gram equivalent of ions

F = force

F_a = short range force of attraction

F_e = electrostatic force

F_g = gravitational force

F_n = normal force

$F(0)$ = flux detected by sensor at axis of collimated beam

$F(\theta)$ = flux detected by sensor at the distance s from the axis of the collimated beam

f = fraction of drops intercepted; net fraction of drops coalesced

f_N = fraction of drops coalesced by N layers of screen

f_s = fraction of drops which inherently coalesce on supports and flow channel

f_t = gross fraction of drops which coalesce

f_1 = fraction of drops coalesced by one layer of screen

$G(\xi)$ = a function of the variable ξ

g = acceleration of gravity

$\vec{g}$ = gravitational acceleration vector

$H(\xi)$ = a function of the variable ξ

h = thickness of continuum film between drop and filament; shortest distance between the surfaces of two equal spheres

h_1 = initial thickness of continuum film

h_2 = thickness of continuum film at which rupture occurs at a specified probability

I = light flux

I_o = flux in incident collimated beam

I_t = flux remaining in collimated beam after passing through a dispersion of thickness t

$I(\theta)$ = flux scattered within the forward cone of half angle θ

i = imaginary root of -1; unit vector in positive x direction

$J(\xi)$ = Bessel function of the first kind of argument ξ

$JY(\xi)$ = $J_1(\xi)Y_1(\xi)$

K = total light scattering coefficient of particle = amount of incident flux of unit intensity scattered in all directions divided by the projected cross section of the particle causing the scattering

$K(\Theta)$ = scattering coefficient which relates the amount of flux of unit intensity which is scattered outside the forward cone of half angle Θ to the projected cross section of the particle causing the scattering

k = Boltzmann's constant = 1.38×10^{-16} erg per molecule per °K

L = length which is not related to drop diameter; float level

$M(\xi)$ = $\xi\ [J_0(\xi)Y_1(\xi) + J_1(\xi)Y_0(\xi)] - J_1(\xi)Y_1(\xi)$

N = number of layers of screen

n = number of runs included in a data correlation

n_0 = ion concentration, gram equivalents per cubic centimeter

P = pressure

P' = $P + \rho_C\Omega$ = sum of pressure and body force potential per unit volume

P_∞ = pressure at infinity

p_F = filament pitch

q = volumetric flow rate

$\bar{q}$ = volumetric charge density, coulombs per cubic centimeter

R = universal gas constant

$R(\Theta)$ = $K(\Theta)/K$

r = radial distance from center of interstice or center of film between drop and filament

S_D = $\gamma_{SC} - \gamma_{SD} - \gamma_{CD}$ = spreading coefficient of drop on filament in the presence of the continuum

s = displacement of aperture of detector from axis of collimated beam

T = absolute temperature

t = thickness of optical cell or dispersion through which light passes

U = velocity of continuum

U_s = settling velocity of drop

U_o = interstitial velocity

U_∞ = upstream velocity

$\vec{U}$ = velocity vector of continuum

$\overset{\rightrightarrows}{U}$ = $\vec{U}/U_\infty$

u_x, u_y, u_z, u_r = velocity components of continuum in x, y, z and radial directions, respectively

V_H = holdup volume between optical cells

$\vec{W}$ = velocity vector of drop or particle

$\overset{\rightrightarrows}{W}$ = $\vec{W}/U_\infty$

w = $u_x - iu_y$ = complex velocity

x = distance from origin along cartesian co-ordinate parallel to upstream velocity

Y = $\cos\left(\frac{2\pi y}{p_F}\right)$ = reduced distance parallel to plane of parallel cylinders

y = distance from origin along cartesian co-ordinate perpendicular to upstream velocity; distance parallel to plane of parallel cylinders

y_s = distance through which drop settles in flowing between optical cells

z = distance along cartesian co-ordinate perpendicular to x and y co-ordinates; axial distance in cylindrical co-ordinates; thickness of screen; complex variable in two dimensional flow = $x + iy$

Greek Symbols

α = $\pi d_P/\lambda$ = dimensionless drop circumference

β = $\frac{1}{18}\,\frac{\rho_D d_P^2 U_\infty}{\mu_C d_F}$ = inertial parameter

β' = $\left(\frac{2\rho_C U_o d_P^2}{\pi\mu_C d_I}\right)^{0.5}$ = modified inertial parameter

Γ = net force, which is directed along the filament surface into the continuum, acting on the liquid-liquid-filament junction

γ = interfacial tension or surface tension

γ_{CD} = interfacial tension between continuous and dispersed phases

γ_F = frictional resistance of filament surface to motion of liquid-liquid-solid boundary per unit length of boundary

γ_{SC} = interfacial tension between filament and continuum

γ_{SD} = interfacial tension between filament and dispersed phase

γ^* = force per unit length resisting breakaway of dispersed phase from filament

δ = $\left[\frac{\epsilon\epsilon_o RT}{E^2 \sum\limits_k n_{ok}\nu_k^2}\right]^{\frac{1}{2}}$ = thickness of electric double layer

ϵ = dielectric constant of continuum; volumetric void fraction of fibrous mat

ϵ_o = permittivity of free space = 8.85×10^{-14} coulomb per volt centimeter

ζ = $\frac{\pi z}{p_F}$ = dimensionless complex variable in Equations (20) and (21); average uni-directional displacement of drop by Brownian diffusion

ζ_{max} = maximum displacement of drop from bypassing stream into position of interception by Brownian diffusion

η = fraction of inherent coalescene between two optical cells occurring upstream of screens

Θ = polar angle at which light is scattered; contact angle between filament and liquid-liquid interface measured through dispersed phase

Θ' = dynamic contact angle

Θ_m = polar angle at which Mellin transformation is truncated

$\Delta\,\Theta$ = angular interval used in numerical approximation of Mellin transformation

λ = root of Equation (29); wave length of incident monochromatic light; wave length of oscillation

μ = viscosity

ν = kinematic viscosity; valence

ξ = $h + r^2/d_P$ = equation of paraboloid of revolution; dummy variable

ρ = density

σ_n = normal stress

τ = time

$\tilde{\tau}$ = $2U_\infty/d_F$

Φ = flow potential

ϕ = volume fraction of drops or spherical particles

ϕ' = relative volume fraction

ψ = electrical potential caused by ion distribution

ψ_o = electrical potential at interface

Ω = body force potential

$\Omega(z)$ = complex expression for vorticity

$\Omega(\tau)$ = amplitude growth function

ω = vorticity

Subscripts

C = continuum

D = drop or dispersed phase

E = downstream optical cell

i = index of particle sizes or drop diameters

j = index of polar angles at which light is scattered

k = index of ionic species

S = solid or filament surface

U = upstream optical cell

BIBLIOGRAPHY

1. Arthur D. Little, Inc., WADD Technical Report 60-263 AD-243251 (1956).

2. Bierman, A., J. Colloid Sci., 10, 231 (1955).

3. Bloomquist, C. R. and Clark, A., Ind. and Eng. Chem., Analytical Ed., 12, 61 (1940).

4. Boll, R. H. and Sliepcevich, C. M., J. Optical Soc. of Am., 46, 200 (1956).

5. Bosanquet, C. H., in appendix to paper of J. C. Stairmand, Trans. Inst. Chem. Eng. (London), 28, 130 (1950).

6. Buchanan, R. H., Australian J. of Applied Science, 3, 233 (1952).

7. Burtis, T. A., Desalting Crude Oil with Fiberglas, M.S. Thesis, University of Texas (1946).

8. Burtis, T. A. and Kirkbride, C. G., Trans. Am. Inst. Chem. Eng., 42, 413 (1946).

9. Carman, P. C., Trans. Inst. Chem. Eng. (London), 15, 150 (1937).

10. Charles, G. E. and Mason, S. G., J. Colloid Sci., 15, 105 (1960).

11. Charles, G. E. and Mason, S. G., J. Colloid Sci., 15, 236 (1960).

12. Chen, C. Y., Chem. Reviews, 55, 595 (1955).

13. Chin, J. H., J. Physical Chem., 59, 841, 845 (1955).

14. Chin, J. H., Particle Size Distributions from Angular Variation of Intensity of Forward Scattered Light, Ph.D. Dissertation, The University of Michigan (1955).

15. Clark, G. C., Light Scattering in Dense Dispersions of Spherical Particles, Ph.D. Dissertation, The University of Michigan (1959).

16. Dallemand, J. E., "Stepwise Regression Program on the IBM 704," GMR-199, General Motors Corporation Research Laboratories, Warren Michigan (November, 1958).

17. Davies, J. T. and Rideal, E. K., Interfacial Phenomena, p. 1-55, 391-3, Academic Press, New York (1961).

18. Derjaguin, B. V., Trans. Faraday Soc., 36, 203, 730 (1940).

19. Derjaguin, B. V. and Titijevskaya, A. S., "Static and Kinetic Stability of Free Foams and Froths," *Second International Congress of Surface Activity*, Vol. I, p. 211, Butterworths, London (1957).

20. Eley, D. D., "Some Possible Factors Involved in Joint Strength," in *Adhesion and Adhesives: Fundamentals and Practice*, p. 21, Society of Chemical Industry, London (1954).

21. Fairs, G. L., *Trans. Inst. Chem. Eng. (London)*, *36*, 476 (1958).

22. Farnand, J. R., Smith, H. M. and Puddington, J. E., *Can. J. Chem. Eng.*, *41*, 94 (1961).

23. Ford, T. F., *J. Physical Chem.*, *64*, 1168 (1960).

24. Fowler, J. L. and Hertel, K. L., *J. Applied Phys.*, *11*, 496 (1940).

25. Fuks, N. A., *Mechanics of Aerosols*, pp. 68-74, 123-9, 240-58, Academy of Sciences of the U.S.S.R., Institute of Scientific Information, Moscow (1955); U.S. Army Chemical Warfare Laboratories Special Publication 4-12.

26. Gallily, I., *J. Colloid Sci.*, *12*, 161 (1957).

27. Gillespie, T., *J. Colloid Sci.*, *13*, 32 (1958).

28. Grootenhuis, P., *Inst. Mech. Eng. Proceedings, (London)*, *168*, 837 (1954).

29. Gumprecht, R.O., *Particle Size Measurements by Light Scattering*, Ph.D. Dissertation, The University of Michigan (1952).

30. Gumprecht, R. O. and Sliepcevich, C. M., *J. Physical Chem.*, *57*, 90 (1953).

31. Hamaker, H. C., *Physica*, *4*, 1058 (1937).

32. Hasimoto, H., *J. Physical Society of Japan*, *13*, 633 (1958).

33. Hughes, R. R. and Gilliland, E. R., *Chem. Eng. Progress*, *48*, 497 (1952).

34. Johnson, R. E. and Dettre, R. H., "Contact Angle Hysteresis," in *Contact Angle, Wettability and Adhesion*, *Advances in Chemistry Series*, *43*, p. 112, American Chemical Society, Washington, D.C. (1964).

35. Jones, S. C., *On the Behavior of a Pulsed Extraction Column*, Ph.D. Dissertation, The University of Michigan (1962).

36. Jones, T. G., Durham, K., Evans, W. P. and Camp, M., *Second International Congress of Surface Activity*, Vol. I, p. 225, Butterworths, London (1957).

37. Kada, H. and Hanratty, T. J., A.I.Ch.E. Journal, 6, 624 (1960).

38. Kemball, C., "Intermolecular Forces and the Strength of Adhesive Joints," in Adhesion and Adhesives: Fundamentals and Practice, p. 69, Society of Chemical Industry, London (1954).

39. Lamb, H., Hydrodynamics, 6th ed., p. 151-5, Dover Publications, New York (1945).

40. Lange, N. A. (ed.), Handbook of Chemistry, 9th ed., Handbook Publishers, Inc., Sandusky, Ohio (1956).

41. Langmuir, I., O.S.R.D. Report No. 865, Serial No. 335 (1942).

42. Levich, V. G., Physicochemical Hydrodynamics, Chapter 9, Prentice-Hall, Englewood Cliffs, New Jersery (1962).

43. MacKay, G. D. M. and Mason, S. G., J. Colloid Sci., 16, 635 (1961).

44. Miyagi, T., J. of the Physical Society of Japan, 13, 493 (1958).

45. Morey, G. W., Properties of Glass, 2nd ed., p. 16, 505, Reinhold Publishing Corp., New York (1954).

46. Neumann, H. J., Die Naturwissenschaften, 50, 544 (1963).

47. Penndorf, R. B., "New Tables of Mie Scattering Functions for Spherical Particles, Part 6," Geophysical Research Papers No. 45, Geophysics Research Directorate, Air Research and Development Command (March, 1956).

48. Perry, J. H. (ed), Chemical Engineers' Handbook, 3rd ed., p. 371, McGraw-Hill, New York (1950).

49. Ramskill, E. A. and Anderson, W., J. Colloid Sci., 6, 416 (1951).

50. Rose, P. M., Mechanisms of Operation of a Fibrous Bed Coalescer, M.S. Thesis, Illinois Institute of Technology, Chicago (June, 1963).

51. Rumscheidt, F. D. and Mason, S. G., J. Colloid Sci., 17, 260 (1962).

52. Sullivan, R. R. and Hertel, K. L., J. Applied Phys., 11, 761 (1940).

53. Tabor, D., in discussion to D. D. Eley, "Some Possible Factors Involved in Joint Strength," in Adhesion and Adhesives: Fundamentals and Practice, p. 21, Society of Chemical Industry, London (1954).

54. Thomas, D. G. and Lapple, C. E., A.I.Ch.E. Journal, 7, 203 (1961).

55. Tomotika, S., Proc. Royal Soc. (London), A150, 322 (1935).

56. Uhl, V. W. and Furini, B. An Overall Survey of Coalescence, Drexel Institute of Technology, Philadelphia (1961).

57. Verwey, E. W. and Overbeek, J. Th. G. Theory of the Stability of Lyophobic Colloids, Elsevier, Amsterdam (1948).

58. Voyutskii, S. S., Kal Yanova, K. A., Panich, R. M. and Fodiman, N. M. Doklady Akad. Nauk. S.S.S.R., 91, 1155-8 (1953).

59. Wang, Y. L. and Longwell, P. A. A.I.Ch.E. Journal, 10, 323 (1964).

60. Wiegand, W. A. Coalescence of Drops in a Liquid Field, M.S. Thesis, Illinois Institute of Technology (June, 1963).

61. Wiggins, E. J., Cambell, W. B. and Maass, O. Canadian J. of Research, 17, 761 (1939).

62. Witzmann, H. Zeitschrift für Elektrochemie, 46, 343 (1940).

63. Wong, J. B., Ranz, W. E. and Johnstone, H. F. J. Applied Phys., 27, 161 (1956).

64. Zisman, W. A. "Relation of Equilibrium Contact Angle to Liquid and Solid Constitution," in Contact Angle, Wettability, and Adhesion, Advances in Chemistry Series, 43, p. 1, American Chemical Society, Washington, D.C. (1964).